Dissertation zur Erlangung des Doktorgrades

der Fakultät für Chemie und Pharmazie

der Ludwig-Maximilians-Universität München

Exploring New Photocatalytic Applications with Covalent Organic Frameworks: Oxygen Evolution, Water-Gas Shift, and Photoredox Catalysis

Stefan Trenker

aus

Marburg, Deutschland

2023

Erklärung

Diese Dissertation wurde im Sinne von § 7 der Promotionsordnung vom 28. November 2011 von Frau Prof. Dr. Bettina Lotsch betreut.

Eidesstattliche Versicherung

Diese Dissertation wurde eigenständig und ohne unerlaubte Hilfe erarbeitet.

München, den 05.09.2023   _____

                                                                              Stefan Trenker

Dissertation eingereicht am: 07.09.2023

1. Gutachterin: Prof. Dr. Bettina Lotsch

2. Gutachter: Prof. Dr. Konstantin Karaghiosoff

Mündliche Prüfung am: 24.10.2023

Acknowledgements

"Alle andern Dinge müssen; der Mensch ist das Wesen, welches will."

Friedrich Schiller

Summary

Due to the ever-increasing impact of man-made climate change on today's society, the 21st century is coined by political, economic, and especially ecologic disruptions. To mitigate global warming, nations and organizations are seeking to reduce greenhouse gas emissions worldwide. Consequently, science and engineering have to provide the technical means to do so. In the example of private transportation, great progress in battery technology has made electric vehicles competitive compared to conventional fuel-powered vehicles. Similarly, both individual households and energy providers can build on ever improving photovoltaic panels. Other research areas, however, are far from being that mature and relevant in everyday life – and thus offer a lot of room for improvement. For example, solar energy cannot only be collected as electric energy *via* solar cells, but it could also be used to store energy in the form of chemical bonds such as hydrogen *via* photocatalytic water splitting. To be economically competitive, the respective photocatalyst material and its performance have to be maximized.

A new, promising class of materials for photocatalytic applications are covalent organic frameworks (COFs) – porous, ordered networks constructed from organic building blocks in a predictable and customizable manner. Over the last century, COFs have shown to be excellent candidates for the photocatalytic hydrogen evolution half-reaction. The other side of overall water splitting, i.e., oxygen evolution, has not been achieved with designated COF photocatalysts before the beginning of this thesis. Possibly, this was due to the thermodynamic and kinetic complications underlying the reaction mechanism. Our approach to tackle photocatalytic oxygen evolution largely built upon our expertise in hydrogen evolution photocatalysis and consisted in combining a light-absorbing COF with a literature-known water oxidation catalyst based on iridium, as outlined in chapter 2. In chemical water oxidation experiments, we could show that the iridium complex was still active after attachment to TAPB-BPY COF via designated bipyridine binding sites. Photocatalytic oxygen evolution, however, could not be achieved. In an extended study, we reviewed and – more importantly – reproduced COFs reported in the literature for oxygen evolution from 2019 on. We could, however, not reproduce the stated oxygen evolution rates, and in general found little reliable literature data to build upon. However, in some cases, we did observe oxygen evolution. We took this as an opportunity to carefully investigate the underlying reaction mechanisms, with a special focus on sacrificial electron acceptors. Especially silver nitrate is often used to substitute the hydrogen evolution half-reaction. Despite identifying and testing four possible pathways for AgNO$_3$ decomposition, none could explain the observed oxygen evolution. Instead, we narrowed down the cause of oxygen evolution – at least in our case – to catalytically active species contaminating the instrumental setup. Though this should be considered a special case, our findings raise awareness for the necessity of carefully conducting and extensively reporting blank experiments. With the help of computational chemistry, we finally identified possible bottlenecks in the photocatalytic oxygen evolution reactions with iridium-loaded TAPB-BPY COF.

In chapter 3, another aspect of oxidative photocatalysis with COFs is discussed. We report on a COF constructed from specifically designed alloxazine linkers. Like their isoalloxazine or flavin isomers,

alloxazines exhibit redox activities that can be exploited for catalytic applications. Inspired by their molecular counterparts, we chose to use our new COF for organic oxidations. More specifically, we investigated aerobic alcohol oxidations with the so-called FEAx-COF as photocatalyst. In contrast to homogeneous alloxazine catalysts, our COF does not only provide easier handling. Also, the incorporation of the chromophore into a conjugated framework increased its light absorption range, so that the COF also functions with longer wavelength green light as opposed to molecular model compounds that require blue or violet illumination. In the context of green chemistry, conducting alcohol oxidations with heterogeneous photocatalysts represents an interesting approach since it avoids the use of hazardous or toxic reagents and instead relies on dioxygen as the terminal oxidant. Also, no noble metal catalysts are required for this specific reaction when using FEAx-COF.

Lastly, in chapter 4 we make use of our experience with iridium-loaded COFs and utilize them as catalyst for a different application, i.e., the water-gas shift (WGS) reaction. Here, the COF acts mainly as a heterogeneous support and not as a photosensitizer. However, the WGS reaction only proceeds upon irradiation of the iridium centers due to the underlying mechanism that involves photo-induced hydrogen formation. Again, we first confirm the retained catalytic activity of the Cp*Ir species bound to COF frameworks – though here we concentrate on reductive catalysis schemes in the form of transfer hydrogenations. Similar to WGS catalysis, hydrogenations of aldehydes to alcohols by iridium complexes proceed *via* intermediate Ir-H species. Subsequently, we test the conversion of CO and H_2O to CO_2 and H_2 and confirm that iridium-loaded COFs catalyze the WGS reaction upon illumination, yet with activities one order of magnitude lower than the parent molecular Ir complex. In a subsequent spectroscopic study, we correlate visible color changes of our reaction mixtures to their catalytic activity, considering the underlying intermediate reduction of orange Ir(III) to blue Ir(I). As we could only observe such light absorption changes in aqueous COF suspensions, but not in solid samples, we hypothesize that the probed series of iridium-loaded COFs only catalyzes the WGS reaction at the solid-liquid interface. Still, by tuning the underlying COF characteristics such as hydrophilicity, WGS catalysis at the solid-gas interface can be envisaged.

Table of Contents

1   Introduction

1.1   Economic and Ecological Background

With the Paris Agreement of 2015, worldwide consent on the need to reduce greenhouse gas emissions was put to record. 194 parties and countries agreed to collaborate in reducing their greenhouse gas emissions in order to limit the anthropogenic increase of the global average temperature to 2 °C.[1,2]

Since most greenhouse gas emissions are caused by the combustion of fossil fuels resulting in CO_2, this ambitious goal can only be achieved by converting processes that currently still depend on energy carriers such as coal, oil, and natural gas.[3–5] Despite the consensus on the need to reduce greenhouse gas emissions, the global CO_2 emission increased by 0.6% annually from 2011-2021.[6] Still, power generation from renewable sources such as sunlight and wind increased by 15% in the same period.[6] According to different models trying to predict the future of energy production and consumption, greenhouse gas emissions are anticipated to ultimately decrease as power generation from fossil fuels loses its share to renewables.[4] Among the available sources of renewable energy, solar energy can be considered especially attractive given that the total irradiance surpasses the global energy need by a factor of around 10,000.[7,8] In fact, solar power is expected to spearhead the growth of environmentally-friendly power generation – partly because constant technical improvements turned photovoltaics into one of the lowest priced source of electricity.[4] The concept of photovoltaics (PV), i.e. the direct conversion of solar irradiation to electrical energy using semiconductor panels, is discussed later within this thesis.
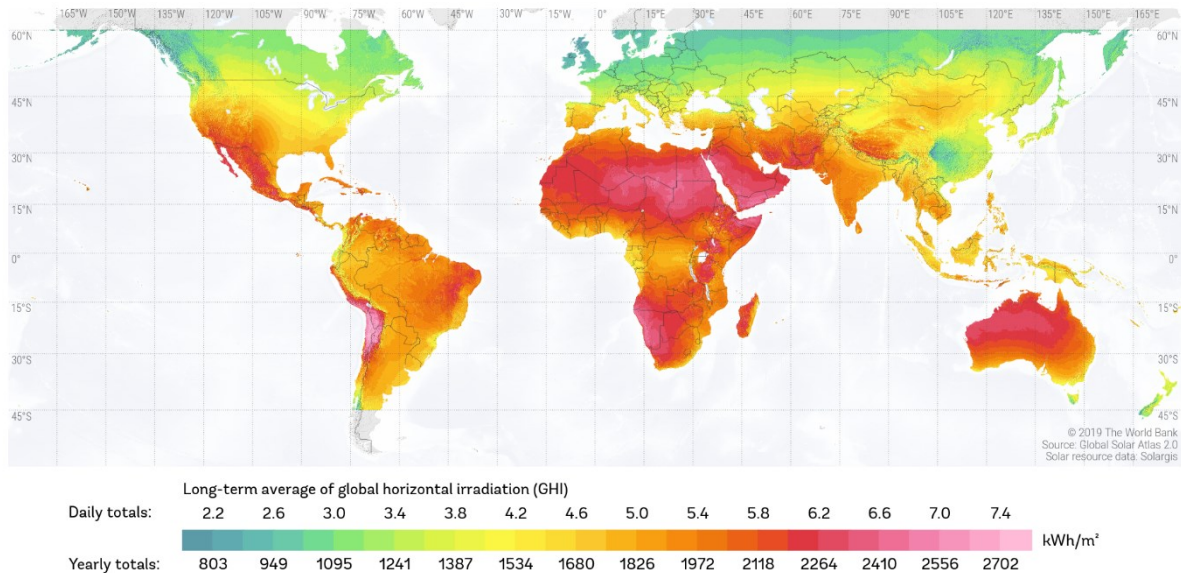
Figure 1-1: Global representation of average GHI values as a measure of PV efficacy. Obtained from the Global Solar Atlas 2.0, developed and operated by Solargis s.r.o. on behalf of the World Bank Group, utilizing Solargis data, with funding provided by the Energy Sector Management Assistance Program (ESMAP).[9]

However, the potential for solar energy collection varies significantly worldwide. Judging from data on the global horizontal irradiation (GHI), which is a key value in predicting the efficiency of photovoltaic

cells, four hotspots can be identified: The Andes, Arabia, Australia, and Africa (Figure 1-1).[10] Especially the latter stands out with roughly 27 million square kilometers exhibiting GHI values above 1800 kWh m^{-2} a^{-1}; in other words, 90% of the African continent shows high potential for photovoltaics.[10] In theory, covering an area of 69,000 km^2 in the Sahara desert with PV cells could provide enough energy to cover the global energy demand of 595 EJ.[6-*]

For comparison, approximately twice the area of solar cells positioned in Germany would be needed for the same energy generation capacity, given an average GHI of 1120 kWh m^{-2} a^{-1} in central Germany.[11] Thus, it would seem evident to produce large amounts of solar power in "hotspot" countries and to transfer them to consumers in places with lower irradiance. This idea initially led to the foundation of the DESERTEC initiative in 2009, and its goal to cover 15% of Europe's energy demand through solar energy collected in the Middle East and northern Africa by 2050.[10,12] However, for political and technical reasons, the DESERTEC project is far from reaching its original goal.[10,13] On the technical side, the planned transfer of large amounts of electricity *via* high-voltage direct current lines from Africa to Europe can be regarded as a major hurdle – and has in principle been replaced by the green hydrogen concept.[14] This color-coded classification simply comprises H$_2$ produced with energy from renewable sources – opposed to grey hydrogen, which is made from fossil fuels for example *via* steam reforming.[15]

Not only does this concept avoid the use of long-distance high-voltage grids; it also exemplifies the storage of electrical energy in chemical bonds. Green hydrogen production allows for the decoupling of energy supply and energy demand. Surplus electricity generated *via* PV or wind turbines, for example, can be first stored in the form of H$_2$ and later – and eventually at distant locations – reconverted to electrical or thermal energy in the absence of sunlight or wind, respectively.

Alternative storage options include, but are not limited to, batteries and pumped-storage hydroelectricity, where energy is stored in electric potential and (gravitational) potential energy, respectively. While both are established forms of storing small (batteries) or large amounts (pumped-storage) of energy, the storage of energy in chemical bonds is by far more suited for long-distance energy transport. Green hydrogen, for example, could be exported either directly as a fluid – which is technically challenging – or after conversion to easier transportable compounds such as methane, methanol, or ammonia.[3]

The ability to transform hydrogen into other similarly valuable chemicals constitutes one of the requisites underlying the so-called sector coupling and especially the closely related power-to-X concept. Sector coupling describes an approach to interconnect the power-producing sector with the energy-consuming sectors transport, buildings, and industry – and ultimately optimize this interplay (Figure 1-2).[5] From an environmental point of view, the ultimate goal would be to completely defossilize all sectors and only use renewable sources for power generation. Note that defossilization is not to be confused with decarbonization, since carbon-based fuels can still be included as energy

---

[*] Area A estimated according to: $A = \dfrac{\text{global energy need(2021)}}{\text{PV yield(Sahara,approx.)}} = \dfrac{18.2\,\text{TW} \cdot 8760\,\text{h a}^{-1}}{2300\,\text{kWh a}^{-1}\,\text{m}^{-2}} \approx 69{,}000\,\text{km}^2$

carriers. Ideally, carbon dioxide emitted in combustion processes for either heat generation or transportation is ultimately recycled, leading to net-zero CO_2 emissions. In order for such carbon utilization schemes to be remotely economically feasible, the underlying carbon capture has to be cost-effective. To date, it is highly favorable to obtain CO_2 from highly concentrated industrial exhausts instead of capturing it directly from the air – the latter is estimated to cost more than 200 € per ton of CO_2, about four or five times as much as capturing it at power plants burning fossil fuels.[3,16]
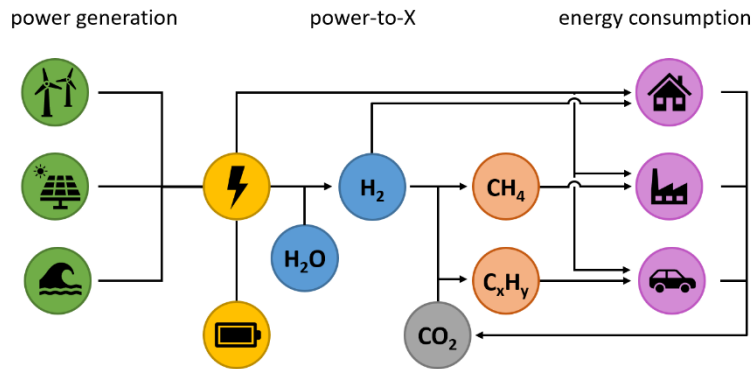
Figure 1-2: Schematic representation of sector coupling and the power-to-X principle.

The prime example for CO_2 recycling processes is its hydrogenation (or methanation) with (green) hydrogen to CH_4. Not only is this conversion the major power-to-gas technology (PtG) in the power-to-X concept, it also comprises the most important gaseous species in sector coupling: H_2, CO_2, and CH_4. Given the infrastructural background and varying needs of each sector, interconversion of these gases can proof essential, since it provides a certain degree of flexibility.[17] Luckily, the required chemical processes are long known and have been optimized over decades, if not centuries.

The transformation of CO_2 into CH_4 has been first described in detail by PAUL SABATIER in the early 20th century during his investigation on hydrogenations of organic compounds for which he was awarded the Nobel Prize in 1912 (Figure 1-3).[18] Using a nickel catalyst and reaction temperatures around 300 °C, SABATIER could achieve almost quantitative conversion of CO_2 to CH_4 according to eq. 1.[19] When using carbon monoxide as reactant instead, lower temperatures of about 230 °C proved sufficient to produce methane (eq. 2).

$$CO_2 + 4\,H_2 \;\rightarrow\; CH_4 + 2\,H_2O \qquad \text{(eq. 1)}$$
$$CO + 3\,H_2 \;\rightarrow\; CH_4 + H_2O \qquad \text{(eq. 2)}$$

$$CO + H_2 \;\rightarrow\; C_xH_y \qquad \text{(eq. 3)}$$

$$CO_2 + H_2 \;\rightarrow\; CO + H_2O \qquad \text{(eq. 4)}$$
$$CO + H_2O \;\rightarrow\; CO_2 + H_2 \qquad \text{(eq. 5)}$$
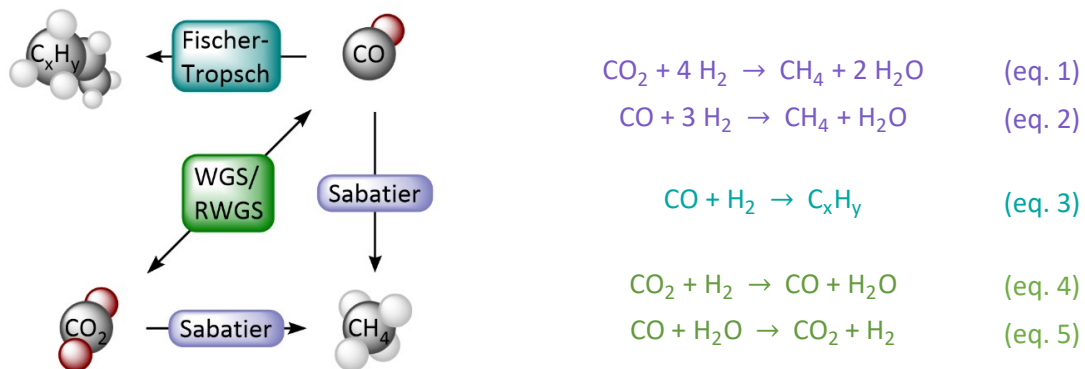
Figure 1-3: Selected transformations of carbon species.

Building up on these findings, FRANZ FISCHER and HANS TROPSCH later developed and patented the production of longer-chain hydrocarbons from carbon monoxide and hydrogen (eq. 3). Later named

after its discoverers, the FISCHER-TROPSCH synthesis provides a synthetic route to fuels or other simple organic compounds.[16] Given the identical gaseous starting materials, it is apparent that the FISCHER-TROPSCH synthesis and the SABATIER process are closely related. In fact, while the FISCHER-TROPSCH synthesis aims for longer hydrocarbon chains, methane is a known but undesired side product. Its formation can be avoided through careful tuning of reaction parameters such as temperature and pressure in accordance with the employed catalysts, which are usually based on iron, nickel, cobalt, or ruthenium.[20,21] Similar to the methanation of CO_2 *via* the SABATIER reaction, carbon dioxide can also be used as feedstock in FISCHER-TROPSCH plants. However, CO_2 is then not directly hydrogenated, but rather converted to CO first *via* the reverse water-gas shift reaction (RWGS, eq. 4).[22] Conveniently, iron-based FISCHER-TROPSCH catalysts also catalyze the RWGS reaction, so that these two processes can in principle run simultaneously in one reactor.[16,21,23] The water-gas shift reaction (WGS, eq. 5) and its reversed counterpart are thus valuable methods for the interconversion of CO and CO_2, as well as hydrogen production.

At large, both the FISCHER-TROPSCH and the SABATIER reaction provide well-proven means to tackle the emerging environmental crisis by enabling the storage of excess energy from preferably renewable power sources such as PV in the form of chemical bonds, i.e., hydrocarbons.

1.2   Natural photosynthesis

The conversion of sunlight into chemical energy is not a new concept. In fact, it is the foundation of life as we know it today and as it has been roughly for the last 2.3 billion years.[24] Around that time, increasing amounts of bacteria began using incident sunlight to split water in order to obtain energy – a process commonly known as photosynthesis. Since oxygen is released as the side product of the underlying chemical reactions, it accumulated in the atmosphere of the formerly anerobic earth, initiating the so-called "Great Oxidation Event".[25] Subsequently, aerobic life emerged and thrived on our planet.[26]

The underlying principles of photosynthesis in most plants can be illustrated in a Z-Scheme (Scheme 1-1), which gets its eponymous shape from the two consecutive cascades that will be briefly outlined in the following. First, electrons in the P680 reaction center of photosystem II (PS II) are photoexcited. The resulting electron holes are replenished by the oxygen-evolution complex (OEC), which uses oxidation of water to dioxygen to provide electrons. The photoexcited electrons in PS II, on the other hand, are passed on to photosystem I (PS I) *via* the electron transport chain (ETC). Here, they in return replenish electron holes stemming from a second photoexcitation process. Finally, the electrons excited in PS I are used to convert nicotinamide adenine dinucleotide phosphate ($NADP^+$) to its reduced form NADPH. Concurrently, the proton gradient originating from electron transfer and water oxidation is used to store energy in the form of adenosine triphosphate (ATP). Both NADPH and ATP are used by plants in the light-independent CALVIN-BENSON cycle to synthesize carbohydrates from carbon dioxide.[27,28]
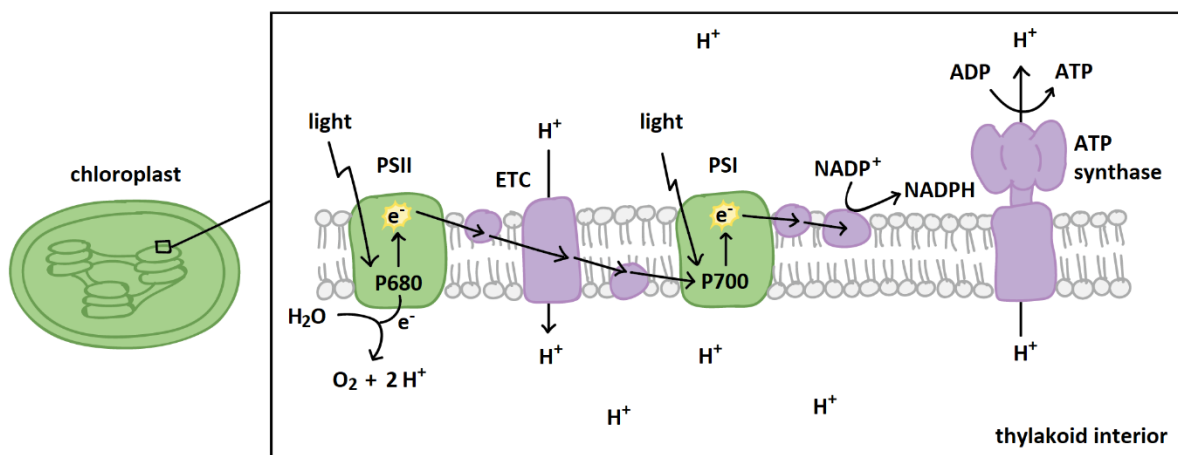
Scheme 1-1: Z-Scheme of natural photosynthesis. Adapted with modifications from [29] (CC BY-NC-SA 4.0).

Despite only showing a very simplified model for the photosynthetic processes, it can be conceived that the underlying and interconnected structural, chemical, and physical aspects needed millions of years of evolutionary fine-tuning in order for photosynthesis to function efficiently.[30] Exemplarily, the detailed processes elapsing in the water-oxidizing OEC shall be discussed, given its high relevance to this work.
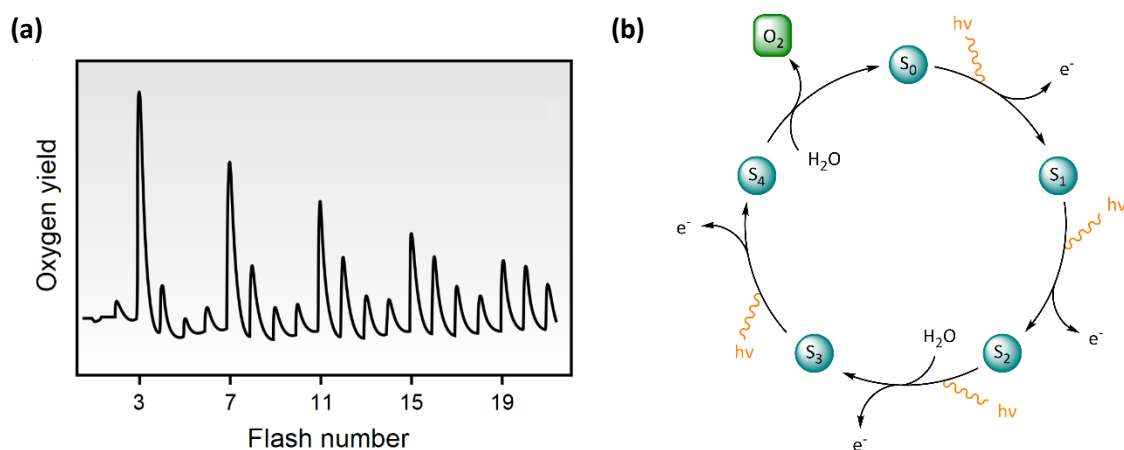
Figure 1-4: (a) Oxygen release of spinach chloroplasts/thylakoids when exposed to short light flashes. Adapted from [31]. Copyright © 2007 Royal Society of Chemistry. (b) Simplified Kok cycle.

The basis for our current understanding of OEC is given in the works of JOLIOT and KOK, who examined the light-dependency of photosynthetic oxygen evolution. They found that when exposing chloroplasts to short pulses of light, increased amounts of oxygen are detected after every forth irradiation (Figure 1-4a).[32,33] This observation led to the definition of the so-called KOK cycle, which proposes that the OEC passes through five states ($S_0 - S_4$, Figure 1-4b). Whereas every step up to S_4 requires one photoexcitation event, oxygen is released in the light-independent step $S_4 - S_0$. In total, one water oxidation cycle in the OEC takes roughly 2 ms.[25] Note that S_1 is the usual resting state of the OEC, which explains the first oxygen release to take place after only three flashes.[31,33] Since its formulation, the KOK cycle has been further refined by identifying several intermediate states.[34,35]

The exact structure of the OEC was unraveled only more than 30 years later and is fundamental to understand the structural aspects behind the states of the KOK cycle. Through synchrotron X-ray diffraction on protein single crystals, the structure of PSII was resolved in 2004 with a resolution of 3.5 angstrom – enough to elucidate the composition and arrangement of the OEC.[36,37] It consists of a cubane-like structure formed by one calcium and three manganese atoms connected *via* four oxygen atoms (Figure 1-5).[38] Furthermore, a forth manganese atom and an additional oxygen atom are linked to the asymmetric cubane, resulting in the overall formula Mn_4CaO_5. Four water molecules are bound to this cluster and partially serve as substrate for the oxygen evolution reaction.[38] In Figure 1-5, blue coloring is used to highlight said substrates. The depicted molecular view on the OEC allows for an in-depth understanding of its changes during the KOK cycle.
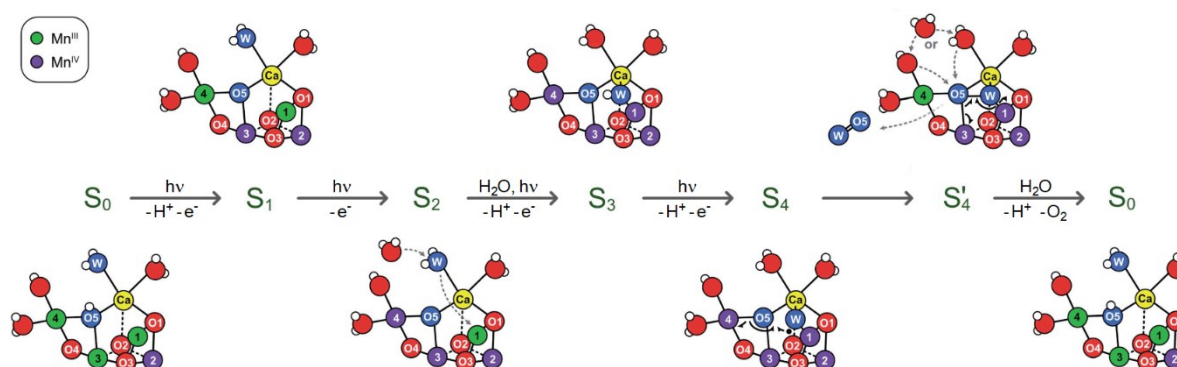
Figure 1-5: Detailed molecular view of the KOK cycle. Color code: white – hydrogen, red – oxygen, green – manganese(III), purple – manganese(IV), yellow – calcium. Oxygen atoms to be released as dioxygen are highlighted in blue and eventually labelled "W". Manganese atoms numbered 1-4 for clarity. Adapted with modifications from [39] (CC BY 3.0).

It stands out that the manganese atoms – both within and outside the cubane motif – vary their oxidation states during the catalytic cycle. In S_0, three of the four manganese atoms are present in their +III oxidation state (green, Figure 1-5). Until S_3, these are stepwise oxidized to Mn(IV) (purple) whilst the OEC re-reduces the P680 in PSII after its photoexcitation. The fourth and final electron transferred during the S3 → S4 transition directly stems from the original water substrate, leaving an oxyl radical bound to Mn1.[40] Subsequently, electronic rearrangements and the associated O-O bond formation lead to the intermediate state S_4', in which the final product is foreshadowed in the form of a complexed peroxide.[41] O_2 is finally formed in the transition leading to S_0, whereas Mn1 and Mn3 are reduced to their original +III oxidation state. O5, lost as part of O_2, is replaced by a new water molecule.

Both the sheer feasibility and the elegance underlying the KOK cycle can in principle be ascribed to the OEC composition. The four redox-active manganese atoms are used to store oxidative equivalents within the cluster before the actual water oxidation takes place. This distribution – accompanied by subsequent charge compensation through deprotonation – evens out the reduction potential of the OEC, enabling fourfold oxidation by just one oxidant ($P680^+$).[25,31,35] From a kinetic point of view, the OEC links the fast light reactions elapsing in PSII with the slow water oxidation reaction.[25]

Furthermore, the arrangement of Mn1, Mn3, and Mn4 in the OEC can be understood as a sort of cavity, which captures and holds the substrates until the final product is released. This way, the catalysis is confined to a small space, preventing the release of intermediate reactive oxygen species (ROS).

1.3 Artificial photosynthesis

Given its efficiency, it is not surprising that researchers sought to copy aspects of natural photosynthesis – be it for scientific curiosity in the underlying processes or the intent to improve industrial processes.[42] In 2008, KANAN and NOCERA reported the synthesis of a water oxidation catalyst (WOC) very similar to the OEC. They found that electrolysis of a cobalt nitrate solution in neutral phosphate buffer leads to deposition of a catalytically active film on the anode.[43] Though the obtained material – later denoted Co-Pi – is amorphous, methods such as X-ray absorption spectroscopy (XAS) revealed its structure to be based on defined interconnected Co(III)-oxo-cubanes (Figure 1-6a).[44,45] Similar to the OEC, Co-Pi can also rely on a self-healing mechanism providing it with a very high – if not infinite – lifetime.[46,47]
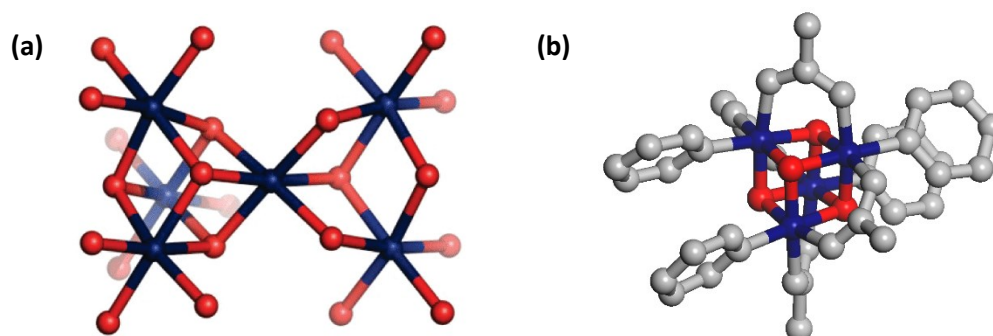

Figure 1-6: The cubane motifs in Co-Pi (a) and $Co_4O_4(Ac)_4(py)_4$ (b) are composed of cobalt (blue) and oxygen atoms (red). (a) Adapted from [44]. Copyright © 2009 American Chemical Society. (b) Ligands depicted in grey, hydrogen atoms omitted for clarity; image constructed from .cif data given in [48].

This cubane motif could even be isolated in the form of molecular clusters such as $Co_4O_4(Ac)_4(py)_4$, which also acts as a water oxidation catalyst (Figure 1-6b).[48–51] In parts, this activity is due to the cooperativity of the metal atoms in the cluster and the stabilization of intermediate high oxidation states of cobalt during catalysis as in the Mn_4CaO_5 cluster.[52,53] Subsequently, the discovery of synthetic cubanes lead to the construction of a structure termed "artificial leaf" – a sophisticated architecture of semiconductors and catalysts that splits water under illumination.[47,54] Unlike actual leaves, NOCERA's "artificial leaf" does not yield oxygen and NADPH, but oxygen and hydrogen according to eq. 6 – which makes it an overall water splitting (OWS) photocatalyst.[47] However, there are a number of different approaches to split water with solar irradiation and storing the obtained energy in chemical bonds as elaborated in the following.

$$2\ H_2O\ \rightarrow\ O_2 + 2\ H_2 \qquad \text{(eq. 6)}$$

$$2\ H_2O\ \rightarrow O_2 + 4\ H^+ + 4\ e^- \qquad \text{(eq. 7)}$$

$$4\ H^+ + 4\ e^-\ \rightarrow\ 2\ H_2 \qquad \text{(eq. 8)}$$
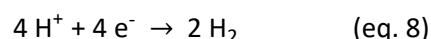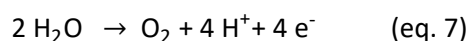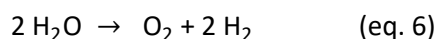
In principle, three schemes can be distinguished when using semiconductors for water splitting: photovoltaic (PV) electrolysis, photoelectrocatalysis (PEC), and photocatalysis (PC).

PV is based on the photovoltaic effect: When photons with energies exceeding the electronic band gap (E_g) hit a semiconductor, electrons from its valence band (VB) are excited to the conduction band (CB), leaving an electron hole (h^+).[55] Without separation, these charge carriers could simply recombine.

However, with proper alignment of p-doped and n-doped regions of a semiconductor such as silicon (p-n-junction), the electron-hole pair can be systematically separated – creating a potential between the N region and the P region that can be used to pass electrons through an external circuit.[56]

Among other possible applications the current and potential of a photovoltaic setup can be used to electrochemically split water. To that extent, an electrolyzer is connected to a series of solar cells (Figure 1-7a). At the anode, water is oxidized to dioxygen according to eq. 7 – the oxygen evolution reaction (OER). The other half-reaction of water splitting – the hydrogen evolution reaction (HER, eq. 8) – consists of the reduction of protons at the cathode.

In theory, a potential of 1.23 V is needed for both reactions to proceed concomitantly. Due to kinetic limitations though, potentials higher than 1.23 V are needed for efficient water splitting.[57] This overpotential can be reduced by using appropriate electrodes or catalysts; the HER for example is catalyzed by precious metals such as platinum, which is why Pt or Pt-coated electrodes are often used as cathodes.[58] The anode, on the other hand, is best loaded with oxygen evolution catalysts such as IrO_2 or RuO_2.[59]
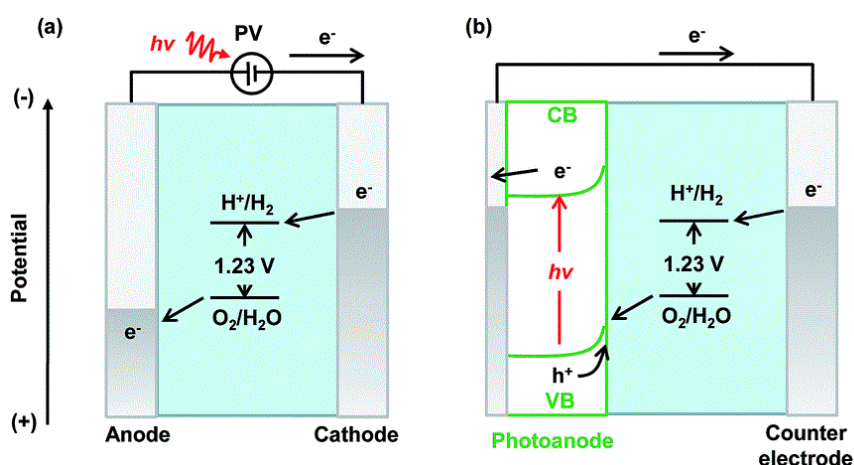
Figure 1-7: Schematic representation of OWS via PV-electrolysis (a), and PEC (b). Modified from [57] with permission. Copyright © 1972 Royal Society of Chemistry.

For PEC, either one or both the electrodes of the PV-electrolysis setup are replaced by a photoelectrode.[59] In the first example reported by FUJISHIMA and HONDA titanium dioxide (rutile) was employed as the photoanode responsible for both light absorption and water oxidation (Figure 1-7b).[55] The excess electrons are used up in the reduction of protons at a separate platinum cathode, releasing hydrogen gas.[60] In contrast to PV-electrolysis setups, the introduction of a semiconductor-electrolyte interface leads to an alteration of the semiconductor's band structure. To account for this process called band bending, usually p-type and n-type semiconductors are used as photocathodes and -anodes, respectively.[59] In the given example of an n-type rutile photoanode (Figure 1-7b) band bending facilitates the flow of electron holes to the water interface where the OER takes place.[59] In addition, an external bias can be or has to be used when splitting water with PEC cells.[8,59] Despite this reduction of bias voltage compared to electrolysis setups, PEC systems are significantly less effective in

converting sunlight to hydrogen. The solar-to-hydrogen efficiency (STH, eq. 9)* for PEC water-splitting under sunlight is in the range of 1 – 20%, whereas PV-electrolysis combinations can reach up to 30% – mostly due to their higher technical maturity (Figure 1-8).[7,8,61,62]

$$\text{STH} = \frac{\text{chemical energy output}}{\text{solar energy input}} = \frac{r_{\text{hydrogen}} \cdot \Delta G}{I_{\text{sun}} \cdot A} \qquad \text{(eq. 9)}$$

1.4 Photocatalysis

Another hydrogen evolution method, i.e. photocatalytic water splitting, aims for the bias-free production of H_2 and O_2 under illumination of one semiconductor material or a combination of several semiconductors. Therefore, photocatalysts (PC) for the OWS reaction have to be carefully chosen and/or adapted to allow for efficient catalysis. To date, photocatalytic STH efficiencies are an order of magnitude smaller than PV- and PEC-based systems (Figure 1-8).[57,61,62] Since light absorption by the semiconductor is the first step of artificial photosynthesis the optical band gap can be regarded as one of the main characteristics of a potential photocatalyst. Incident photons need to have higher energy than the optical band gap of the photocatalyst to excite an electron from the VB to the CB. In the context of overall water splitting, this energy also needs to exceed 1.23 eV in order to be thermodynamically sufficient (Figure 1-8a, (eq. 10).[59] This corresponds to the GIBBS free energy change of 237 kJ per mole of H_2O converted.†

$$H_2O \rightarrow \tfrac{1}{2}O_2 + H_2 \qquad \Delta E^0 = 1.23 \text{ V} \qquad \text{(eq. 10)}$$
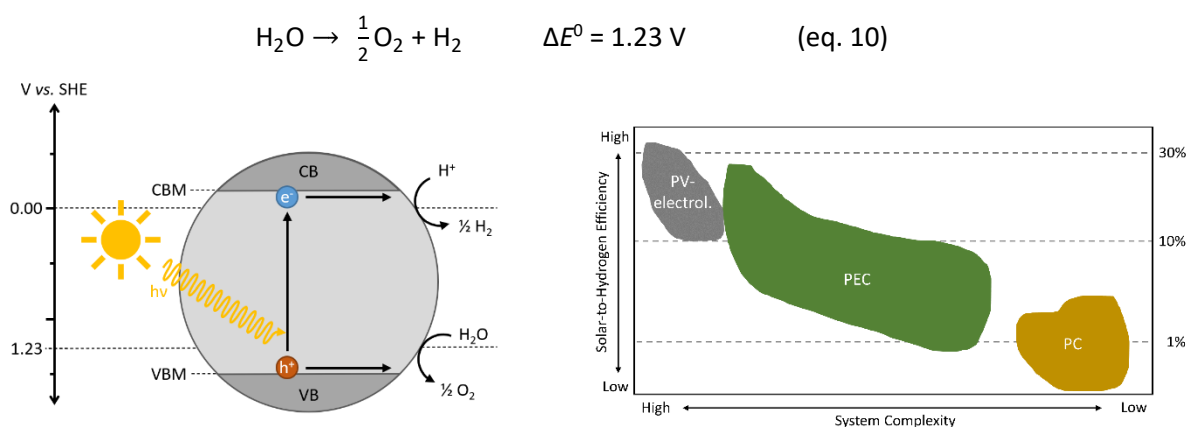
Figure 1-8: Energy scheme for a water splitting photocatalyst referenced to the standard hydrogen electrode (SHE) with the respective half reactions (left). Solar-to-hydrogen efficiency comparison for various water splitting systems (right). Modified from [7] with permission. Copyright © 1972 Royal Society of Chemistry.

According to the PLANCK-EINSTEIN relation‡ a photon energy of 1.23 eV translates into a wavelength of 1000 nm and thus infrared light. In reality, however, usually visible light or even ultraviolet light is needed for efficient photocatalytic water splitting in order to overcome both reductive and oxidative overpotentials.[63] Thus optical band gaps in the range of 1.6 – 2.4 eV are recommended.[7,64] On the

---

* With the hydrogen evolution rate r_{hydrogen}, the Gibbs free energy ΔG, the irradiance I_{sun}, and the area A.
† According to the Nernst equation: $\Delta G = -z \cdot F \cdot E$ With the number of transferred electrons z (here -2), the Faraday constant F (96485 C mol^{-1}), and the Energy E (here $E = \Delta E^0 = 1.23$ V)
‡ $E = h \cdot v = h \cdot c \cdot \lambda^{-1}$ With the PLANCK constant h, the frequency v, speed of light c, and the wavelength λ.

contrary, the larger E_g, the smaller the portion of visible light that can be utilized in the photocatalytic process and the lower the efficiency of the PC setup.[57,65]

However, it is not sufficient to only adjust the band gap energy of a potential photocatalyst for water splitting – also both the valence and the conduction band edge have to be positioned appropriately. In order to render the HER possible, the value for the conduction band minimum (CBM) has to be more negative than the proton reduction potential (Figure 1-8a). Concurrently, the valence band maximum (VBM) has to be more positive than the redox potential for water oxidation in order for overall water splitting to be thermodynamically feasible. Even when the CBM and the VBM straddle the hydrogen and oxygen evolution potential, visible light photocatalysts are often reliant on co-catalysts reducing the overpotential.[63,66] In an early example with TiO_2 as semiconductor, full water splitting could be achieved upon near-UV irradiation (>300 nm) after loading the surface of colloidal TiO_2 particles with RuO_2 and Pt.[67] In 2016, WANG and coworkers could achieve the same goal using a carbon nitride photocatalyst decorated with Pt and CoO_x, which was also active under visible light irradiation (>420 nm).[68]

As for water electrolysis (*vide supra*), platinum is one of the most frequently used co-catalytic species for the photocatalytic HER due to its high activity.[66,69,70] Alternative co-catalysts can be based on likewise precious metals such as ruthenium or rhodium, or more abundant elements such as nickel or cobalt, for example.[71,72] Similarly, some of the best water oxidation co-catalysts (WOCs) are also derived from precious metals, namely the oxides of iridium and ruthenium (IrO_2 and RuO_2).[73,74] Especially cobalt oxide, manganese oxide, and their derivatives represent non-noble metal alternatives for water oxidation catalysis, as exemplified earlier with Co-Pi.[66]

In general, both HER and OER co-catalysts help in preventing electron-hole recombination by selectively trapping electrons and holes, respectively.[75] This effect can be further amplified by decreasing the particle size and increasing the crystallinity of the photocatalyst; the former reduces the diffusion length of the charge carriers to the particle interface, whereas the latter leads to fewer crystal defects which promote e^-/h^+ recombination.[8,63,71,75] In addition, co-catalysts for the OER help in preventing corrosion of the underlying photocatalyst by consuming or trapping the electron holes which could otherwise harm the semiconductor.[66] Thus, WOCs ideally possess high oxidative stability themselves – along with hydrolytic stability in order not to decompose under the aqueous conditions used in water splitting photocatalysis.[64,73] Robustness is generally ascribed to nanoparticulate, heterogeneous WOCs rather than homogeneous, molecular species – which, one the other hand, are more suitable for mechanistic studies.[73] Similarly, the light-absorbing species in photocatalytic processes do not have to be heterogeneous, but can also consist of molecular photosensitizers.[76,77] Heterogeneous systems have the advantage of easier separation from reaction media, though.

1.5   Tailored Organic Semiconductors

1.5.1   Reticular Chemistry and Metal-Organic Frameworks

Heterogeneous inorganic photocatalysts such as $BiVO_4$, $SrTiO_3$, and the archetypical TiO_2 can be regarded long-known, especially since they exist naturally as minerals.[66] Consequently, their synthesis relies on common inorganic techniques such as precipitation, calcination, or solid-state reactions. Depending on the photocatalyst of interest, doping or metal loading may be used to alter the optical and catalytic properties.[78] Otherwise, – despite being able to utilize basically every chemical element for their construction – the tunability of inorganic photocatalysts is practically limited.[63]

Polymeric organic photocatalysts, on the other hand, constitute a promising class of materials for various photocatalytic applications due to their essentially unlimited molecular-level tunability.[79] Fundamentally, this variability is based on the underlying organic precursors that themselves are tunable as discussed later in this chapter. More specifically, a relatively new chemical paradigm provides just the means needed to design heterogeneous organic photocatalysts and tune their properties. Termed "reticular chemistry", it describes the rational synthesis of ordered structures through assembly of molecular building blocks.[80] Prerequisite to every reticular design approach is the directionality, integrity, and rigidity of the linker molecules, and their strong bonding among each other.[80,81] Only then can a predetermined framework be constructed from chemically and geometrically suitable building blocks as illustrated for a metal-organic framework (MOF, Figure 1-9).
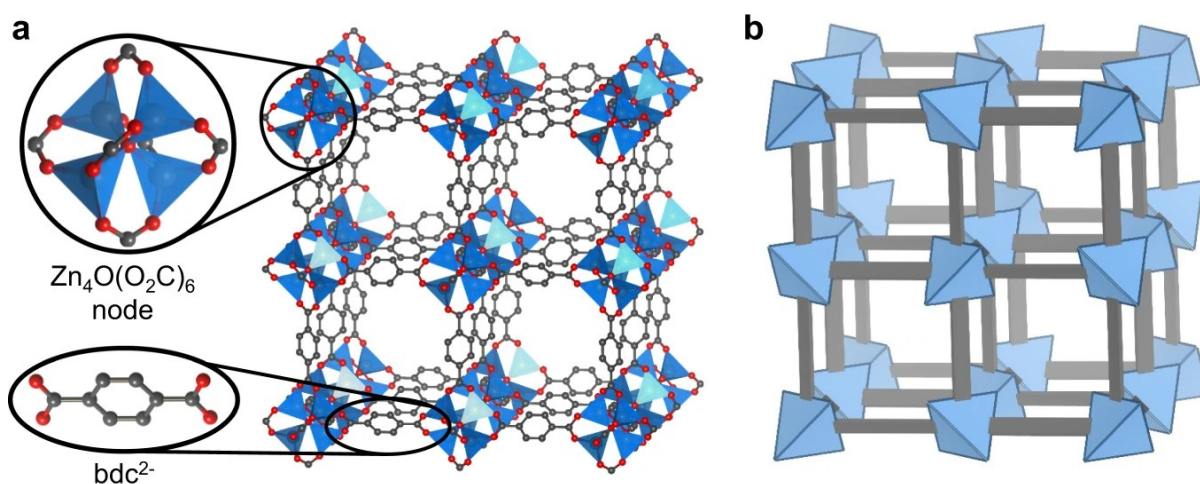
Figure 1-9: Structure of MOF-5 (a). Schematic representation of the underlying pcu topology (b). Reprinted with modifications from [82]. (CC BY 4.0). C atoms, Zn tetrahedra/cluster, and O atoms are shown in grey, blue, and red, respectively. H atoms omitted for clarity.

MOF-5 is one of the earliest reported MOFs, and as such can be regarded one of the prime examples of reticular chemistry.[81] It is composed of tetranuclear zinc clusters connected *via* 1,4-benzenedicarboxylate linkers (bdc^{2-}, Figure 1-9a).[83] Due to the distinct and sixfold carboxylate-capped [$Zn_4O(O_2C)$] nodes, the combination with a linear and bidentate linker leads to a primitive cubic network – both rationally and synthetically (Figure 1-9b).[82] Subsequently, one can envisage so-called isoreticular MOFs, which share the same network connectivity (or topology), but differ in aspects such as linker composition or size. [84,85] In the case of simple linker elongation, for example, this would lead

to an increased unit cell and consequently to larger voids in the structure.[80] On the one hand it has to be noted here that their inherent porosity is one of the most interesting features of MOFs, allowing for applications such as gas storage and separation, or atmospheric water harvesting.[86,87]

On the other hand, the example of linker elongation in MOFs nicely insinuates the subtle interplay between building block and final material which is what renders reticular chemistry so appealing. Since the core feature lies in the formation of ordered networks from molecular building blocks, careful design and fine-tuning of said linkers consequently allows to configure a material depending on the particular needs it has to fulfill. Furthermore, since the MOF linkers are partially organic in nature, basically any desired building block can be synthesized by means of synthetic organic chemistry – according to the principle "If you can dream it, you can do it".[88]

Though the synthetic principle behind MOFs allows for facile synthesis of targeted frameworks with high crystallinity, it does come with disadvantages. The underlying coordinative bonds are a bottleneck in terms of chemical stability, especially under aqueous conditions or in other chemically harsh environments.[89,90] Various pre- and post-synthetic methodologies have been developed to deal with this issue and to broaden the field of application for MOFs, for example by strengthening the interaction between metal ion and organic linker.[91] Another approach, namely the substitution of coordinative with covalent bonds, ultimately led to the emergence of a new class of materials.

1.5.2   Covalent Organic Frameworks

Similar to MOFs, covalent organic frameworks are based on the principles of reticular chemistry. They are formed through interconnection of compatible organic molecules, with the dist feature that the linkage motifs within the networks are covalent bonds. In general, this provides materials with high chemical stability, while still facilitating porosity, crystallinity, and functionality, as elaborated in the following.[92]

The research field of covalent organic frameworks (COFs) was first explored by the YAGHI group in 2005 with the synthesis of COF-1 and COF-5, both of which are constituted of boron-containing building blocks or linkers.[93] In the case of COF-1, condensation of multiple molecules of 1,4-benzene diboronic acid (BDBA) leads to two-dimensional layers with boroxine linkages. On the other hand, co-condensation of BDBA with 2,3,6,7,10,11-hexahydroxytriphenylene (HHTP) leads to COF-5, in which the original building blocks are interconnected *via* boronate ester motifs.
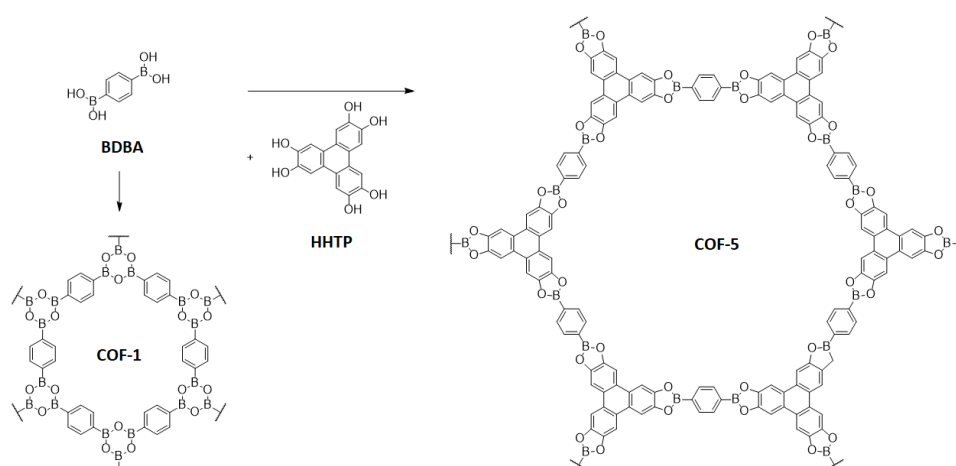
Scheme 1-2: Molecular structures of boron-based COF-1 and COF-5.

These two early examples nicely illustrate the fundamentals of COF-chemistry. Since the linkers as well as the resulting linkage motifs are planar in either case, both COF-1 and COF-5 are composed of two-dimensional layers with hexagonal topology. This connectivity is predetermined through the use of building blocks with C_2 and/or C_2 and C_3 symmetry, respectively. Following the laws of reticular design, variation of the linker symmetry is the key to designing different topologies – given that the functional groups are suitable. In case non-planar building blocks are employed, three-dimensional COFs can also be constructed (Figure 1-10). The resulting 3D COFs principally feature higher crystallinity than 2D COFs, due to the formation of covalent bonds in all directions.[94]

2D COFs, on the other hand, exhibit covalent connectivity only within the layers. Nevertheless – if not specifically targeting single-layer COFs – 2D COFs also form three-dimensional crystallites through weak interactions between individual layers. In the case of COF-1 and COF-5, these are B···O and π-π interactions, respectively.[93] Especially the latter are stereotypical for 2D-COFs due to the mostly aromatic nature of the building blocks.[95] If the layers stack in an eclipsed manner, the alignment of void space gives rise to one-dimensional pores.
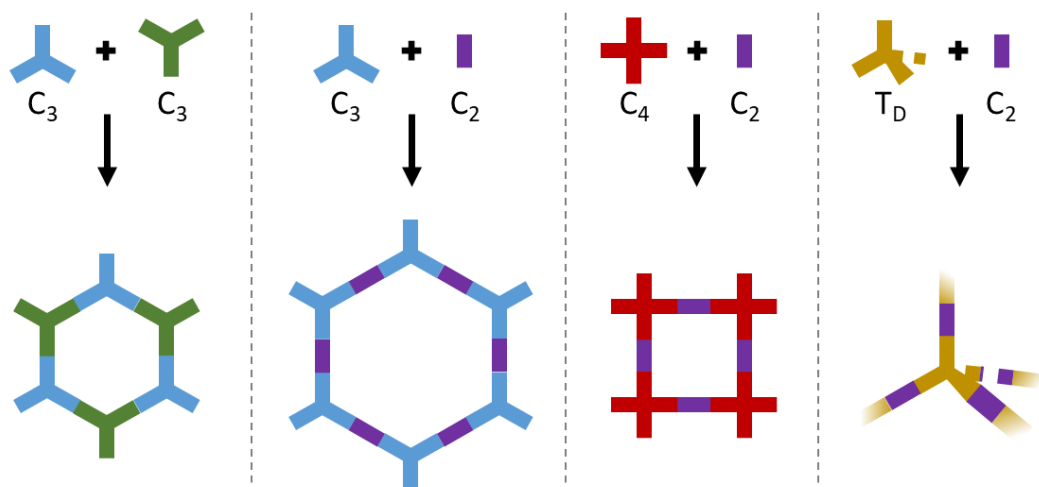
Figure 1-10: Construction principle of selected topologies typically reported for COFs with the underlying building block and their symmetry.

A second aspect that COF-1 and COF-5 rely on and nicely illustrate is the concept of dynamic covalent chemistry (DCC). DCC describes the formation of covalent bonds under reversible reactions conditions, so that bonds in macromolecules or polymers, for example, can be repeatedly formed and broken.[96] In COF chemistry, reversible bond formation has the advantage that during synthesis, the framework can rearrange and cure thermodynamically unstable defects in its structure. This "self-healing" or "error correction" effect helps in developing crystalline networks from initially amorphous gels.[94,97] Through perfection of this method, several single-crystalline COFs have been prepared to date.[98–102]

In following reports, the number of COFs has been subsequently extended through the combination of ever new boronic acid linkers.[95,103–109] However, the high reversibility in boronate condensation underlying these networks has both advantages and drawbacks. On the one hand, boron-based COFs with high crystallinity can be obtained rather easily, given the fast error correction of boronate ester linkages.[110] On the other hand, the first reported COFs are prone to hydrolysis for the exact same reason.[111] This might not impede their use in optics, electronics, and gas sorption, but prevents broad application in fields strongly relying on aqueous media, such as catalysis, and biology.[112]

Nevertheless, COF-1, COF-5, and their successors can still be regarded as a milestone in material science in particular or chemistry in general. It was thus only a matter of time until the given knowledge of DCC and reticular chemistry was further applied to enlarge the newly founded research field.[96] Among others, this endeavor resulted in the discovery of imine-COFs, which are usually formed through condensation of aldehyde- and amine-decorated building blocks.[113–117] In contrast to boron-based linkages, the chemical equilibrium of imine formation and disintegration can be induced through addition of, e.g., Brønsted or Lewis acid catalysts.[118]
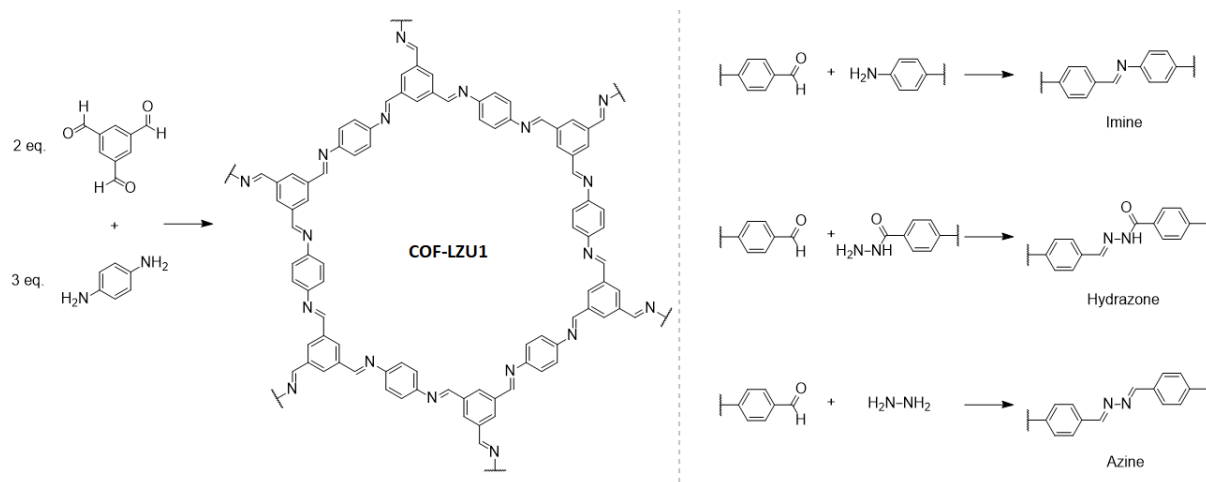
Scheme 1-3: Synthesis of COF-LZU1, one of the first two-dimensional imine-linked COFs. Right: Condensation of aldehydes with varying nitrogen-based linkers yielding three archetypical C-N linkages.

Soon, imine-COFs became one of the most common classes of COFs, mostly owing to the accessibility and commercial availability of both suitable amine and aldehyde linkers.[110,117] Owing to this variety in building blocks, imine-based COFs have found application in diverse fields such as organic catalysis,[114,119] gas storage and separation,[120–126] (opto-)electronics,[127,128] and filtration.[120,129] A reason for this high versatility lies in the higher stability of the imine bond compared to the precedent boronate ester or boroxine linkages.[117,130] Similar progress can be ascribed to classes of COFs linked by a very similar C-N linkage, namely hydrazone and azine, constructed via condensation of an aldehyde with a hydrazide or hydrazine, respectively (Scheme 1-3).[125,131–133] Compared to imine COFs, both azine and hydrazone COFs exhibit higher stability towards hydrolysis.[94,134]

Recently, C=C bonds were established as COF linkages, providing stability even against concentrated acids and bases, allowing for application under harsh conditions.[135–137] First examples were obtained by KNOEVENAGEL condensation of cyanomethyl groups with aldehydes, yielding 2D COFs.[138,139] The cyano substituent activates the adjacent methylene group for deprotonation by a Brønsted base such as cesium carbonate.[140] Nucleophilic attack of the carbanion towards the aldehyde and subsequent elimination of water leads to cyano-substituted C=C double bonds (Scheme 1-4).
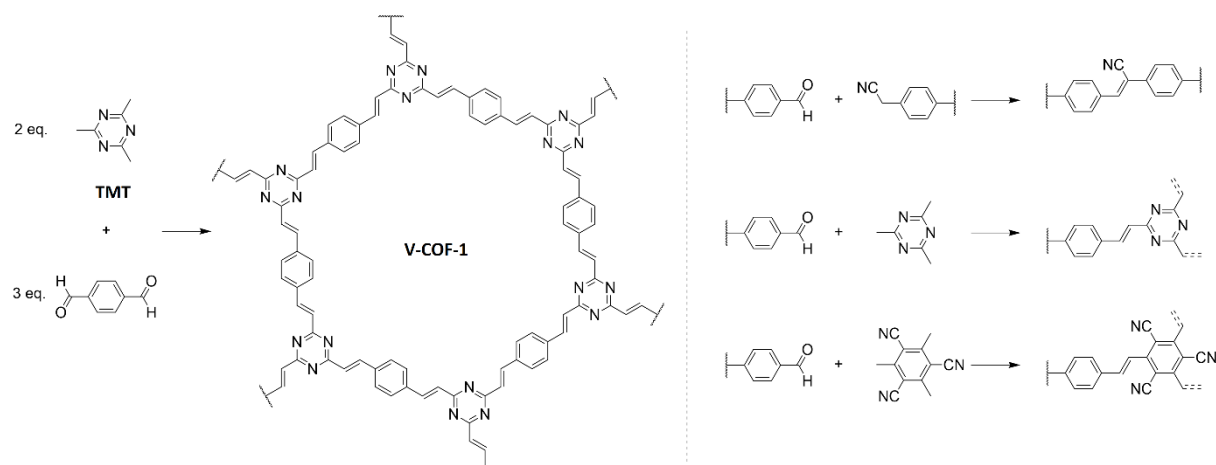
Scheme 1-4: Synthesis of V-COF-1, one of the first two-dimensional vinylene-linked COFs (left). Right: Condensation of aldehydes with varying electron-deficient linkers yielding C-C linkages.

In 2019, four research groups independently reported the synthesis of unsubstituted vinylene-linked COFs.[141–144] In all cases 2,4,6-trimethyl-1,3,5-triazine (TMT) was used as the electron deficient building block, practically replacing the cyanomethyl-substituted linkers known from KNOEVENAGEL condensations (*vide supra*). Under suitable conditions – namely catalysis by strong Brønsted acids or bases – TMT and complementary aldehyde linkers can undergo aldol condensation yielding unsubstituted vinylene bonds (Scheme 1-4). Though both the KNOEVENAGEL and the Aldol polycondensation yield highly robust COFs, their limited reversibility impedes error-correction of the network during synthesis, consequently making it difficult to obtain crystalline materials.[145] Nevertheless, vinylene-linked COFs are experiencing increasing interest. Since – in contrast to C-N-linked COFs – their linkages are not polarized, full delocalization of π-electrons over the two-dimensional COF layers is facilitated.[146,147] This characteristic consequently enhances charge transport within the COF.[148,149] Together with their high molecular and optical tunability, chemical stability, and large surface areas, this makes COFs highly promising materials for photocatalysis.

1.5.3 Photocatalysis with COFs

Prominently, COFs have been used as heterogeneous photosensitizers for photocatalytic hydrogen evolution from water, for example. As such, the COF absorbs visible light, which results in the formation of electron-hole pairs as described earlier. In the first reports and in most examples of COF photocatalysts for HER to this date, metallic platinum is employed as co-catalyst.[132,133,135,150–152] Usually deposited on the outer surface of COF particles in the form of Pt nanoparticles, it catalyzes the proton reduction reaction by decreasing the overpotential for H_2 evolution.[153] Figure 1-11 exemplarily shows both the deposited Pt nanoparticles as well as the subsequent hydrogen evolution with a COF photocatalyst, i.e., TFPT-COF - the first literature example.[133]
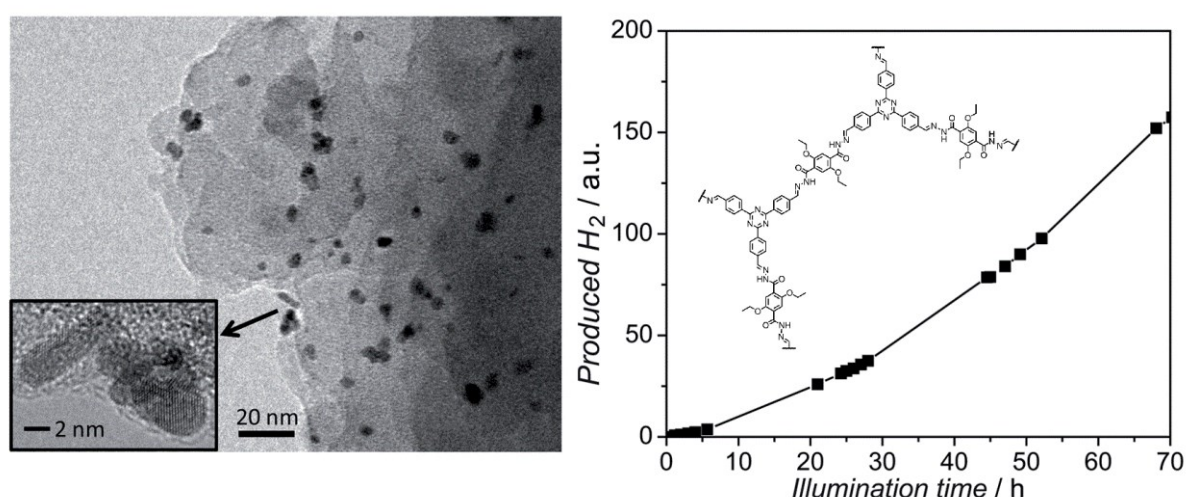
Figure 1-11: TEM images visualizing metallic Pt nanoparticles deposited on TFPT-COF (left). Photocatalytic hydrogen evolution experiment with and molecular structure of TFPT-COF (right). Adapted from [133] (CC BY 3.0).

In recent years, however, efforts have been made to replace rare and expensive Pt by more earth-abundant metal co-catalysts.[150,154] In a first example, our group used non-precious cobaloxime to catalyze the HER with N2-COF acting as the photosensitizer.[155] Later, our group further refined the cobaloxime-catalyzed HER with COFs by covalently attaching the co-catalysts to the framework

through Huisgen-type cycloaddition ("click-reaction").[156] Apart from avoiding precious metals, this approach allows for more detailed mechanistic insights on the single site catalysts, for example by probing catalyst-pore wall interactions.[156] In addition, molecular co-catalysts can be tuned to the respective needs more easily using the vast toolbox of organic synthesis. Besides, due to the high tunability inherent to COFs, there are other approaches to more efficient hydrogen evolution photocatalysis with COFs. These include, but are not limited to, band position tuning,[132] hydrophilicity tuning,[132,157,158] addition of external dyes,[158,159] and pH variation.[160]

Though hydrogen evolution photocatalysis seems expedient in the context of solar energy generation, it can be considered an undesired side reaction in particular cases.[148] Photocatalytic CO_2 reduction represents such an example. Instead of using photoexcited electrons to reduce protons to dihydrogen, the CO_2 reduction reaction (CO_2RR) aims at utilizing e^- for the production of carbon monoxide, methane, MeOH, or other value-added carbon-based products.[161] From an environmental aspect, CO_2RR has the advantage of not only yielding solar fuels or fine chemicals, but also consuming the greenhouse gas CO_2 in the process. However, if CO_2RR is to produce – for example – CH_4, a total of eight electrons has to be transferred, which is significantly more kinetically challenging than HER requiring only two e^-.[162]

It is thus not surprising that upon exploration of the CO_2RR with COF photocatalysts mostly carbon monoxide production is observed.[79,163–166] In 2018, the groups of Zhang and Huang reported the synthesis of Re-COF and its successful application as CO_2 photoreduction catalyst with CO generation rates of about 0.75 mmol g^{-1} h^{-1} and a selectivity of 98%.[167] Re-COF is named after the co-catalytic rhenium species tethered to the COF *via* bipyridine sites covering the pore walls. This heterogenization approach leads to even higher activities than the free rhenium catalyst species, i.e., [Re(bpy)(CO)$_3$Cl], also known as Lehn's catalyst.[168,169]

Interestingly, COFs are not only attractive candidates for CO_2RR photocatalysis because of their light-harvesting properties and their high surface areas. A special feature lies in their tunable porosity, which allows for rational design of materials with high CO_2 adsorption capacity.[170–172] Also, the systematic introduction of CO_2 adsorption sites such as nitrogen atoms helps to accumulate CO_2 inside the COF pores, and thus at the site of catalysis.[117,124–126]

In conclusion, the amount of examples of COF (photo-)catalysts again highlights the variability and tunability of this relatively new class of materials. However, the focus of early reports on COF photocatalysis seems to have been on reductive reactions such as the HER and CO_2RR outlined above. This makes sense in the first place, since these reactions appeal to a larger audience as they store solar energy in chemical bonds. Research on hydrogen evolution, for example, benefits from the current discussion on sustainable energy management and power-to-X technologies as elaborated earlier. For photocatalytic hydrogen evolution from water, however, all focus lies on the reduction of protons to H_2 (eq. 8). In these cases, the other half-reaction – the oxidation of water to dioxygen – is replaced by oxidations of so-called sacrificial electron donors (SEDs). As elaborated in chapter 2, avoiding the kinetically demanding water oxidation half-reaction typically boosts the hydrogen evolution performance.

In fact, oxygen evolution photocatalysis was tried with COFs as early as the first report on COF HER photocatalysis.[133] To this extent, TFPT-COF was loaded with iridium oxide nanoparticles, suspended in aqueous phosphate buffer, and illuminated in the presence of either silver nitrate or sodium persulfate as sacrificial electron acceptor.[133] However, in neither case could oxygen evolution be detected so that TFPT-COF made history only as the first COF for hydrogen evolution and not as a full water splitting photocatalyst. After that, it took more than five years until first reports on COFs specifically for photocatalytic OER were published. The following paragraph aims for the comparison of these research papers regarding the structure and properties of the employed COFs. A tabular listing is given in the appendix (Table S2-6).

sp^2c-COF was synthesized in 2017 by the group of DONGLIN JIANG as one of the first examples of C=C-linked COFs as it is constructed from a tetratopic pyrene aldehyde (TFPPy) and linear 1,4-phenylenediacetonitrile (PDAN) via KNOEVENAGEL polycondensation (Figure 1-12).[139] As the name suggests, sp^2c-COF comprises mostly sp^2-hybridized carbons which enable full π-conjugation within the two-dimensional COF sheets. Mid 2019 the same group reported the use of sp^2c-COF for photocatalytic hydrogen evolution, making use of improved charge carrier transport caused by the high degree of conjugation.[135] Given the sufficiently negative value of -5.74 eV (vs. vac.) for the VBM, sp^2c-COF was also tested as a photocatalyst for the water oxidation half-reaction. In fact, using $Co(NO_3)_2$ as co-catalyst and $AgNO_3$ as sacrificial electron acceptor, an oxygen evolution rate of about 22 µmol g^{-1} h^{-1} could be achieved.[135] The photocatalytic hydrogen evolution, for comparison, was orders of magnitude more efficient with 1360 µmol g^{-1} h^{-1}. Attempts for overall water splitting with sp^2c-COF were not shown. The same applies for following reports on vinylene-linked COF photocatalysts by the group of FAN ZHANG. g-$C_{40}N_3$-COF, g-$C_{52}N_6$-COF, and g-$C_{54}N_6$-COF all show photocatalytic HER, but significantly lower oxygen evolution rates.[173,174] The two half-reactions were tested separately, again with cobalt nitrate as the water oxidation co-catalyst and silver nitrate as the sacrificial electron donor for the OER.
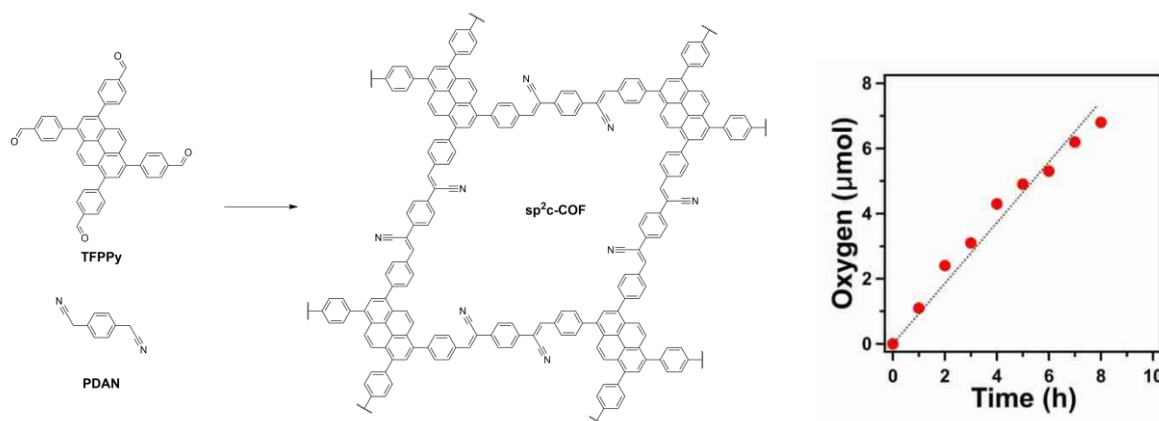

Figure 1-12: Building blocks and structure of sp^2c-COF (left) and the reported plot showing photocatalytic oxygen evolution (right). Reproduced from [135] with permission. Copyright © 2016 Elsevier Science & Technology Journals.

In a different approach, LU and coworkers combine the oxygen evolution half-reaction with photocatalytic CO_2 reduction as the reductive half-reaction instead of HER.[175-*] As in the reports on sp²c-COF, the water oxidation reaction only serves the purpose of providing electrons and is not discussed in detail on its own. However, neither OER co-catalysts nor sacrificial reagents are used. The employed photocatalytic TTCOF is based on tetrathiafulvalenes (TTF) and porphyrin units (TAPP-M), the latter of which can chelate various metal ions such as Zn, Ni, and Cu (Scheme 1-5). According to the authors, the targeted CO_2 reduction takes place at the metal sites whereas the water oxidation half-reaction supposedly proceeds at the TTF moieties.[175] This is rationalized with the underlying linker electronics – as TTF and TAPP-M are considered electron-rich and electron-deficient, respectively, they are presumed to center the HOMO/VBM (TTF) and LUMO/CBM (TAPP-M).[175] Photoexcited electrons would therefore preferentially move to the porphyrins and reduce CO_2 in its close proximity. Consequently, since no external co-catalyst is employed in the case of TTCOF-M, water molecules are oxidized through electron holes located at the TTF sites in a metal-free process.[175] This might explain the low oxygen evolution rate of 0.98 µmol g^{-1} h^{-1} for M = Zn.
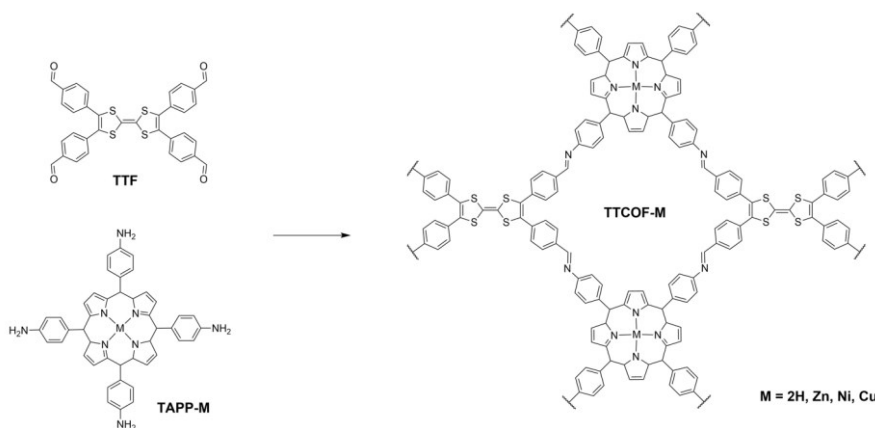
Scheme 1-5: Building blocks and structure of TTCOF-M.

Surprisingly, more examples of metal-free water oxidation photocatalysis with organic polymers have been reported. CHEN *et al*. synthesized a series of three covalent triazine frameworks (CTFs) with and without integrated **-C≡C-** motifs (Figure 1-13), all of which are capable of reducing O_2 to H_2O_2 under illumination.[176] In addition, CTF-BPDCN lacking acetylene functions was shown to photocatalytically evolve oxygen from aqueous $NaIO_3$ solutions in the absence of a water oxidation co-catalyst (Figure 1-13). That was not the case for the derivates CTF-BDDBN and CTF-EDDBN, though. With valence band maxima of -6.31 and -6.59 eV *vs*. vac., respectively, CTF-BDDBN and CTF-EDDBN have such high oxidizing capability that they oxidize water to hydrogen peroxide instead ($E^{ox.} \approx 5.8$ eV at pH 7).[176] It can be concluded that in this case the two-electron water oxidation to H_2O_2 is kinetically favored over the four-electron water oxidation to O_2.

---

* In an earlier report, FU and coworkers similarly reported photocatalytic CO_2 reduction coupled to water oxidation with metal-free COFs such as N_3-COF. However, the VBM stated therein (-4.95 eV) would not be sufficiently negative for water oxidation, and no proof for oxygen evolution is given (*Appl. Catal*. B. **2018**, *239*, 46–51. DOI: 10.1016/j.apcatb.2018.08.004).
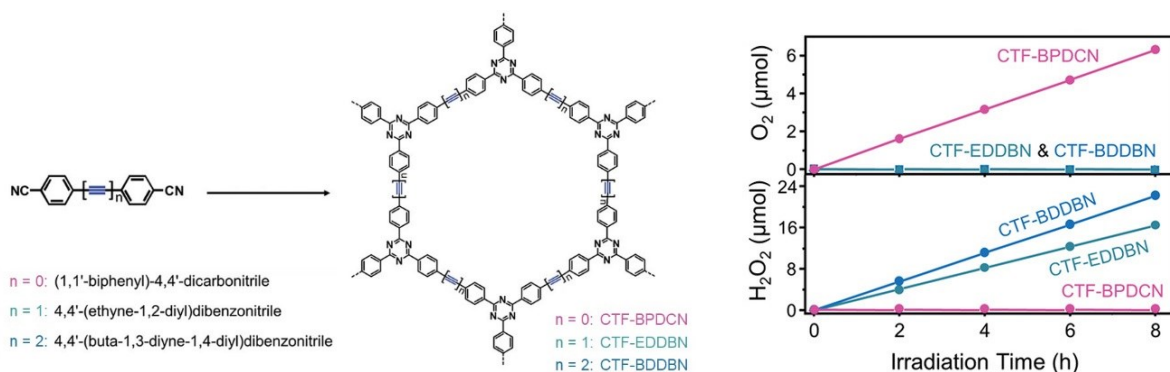
Figure 1-13: Molecular structure (left) and photocatalytic activity (right) of a series of CTFs. Photocatalysis done under argon and with NaIO₃ as sacrificial electron acceptor. Modified from [176] with permission. Copyright © 1989 John Wiley & Sons - Books.

Recently, the ketoenamine-linked TpBpy-COF was reported as the first of its kind capable of photocatalytic overall water splitting. TpBpy-COF can be synthesized solvothermally from 1,3,5-triformylphloroglucinol (Tp) and 2,2'-bipyridine-5,5'-diamine, and is well endowed for applications in aqueous media through its highly stable keto-enamine linkage (Figure 1-13).[177,178] TpBpy-COF has a VBM of 1.79 V and a CBM of -0.41 V vs. NHE, and thus is thermodynamically able to drive overall water splitting.[179] In comparison, the isoreticular TpBD-COF made up from a biphenyl instead of a bipyridine linker has a significantly less positive VBM of 1.45 V, and thus less driving force for the OER. This example nicely illustrates that the incorporation of nitrogen instead of carbon atoms into a framework can lead to more promising catalysts for oxygen evolution photocatalysis.

In fact, TpBpy-COF was reported to evolve O₂ upon illumination in the presence of a sacrificial electron acceptor, whereas TpBD-COF remains inactive.[179] More importantly, TpBpy-COF can also be used as photocatalyst for overall water splitting in the absence of sacrificial agents. In particular, highest activity could be achieved when employing the COF in the form of 3–4 nm thick nanosheets with incorporated Pt nanoparticles as co-catalyst. Under optimal conditions, OER and HER rates of around 1 and 2 µmol h^{-1} could be achieved, respectively. The STH efficiency was determined to be 0.23%. Despite allegedly bearing catalytic sites within the framework that would allow for metal-free water splitting – namely Tp for HER and bipyridine for OER (Figure 1-14) – TpBpy-COF does not photocatalytically split water in the absence of Pt co-catalyst.[179]
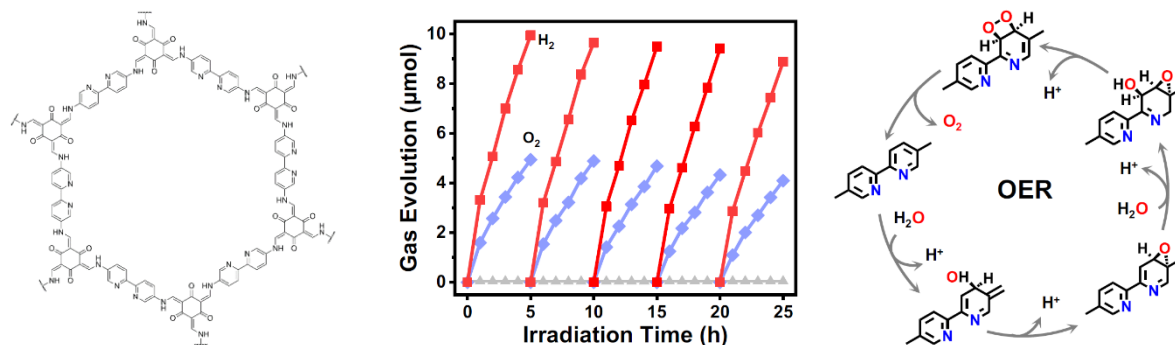

Figure 1-14: Molecular structure (left) and photocatalytic activity (middle) of TpBpy-COF nanosheets. Photocatalysis done under vacuum and with visible light (>420 nm, 300 W Xe lamp). The OER is proposed to proceed at the bipyridine motifs (right). Reproduced with modifications from [179] (CC BY 4.0).

Though high oxygen evolution performance could in principle endow COFs or other photocatalysts with the ability to efficiently evolve hydrogen without the need for sacrificial electron donors, the opposite is still the case.[180] As the example of TpBpy-COF above shows, HER rates in overall water splitting schemes are in the range of minor $\mu mol\ g^{-1}\ h^{-1}$ values. On the contrary, when using SEDs, ever larger HER rates up to 197 mmol $g^{-1}\ h^{-1}$ are reported.[181–183] This only highlights the classification of the OER half-reaction as the bottleneck in overall water splitting photocatalysis. To circumvent this problem and at the same time avoid using SEDs to quench photo-generated electron holes, reductive half-reactions such as HER and CO_2RR can alternatively be coupled to alternative oxidative reactions providing the required electrons.[184] For example, the oxidation of methanol as a typical SED ultimately yields CO_2, whereas water oxidation leads to O_2 – both of which are practically of no commercial value.[185,186] On the contrary, the toolbox of organic photoredox chemistry can provide selective oxidation reactions that supply reductive half-reactions with electrons and at the same time yield value-added fine chemicals. Examples typically include, but are not limited to, alkane dehydrogenation, cross-coupling reactions, and alcohol oxidation.[185] In the case of TFPT-COF – the first COF reported for HER (Figure 1-11) – the oxidation of SEDs could be replaced by benzylamine dehydrogenation.[187] Upon irradiation of platinum-decorated TFPT-COF, H_2 and *N*-benzylidenebenzylamine could be formed with rates of 501.8 $\mu mol\ g^{-1}\ h^{-1}$ and 477.3 $\mu mol\ g^{-1}\ h^{-1}$, respectively. Though 1970 $\mu mol\ H_2\ g^{-1}\ h^{-1}$ could be achieved in sacrificial HER systems with the same COF,[133] this example can still be considered a successful proof of concept that will be followed by other reports on hydrogen evolution combined with oxidative organic photocatalysis.[185]

1.6   Objectives

As elaborated in the previous paragraphs, COFs represent a material class with good prospects as heterogeneous photocatalysts due to their defined and crystalline structure, large surface areas, and absorption of visible light. This has been showcased multiple times in the last decade especially for the hydrogen evolution half-reaction, given the potentially increasing economic importance of hydrogen gas. The other half-reaction, i.e., the oxygen evolution reaction, has however attracted less attention. This fact, and the associated struggle to fabricate overall water-splitting COF photocatalysts, indicates that the kinetic limitations underlying the OER are hard to master. In the last years, a small number of literature reports give examples for COFs capable of oxidizing water under visible light illumination and with the help of cobalt co-catalysts and silver nitrate as sacrificial electron acceptor. The exact interaction between COF and often undefined cobalt species is, however, rarely discussed.

In chapter 2, we present an alternative approach to the problematic water oxidation half-reaction that aims for higher control of the co-catalytic species. Using a heterogenization scheme, we decorate a bipyridine-based COF with molecularly defined iridium water oxidation catalysts which allow for in-depth characterization. Their retained catalytic activity is illustrated in chemical water oxidation experiments and subsequently put to test in photocatalytic setups. Here, we compare our iridium-loaded COF to literature-known cobalt-analogues and use, among others, computational methods to evaluate and understand the underlying mechanistic steps and the kinetic and thermodynamic challenges associated therewith.

Chapter 3 exemplifies similar synthetic strategies but focusses on other photocatalytic applications. There, inspired by natural redox cofactors, we build up a COF from tailored alloxazine chromophores. Subsequently, we investigate the effect of the dye incorporation into the backbone and compare our COF as a metal-free heterogeneous photocatalyst to homogeneous alloxazine counterparts. Instead of photocatalytic water splitting, we explore aerobic alcohol oxidations, which could in principle be coupled to reductive half-reactions such as the HER.

Finally, in chapter 4 we explore the limits of COFs for catalytic applications even further. Making use of the versatility of the Cp*Ir complex used for water oxidation in chapter 2, we investigate reductive catalysis schemes as well. More precisely, we demonstrate the applicability of iridium-loaded COFs for the light-assisted water-gas shift reaction. To the best of our knowledge, WGS catalysis with COFs has not been explored, possibly due to the usually required high reaction temperatures – which we avoid by making use of the light-triggered hydrogen release in iridium hydrides.

1.7   References

1   Gesetz zu dem Übereinkommen von Paris vom 12. Dezember 2015, *Bundesgesetzblatt* **2016**, *26*, 1082.

2   UN, Status of the Paris Agreement, https://treaties.un.org/pages/ViewDetails. aspx?src=TREATY&mtdsg_no=XXVII-7-d&chapter=27&clang=_en, (accessed 12 January 2023).

3   C. Vogt, M. Monai, G. J. Kramer, B. M. Weckhuysen, *Nat. Catal.* **2019**, *2*, 188–197.

4   International Energy Agency (IEA), *World Energy Outlook 2020*, International Energy Agency, Paris **2020,** www.iea.org/weo.

5   M. Sterner, M. Specht, *Energies* **2021**, *14*, 6594.

6   BP p.l.c., *Statistical Review of World Energy 2021*, London **2022,** https://www.bp.com/en/global/corporate/energy-economics/statistical-review-of-world-energy.html, (accessed 12 January 2023).

7   J. H. Kim, D. Hansora, P. Sharma, J.-W. Jang, J. S. Lee, *Chem. Soc. Rev.* **2019**, *48*, 1908–1971.

8   T. Grewe, M. Meggouh, H. Tüysüz, *Chem. Asian J.* **2016**, *11*, 22–42.

9   Global Solar Atlas, https://globalsolaratlas.info, (accessed 12 December 2022).

10   R. Prăvălie, C. Patriche, G. Bandoc, *J. Clean. Prod.* **2019**, *209*, 692–721.

11   C. Kost, S. Shammugam, V. Fluri, D. Peper, A. Davoodi Memar, T. Schlegl, *Levelized Cost of Electricity- Renewable Energy Technologies* **2021,** https://www.ise.fraunhofer.de/ en/publications/studies/cost-of-electricity.html, (accessed 9 December 2022).

12   Der Desertec-Atlas. Ein Weltatlas zu den erneuerbaren Energien, CEP Europäische Verl.-Anstalt, Leipzig **2011**.

13   D. Clery, *Science* **2010**, *329*, 782–783.

14   E. Hamedat, Green hydrogen - A bridge between Europe and North Africa?, https://www.diplomatisches-magazin.de/en/article/ifair-gruener-wasserstoff-eine-bruecke-zwischen-europa-und-nordafrika/, (accessed 12 April 2023).

15   A. Ajanovic, M. Sayer, R. Haas, *Int. J. Hydrog. Energy* **2022**, *47*, 24136–24154.

16   V. Dieterich, A. Buttler, A. Hanel, H. Spliethoff, S. Fendt, *Energy Environ. Sci.* **2020**, *13*, 3207–3252.

17   S. Rönsch, J. Schneider, S. Matthischke, M. Schlüter, M. Götz, J. Lefebvre, P. Prabhakaran, S. Bajohr, *Fuel* **2016**, *166*, 276–296.

18   The Nobel Prize in Chemistry 1912, https://www.nobelprize.org/prizes/chemistry/1912/summary/, (accessed 11 January 2023).

19   P. Sabatier, *Die Katalyse in der organischen Chemie*, Akademische Verlagsgesellschaft m.b.H, Leipzig, 1st edn. **1914**.

20   H. Schulz, *Appl. Catal. A* **1999**, *186*, 3–12.

21   M. E. Dry, *Catal. Today* **2002**, *71*, 227–241.

22   O. O. James, B. Chowdhury, M. A. Mesubi, S. Maity, *RSC Adv.* **2012**, *2*, 7347.

23   T. Riedel, M. Claeys, H. Schulz, G. Schaub, S.-S. Nam, K.-W. Jun, M.-J. Choi, G. Kishan, K.-W. Lee, *Appl. Catal. A* **1999**, *186*, 201–213.

24   P. M. H. Kroneck, M. E. Sosa Torres, Sustaining Life on Planet Earth: Metalloenzymes Mastering Dioxygen and Other Chewy Gases, Springer International Publishing, Cham **2015**.

25   W. Lubitz, M. Chrysina, N. Cox, *Photosynth. Res.* **2019**, *142*, 105–125.

26   M. F. Hohmann-Marriott, R. E. Blankenship, *Annu. Rev. Plant Biol.* **2011**, *62*, 515–548.

27   M. Calvin, *Science* **1962**, *135*, 879–889.

28   T. D. Sharkey, *Photosynth. Res.* **2019**, *140*, 235–252.

29   Khan Academy, The light-dependent reactions, https://www.khanacademy.org/science/ap-biology/cellular-energetics/photosynthesis/a/light-dependent-reactions, (accessed 12 January 2023).

30   T. Oliver, P. Sánchez-Baracaldo, A. W. Larkum, A. W. Rutherford, T. Cardona, *Biochim. Biophys. Acta Bioenerg.* **2021**, *1862*, 148400.

31   J. Messinger, G. Renger, in *Primary Processes of Photosynthesis, Part 2*, ed. G. Renger, Royal Society of Chemistry, Cambridge **2007**, pp. 291–349.

32   P. Joliot, Barbieri G., R. Chabaud, *Photochem. Photobiol.* **1969**, *10*, 309–329.

33   B. Kok, B. Forbush, M. McGloin, *Photochem. Photobiol.* **1970**, *11*, 457–475.

34   A. Klauss, M. Haumann, H. Dau, *Proc. Natl. Acad. Sci. U.S.A.* **2012**, *109*, 16035–16040.

35   H. Dau, M. Haumann, *Biochim. Biophys. Acta* **2007**, *1767*, 472–483.

36   K. N. Ferreira, T. M. Iverson, K. Maghlaoui, J. Barber, S. Iwata, *Science* **2004**, *303*, 1831–1838.

37   J. Barber, *Cold Spring Harb. Symp. Quant. Biol.* **2012**, 77, 295–307.

38   Y. Umena, K. Kawakami, J.-R. Shen, N. Kamiya, *Nature* **2011**, *473*, 55–60.

39   C. de Lichtenberg, C. J. Kim, P. Chernev, R. J. Debus, J. Messinger, *Chem. Sci.* **2021**, *12*, 12763–12775.

40   P. E. M. Siegbahn, *Biochim. Biophys. Acta* **2013**, *1827*, 1003–1019.

41   L. O. Björn, *Oxygen* **2022**, *2*, 337–347.

42   D. Gust, T. A. Moore, *Science* **1989**, *244*, 35–41.

43   M. W. Kanan, D. G. Nocera, *Science* **2008**, *321*, 1072–1075.

44   M. Risch, V. Khare, I. Zaharieva, L. Gerencser, P. Chernev, H. Dau, *J. Am. Chem. Soc.* **2009**, *131*, 6936–6937.

45   M. W. Kanan, J. Yano, Y. Surendranath, M. Dincă, V. K. Yachandra, D. G. Nocera, *J. Am. Chem. Soc.* **2010**, *132*, 13692–13701.

46   C. Costentin, D. G. Nocera, *Proc. Natl. Acad. Sci. U.S.A.* **2017**, *114*, 13380–13384.

47   D. G. Nocera, *Acc. Chem. Res.* **2012**, *45*, 767–776.

48   R. Chakrabarty, S. J. Bora, B. K. Das, *Inorg. Chem.* **2007**, *46*, 9450–9462.

49   A. M. Ullman, Y. Liu, M. Huynh, D. K. Bediako, H. Wang, B. L. Anderson, D. C. Powers, J. J. Breen, H. D. Abruña, D. G. Nocera, *J. Am. Chem. Soc.* **2014**, *136*, 17681–17688.

50   N. S. McCool, D. M. Robinson, J. E. Sheats, G. C. Dismukes, *J. Am. Chem. Soc.* **2011**, *133*, 11446–11449.

51   X. Zhou, F. Li, H. Li, B. Zhang, F. Yu, L. Sun, *ChemSusChem* **2014**, *7*, 2453–2456.

52   J. Amtawong, A. I. Nguyen, T. D. Tilley, *J. Am. Chem. Soc.* **2022**, *144*, 1475–1492.

53   M. D. Kärkäs, B. Åkermark, *Dalton Trans.* **2016**, *45*, 14421–14461.

54   S. Y. Reece, J. A. Hamel, K. Sung, T. D. Jarvi, A. J. Esswein, J. J. H. Pijpers, D. G. Nocera, *Science* **2011**, *334*, 645–648.

55   A. Mills, S. Le Hunte, *J. Photochem. Photobiol. A* **1997**, *108*, 1–35.

56   A. S. Al-Ezzi, M. N. M. Ansari, *Appl. Syst. Innov.* **2022**, *5*, 67.

57   T. Hisatomi, K. Domen, *Faraday Discuss.* **2017**, *198*, 11–35.

58   S. Berardi, S. Drouet, L. Francàs, C. Gimbert-Suriñach, M. Guttentag, C. Richmond, T. Stoll, A. Llobet, *Chem. Soc. Rev.* **2014**, *43*, 7501–7519.

59   M. G. Walter, E. L. Warren, J. R. McKone, S. W. Boettcher, Q. Mi, E. A. Santori, N. S. Lewis, *Chem. Rev.* **2010**, *110*, 6446–6473.

60   A. Fujishima, K. Honda, *Nature* **1972**, *238*, 37–38.

61   D. Bahnemann, P. Robertson, C. Wang, W. Choi, H. Daly, M. Danish, H. de Lasa, S. Escobedo, C. Hardacre, T. H. Jeon, B. Kim, H. Kisch, W. Li, M. Long, M. Muneer, N. Skillen, J. Zhang, *J. Phys. Energy* **2023**, *5*, 12004.

62   N. Pirrone, F. Bella, S. Hernández, *Green Chem.* **2022**, *24*, 5379–5402.

63   A. Kudo, Y. Miseki, *Chem. Soc. Rev.* **2009**, *38*, 253–278.

64   S. Lin, H. Huang, T. Ma, Y. Zhang, *Adv. Sci.* **2021**, *8*, 2002458.

65   C. Dai, B. Liu, *Energy Environ. Sci.* **2020**, *13*, 24–52.

66   Q. Wang, K. Domen, *Chem. Rev.* **2020**, *120*, 919–985.

67   D. Duonghong, E. Borgarello, M. Graetzel, *J. Am. Chem. Soc.* **1981**, *103*, 4685–4690.

68   G. Zhang, Z.-A. Lan, L. Lin, S. Lin, X. Wang, *Chem. Sci.* **2016**, *7*, 3062–3066.

69   S. Trasatti, *J. Electroanal. Chem. Interfacial Electrochem.* **1972**, 39, 163–184.

70   E. Amouyal, *Sol. Energy Mater. Sol. Cells* **1995**, *38*, 249–276.

71   A. Kudo, *Pure Appl. Chem.* **2007**, *79*, 1917–1927.

72   P. Du, R. Eisenberg, *Energy Environ. Sci.* **2012**, *5*, 6012.

73   J. R. Swierk, T. E. Mallouk, *Chem. Soc. Rev.* **2013**, *42*, 2357–2387.

74   A. Harriman, I. J. Pickering, J. M. Thomas, *J. Chem. Soc. Faraday Trans. 1* **1988**, *84*, 2795–2806.

75   R. M. Navarro Yerga, M. C. Alvarez Galván, F. Del Valle, J. A. La Villoria de Mano, J. L. G. Fierro, *ChemSusChem* **2009**, *2*, 471–485.

76   E. S. Andreiadis, M. Chavarot-Kerlidou, M. Fontecave, V. Artero, *Photochem. Photobiol.* **2011**, *87*, 946–964.

77   N. A. Romero, D. A. Nicewicz, *Chem. Rev.* **2016**, *116*, 10075–10166.

78   S. Al Jitan, G. Palmisano, C. Garlisi, *Catalysts* **2020**, *10*, 227.

79   T. Banerjee, F. Podjaski, J. Kröger, B. P. Biswal, B. V. Lotsch, *Nat. Rev. Mater.* **2021**, *6*, 168–190.

80   N. L. Rosi, J. Eckert, M. Eddaoudi, D. T. Vodak, J. Kim, M. O'Keeffe, O. M. Yaghi, *Science* **2003**, *300*, 1127–1129.

81 R. Freund, S. Canossa, S. M. Cohen, W. Yan, H. Deng, V. Guillerm, M. Eddaoudi, D. G. Madden, D. Fairen-Jimenez, H. Lyu, L. K. Macreadie, Z. Ji, Y. Zhang, B. Wang, F. Haase, C. Wöll, O. Zaremba, J. Andreo, S. Wuttke, C. S. Diercks, *Angew. Chem. Int. Ed.* **2021**, *60*, 23946–23974.

82 R. Pallach, J. Keupp, K. Terlinden, L. Frentzel-Beyme, M. Kloß, A. Machalica, J. Kotschy, S. K. Vasa, P. A. Chater, C. Sternemann, M. T. Wharmby, R. Linser, R. Schmid, S. Henke, *Nat. Commun.* **2021**, *12*, 4097.

83 H. Li, M. Eddaoudi, M. O'Keeffe, O. M. Yaghi, *Nature* **1999**, *402*, 276–279.

84 O. M. Yaghi, M. O'Keeffe, N. W. Ockwig, H. K. Chae, M. Eddaoudi, J. Kim, *Nature* **2003**, *423*.

85 J. Guo, D. Jiang, *ACS Cent. Sci.* **2020**, *6*, 869–879.

86 W. Xu, O. M. Yaghi, *ACS Cent. Sci.* **2020**, *6*, 1348–1354.

87 R. Freund, O. Zaremba, G. Arnauts, R. Ameloot, G. Skorupskii, M. Dincă, A. Bavykina, J. Gascon, A. Ejsmont, J. Goscianska, M. Kalmutzki, U. Lächelt, E. Ploetz, C. S. Diercks, S. Wuttke, *Angew. Chem. Int. Ed.* **2021**, *60*, 23975–24001.

88 C. Ramirez, FINALLY, the Origin of "If You Can Dream It, You Can Do It", https://magicmadebydisney.com/2021/04/27/finally-the-origin-of-if-you-can-dream-it-you-can-do-it/, (accessed 17 May 2023).

89 M. Gu, S.-C. Wang, C. Chen, D. Xiong, F.-Y. Yi, *Inorg. Chem.* **2020**, *59*, 6078–6086.

90 F.-Y. Yi, R. Zhang, H. Wang, L.-F. Chen, L. Han, H.-L. Jiang, Q. Xu, *Small Methods* **2017**, *1*, 1700187.

91 M. Ding, X. Cai, H.-L. Jiang, *Chem. Sci.* **2019**, *10*, 10209–10230.

92 C. S. Diercks, O. M. Yaghi, *Science* **2017**, *355*, eaal1585.

93 A. P. Côté, A. I. Benin, Ockwig, Nathan, W., M. O'Keeffe, A. J. Matzger, O. M. Yaghi, *Science* **2005**, *310*, 1164–1166.

94 F. Haase, B. V. Lotsch, *Chem. Soc. Rev.* **2020**, *49*, 8469–8500.

95 A. P. Côté, H. M. El-Kaderi, H. Furukawa, J. R. Hunt, O. M. Yaghi, *J. Am. Chem. Soc.* **2007**, *129*, 12914–12915.

96 S. J. Rowan, S. J. Cantrill, G. R. L. Cousins, J. K. M. Sanders, J. F. Stoddart, *Angew. Chem. Int. Ed.* **2002**, *41*, 898–952.

97 X. Feng, X. Ding, D. Jiang, *Chem. Soc. Rev.* **2012**, *41*, 6010–6022.

98 Y.-B. Zhang, J. Su, H. Furukawa, Y. Yun, F. Gándara, A. Duong, X. Zou, O. M. Yaghi, *J. Am. Chem. Soc.* **2013**, *135*, 16336–16339.

99 A. M. Evans, L. R. Parent, N. C. Flanders, R. P. Bisbey, E. Vitaku, M. S. Kirschner, R. D. Schaller, L. X. Chen, N. C. Gianneschi, W. R. Dichtel, *Science* **2018**, *361*, 52–57.

100 T. Ma, E. A. Kapustin, S. X. Yin, L. Liang, Z. Zhou, J. Niu, L.-H. Li, Y. Wang, J. Su, J. Li, X. Wang, W. D. Wang, W. Wang, J. Sun, O. M. Yaghi, *Science* **2018**, *361*, 48–52.

101 A. Natraj, W. Ji, J. Xin, I. Castano, D. W. Burke, A. M. Evans, M. J. Strauss, M. Ateia, L. S. Hamachi, N. C. Gianneschi, Z. A. ALOthman, J. Sun, K. Yusuf, W. R. Dichtel, *J. Am. Chem. Soc.* **2022**, *144*, 19813–19824.

102 Z. Zhou, L. Zhang, Y. Yang, I. J. Vitorica-Yrezabal, H. Wang, F. Tan, L. Gong, Y. Li, P. Chen, X. Dong, Z. Liang, J. Yang, C. Wang, Y. Hong, Y. Qiu, A. Gölzhäuser, X. Chen, H. Qi, S. Yang, W. Liu, J. Sun, Z. Zheng, *Nat. Chem.* **2023**, *15*, 841–847.

103 R. W. Tilford, W. R. Gemmill, H.-C. zur Loye, J. J. Lavigne, *Chem. Mater.* **2006**, *18*, 5296–5301.

104 H. M. El-Kaderi, J. R. Hunt, J. L. Mendoza-Cortés, A. P. Côté, R. E. Taylor, M. O'Keeffe, O. M. Yaghi, *Science* **2007**, *316*, 268–272.

105 S. Wan, J. Guo, J. Kim, H. Ihee, D. Jiang, *Angew. Chem. Int. Ed.* **2008**, *47*, 8826–8830.

106   S. Wan, J. Guo, J. Kim, H. Ihee, D. Jiang, *Angew. Chem. Int. Ed.* **2009**, *48*, 5439–5442.

107   E. L. Spitler, W. R. Dichtel, *Nat. Chem.* **2010**, *2*, 672–677.

108   M. Dogru, A. Sonnauer, A. Gavryushin, P. Knochel, T. Bein, *Chem. Commun.* **2011**, *47*, 1707–1709.

109   X. Ding, J. Guo, X. Feng, Y. Honsho, J. Guo, S. Seki, P. Maitarad, A. Saeki, S. Nagase, D. Jiang, *Angew. Chem. Int. Ed.* **2011**, *50*, 1289–1293.

110   C. Qian, L. Feng, W. L. Teo, J. Liu, W. Zhou, D. Wang, Y. Zhao, *Nat. Rev. Chem.* **2022**, *6*, 881–898.

111   L. M. Lanni, R. W. Tilford, M. Bharathy, J. J. Lavigne, *J. Am. Chem. Soc.* **2011**, *133*, 13975–13983.

112   Y. Du, H. Yang, J. M. Whiteley, S. Wan, Y. Jin, S.-H. Lee, W. Zhang, *Angew. Chem. Int. Ed.* **2016**, *55*, 1737–1741.

113   F. J. Uribe-Romo, J. R. Hunt, H. Furukawa, C. Klöck, M. O'Keeffe, O. M. Yaghi, *J. Am. Chem. Soc.* **2009**, *131*, 4570–4571.

114   S.-Y. Ding, J. Gao, Q. Wang, Y. Zhang, W.-G. Song, C.-Y. Su, W. Wang, *J. Am. Chem. Soc.* **2011**, *133*, 19816–19822.

115   S. Wan, F. Gándara, A. Asano, H. Furukawa, A. Saeki, S. K. Dey, L. Liao, M. W. Ambrogio, Y. Y. Botros, X. Duan, S. Seki, J. F. Stoddart, O. M. Yaghi, *Chem. Mater.* **2011**, *23*, 4094–4097.

116   M. G. Rabbani, A. K. Sekizkardes, Z. Kahveci, T. E. Reich, R. Ding, H. M. El-Kaderi, *Chem. Eur. J.* **2013**, *19*, 3324–3328.

117   C. R. DeBlase, W. R. Dichtel, *Macromolecules* **2016**, *49*, 5297–5305.

118   M. Matsumoto, R. R. Dasari, W. Ji, C. H. Feriante, T. C. Parker, S. R. Marder, W. R. Dichtel, *J. Am. Chem. Soc.* **2017**, *139*, 4999–5002.

119   S. T. Emmerling, F. Ziegler, F. R. Fischer, R. Schoch, M. Bauer, B. Plietker, M. R. Buchmeiser, B. V. Lotsch, *Chem. Eur. J.* **2022**, *28*, e202104108.

120   Z. Wang, S. Zhang, Y. Chen, Z. Zhang, S. Ma, *Chem. Soc. Rev.* **2020**, *49*, 708–735.

121   J. Fu, S. Das, G. Xing, T. Ben, V. Valtchev, S. Qiu, *J. Am. Chem. Soc.* **2016**, *138*, 7673–7680.

122   Y. Ying, S. B. Peh, H. Yang, Z. Yang, D. Zhao, *Adv. Mater.* **2022**, *34*, e2104946.

123   S. Yuan, X. Li, J. Zhu, G. Zhang, P. van Puyvelde, B. van der Bruggen, *Chem. Soc. Rev.* **2019**, *48*, 2665–2681.

124   H. Lyu, H. Li, N. Hanikel, K. Wang, O. M. Yaghi, *J. Am. Chem. Soc.* **2022**, *144*, 12989–12995.

125   K. Gottschling, L. Stegbauer, G. Savasci, N. A. Prisco, Z. J. Berkson, C. Ochsenfeld, B. F. Chmelka, B. V. Lotsch, *Chem. Mater.* **2019**, *31*, 1946–1955.

126   Y. Zeng, R. Zou, Y. Zhao, *Adv. Mater.* **2016**, *28*, 2855–2873.

127   M. Dogru, T. Bein, *Chem. Commun.* **2014**, *50*, 5531–5546.

128   C. R. DeBlase, K. Hernández-Burgos, K. E. Silberstein, G. G. Rodríguez-Calero, R. P. Bisbey, H. D. Abruña, W. R. Dichtel, *ACS nano* **2015**, *9*, 3178–3183.

129   J. L. Fenton, D. W. Burke, D. Qian, M. O. d. La Cruz, W. R. Dichtel, *J. Am. Chem. Soc.* **2021**, *143*, 1466–1473.

130   D. N. Bunck, W. R. Dichtel, *J. Am. Chem. Soc.* **2013**, *135*, 14952–14955.

131   F. J. Uribe-Romo, C. J. Doonan, H. Furukawa, K. Oisaki, O. M. Yaghi, *J. Am. Chem. Soc.* **2011**, *133*, 11478–11481.

132   V. S. Vyas, F. Haase, L. Stegbauer, G. Savasci, F. Podjaski, C. Ochsenfeld, B. V. Lotsch, *Nat. Commun.* **2015**, *6*, 8508.

133   L. Stegbauer, K. Schwinghammer, B. V. Lotsch, *Chem. Sci.* **2014**, *5*, 2789–2793.

134   S. Xu, Z. Liao, A. Dianat, S.-W. Park, M. A. Addicoat, Y. Fu, D. L. Pastoetter, F. G. Fabozzi, Y. Liu, G. Cuniberti, M. Richter, S. Hecht, X. Feng, *Angew. Chem. Int. Ed.* **2022**, *61*, e202202492.

135   E. Jin, Z. Lan, Q. Jiang, K. Geng, G. Li, X. Wang, D. Jiang, *Chem* **2019**, *5*, 1632–1647.

136   R. Chen, J.-L. Shi, Y. Ma, G. Lin, X. Lang, C. Wang, *Angew. Chem. Int. Ed.* **2019**, *58*, 6430–6434.

137   S. Wang, X.-X. Li, L. Da, Y. Wang, Z. Xiang, W. Wang, Y.-B. Zhang, D. Cao, *J. Am. Chem. Soc.* **2021**, *143*, 15562–15566.

138   X. Zhuang, W. Zhao, F. Zhang, Y. Cao, F. Liu, S. Bi, X. Feng, *Polym. Chem.* **2016**, *7*, 4176–4181.

139   E. Jin, M. Asada, Q. Xu, S. Dalapati, M. A. Addicoat, M. A. Brady, H. Xu, T. Nakamura, T. Heine, Q. Chen, D. Jiang, *Science* **2017**, *357*, 673–676.

140   D. Becker, B. P. Biswal, P. Kaleńczuk, N. Chandrasekhar, L. Giebeler, M. Addicoat, S. Paasch, E. Brunner, K. Leo, A. Dianat, G. Cuniberti, R. Berger, X. Feng, *Chem. Eur. J.* **2019**, *25*, 6562–6568.

141   A. Acharjya, P. Pachfule, J. Roeser, F.-J. Schmitt, A. Thomas, *Angew. Chem. Int. Ed.* **2019**, *58*, 14865–14870.

142   H. Lyu, C. S. Diercks, C. Zhu, O. M. Yaghi, *J. Am. Chem. Soc.* **2019**, *141*, 6848–6852.

143   S. Wei, F. Zhang, W. Zhang, P. Qiang, K. Yu, X. Fu, D. Wu, S. Bi, *J. Am. Chem. Soc.* **2019**, *141*, 14272–14279.

144   T. Jadhav, Y. Fang, W. Patterson, C.-H. Liu, E. Hamzehpoor, D. F. Perepichka, *Angew. Chem.* **2019**, *131*, 13891–13895.

145   Y. Zhao, H. Liu, C. Wu, Z. Zhang, Q. Pan, F. Hu, R. Wang, P. Li, X. Huang, Z. Li, *Angew. Chem. Int. Ed.* **2019**, *58*, 5376–5381.

146   S. Xu, M. Richter, X. Feng, *Acc. Mater. Res.* **2021**, *2*, 252–265.

147   X. Li, *Mater. Chem. Front.* **2021**, *5*, 2931–2949.

148   D.-G. Wang, T. Qiu, W. Guo, Z. Liang, H. Tabassum, D. Xia, R. Zou, *Energy Environ. Sci.* **2021**, *14*, 688–728.

149   S. Ma, T. Deng, Z. Li, Z. Zhang, J. Jia, G. Wu, H. Xia, S.-W. Yang, X. Liu, *Angew. Chem. Int. Ed.* **2022**, *61*, e202208919.

150   Y. Li, X. Song, G. Zhang, L. Wang, Y. Liu, W. Chen, L. Chen, *ChemSusChem* **2022**, *15*, e202200901.

151   X. Huang, Y.-B. Zhang, *Chem. Lett.* **2021**, *50*, 676–686.

152   L. Stegbauer, S. Zech, G. Savasci, T. Banerjee, F. Podjaski, K. Schwinghammer, C. Ochsenfeld, B. V. Lotsch, *Adv. Energy Mater.* **2018**, *8*, 1703278.

153   T. Banerjee, K. Gottschling, G. Savasci, C. Ochsenfeld, B. V. Lotsch, *ACS Energy Lett.* **2018**, *3*, 400–409.

154   L. Sun, M. Lu, Z. Yang, Z. Yu, X. Su, Y.-Q. Lan, L. Chen, *Angew. Chem. Int. Ed.* **2022**, *61*, e202204326.

155   T. Banerjee, F. Haase, G. Savasci, K. Gottschling, C. Ochsenfeld, B. V. Lotsch, *J. Am. Chem. Soc.* **2017**, *139*, 16228–16234.

156   K. Gottschling, G. Savasci, H. Vignolo-González, S. Schmidt, P. Mauker, T. Banerjee, P. Rovó, C. Ochsenfeld, B. V. Lotsch, *J. Am. Chem. Soc.* **2020**, *142*, 12146–12156.

157   T. Banerjee, B. V. Lotsch, *Nat. Chem.* **2018**, *10*, 1175–1177.

158   X. Wang, L. Chen, S. Y. Chong, M. A. Little, Y. Wu, W.-H. Zhu, R. Clowes, Y. Yan, M. A. Zwijnenburg, R. S. Sprick, A. I. Cooper, *Nat. Chem.* **2018**, *10*, 1180–1189.

159   W.-K. Han, Y. Liu, X. Yan, Y. Jiang, J. Zhang, Z.-G. Gu, *Angew. Chem. Int. Ed.* **2022**, *61*, e202208791.

160   J. Yang, A. Acharjya, M.-Y. Ye, J. Rabeah, S. Li, Z. Kochovski, S. Youk, J. Roeser, J. Grüneberg, C. Penschke, M. Schwarze, T. Wang, Y. Lu, R. van de Krol, M. Oschatz, R. Schomäcker, P. Saalfrank, A. Thomas, *Angew. Chem. Int. Ed.* **2021**, *60*, 19797–19803.

161   Z.-J. Wang, H. Song, H. Liu, J. Ye, *Angew. Chem. Int. Ed.* **2020**, *59*, 8016–8035.

162   J. Khan, Y. Sun, L. Han, *Small Methods* **2022**, *6*, e2201013.

163   Z. Fu, X. Wang, A. M. Gardner, X. Wang, S. Y. Chong, G. Neri, A. J. Cowan, L. Liu, X. Li, A. Vogel, R. Clowes, M. Bilton, L. Chen, R. S. Sprick, A. I. Cooper, *Chem. Sci.* **2020**, *11*, 543–550.

164   W. Zhong, R. Sa, L. Li, Y. He, L. Li, J. Bi, Z. Zhuang, Y. Yu, Z. Zou, *J. Am. Chem. Soc.* **2019**, *141*, 7615–7621.

165   I. Hazra Chowdhury, A. Hazra Chowdhury, P. Sarkar, S. M. Islam, *ChemNanoMat* **2021**, *7*, 580–591.

166   J. Ding, X. Guan, J. Lv, X. Chen, Y. Zhang, H. Li, D. Zhang, S. Qiu, H.-L. Jiang, Q. Fang, *J. Am. Chem. Soc.* **2023**, *145*, 3248–3254.

167   S. Yang, W. Hu, X. Zhang, P. He, B. Pattengale, C. Liu, M. Cendejas, I. Hermans, X. Zhang, J. Zhang, J. Huang, *J. Am. Chem. Soc.* **2018**, *140*, 14614–14618.

168   J. Hawecker, J.-M. Lehn, R. Ziessel, *J. Chem. Soc., Chem. Commun.* **1983**, 536–538.

169   J. Hawecker, J.-M. Lehn, R. Ziessel, *J. Chem. Soc., Chem. Commun.* **1984**, 328–330.

170   W. Zhou, Q.-W. Deng, G.-Q. Ren, L. Sun, L. Yang, Y.-M. Li, D. Zhai, Y.-H. Zhou, W.-Q. Deng, *Nat. Commun.* **2020**, *11*, 4481.

171   Y.-Z. Cheng, X. Ding, B.-H. Han, *ChemPhotoChem* **2021**, *5*, 406–417.

172   X. Li, J. Yu, M. Jaroniec, *Chem. Soc. Rev.* **2016**, *45*, 2603–2636.

173   J. Xu, C. Yang, S. Bi, W. Wang, Y. He, D. Wu, Q. Liang, X. Wang, F. Zhang, *Angew. Chem. Int. Ed.* **2020**, *59*, 23845–23853.

174   S. Bi, C. Yang, W. Zhang, J. Xu, L. Liu, D. Wu, X. Wang, Y. Han, Q. Liang, F. Zhang, *Nat. Commun.* **2019**, *10*, 2467.

175   M. Lu, J. Liu, Q. Li, M. Zhang, M. Liu, J.-L. Wang, D.-Q. Yuan, Y.-Q. Lan, *Angew. Chem. Int. Ed.* **2019**, *58*, 12392–12397.

176   L. Chen, L. Wang, Y. Wan, Y. Zhang, Z. Qi, X. Wu, H. Xu, *Adv. Mater.* **2020**, *32*, e1904433.

177   S. Kandambeth, A. Mallick, B. Lukose, M. V. Mane, T. Heine, R. Banerjee, *J. Am. Chem. Soc.* **2012**, *134*, 19524–19527.

178   B. P. Biswal, S. Chandra, S. Kandambeth, B. Lukose, T. Heine, R. Banerjee, *J. Am. Chem. Soc.* **2013**, *135*, 5328–5331.

179   Y. Yang, X. Chu, H.-Y. Zhang, R. Zhang, Y.-H. Liu, F.-M. Zhang, M. Lu, Z.-D. Yang, Y.-Q. Lan, *Nat. Commun.* **2023**, *14*, 593.

180   Y. Fang, Y. Hou, X. Fu, X. Wang, *Chem. Rev.* **2022**, *122*, 4204–4256.

181   Z. Mi, T. Zhou, W. Weng, J. Unruangsri, K. Hu, W. Yang, C. Wang, K. A. I. Zhang, J. Guo, *Angew. Chem. Int. Ed.* **2021**, *60*, 9642–9649.

182   R. Shen, X. Li, C. Qin, P. Zhang, X. Li, *Adv. Energy Mater.* **2023**, *13*, 2203695.

183   C.-C. Gu, F.-H. Xu, W.-K. Zhu, R.-J. Wu, L. Deng, J. Zou, B.-C. Weng, R.-L. Zhu, *Chem. Commun.* **2023**, *59*, 7302–7320.

184   M. Z. Rahman, T. Edvinsson, J. Gascon, *Nat. Rev. Chem.* **2022**, *6*, 243–258.

185   M.-Y. Qi, M. Conte, M. Anpo, Z.-R. Tang, Y.-J. Xu, *Chem. Rev.* **2021**, *121*, 13051–13085.

186   J. Schneider, D. W. Bahnemann, *J. Phys. Chem. Lett.* **2013**, *4*, 3479–3483.

187   Y. Xia, B. Zhu, L. Li, W. Ho, J. Wu, H. Chen, J. Yu, *Small* **2023**, e2301928.

2 Identifying Kinetic Bottlenecks in the Photocatalytic Oxygen Evolution with Covalent Organic Frameworks

Stefan Trenker, Hugo A. Vignolo-Gonzalez, Liang Yao, Martijn Zwijnenburg, Bettina V. Lotsch

Manuscript to be submitted

2.1 Abstract

Covalent organic frameworks (COFs) have emerged as promising semiconducting materials for photocatalytic applications due to their large surface area, high crystallinity, and vast synthetic tunability. This is especially noticeable in the context of photocatalytic water splitting, where many COFs have been employed for the hydrogen evolution half-reaction. There, sacrificial reagents typically replace the kinetically demanding oxygen evolution half-reaction. On the contrary, only few reports focus on (sacrificial) water oxidation with COF photocatalysts. In most of these cases, cobalt species as oxygen evolution co-catalyst, often with limited insight into their structure and detailed role in the catalysis. Herein, we use heterogenization of a molecularly defined iridium half-sandwich complex onto a bipyridine-based COF (Ir@TAPB-BPY COF) to provide detailed structural insights, which ensures the integrity of the targeted co-catalyst. First, we demonstrate the retained catalytic activity of the anchored Cp*Ir(III) motifs in chemical water oxidation experiments. Following photocatalytic tests also indicate oxygen evolution activity, which in careful control experiments could be traced back to contaminants. Ir@TAPB-BPY COF and – more surprisingly – also two literature-known oxygen evolving COFs proved to be inactive in our tests. Using computational methods, we trace back the missing performance to kinetic limitations of the anchored co-catalytic species. This work demonstrates the pitfalls associated with low-performing oxygen evolution photocatalysts as well as the indispensability of control experiments and their careful evaluation.

2.2 Introduction

Covalent Organic Frameworks (COFs) are a new class of organic polymers that combine high crystallinity, defined porosity, and chemical stability.[1–6] The structural modularity resulting from the use of tunable molecules as building blocks allows for the extensive and systematic alteration of the resulting materials' chemical and optoelectronic properties. Recent examples include pore-size tuning through linker elongation[7], and introduction of redox activity based on suitable linkers.[8,9] Special interest in COFs has been piqued for their potential as photocatalysts, e.g. for solar water splitting, which makes use of their intrinsic light absorption and high surface area, along with the molecular level tunability of the chromophoric units and thus optoelectronic properties.[10–13] However, photocatalytic water splitting with COFs has generally focused on the reductive half reaction, that is, hydrogen evolution (eq 2-1).[14] In this case, the other half of water splitting – the oxidation of water to dioxygen (eq. 2-2) – is suppressed through the use of a sacrificial electron donor (SED), enabling mechanistic insights into and optimization of the hydrogen evolution reaction (HER, Scheme 2-1).[14,15] For the photocatalytic HER to occur efficiently, COFs have been equipped with various co-catalytic species (proton reduction catalyst, PRC) such as Pt nanoparticles or cobalt complexes.[14,16] By matching COF composition with the right choice of SED and co-catalysts, sacrificial hydrogen evolution rates as high as 197 mmol g^{-1} h^{-1} could be achieved to date.[17–27]

$$4\,H^+ + 4\,e^- \rightarrow 2\,H_2 \qquad \text{(eq. 2-1)}$$

$$2\,H_2O \rightarrow O_2 + 4\,H^+ + 4\,e^- \qquad \text{(eq. 2-2)}$$

$$2\,H_2O \rightarrow O_2 + 2\,H_2 \qquad \text{(eq. 2-3)}$$
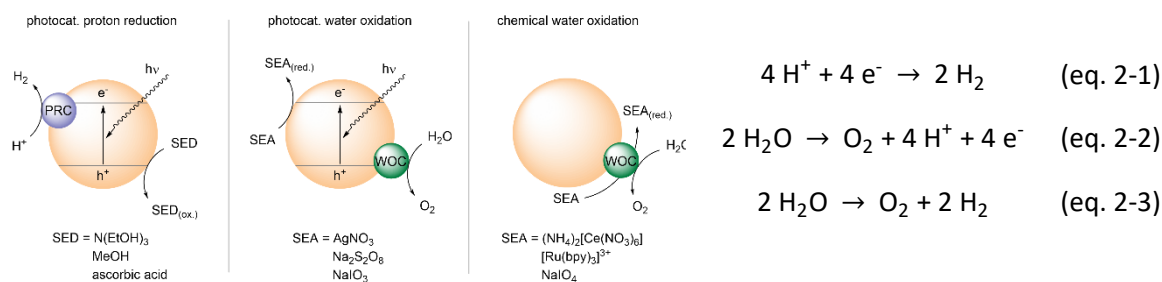
Scheme 2-1: Sketch of water splitting half reactions with semiconductor and sacrificial agents compared to chemical water oxidation (left) and reaction equations associated with water splitting (right).

On the other hand, the oxygen evolution reaction (OER) is rarely explored with COFs. It requires a strongly positive valence band and involves transfer of four electrons along with the formation of an oxygen-oxygen bond, which makes it significantly more challenging compared to two-electron transfer HER, both thermodynamically and kinetically.[15,28–31] Whereas the electrons are drawn off through reduction of a sacrificial electron acceptor (SEA), the electron holes are used to oxidize water. Given the standard potential for the oxidation of water to oxygen (E^0 = 1.23 V *vs*. NHE), a sufficiently positive valence band is a major prerequisite for a semiconductor to be thermodynamically suitable for water oxidation photocatalysis. As shown both computationally and experimentally for conjugated polymers, electron-poor and nitrogen-rich monomers shift the ionization potential (valence band) to more positive values, in turn increasing the thermodynamic driving force for water oxidation with the eventual photocatalyst.[32–34]

In addition, to overcome the kinetic limitations associated with oxygen evolution, water oxidation catalysts (WOCs) are often employed. Traditionally, WOCs are composed of transition metals such as

Ru, Ir, Co, Ni, either as heterogeneous oxide-based catalysts[35,36] or in the form of molecular species.[30,37–39] Research on COFs for photocatalytic water oxidation has so far focused on co-catalysts based on cobalt (Table S2-6).[40–44] The highest oxygen evolution rate yet was achieved using a benzotrithiophene-based imine COF, which was reported to evolve 665 μmol g^{-1} h^{-1} after loading with 16 wt% $Co(ClO_4)_2$.[45]

Oxygen evolution with metal-organic frameworks (MOFs), on the other hand, shows a higher variety of co-catalytic species. LIANG et al. report the immobilization of a Ru(terpy) complex on MIL-101(Cr), and investigate the catalytic efficacy and stability depending on the binding site (terpy = 2,2';6',2"-terpyridine).[46] Similarly, WANG and coworkers construct UiO-67 with heterogenized half-sandwich IrCp* complexes for a detailed mechanistic water oxidation study (Cp* = pentamethylcyclo-pentadienyl).[47,48] However, in these examples the metalated MOFs were not reported for photocatalytic, but rather chemical water oxidation with cerium(IV) ammonium nitrate (CAN) as the oxidant (Scheme 2-1). Due to its instability above pH 1, experiments with CAN can only be conducted under strongly acidic conditions. Alternative terminal oxidants such as sodium periodate and potassium peroxymonosulfate can be employed under neutral conditions, but are prone to undesired oxygen transfer pathways.[49–51] COF photocatalysts for water oxidation on the other hand mostly utilize silver nitrate as the SEA, especially when relying on cobalt as co-catalytic species.[40–43] Only rarely alternative photocatalytic SEAs such as sodium persulfate[45] or chemical water oxidation reagents such as CAN are used.[52]

In this work, we broaden the scope of oxygen evolution with COFs by developing a novel iridium-loaded COF and testing its activity with several commonly used SEAs in both photocatalytic and chemical water oxidation setups. Iridium, both heterogeneously in the form of its oxide and homogeneously as Ir complexes, is one of the most active elements for oxygen evolution catalysis.[53,54] Among molecular Ir WOCs, iridium half-sandwich complexes with Cp* ligands have emerged as prototypical species for (photo-)chemical water oxidation[55–59] as well as photoelectrocatalysis[60–64] and electrocatalysis.[65–68] In addition, IrO_2-decorated photocatalysts have been reported for oxygen evolution from water both in the presence[69,70] and absence[71] of SEAs. In the latter case, Bai et al. could achieve overall water splitting with a conjugated polymer which emerged from both experimental and computational screening of the two water-splitting half-reactions.[32,71–74]

Since iridium is a scarce element, heterogenization of catalytically active mononuclear Ir complexes onto a suitable COF photocatalyst provides a means to achieve highest possible noble-metal atom utilisation.[57,75] First, we study chemical water oxidation to prove the retained catalytic activity of IrCp* when anchored to an imine COF via bipyridine sites. When testing the photocatalytic activity of the IrCp*-decorated COF though, we only find parasitic oxygen evolution that could be traced back to contaminated glassware in rigorous blank experiments. Similarly, reproduction of literature examples also failed to yield reliable oxygen evolution with COF photocatalysts with Co as co-catalyst. Using both experimental and computational analysis, we identify kinetic bottlenecks as the source for lacking oxygen evolution activity when using our iridium-loaded COF. Drawing on these results, our study

provides a guideline for future research in the field of sacrificial oxygen evolution with heterogeneous organic photocatalysis.

2.3   Results and Discussion

We choose TAPB-BPY COF as the model system for this study. It is formed through the condensation of 1,3,5-tris(4-aminophenyl)benzene (**TAPB**) and 2,2'-bipyridyl-5,5'-dialdehyde (**BPY-CHO**), which connect *via* the creation of imine bonds to form a two-dimensional COF under solvothermal conditions. Consequently, TAPB-BPY COF features an ordered, porous structure decorated with bipyridine moieties, which can be utilized to coordinate metal species in general, and water oxidation catalysts in particular.[76] The latter has been shown by the groups of LI, LI, and YANG for the exact same COF, where coordinating cobalt ions to TAPB-BPY COF enabled photocatalytic water oxidation.[40] According to the authors, this demonstrates that TAPB-BPY COF in principle has a low-lying valence band and is thus thermodynamically capable of oxidizing water (Table S2-1).

Intrigued by these results, we expanded the scope of water oxidation co-catalysts used in conjunction with COFs. Making use of the bipyridine sites covering the pore walls of TAPB-BPY COF, we devised an iridium analogue of cobalt-loaded TAPB-BPY COF – Ir@TAPB-BPY COF – which features chelated IrCp* motifs (Figure 2-1). Whereas the molecularly defined Ir co-catalyst should introduce high catalytic activity, the surrounding COF provides both high spatial distribution and stability for the metal complex through its bipyridine sites.[75] Besides constituting promising molecular iridium WOCs,[54] IrCp* species are excellent catalysts for a variety of reactions such as organic oxidations[77] and reductions,[78,79] as well as CO_2 hydrogenation.[80] Altogether, these possibilities suggest the usability of Ir@TAPB-BPY COF for applications also beyond the oxygen evolution reaction covered within this report.
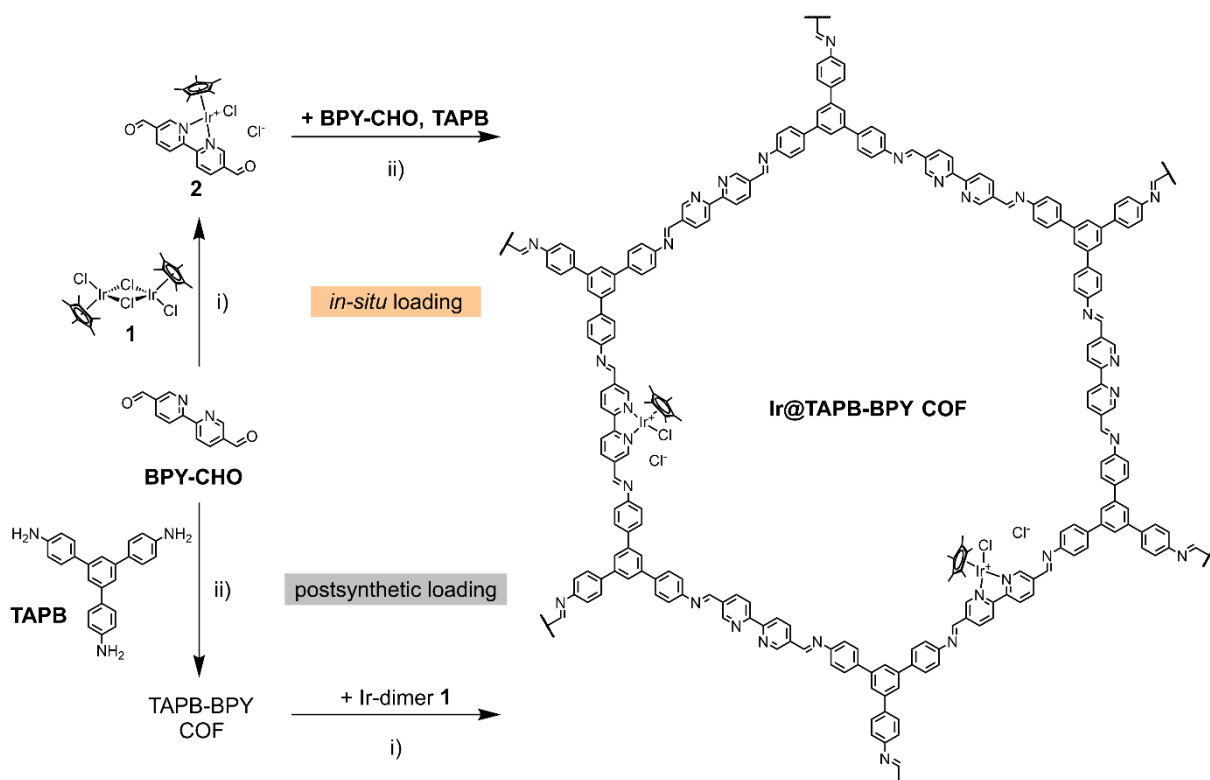
Figure 2-1: Synthetic approaches to IrCp*-loaded TAPB-BPY COF. Reaction conditions: i) solvent, 2-20 h, rt. ii) mesitylene/1,4-dioxane, 6M AcOH, 120 °C, 72 h.

The targeted iridium complex can be easily bound to the bipyridine moieties in TAPB-BPY COF through reaction with the respective dimer $[Cp*IrCl_2]_2$ **1**. Using an excess of **1**, a maximum loading of about 14 wt% could be achieved as confirmed by inductively coupled plasma optical emission spectrometry (ICP-OES). Scanning electron microscopy (SEM) confirms the homogeneous distribution of iridium over the COF particles (Figure S2-43). However, we found that this procedure leads to a drastic decrease in crystallinity and porosity judging from diffraction patterns and sorption isotherms, respectively (Figure S2-1, Figure S2-2). Reactions of **1** with an isoreticular imine COF lacking bipyridine units confirm that Ir neither binds to the imine groups nor deposits in the form of nanoparticles (Figure S2-3).[81]

In order to retain the crystalline and porous nature of TAPB-BPY COF after loading with **1**, we employed an *in-situ* rather than the postsynthetic approach. By reaction of the original linker **BPY-CHO** with the iridium precursor **1**, we can easily synthesize the metalated building block **2** which can be subsequently used for the construction of iridium-loaded TAPB-BPY COF (Figure 2-1).[82–84] Not only does this approach allow to precisely tune the iridium content of the resulting Ir@TAPB-BPY COF (Figure S2-5), it also yields highly-ordered materials judging from X-ray powder diffraction (XRPD) data (Figure 2-2a). Analogous to pristine TAPB-BPY COF, Ir@TAPB-BPY COF exhibits distinct reflections at 2Θ = 2.29° (100), 4.06° (1-20), 4.64° (200), 6.21° (2-30), 8.26° (130) and a weak stacking reflection at 25.4°. As an approximation to account for 10% metalated linker **2**, we constructed a unit cell similar to metal-free TAPB-BPY COF but with additional IrCp*Cl moieties occupying 1/12 of the bipyridine sites (Figure 2-2a). Due to the concomitant decrease in symmetry, the space group changed from *P*6 to *P1*. The unit cell parameters obtained from Pawley refinement of the experimental powder pattern (R_{wp} 7.56%) are $a = b = 44.35$ Å, $c = 14.00$ Å, $\alpha = 90°$, $\beta = 90°$, $\gamma = 120°$ (Figure S2-4).
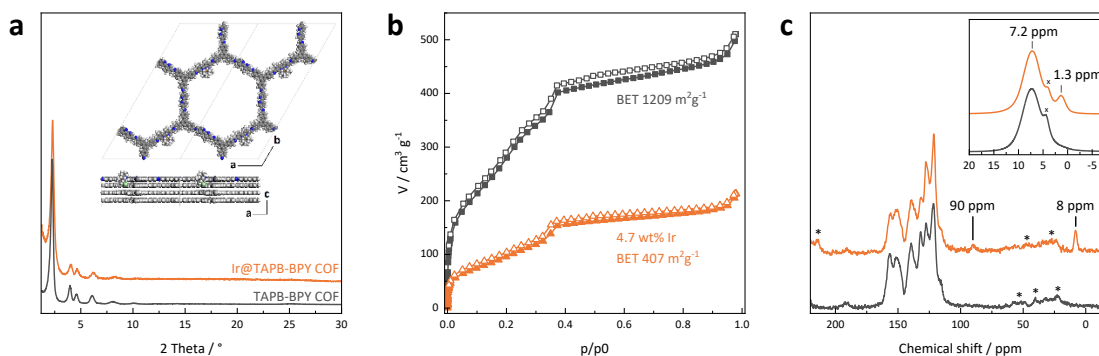
Figure 2-2: (a) XRPD pattern of TAPB-COF (grey) and Ir@TAPB-COF (orange). (b) Nitrogen sorption isotherm of TAPB-COF (grey) and Ir@TAPB-COF (orange) at 77 K. Filled and open symbols represent the adsorption and the desorption branches, respectively. (c) 13C ssNMR spectrum of TAPB-COF (grey) and Ir@TAPB-COF (orange). Asterisks mark spinning side bands. The inset shows ^{1}H ssNMR spectra, with crosses marking residual water signals.

Comparing the connectivity of both COFs *via* Fourier transform infrared (FTIR) spectroscopy, we could not detect significant differences (Figure S2-7). Both Ir@TAPB-BPY COF and metal-free TAPB-BPY COF show the appearance of a new imine signal at 1623 cm^{-1} ($v_{C=N(stretch)}$), which – concomitant with the absence of amine bands (v_{N-H} = 3200 – 3500 cm^{-1}) – hints to the successful condensation of TAPB with **2** or **BPY-CHO**, respectively (Figure S2-8).

Nitrogen sorption analysis reveals type IV isotherms for both metal-free and Ir@TAPB-BPY COF, though with varying BET surface areas of 1209 and 407 m^2 g^{-1}, respectively (Figure 2-2b).[85] In a series with iridium content ranging from 2 to 6 wt%, however we see no correlation of the loading degree with the surface area (Figure S2-5). The derived pore size distributions (PSDs) for both pristine TAPB-BPY COF and Ir@TAPB-BPY COF show pores centered around 3.9 nm (Figure S2-9).

Transmission electron microscopy (TEM) visualizes the mesopores inherent to Ir@TAPB-BPY COF, and Fast-Fourier Transform (FFT) analysis confirms a periodicity of 3.6 nm in good agreement with sorption and XPRD data (Figure S2-39). We could not find any indication of metal-containing (nano-)particles covering the COF. Likewise, scanning electron microscopy (SEM) and elemental mapping show agglomerated micrometer-sized particles with an even distribution of N, C, Ir, and Cl, which indicates successful heterogenization of the targeted iridium complex onto TAPB-BPY COF (Figure S2-40, Figure S2-41).

^{13}C solid-state nuclear magnetic resonance (ssNMR) was then conducted to assess the presence of the Cp* ligand and thus the integrity of the target complex. The COF's aromatic signals in the range between 160 and 110 ppm do not change significantly upon Ir loading (Figure 2-2c). On the other hand, two new signals at 90 and 8 ppm can be assigned to the methine and methyl groups of the Cp* ligand, respectively. Concomitantly, a new signal at 1.3 ppm in the ^{1}H ssNMR spectrum of Ir@TAPB-BPY COF shows the presence of the methyl protons.

Furthermore, we conducted X-ray photoelectron spectroscopy (XPS) to confirm both the binding of the iridium species to the bipyridine sites of the heterogeneous support as well as its chemical state. The Ir 4f$_{7/2}$ peak of Ir@TAPB-BPY COF is detected at 62.7 eV, which is in good agreement with literature values (62.7 eV)[86] for the Ir^{III} center of [Cp*Ir(bpy)Cl]Cl (Figure S2-16). Upon iridium incorporation, the

nitrogen 1s signal for the imine and pyridyl nitrogen atoms shifts from 398.7 to 399.0 eV, indicative of the binding of Ir to the framework.

In order to ascertain the retained activity of the Ir species after binding to the COF, we performed chemical water oxidation experiments in a specifically designed flow reactor (Figure 2-3).[87] By using a continuous flow of inert gas with a slight overpressure of up to 250 mbar, we circumvent the leaking of oxygen into the apparatus and achieve high sensitivities. Online optical trace oxygen sensors allow for almost lag-free and instrumentally simple oxygen detection. Together, these factors allow us to conduct economical small-scale experiments, namely 5 mg COF dispersed in 5 mL sacrificial solution for a typical experiment. We previously discussed the layout and reliability of this setup.[87,88]
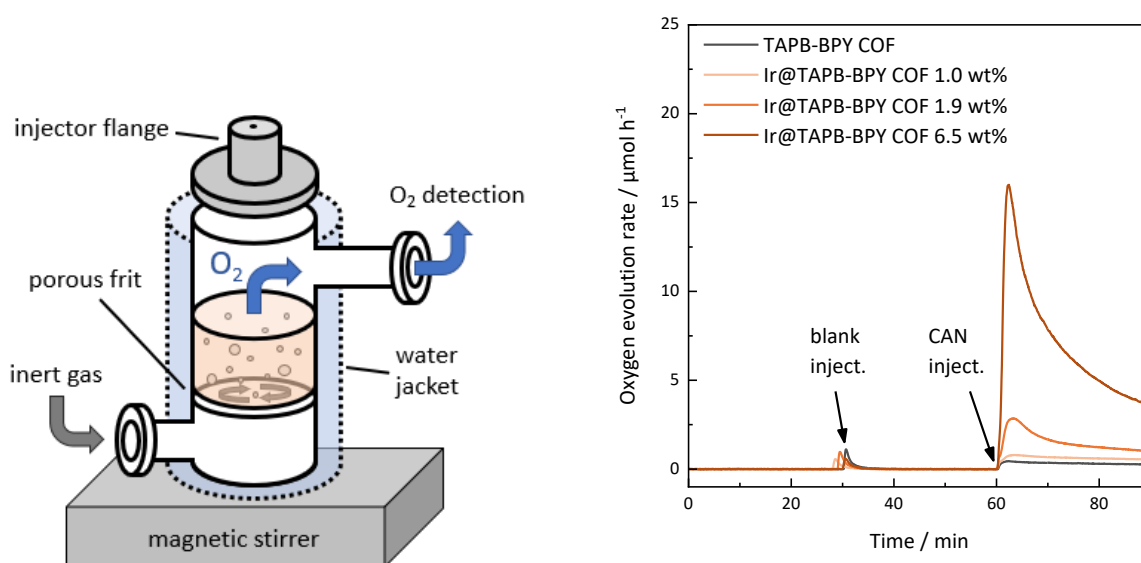
Figure 2-3: Left: Schematic experimental setup for the chemical water oxidation experiments. Right: Chemical water oxidation experiments with TAPB-BPY COF at varying iridium loadings.

In a typical experiment with CAN as the terminal oxidant, we suspended the COF in 0.1 M nitric acid (pH 1). After a blank injection of HNO_3 (aq.) to evaluate the amount of trace oxygen introduced per injection, we added a degassed portion of the sacrificial through a gas-tight septum injector nut (Figure 2-3). As expected, both pristine aqueous nitric acid as well as non-metalated TAPB-BPY COF do not show oxygen evolution upon CAN addition (Table 2-1, entries 1+2, Figure S2-78).

Iridium species, including [Cp*Ir(bpy)Cl]Cl, have in fact been first reported as water oxidation catalyst under these exact conditions.[66,89] Indeed, we found that Ir@TAPB-BPY COF shows substantial oxygen evolution, with turnover frequencies (TOFs) in the range of 2.52 – 4.08 h^{-1} depending on the Ir loading (Table 2-1, entries 3-5, Figure 2-3). Also, Ir@TAPB-BPY COF exhibits turnover numbers of >1 and continuous oxygen evolution over two hours (Figure S2-79), which hints to a catalytic OER process instead of a degradation process releasing O_2. These results indicate the general preservation of catalytic activity of the Cp*Ir moiety bound to TAPB-BPY COF, despite showing activity two orders of magnitude lower than the molecular WOC in both our own (Table 2-1, entries 6+7), and literature experiments (Table 2-1, entries 8+9).

Table 2-1: Chemical water oxidation experiments with Ir@TAPB-BPY COF.

Entry	COF	µmol Ir	[Ir] / µM	O$_2$ evolution[a]	TOF[a] / h^{-1}
1	HNO$_3$ blank	-	-	0.111 µmol	-
2	TAPB-BPY COF	-	-	0.161 µmol	-
3	Ir@TAPB-BPY COF	0.25	50	0.327 µmol	2.52
4	Ir@TAPB-BPY COF	0.48	96	0.765 µmol	3.18
5	Ir@TAPB-BPY COF	1.68	336	3.457 µmol	4.08
6	[Cp*Ir(bpy)Cl]Cl	0.25	50	26.864 µmol	214
7	[Cp*Ir(bpy)Cl]Cl	0.025	5	2.654 µmol	212
8[b]	[Cp*Ir(bpy)Cl]Cl	0.025	5	1.625 µmol	130
9[c]	[Cp*Ir(bpy)Cl]Cl	0.30	7.1	37.8 µmol	252
10[d]	Ir@TAPB-BPY COF	0.25	50	0.494 µmol	3.94
11[d]	Filtrate (entry 10)	0.05	10	0.110 µmol	4.40

Reaction conditions: 5.0 mg COF in 78 mM CAN (in 5.0 mL 0.1 M HNO$_3$). [a] after/within 30 minutes [b] value extracted from graph. Ref. [63] [c] data obtained in experiments with 28 mM CAN and volumetric detection. TON value extracted from graph. Ref. [87] [d] Experiment conducted in D$_2$O instead of H$_2$O.

However, such a substantial difference in activity brings up doubts about the actual active species, since even small amounts of leached catalyst could catalyze the OER rather than COF-bound iridium. We thus subjected the reaction mixture filtrate to another oxygen evolution experiment under identical conditions, which lead to a decreased oxygen evolution of 0.110 µmol compared to 0.494 µmol (Table 2-1, entries 10+11; Figure S2-82). Interestingly, ICP analysis reveals the leakage of 20% iridium from Ir@TAPB-BPY into the reaction solution (Table S2-11), so that the TOF of the leaked iridium species in solution is similar to that of the parent Ir@TAPB-BPY COF. We thus postulate that COF-bound iridium – rather than a highly active molecular species – accounts for most of the catalytic activity observed with Ir@TAPB-BPY COF. It can also not be fully excluded that residual nanoparticular Ir@TAPB-BPY COF accounts for the catalytic activity of the filtrate. However, SEM elemental mapping suggests that the uniform distribution of both Ir and Cl over Ir@TAPB-BPY COF is preserved after catalysis with CAN, but also deposition of Ce on the COF (Figure S2-90, Figure S2-91). TEM analysis confirms the presence of CeO$_x$ nanoparticles, but at the same time refutes that of iridium-rich oxidic nanoparticles which could also be catalytically active (Figure S2-92).[90–92] This is further corroborated by XPS analysis, which shows unchanged Ir peak positions and no signs of IrO$_x$ (Figure S2-19).[48,91] The signals for the Ce depositions are characteristic for Ce(III) species, in line with the expected reduction of CAN during catalysis (Figure S2-18).

NMR spectroscopy of the filtrate after water oxidation catalysis with Ir@TAPB-BPY COF in 78 mM CAN shows the presence of formic acid and acetic acid indicative of the oxidative cleavage of the Cp* ring (Figure S2-88).[48,90,92] It has been proposed elsewhere that the oxidation or complete loss of the Cp* ligand does not impair the catalytic activity of Ir-based WOCs, and that some bidentate ligands such as bipyridine do not degrade.[48,92–97] In fact, such oxidative modification has been reported to be essential for the catalytic activity of some Cp*-based Ir WOCs.[48,92] Accordingly, we could see little oxygen evolution from Ir@TAPB-BPY COF in 10 mM CAN in contrast to 78 mM CAN (Figure S2-83). Similar to molecular [Cp*Ir(bpy)Cl]Cl, Ir@TAPB-BPY COF shows highest catalytic activity in the range of 50 mM CAN (Figure S2-84 - Figure S2-86).[66]

Unfortunately, potential catalyst leaching is not the only drawback of chemical water oxidation with CAN in acidic media. XRPD of the retrieved Ir@TAPB-BPY COF indicates a loss of long-range order after treatment with CAN, especially at higher concentrations (). Consistently, nitrogen sorption analysis and TEM reveal the gradual loss of structural porosity when increasing the CAN concentration from 10 mM to 78 mM (Figure S2-96, Figure S2-92). FTIR spectroscopy hints to oxidation of either the framework or the Cp* ligand, as the broad band around 3300 cm^{-1} is assigned to O-H stretching modes (Figure S2-95).[48,91,92] More importantly, FTIR spectroscopy shows the partial loss of imine stretching vibrations originally present in Ir@TAPB-BPY COF, while at the same time we observe a new feature around 1654 cm^{-1} which we ascribe to amide groups resulting from imine oxidation through CAN.[98] Likewise, postcatalytic ssNMR spectroscopy reveals the loss of the ^{13}C imine signal at 156 ppm, whereas a distinct amide signal cannot be assigned beyond doubt (Figure S2-97). Besides, both the signals for the COF backbone as well as the Cp* ring are preserved, showing that neither is completely decomposed.

Though driving WOC with CAN allows for a fast assessment of the catalytic activity of Ir@TAPB-BPY COF, the acidic and highly oxidative conditions during catalysis are detrimental to the COF stability. This is less problematic when switching to the targeted water oxidation photocatalysis since the respective SEAs can usually be used under neutral conditions and have less positive redox potentials (Figure S2-99). That said, photocatalytic water oxidation is mechanistically more complex, as it relies on successful charge carrier generation within the COF upon illumination, and transport of the electron holes to the Ir catalyst. It thus involves both components – the COF light absorber and the Ir catalyst, and hence relies on the matching of their electronic levels both relative to each other and with respect to the water oxidation potential.

The catalytic activity of Ir@TAPB-BPY COF for photocatalytic oxygen evolution was examined in the same flow reactor after replacing the injector nut through an optical quartz glass window (Figure S2-11).[87] After exemplarily confirming the functionality of our setup with the literature-known catalytic systems [Cp*Ir(bpy)Cl]Cl + [Ru(bpy)$_3$]Cl$_2$ and RuO$_2$ + TiO$_2$ (Figure S2-74), we conducted photocatalytic experiments with Ir@TAPB-BPY COF in the presence of sodium persulfate as SEA.[87,99] Unfortunately, we could neither detect significant amounts of oxygen under illumination with AM 1.5-filtered nor with visible light (>420 nm, Figure S2-75). Only with full-spectral illumination could we measure oxygen evolution over the course of 14 hours with rates of up to 0.75 µmol h^{-1} or 150 µmol h^{-1} g^{-1} (Figure S2-76). However, we do not attribute these findings to actual water oxidation by the COF, but rather to decomposition of S$_2$O$_8^{2-}$ as discussed in the supporting information (chapter 6.2).

We thus investigated silver nitrate as an alternative SEA, which is more commonly used in water oxidation photocatalysis but brings about the disadvantage of undesired deposition of elemental silver.[100] Over the course of a photocatalytic experiment this can significantly alter the optical properties of the photocatalyst.[72,101,102]
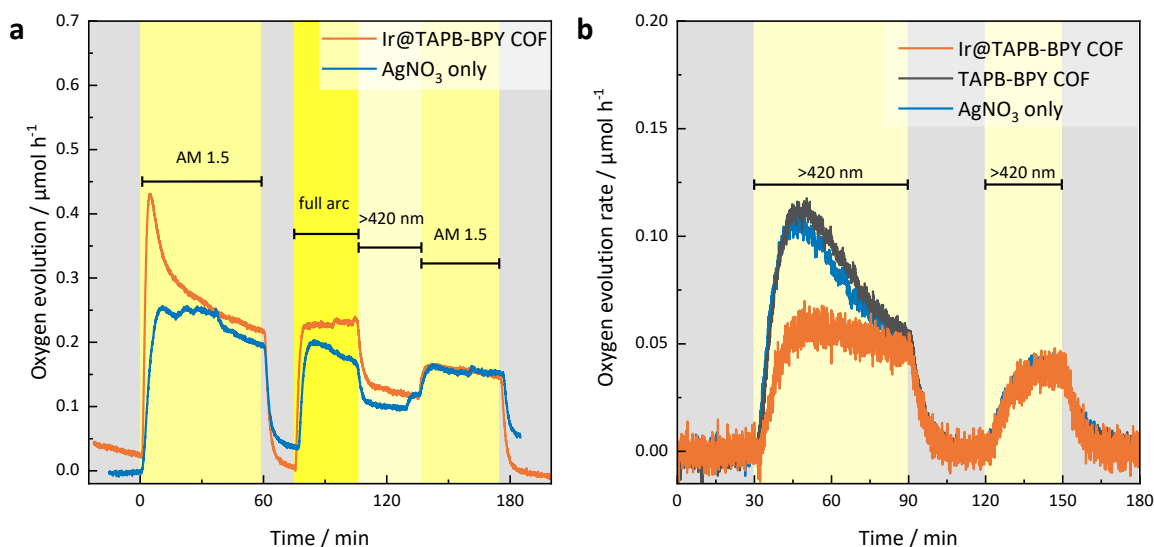
Figure 2-4: Photocatalysis experiments with AgNO$_3$ as sacrificial electron acceptor. Reaction conditions 5.0 mg COF, AgNO$_3$ (10 mM, 5.0 mL water), illumination with a 300 W Xe lamp and optical filters as specified. Grey areas represent dark reaction conditions.

We found that illumination of a suspension of Ir@TAPB-BPY COF in aqueous silver nitrate with a conventional 300 Xe lamp leads to distinct oxygen evolution of 0.1 – 0.4 µmol h^{-1} depending on the incident wavelength range (Figure 2-4a). Both AM 1.5 filtered and unfiltered full spectral illumination gave somewhat higher rates than visible light (>420 nm) which does not exceed values of 0.2 µmol h^{-1}. Most surprisingly, when conducting a control measurement with only silver nitrate solution and visible light we obtained an oxygen trace similar to those of both Ir@TAPB-BPY and TAPB-BPY COF under the same conditions (Figure 2-4b). Given that both photosensitizer and WOC are missing in this experiment, no oxygen evolution was expected to take place.

We thus set out to understand this finding and elucidate the exact role of silver nitrate in photocatalysis. To this end, we defined four possible decomposition pathways for AgNO$_3$ which are discussed in detail in the supporting information (chapter 6.2). Through several control experiments, we could not confirm light-induced AgNO$_3$ decomposition to be the reason for the observed oxygen evolution. Ultimately, we found that trace amounts of ruthenium-loaded tungsten oxide nanoparticles (RuO$_2$@WO$_3$) might have led to undesired water oxidation in our case. Said contaminants were found in the top layer of the reactor's glass frit (Figure 2-3) and are traced back to experiments previously conducted in the same reactor.[88] Irradiation of identical AgNO$_3$ solutions in a pristine and uncontaminated flow reactor does not lead to oxygen evolution (Figure 2-5). Similar to the AgNO$_3$ blank experiments, photocatalysis experiments with Ir@TAPB-BPY COF conducted in a pristine reactor also indicate no significant O$_2$ generation (Figure S2-72), suggesting that its previously observed activity (Figure 2-4) can be solely ascribed to contaminations. Note that RuO$_2$@WO$_3$ nanoparticles are not active under chemical water oxidation conditions and thus not refute the catalytic activity of Ir@TAPB-BPY COF when using CAN (*vide supra*, Figure S2-98). Due to the milder reaction conditions during photocatalysis compared to chemical water oxidation, Ir@TAPB-BPY COF could be recovered with retained crystallinity and porosity, albeit showing deposited Ag / AgCl particles (Figure S2-13, Figure S2-14, Figure S2-45 - Figure S2-13). XPS confirms the deposition of silver species (Figure S2-18) and at

the same time reveals unchanged iridium binding energy, indicating the preservation of anchored iridium complexes (Figure S2-19).
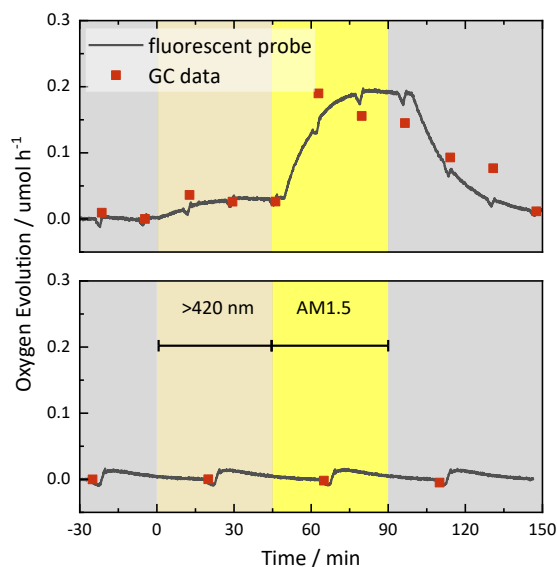
Figure 2-5: Comparative photolysis of silver nitrate solutions in a contaminated (top) and a pristine flow photoreactor (bottom). Reaction conditions: 10 mM AgNO$_3$, 5 mL, AAA solar simulator, 1 sun, optical filters as annotated. Simultaneous oxygen measurement *via* gas chromatography and fluorescent sensors under flow conditions. Periodic peaks are due to pressure variations upon GC sampling.

Though trace metal impurities and their role in catalysis should always be considered – as highlighted for example by repeated reports on "metal-free" SUZUKI–MIYAURA cross-couplings[103–109] – sometimes significant effort has to be taken to avoid data misinterpretation.

Unfortunately, comparable blank experiments have not been conducted in other literature reports on COF photocatalysts and are only rarely ever mentioned (Table S2-7). We thus tried to reproduce some of the few examples for oxygen evolution with COF photocatalysts, namely "BpCo-COF-1" as well as cobalt-loaded "I-TST", which we will refer to as Co@TAPB-BPY COF and Co@TTI-COF in the following (Scheme 2-2).[40,42,110] Both have been reported for OER in conjunction with AgNO$_3$ as SEA, and can be prepared from commercially available building blocks. Material characterization with respect to crystallinity, porosity, and metal content shows conformity between our reproduced COFs and the respective literature data (Figure S2-20 - Figure S2-26). For Co@TAPB-BPY COF, we found cobalt evenly distributed over the spherical particles, in line with the proposed binding of Co^{2+} to the frameworks' bipyridine (Figure S2-49, Figure S2-50). For Co@TTI-COF, SEM and TEM imaging revealed heterogenous deposition of amorphous CoO$_x$ species (Figure S2-51 - Figure S2-52).[42]
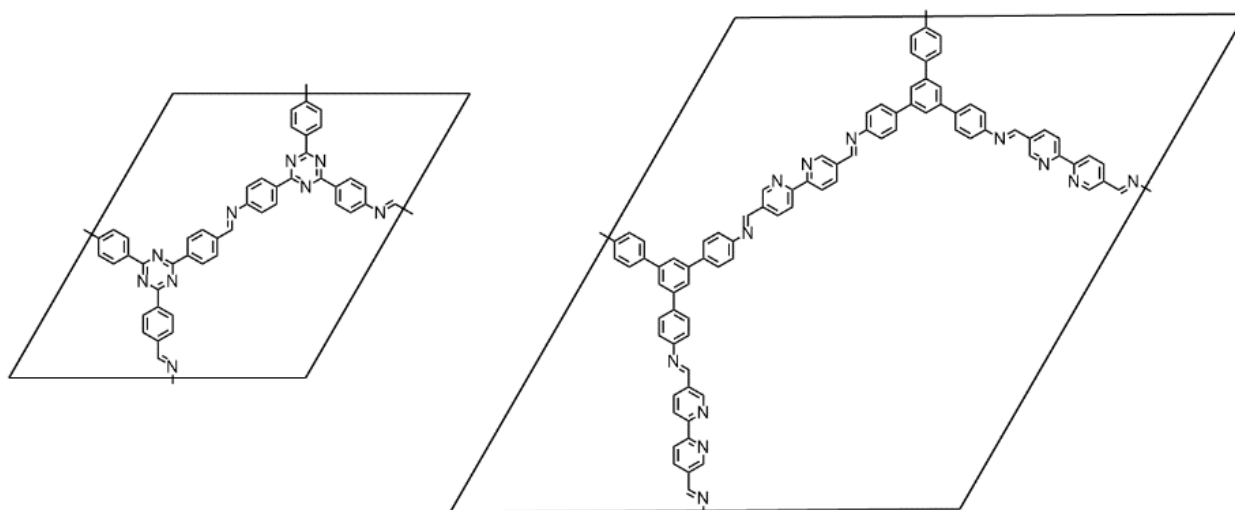
Scheme 2-2: Unit cells as schematic representation of TTI-COF (left) and TAPB-BPY COF (right).

However, when assessing the photocatalytic activity of Co@TAPB-BPY and Co@TTI-COF, we could not confirm the reported oxygen evolution rates. In fact, no significant amounts of evolved oxygen could be detected at all, even though we meticulously followed the given protocol (Figure 2-6). Only when using glassware contaminated with $RuO_2@WO_3$ we could measure apparent oxygen evolution, with rates of 0.05 - 0.10 µmol h^{-1} – similar to Ir@TAPB-BPY COF or $AgNO_3$ blanks (Figure S2-69, Figure S2-70, *vide supra*). Attempts to achieve distinct oxygen evolution by the COFs through variation of the reaction parameters were unsuccessful (Table S2-8, Table S2-9). More interestingly, during this screening, we obtained apparent OER rates in the range of 8–200 µmol g^{-1} h^{-1} which coincidentally match the literature activity of Co@TAPB-BPY COF and Co@TTI-COF of 152 and 37 µmol g^{-1} h^{-1}, respectively. Though such direct comparison is difficult due to divergent experimental setups, it can be deduced that the reported OER activities are in the same order of magnitude as the background oxygen evolution we traced back to contaminated glassware. Altogether, these findings lead us to postulate that also in our reproduction attempts of literature examples oxygen evolution was mostly caused by catalytically active contaminants, rather than by photocatalytic activity of the respective COFs.
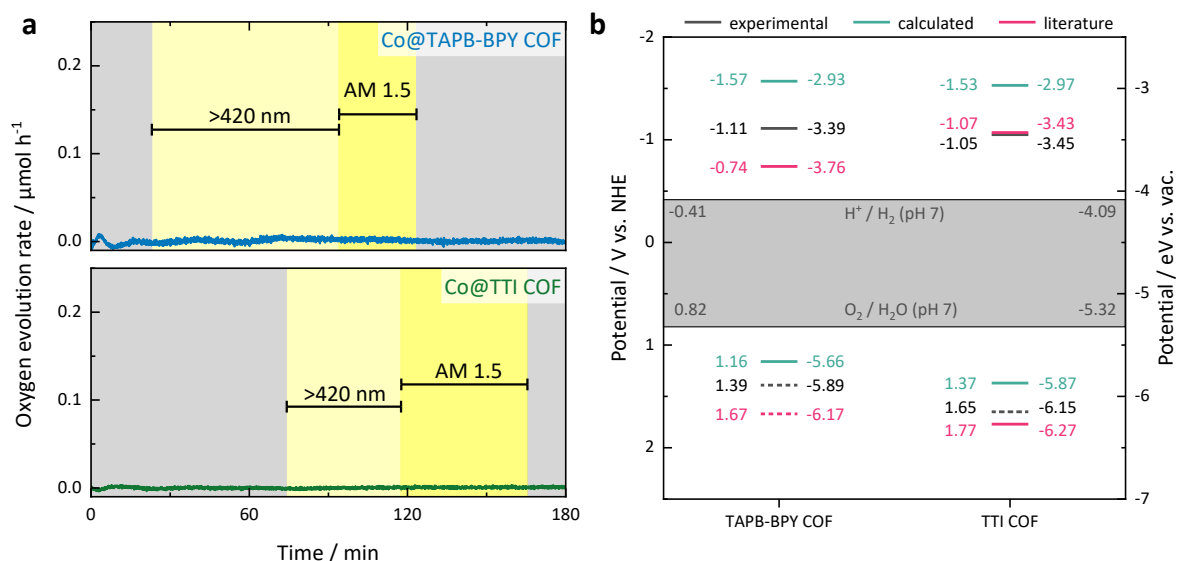
Figure 2-6: (a) Reproduction of photocatalytic oxygen evolution experiments with literature-known COFs. Reaction conditions: 2.0 mg Co@TAPB-BPY COF (1.0 wt% Co), AgNO₃ (5 mM, 20 mL), bulk reactor (top) or: 1.0 mg Co@TTI-COF (0.9 wt% Co), AgNO₃ (10 mM, 5 mL), 10 mg La₂O₃, flow reactor (bottom). Both experiments were performed with an AAA solar simulator at 1 sun and with optical filters as annotated. (b) Comparison of experimentally determined band positions (*via* CV in MeCN; black), computationally predicted ionization potentials and electron affinities (in MeCN, turquoise), and literature values (pink) for TAPB-BPY COF and TTI COF. Dashed lines represent values obtained indirectly, for example VBM calculated from the CBM *via* subtraction of the optical band gap. Potentials for the water splitting half reactions illustrated as grey area. See Table S2-1 and Table S2-2 for details.

In order to assure that water oxidation catalysis is thermodynamically feasible with both TAPB-BPY COF and TTI-COF, we approximated their band positions through cyclovoltammetry (CV, Figure S2-26). Given a water oxidation potential of -5.32 eV *vs.* vac at pH 7 (0.82 V *vs.* SHE), both TAPB-BPY COF (E_{VB} = -5.89 eV / 1.39 V *vs.* SHE) and especially TTI-COF (E_{VB} = -6.15 eV / 1.65 V *vs.* SHE) show sufficient thermodynamic driving force for oxygen evolution. These values also roughly match the reported band positions for TAPB-BPY COF and TTI-COF (Table S2-1, Figure 2-6).

To complement the electrochemical assessment based on CV, we performed DFT calculations on representative cluster fragments of the TAPB-BPY and TTI COFs (Figure S2-30) embedded in a dielectric continuum to describe the effect of the water or other solvents in the pores of the COF and surrounding the COF particles. Though this approach does not take into account periodicity and layer stacking, it allows for an assessment of the effect of the dielectric screening of the water or other solvents the COF is dispersed in on its electronic properties.[24] Previous work demonstrated that such DFT cluster calculations in the case of linear conjugated polymers accurately predict the IP and EA values of dry polymer solids measured by experimental photoelectron spectroscopy when using a relative dielectric permittivity of 2 (organic solid) for the continuum.[34,111] When using a relative dielectric permittivity of 80.1 (water) DFT cluster calculations can successfully explain the trends in the activity of such polymeric solids for sacrificial hydrogen evolution from water/SED mixtures.[73,74,112–114] For TAPB-BPY COF the ionization potential (IP) and electron affinity (EA) obtained with the B3LYP DFT functional are 1.16 and -1.57 V *vs.* SHE, respectively (in acetonitrile; for values in water see Table S2-2). For TTI-COF, the IP and EA were predicted at 1.37 and -1.53 V *vs.* SHE, respectively. Despite showing more negative values compared to the experimentally determined band positions, these calculations confirm the

trend that both TAPB-BPY COF and TTI-COF should thermodynamically be suited for water oxidation catalysis, and that TTI-COF has a more positive valence band maximum / IP than TAPB-BPY COF, hence a larger driving force for water oxidation (Figure 2-6).

This statement also holds true for Ir@TAPB-BPY, for which CV reveals valence band maxima identical to TAPB-BPY COF (1.39 V *vs*. SHE / -5.89 eV *vs*. vac.; Figure S2-27, Table S2-1). Interestingly, the underlying CV curves do not show any evidence of iridium redox features such as the Ir[III/IV] couple which would be expected as a reversible wave in the range of 0.6–0.8 V vs. Fc/Fc[+] (Figure S2-28).[58,66,86,115] Similar observations have recently been made for other COFs loaded with molecularly defined iridium species.[116,117] This could be a hint of strong electronic coupling between the heterogenized molecular iridium species and the TAPB-BPY COF, similar to that observed by SURENDRANATH and co-workers for homogeneous complexes conjugated to graphite, called graphite-conjugated catalysts (GCC). The authors found that after binding rhodium, ruthenium, or rhenium complexes to graphitic carbon *via* terminal phenazine sites the electrocatalytic activity and the underlying mechanisms drastically changed compared to the molecular analogues.[118–120] In a nutshell, the catalysis – in their case, CO_2 reduction and hydrogen evolution – proceeded without the metal complex changing its oxidation state, as opposed to similar molecular catalysts in solution.[118,121] We note that in our case iridium is bound to an extended π-system *via* bipyridine sites resembling phenazine, and that during catalysis charges could be stored on the COF instead of the bound metal atom. A recent review discusses this concept explicitly for COFs in the context of electrocatalytic CO_2 reduction.[122]

Based on the assumption that photocatalytic water oxidation with Ir@TAPB-BPY COF similarly involves a mechanism where the metal oxidation state does not change, we use DFT to calculate the free energy profile of water oxidation at a redox-innocent iridium complex bound to an exemplary TAPB-BPY COF fragment. We note that the four electron transfers underlying water oxidation differ significantly in their respective free energy changes (Scheme 2-3, Figure S2-33). TAPB-BPY COF might especially be struggling to drive step (2) with photogenerated holes (ΔG^0 = 1.30 eV, E_{VB} = 1.16/1.39 V vs. NHE, Figure 2-6). By considering only proton-coupled electron transfers (PCETs) eventual transition barriers associated with either e[-] or H^{+} transfer are neglected, so our ΔG^0 values can be regarded lower estimates.[123,124] Chemical water oxidation with CAN (*vide supra*), however, can seemingly overcome the supposedly limiting kinetics of the individual oxidation events in Ir@TAPB-BPY COF due to its high potential of *ca*. 1.75 V at pH 1.[49] The free energy change for step (2) at pH 0 was calculated to be 1.71 eV (Figure S2-32).

ΔG^0 at pH 7

	(1)	**(2)**	**(3)**	**(4)**
	1.16 eV	1.30 eV	0.60 eV	0.03 eV

Ir(III)-H$_2$O $\longrightarrow$ Ir(III)-OH[•] $\longrightarrow$ Ir(III)-O(H)OH $\longrightarrow$ Ir(III)-OOH $\longrightarrow$ Ir(III)-H$_2$O

- e[-]	- e[-]	- e[-]	- e[-]
- H^{+}	- H^{+}	- H^{+}	- H^{+}
	+ H$_2$O		- O$_2$
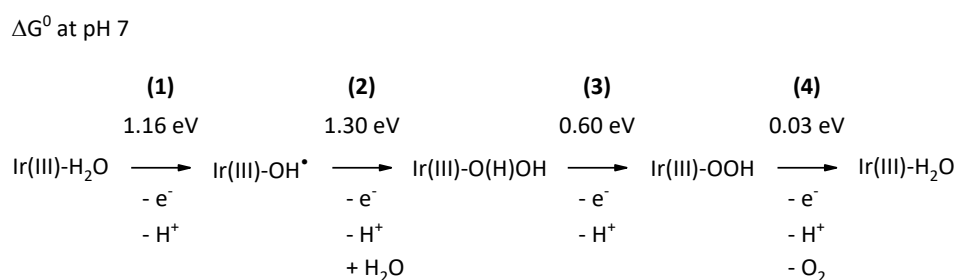
Scheme 2-3: Schematic reaction pathway for water oxidation on Ir@TAPB-BPY COF assuming redox-innocent Ir(III) centers according to the GCC principle. Changes in free energy given in eV at pH 7.

For Co@TAPB-BPY COF, the predicted free energy changes for water oxidation indicate even stronger kinetic limitations. Here, oxidation of COF-bound Co-OH species and subsequent formation of the O-O bond is associated with $\Delta G^0 = 1.64$ eV at pH 7 (Figure S2-34) which would be achievable given literature values for E_{VB} of 1.67 V vs. NHE, but not with our experimentally determined and calculated values of 1.39 and 1.16 V, respectively (Figure 2-6).

We note that highly positive valence bands are unconditional prerequisites for oxygen evolution with COF photocatalysts – but that successful catalysis cannot be inferred from low-lying valence bands alone. Due to the slow kinetics and demanding mechanisms underlying the OER, photocatalytic water oxidation with COFs is – compared to photocatalytic HER with COFs – significantly more reliant on high overpotentials of at least 300 mV.[14,125] The question as to whether the inability to provide enough driving force for every step of the water oxidation mechanism also applies to our unsuccessful reproduction of oxygen evolution with literature COFs will be the subject of follow-up studies. We note that apart from low overpotentials several other bottlenecks can limit photocatalytic oxygen evolution, which have not been discussed in detail within the scope of this work. These include efficient light absorption, charge separation and transfer, framework stability, and COF-cocatalyst interactions.

Conclusion

In summary, we successfully synthesized a new 2D-COF equipped with Cp*Ir motifs and demonstrated its catalytic activity for chemical water oxidation with CAN. Subsequently, we used Ir@TAPB-BPY COF to broaden the scope of photocatalytic water oxidation with tailored organic frameworks. We could in fact detect oxygen upon illumination of this COF suspended in silver nitrate with visible light. However, a series of blank measurements revealed that the activity of both Ir@TAPB-BPY COF as well as two literature examples was only based on catalytically active contaminants. In no case did we observe oxygen evolution that could be clearly linked to photocatalytic water oxidation by the COFs.

Chemical water oxidation, however, was successfully applied to show the retained catalytic activity of the WOC in Ir@TAPB-BPY COF. By doing so and subsequently comparing chemical water oxidation and our photocatalytic oxygen evolution experiment, we could identify kinetic limitations inherent to Ir@TAPB-BPY COF as a possible bottleneck in water oxidation. This finding was further corroborated with DFT calculations showing that the four required steps in water oxidation at a COF-bound iridium center suffer from unevenly distributed free energy changes which could only be overcome by a strong oxidant such as CAN, but not photogenerated holes.

With this discovery, we wish to create awareness for the ambiguous role sacrificials or contaminations may have in oxygen evolution photocatalysis. In a best practice setting the usual screening of the catalytic species and their loading should be followed up with testing of several SEAs, including chemical water oxidation reagents, to find the best reaction conditions and rule out data misinterpretation.

Author Contributions

S.T. led the project, performed syntheses and experiments, and wrote the manuscript with input from L.Y. and H.A.V.-G. L.Y. prepared COF samples for electrochemical characterization. H.A.V.-G. designed

experimental setups for (photo-)catalysis and oxygen detection and helped with data analysis. M.Z. performed quantum-chemical calculations. B.V.L. and L.Y. supervised the research, discussed the data, and co-wrote the paper. All Authors read and commented on the manuscript.

2.4   References

1   J. L. Segura, M. J. Mancheño, F. Zamora, *Chem. Soc. Rev.* **2016**, *45*, 5635–5671.

2   D.-G. Wang, T. Qiu, W. Guo, Z. Liang, H. Tabassum, D. Xia, R. Zou, *Energy Environ. Sci.* **2021**, *14*, 688–728.

3   K. Geng, T. He, R. Liu, S. Dalapati, K. T. Tan, Z. Li, S. Tao, Y. Gong, Q. Jiang, D. Jiang, *Chem. Rev.* **2020**, *120*, 8814–8933.

4   M. S. Lohse, T. Bein, *Adv. Funct. Mater.* **2018**, *28*, 1705553.

5   F. Haase, B. V. Lotsch, *Chem. Soc. Rev.* **2020**, *49*, 8469–8500.

6   C. S. Diercks, O. M. Yaghi, *Science* **2017**, *355*.

7   S. T. Emmerling, R. Schuldt, S. Bette, L. Yao, R. E. Dinnebier, J. Kästner, B. V. Lotsch, *J. Am. Chem. Soc.* **2021**, *143*, 15711–15722.

8   K. Muggli, L. Spies, D. Bessinger, F. Auras, T. Bein, *ACS Nanosci. Au* **2023**, *3*, 153–160.

9   E. Vitaku, C. N. Gannett, K. L. Carpenter, L. Shen, H. D. Abruña, W. R. Dichtel, *J. Am. Chem. Soc.* **2020**, *142*, 16–20.

10   S. Trenker, L. Grunenberg, T. Banerjee, G. Savasci, L. M. Poller, K. I. M. Muggli, F. Haase, C. Ochsenfeld, B. V. Lotsch, *Chem. Sci.* **2021**, *12*, 15143–15150.

11   S. Yang, W. Hu, X. Zhang, P. He, B. Pattengale, C. Liu, M. Cendejas, I. Hermans, X. Zhang, J. Zhang, J. Huang, *J. Am. Chem. Soc.* **2018**, *140*, 14614–14618.

12   H. Wang, H. Wang, Z. Wang, L. Tang, G. Zeng, P. Xu, M. Chen, T. Xiong, C. Zhou, X. Li, D. Huang, Y. Zhu, Z. Wang, J. Tang, *Chem. Soc. Rev.* **2020**, *49*, 4135–4165.

13   X. Chen, K. Geng, R. Liu, K. T. Tan, Y. Gong, Z. Li, S. Tao, Q. Jiang, D. Jiang, *Angew. Chem. Int. Ed.* **2020**, *59*, 5050–5091.

14   T. Banerjee, K. Gottschling, G. Savasci, C. Ochsenfeld, B. V. Lotsch, *ACS Energy Lett.* **2018**, *3*, 400–409.

15   Y. Bai, K. Hippalgaonkar, R. S. Sprick, *J. Mater. Chem. A* **2021**, *9*, 16222–16232.

16   X. Huang, Y.-B. Zhang, *Chem. Lett.* **2021**, *50*, 676–686.

17   S. Ma, T. Deng, Z. Li, Z. Zhang, J. Jia, G. Wu, H. Xia, S.-W. Yang, X. Liu, *Angew. Chem. Int. Ed.* **2022**, *61*, e202208919.

18   R. Shen, X. Li, C. Qin, P. Zhang, X. Li, *Adv. Energy Mater.* **2023**, *13*, 2203695.

19   B. P. Biswal, H. A. Vignolo-González, T. Banerjee, L. Grunenberg, G. Savasci, K. Gottschling, J. Nuss, C. Ochsenfeld, B. V. Lotsch, *J. Am. Chem. Soc.* **2019**, *141*, 11082–11092.

20   V. S. Vyas, F. Haase, L. Stegbauer, G. Savasci, F. Podjaski, C. Ochsenfeld, B. V. Lotsch, *Nat. Commun.* **2015**, *6*, 8508.

21   T. Banerjee, F. Haase, G. Savasci, K. Gottschling, C. Ochsenfeld, B. V. Lotsch, *J. Am. Chem. Soc.* **2017**, *139*, 16228–16234.

22   L. Stegbauer, K. Schwinghammer, B. V. Lotsch, *Chem. Sci.* **2014**, *5*, 2789–2793.

23   K. Gottschling, G. Savasci, H. Vignolo-González, S. Schmidt, P. Mauker, T. Banerjee, P. Rovó, C. Ochsenfeld, B. V. Lotsch, *J. Am. Chem. Soc.* **2020**, *142*, 12146–12156.

24   X. Wang, L. Chen, S. Y. Chong, M. A. Little, Y. Wu, W.-H. Zhu, R. Clowes, Y. Yan, M. A. Zwijnenburg, R. S. Sprick, A. I. Cooper, *Nat. Chem.* **2018**, *10*, 1180–1189.

25   F.-M. Zhang, J.-L. Sheng, Z.-D. Yang, X.-J. Sun, H.-L. Tang, M. Lu, H. Dong, F.-C. Shen, Y. Liu, Y.-Q. Lan, *Angew. Chem. Int. Ed.* **2018**, *57*, 12106–12110.

26   J. Yang, A. Acharjya, M.-Y. Ye, J. Rabeah, S. Li, Z. Kochovski, S. Youk, J. Roeser, J. Grüneberg, C. Penschke, M. Schwarze, T. Wang, Y. Lu, R. van de Krol, M. Oschatz, R. Schomäcker, P. Saalfrank, A. Thomas, *Angew. Chem. Int. Ed.* **2021**, *60*, 19797–19803.

27   C.-C. Gu, F.-H. Xu, W.-K. Zhu, R.-J. Wu, L. Deng, J. Zou, B.-C. Weng, R.-L. Zhu, *Chem. Commun.* **2023**, *59*, 7302–7320.

28   J. K. Hurst, *Science* **2010**, *328*, 315–316.

29   S. Berardi, S. Drouet, L. Francàs, C. Gimbert-Suriñach, M. Guttentag, C. Richmond, T. Stoll, A. Llobet, *Chem. Soc. Rev.* **2014**, *43*, 7501–7519.

30   X. Sala, I. Romero, M. Rodríguez, L. Escriche, A. Llobet, *Angew. Chem.* **2009**, *121*, 2882–2893.

31   D. G. Nocera, *Acc. Chem. Res.* **2012**, *45*, 767–776.

32   P. Guiglion, C. Butchosa, M. A. Zwijnenburg, *J. Mater. Chem. A* **2014**, *2*, 11996–12004.

33   P. Guiglion, C. Butchosa, M. A. Zwijnenburg, *Macromol. Chem. Phys.* **2016**, *217*, 344–353.

34   P. Guiglion, A. Monti, M. A. Zwijnenburg, *J. Phys. Chem. C* **2017**, *121*, 1498–1506.

35   F. Jiao, H. Frei, *Energy Environ. Sci.* **2010**, *3*, 1018.

36   A. Harriman, I. J. Pickering, J. M. Thomas, *J. Chem. Soc. Faraday Trans. 1* **1988**, *84*, 2795–2806.

37   J. D. Blakemore, R. H. Crabtree, G. W. Brudvig, *Chem. Rev.* **2015**, *115*, 12974–13005.

38   M. D. Kärkäs, O. Verho, E. V. Johnston, B. Åkermark, *Chem. Rev.* **2014**, *114*, 11863–12001.

39   M. D. Kärkäs, B. Åkermark, *Dalton Trans.* **2016**, *45*, 14421–14461.

40   J. Chen, X. Tao, C. Li, Y. Ma, L. Tao, D. Zheng, J. Zhu, H. Li, R. Li, Q. Yang, *Appl. Catal. B* **2020**, *262*, 118271.

41   S. Bi, C. Yang, W. Zhang, J. Xu, L. Liu, D. Wu, X. Wang, Y. Han, Q. Liang, F. Zhang, *Nat. Commun.* **2019**, *10*, 2467.

42   Y. Wan, L. Wang, H. Xu, X. Wu, J. Yang, *J. Am. Chem. Soc.* **2020**, *142*, 4508–4516.

43   E. Jin, Z. Lan, Q. Jiang, K. Geng, G. Li, X. Wang, D. Jiang, *Chem* **2019**, *5*, 1632–1647.

44   S. Chai, X. Chen, X. Zhang, Y. Fang, R. S. Sprick, X. Chen, *Environ. Sci. Nano* **2022**, *9*, 2464–2469.

45   Y. He, G. Liu, Z. Liu, J. Bi, Y. Yu, L. Li, *ACS Energy Lett.* **2023**, *8*, 1857–1863.

46   X. Liang, S. Yang, J. Yang, W. Sun, X. Li, B. Ma, J. Huang, J. Zhang, L. Duan, Y. Ding, *Appl. Catal. B* **2021**, *291*, 120070.

47   C. Wang, Z. Xie, K. E. deKrafft, W. Lin, *J. Am. Chem. Soc.* **2011**, *133*, 13445–13454.

48   C. Wang, J.-L. Wang, W. Lin, *J. Am. Chem. Soc.* **2012**, *134*, 19895–19908.

49   A. R. Parent, R. H. Crabtree, G. W. Brudvig, *Chem. Soc. Rev.* **2013**, *42*, 2247–2252.

50   R. Pokhrel, M. K. Goetz, S. E. Shaner, X. Wu, S. S. Stahl, *J. Am. Chem. Soc.* **2015**, *137*, 8384–8387.

51   D. G. H. Hetterscheid, J. N. H. Reek, *Eur. J. Inorg. Chem.* **2014**, *2014*, 742–749.

52   S. Karak, V. Stepanenko, M. A. Addicoat, P. Keßler, S. Moser, F. Beuerle, F. Würthner, *J. Am. Chem. Soc.* **2022**, *144*, 17661–17670.

53   J. Gao, Y. Liu, B. Liu, K.-W. Huang, *ACS Nano* **2022**, *16*, 17761–17777.

54   J. M. Thomsen, D. L. Huang, R. H. Crabtree, G. W. Brudvig, *Dalton Trans.* **2015**, *44*, 12452–12472.

55   A. Volpe, A. Sartorel, C. Tubaro, L. Meneghini, M. Di Valentin, C. Graiff, M. Bonchio, *Eur. J. Inorg. Chem.* **2014**, *2014*, 665–675.

56   A. Volpe, M. Natali, C. Graiff, A. Sartorel, C. Tubaro, M. Bonchio, *Dalton Trans.* **2020**, *49*, 2696–2705.

57   I. Corbucci, F. Zaccaria, R. Heath, G. Gatto, C. Zuccaccia, M. Albrecht, A. Macchioni, *ChemCatChem* **2019**, *11*, 5353–5361.

58   S. Mukhopadhyay, R. S. Singh, A. Biswas, D. S. Pandey, *Chem. Commun.* **2016**, *52*, 3840–3843.

59   J. M. Koelewijn, M. Lutz, W. I. Dzik, R. J. Detz, J. N. H. Reek, *ACS Catal.* **2016**, *6*, 3418–3427.

60   A. Petronilho, M. Rahman, J. A. Woods, H. Al-Sayyed, H. Müller-Bunz, J. M. Don MacElroy, S. Bernhard, M. Albrecht, *Dalton Trans.* **2012**, *41*, 13074–13080.

61   P. K. Poddutoori, J. M. Thomsen, R. L. Milot, S. W. Sheehan, C. F. A. Negre, V. K. R. Garapati, C. A. Schmuttenmaer, V. S. Batista, G. W. Brudvig, A. van der Est, *J. Mater. Chem. A* **2015**, *3*, 3868–3879.

62   K. L. Materna, J. Jiang, K. P. Regan, C. A. Schmuttenmaer, R. H. Crabtree, G. W. Brudvig, *ChemSusChem* **2017**, *10*, 4526–4534.

63   R. J. Kamire, K. L. Materna, W. L. Hoffeditz, B. T. Phelan, J. M. Thomsen, O. K. Farha, J. T. Hupp, G. W. Brudvig, M. R. Wasielewski, *J. Phys. Chem. C* **2017**, *121*, 3752–3764.

64   G. F. Moore, J. D. Blakemore, R. L. Milot, J. F. Hull, H. Song, L. Cai, C. A. Schmuttenmaer, R. H. Crabtree, G. W. Brudvig, *Energy Environ. Sci.* **2011**, *4*, 2389.

65   S. W. Sheehan, J. M. Thomsen, U. Hintermair, R. H. Crabtree, G. W. Brudvig, C. A. Schmuttenmaer, *Nat. Commun.* **2015**, *6*, 6469.

66   J. D. Blakemore, N. D. Schley, D. Balcells, J. F. Hull, G. W. Olack, C. D. Incarvito, O. Eisenstein, G. W. Brudvig, R. H. Crabtree, *J. Am. Chem. Soc.* **2010**, *132*, 16017–16029.

67   N. D. Schley, J. D. Blakemore, N. K. Subbaiyan, C. D. Incarvito, F. D'Souza, R. H. Crabtree, G. W. Brudvig, *J. Am. Chem. Soc.* **2011**, *133*, 10473–10481.

68   J. M. Thomsen, S. W. Sheehan, S. M. Hashmi, J. Campos, U. Hintermair, R. H. Crabtree, G. W. Brudvig, *J. Am. Chem. Soc.* **2014**, *136*, 13826–13834.

69   K. Maeda, K. Domen, *Angew. Chem. Int. Ed.* **2012**, *51*, 9865–9869.

70   A. Miura, T. Oshima, K. Maeda, Y. Mizuguchi, C. Moriyoshi, Y. Kuroiwa, Y. Meng, X.-D. Wen, M. Nagao, M. Higuchi, K. Tadanaga, *J. Mater. Chem. A* **2017**, *5*, 14270–14277.

71   Y. Bai, C. Li, L. Liu, Y. Yamaguchi, M. Bahri, H. Yang, A. Gardner, M. A. Zwijnenburg, N. D. Browning, A. J. Cowan, A. Kudo, A. I. Cooper, R. S. Sprick, *Angew. Chem. Int. Ed.* **2022**, *61*, e202201299.

72   R. S. Sprick, Z. Chen, A. J. Cowan, Y. Bai, C. M. Aitchison, Y. Fang, M. A. Zwijnenburg, A. I. Cooper, X. Wang, *Angew. Chem. Int. Ed.* **2020**, *59*, 18695–18700.

73   M. Sachs, R. S. Sprick, D. Pearce, S. A. J. Hillman, A. Monti, A. A. Y. Guilbert, N. J. Brownbill, S. Dimitrov, X. Shi, F. Blanc, M. A. Zwijnenburg, J. Nelson, J. R. Durrant, A. I. Cooper, *Nat. Commun.* **2018**, *9*, 4968.

74   R. S. Sprick, B. Bonillo, R. Clowes, P. Guiglion, N. J. Brownbill, B. J. Slater, F. Blanc, M. A. Zwijnenburg, D. J. Adams, A. I. Cooper, *Angew. Chem. Int. Ed.* **2016**, *55*, 1792–1796.

75   A. Macchioni, *Eur. J. Inorg. Chem.* **2019**, *2019*, 7–17.

76   Q. Guan, L.-L. Zhou, Y.-B. Dong, *Chem. Soc. Rev.* **2022**, *51*, 6307–6416.

77   S. Abednatanzi, P. Gohari Derakhshandeh, P. Tack, F. Muniz-Miranda, Y.-Y. Liu, J. Everaert, M. Meledina, F. Vanden Bussche, L. Vincze, C. V. Stevens, V. van Speybroeck, H. Vrielinck, F. Callens, K. Leus, P. van der Voort, *Appl. Catal. B* **2020**, *269*, 118769.

78   Z. Yang, Z. Zhu, R. Luo, X. Qiu, J. Liu, J.-K. Yang, W. Tang, *Green Chem.* **2017**, *19*, 3296–3301.

79 T. P. Brewster, A. J. M. Miller, D. M. Heinekey, K. I. Goldberg, *J. Am. Chem. Soc.* **2013**, *135*, 16022–16025.

80 K. Park, G. H. Gunasekar, N. Prakash, K.-D. Jung, S. Yoon, *ChemSusChem* **2015**, *8*, 3410–3413.

81 J. Hu, H. Mehrabi, Y.-S. Meng, M. Taylor, J.-H. Zhan, Q. Yan, M. Benamara, R. H. Coridan, H. Beyzavi, *Chem. Sci.* **2021**, *12*, 7930–7936.

82 M. Bhadra, H. S. Sasmal, A. Basu, S. P. Midya, S. Kandambeth, P. Pachfule, E. Balaraman, R. Banerjee, *ACS Appl. Mater. Interfaces* **2017**, *9*, 13785–13792.

83 J. Chen, P. Zhao, D. Li, L. Liu, H. Li, *Ind. Eng. Chem. Res.* **2020**, *59*, 9423–9431.

84 J. Chen, H. Li, M. Zhong, Q. Yang, *Green Chem.* **2016**, *18*, 6493–6500.

85 M. Thommes, K. Kaneko, A. V. Neimark, J. P. Olivier, F. Rodriguez-Reinoso, J. Rouquerol, K. S. Sing, *Pure Appl. Chem.* **2015**, *87*, 1051–1069.

86 T. Zhang, K. E. deKrafft, J.-L. Wang, C. Wang, W. Lin, *Eur. J. Inorg. Chem.* **2014**, *2014*, 698–707.

87 H. A. Vignolo-González, S. Laha, A. Jiménez-Solano, T. Oshima, V. Duppel, P. Schützendübe, B. V. Lotsch, *Matter* **2020**, *3*, 464–486.

88 H. A. Vignolo-González, A. Gouder, S. Laha, V. Duppel, S. Carretero-Palacios, A. Jiménez-Solano, T. Oshima, P. Schützendübe, B. V. Lotsch, *Adv. Energy Mater.* **2023**, *13*, 2203315.

89 J. F. Hull, D. Balcells, J. D. Blakemore, C. D. Incarvito, O. Eisenstein, G. W. Brudvig, R. H. Crabtree, *J. Am. Chem. Soc.* **2009**, *131*, 8730–8731.

90 A. Savini, P. Belanzoni, G. Bellachioma, C. Zuccaccia, D. Zuccaccia, A. Macchioni, *Green Chem.* **2011**, *13*, 3360.

91 D. Hong, M. Murakami, Y. Yamada, S. Fukuzumi, *Energy Environ. Sci.* **2012**, *5*, 5708–5716.

92 D. B. Grotjahn, D. B. Brown, J. K. Martin, D. C. Marelius, M.-C. Abadjian, H. N. Tran, G. Kalyuzhny, K. S. Vecchio, Z. G. Specht, S. A. Cortes-Llamas, V. Miranda-Soto, C. van Niekerk, C. E. Moore, A. L. Rheingold, *J. Am. Chem. Soc.* **2011**, *133*, 19024–19027.

93 G. Menendez Rodriguez, F. Zaccaria, S. van Dijk, C. Zuccaccia, A. Macchioni, *Organometallics* **2021**, *40*, 3445–3453.

94 U. Hintermair, S. M. Hashmi, M. Elimelech, R. H. Crabtree, *J. Am. Chem. Soc.* **2012**, *134*, 9785–9795.

95 C. Zuccaccia, G. Bellachioma, O. Bortolini, A. Bucci, A. Savini, A. Macchioni, *Chem. Eur. J.* **2014**, *20*, 3446–3456.

96 S. Zhang, H. Wang, M. Li, J. Han, S. Inagaki, X. Liu, *Dalton Trans.* **2017**, *46*, 9369–9374.

97 X. Liu, Y. Maegawa, Y. Goto, K. Hara, S. Inagaki, *Angew. Chem. Int. Ed.* **2016**, *55*, 7943–7947.

98 P. J. Waller, S. J. Lyle, T. M. Osborn Popp, C. S. Diercks, J. A. Reimer, O. M. Yaghi, *J. Am. Chem. Soc.* **2016**, *138*, 15519–15522.

99 I. Corbucci, K. Ellingwood, L. Fagiolari, C. Zuccaccia, F. Elisei, P. L. Gentili, A. Macchioni, *Catal. Today* **2017**, *290*, 10–18.

100 J. Schneider, D. W. Bahnemann, *J. Phys. Chem. Lett.* **2013**, *4*, 3479–3483.

101 I. Ivanova, T. A. Kandiel, Y.-J. Cho, W. Choi, D. Bahnemann, *ACS Catal.* **2018**, *8*, 2313–2325.

102 F. A. Frame, T. K. Townsend, R. L. Chamousis, E. M. Sabio, T. Dittrich, N. D. Browning, F. E. Osterloh, *J. Am. Chem. Soc.* **2011**, *133*, 7264–7267.

103 N. E. Leadbeater, M. Marco, *Angew. Chem. Int. Ed.* **2003**, *42*, 1407–1409.

104 N. E. Leadbeater, M. Marco, *J. Org. Chem.* **2003**, *68*, 5660–5667.

105 R. K. Arvela, N. E. Leadbeater, M. S. Sangi, V. A. Williams, P. Granados, R. D. Singer, *J. Org. Chem.* **2005**, *70*, 161–168.

106 I. Thomé, A. Nijs, C. Bolm, *Chem. Soc. Rev.* **2012**, *41*, 979–987.

107 M. Avanthay, R. B. Bedford, C. S. Begg, D. Böse, J. Clayden, S. A. Davis, J.-C. Eloi, G. P. Goryunov, I. V. Hartung, J. Heeley, K. A. Khaikin, M. O. Kitching, J. Krieger, P. S. Kulyabin, A. J. J. Lennox, R.

Nolla-Saltiel, N. E. Pridmore, B. J. S. Rowsell, H. A. Sparkes, D. V. Uborsky, A. Z. Voskoboynikov, M. P. Walsh, H. J. Wilkinson, *Nat. Catal.* **2021**, *4*, 994–998.

108 Z. Novák, R. Adamik, J. T. Csenki, F. Béke, R. Gavaldik, B. Varga, B. Nagy, Z. May, J. Daru, Z. Gonda, G. L. Tolnai, *Nat. Catal.* **2021**, *4*, 991–993.

109 J. K. Vinod, A. K. Wanner, E. I. James, K. Koide, *Nat. Catal.* **2021**, *4*, 999–1001.

110 V. S. Vyas, M. Vishwakarma, I. Moudrakovski, F. Haase, G. Savasci, C. Ochsenfeld, J. P. Spatz, B. V. Lotsch, *Adv. Mater.* **2016**, *28*, 8749–8754.

111 D. J. Woods, S. A. J. Hillman, D. Pearce, L. Wilbraham, L. Q. Flagg, W. Duffy, I. McCulloch, J. R. Durrant, A. A. Y. Guilbert, M. A. Zwijnenburg, R. S. Sprick, J. Nelson, A. I. Cooper, *Energy Environ. Sci.* **2020**, *13*, 1843–1855.

112 C. B. Meier, R. Clowes, E. Berardo, K. E. Jelfs, M. A. Zwijnenburg, R. S. Sprick, A. I. Cooper, *Chem. Mater.* **2019**, *31*, 8830–8838.

113 R. S. Sprick, C. M. Aitchison, E. Berardo, L. Turcani, L. Wilbraham, B. M. Alston, K. E. Jelfs, M. A. Zwijnenburg, A. I. Cooper, *J. Mater. Chem. A* **2018**, *6*, 11994–12003.

114 R. S. Sprick, L. Wilbraham, Y. Bai, P. Guiglion, A. Monti, R. Clowes, A. I. Cooper, M. A. Zwijnenburg, *Chem. Mater.* **2018**, *30*, 5733–5742.

115 E. V. Sackville, F. Marken, U. Hintermair, *ChemCatChem* **2018**, *10*, 4280–4291.

116 A. Jati, K. Dey, M. Nurhuda, M. A. Addicoat, R. Banerjee, B. Maji, *J. Am. Chem. Soc.* **2022**, *144*, 7822–7833.

117 A. López-Magano, B. Ortín-Rubio, I. Imaz, D. Maspoch, J. Alemán, R. Mas-Ballesté, *ACS Catal.* **2021**, *11*, 12344–12354.

118 S. Oh, J. R. Gallagher, J. T. Miller, Y. Surendranath, *J. Am. Chem. Soc.* **2016**, *138*, 1820–1823.

119 M. N. Jackson, S. Oh, C. J. Kaminsky, S. B. Chu, G. Zhang, J. T. Miller, Y. Surendranath, *J. Am. Chem. Soc.* **2018**, *140*, 1004–1010.

120 M. N. Jackson, Y. Surendranath, *Acc. Chem. Res.* **2019**, *52*, 3432–3441.

121 M. N. Jackson, C. J. Kaminsky, S. Oh, J. F. Melville, Y. Surendranath, *J. Am. Chem. Soc.* **2019**, *141*, 14160–14167.

122 W. Nie, D. E. Tarnopol, C. C. McCrory, *Curr. Opin. Electrochem.* **2021**, *28*, 100716.

123 J. Rossmeisl, A. Logadottir, J. K. Nørskov, *Chem. Phys.* **2005**, *319*, 178–184.

124 K. Ikeda, Y. Hori, M. H. Mahyuddin, Y. Shiota, A. Staykov, T. Matsumoto, K. Yoshizawa, S. Ogo, *Inorg. Chem.* **2019**, *58*, 7274–7284.

125 J. Hessels, R. J. Detz, M. T. M. Koper, J. N. H. Reek, *Chem. Eur. J.* **2017**, *23*, 16413–16418.

3   A Flavin-inspired Covalent Organic Framework for Photocatalytic Alcohol Oxidation

Stefan Trenker, Lars Grunenberg, Tanmay Banerjee, Gökcen Savasci, Laura M. Poller, Katharina I. M. Muggli, Frederik Haase, Christian Ochsenfeld, and Bettina V. Lotsch
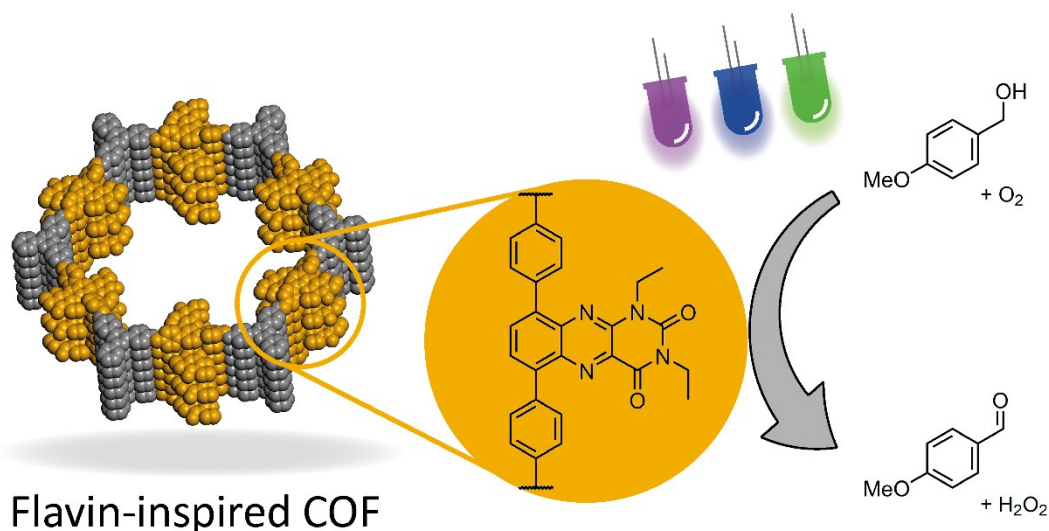
Flavin-inspired COF

3.1   Abstract

Covalent organic frameworks (COFs) offer a number of key properties that predestine them to be used as heterogeneous photocatalysts, including intrinsic porosity, long-range order, and light absorption. Since COFs can be constructed from a practically unlimited library of organic building blocks, these properties can be precisely tuned by choosing suitable linkers. Herein, we report the construction and use of a novel COF (FEAx-COF) photocatalyst, inspired by natural flavin cofactors. We show that the functionality of the alloxazine chromophore incorporated into the COF backbone is retained and study the effects of this heterogenization approach by comparison with similar molecular photocatalysts. We find that the integration of alloxazine chromophores into the framework significantly extends the absorption spectrum into the visible range, allowing for photocatalytic oxidation of benzylic alcohols to aldehydes even with low-energy visible light. In addition, the activity of the heterogeneous COF photocatalyst is less dependent on the chosen solvent, making it more versatile compared to molecular alloxazines. Finally, the use of oxygen as the terminal oxidant renders FEAx COF a promising and "green" heterogeneous photocatalyst.

3.2   Introduction

Metal-free photocatalysis is a promising strategy to address the ever-growing demand for green fuels and fine chemicals. Covalent organic frameworks (COFs), constructed from building blocks composed of earth abundant and light elements, are an emerging class of crystalline and porous polymers with significant potential in this regard. COFs have been explored as heterogeneous photocatalysts for solar hydrogen evolution,[1,2] CO$_2$ reduction,[3] H$_2$O$_2$ generation,[4] for example, and recent examples of C–H functionalization,[5–7] sulfoxidation,[7–10] and amine oxidation[7,11] highlight their usefulness as photoredoxcatalysts. This catalytic versatility is mainly owed to the modular building principle underlying COF chemistry. Therefore, by choosing appropriate building blocks, structural and electronic characteristics of the final material such as pore size[12] and optoelectronic properties[13] - and thus ultimately its reactivity - can be tuned to the desired effect. Integration of suitable linker functionalities into the framework is therefore of prime importance in this regard, as recently exemplified by the induction of chirality[14] or redox-activity[15] to the COF backbone.

Photoredox catalysis is particularly useful in organic chemistry to overcome the activation energy of a particular reaction, to enable milder reaction conditions, or to grant access to orthogonal reaction products and pathways which are not accessible by classical methods. However, photoredox catalysis is often conducted using precious transition-metal complexes.[16–19] In recent times though, a number of metal-free approaches using organic chromophores have been reported: Fluorenone,[20] acridinium ions,[21,22] and Eosin Y[23] are just a few examples.

Mostly owing to their ability to participate in both one- and two-electron redox reactions, flavins, derived from the vitamin riboflavin, represent a particularly interesting family of organic photocatalysts (Scheme 3-1). Depending on the substitution pattern, flavin derivatives can be used for a plethora of catalytic reactions, such as esterifications,[24] alkene hydrogenation,[25] or oxidation of amines,[26–28] sulfides,[26,27,29–32] and alcohols.[32–40]

Flavin   Isoalloxazine   Alloxazine

Scheme 3-1: Molecular structure of Flavin and (Iso)alloxazine. For Riboflavin R = ribityl.

Alloxazines, isomers of the isoalloxazine heterocycle inherent to flavins,[41] have attracted less attention in comparison. Nevertheless, alloxazines have been shown to be superior singlet oxygen sensitizers,[42] and more efficient photocatalysts in [2+2] cycloaddition reactions.[43,44] Also, alloxazines are easier to synthesize and more photostable than isoalloxazines.[45] Despite their versatility, alloxazines and isoalloxazines have been primarily explored as homogeneous catalysts, limiting their practical applicability with regard to product-catalyst separation and recyclability. Several immobilization approaches have been studied to circumvent this problem, including anchoring flavins to mesoporous

silica,[32,46] TiO_2,[47] BiOCl,[48] or polydopamine.[49] In these examples, however, the heterogeneous support seldom actively participates in the catalytic reactions.

Herein, we use an alloxazine building block in a bottom-up approach to construct a bio-inspired covalent organic framework that acts as a heterogeneous material with intrinsic photocatalytic activity. Direct comparison with similar homogeneous photocatalysts shows that this heterogenization approach not only leads to retention, but rather to the enhancement of the applicability towards "green" photocatalysis. To the best of our knowledge, this is the first report on a metal-free COF photocatalyst based on a bio-mimetic chromophore which is capable of selectively oxidizing benzylic alcohols to aldehydes using oxygen as the terminal oxidant.[50,51]

3.3   Results and Discussion

FEAx-COF was synthesized by condensation of 1,3-diethyl-6,9-bis-(4-formylphenyl)alloxazine (FEAx) with 2,4,6-tris(4-aminophenyl)-1,3,5-triazine (TAPT) under solvothermal conditions (Figure 3-1a). The FEAx building block was obtained from 4,7-dibromo-2,1,3-benzothiadiazole as described in the supporting information. The ethyl substituents at N-1 and N-3 (a) proved to be essential for the synthesis of FEAx-COF by providing both high solubility and photostability of the building block by preventing phototautomerism.[45,52,53] Attempts to synthesize an analogous non-alkylated COF failed, potentially due to strong intermolecular hydrogen bonding (Figure S3-5). The successful condensation of FEAx and TAPT was confirmed by Fourier transform infrared (FTIR) spectroscopy, as evident from the appearance of the imine signal at 1624 cm^{-1} ($v_{C=N(stretch)}$) and concomitant disappearance of both amine (v_{N-H} = 3200 – 3500 cm^{-1}) and aldehyde ($v_{C=O}$ = 1692 cm^{-1}) stretching vibrations of the starting materials (Figure 3-1b, Figure S3-7).
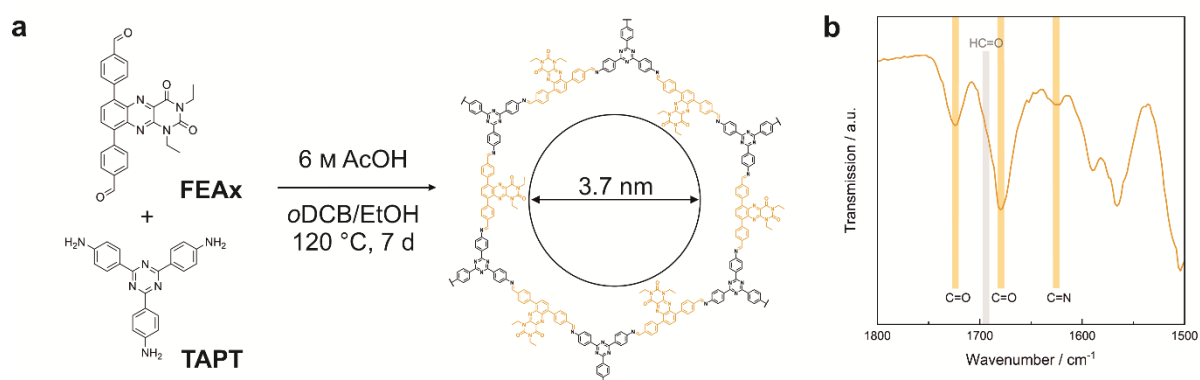
Figure 3-1: (a) Synthesis and molecular structure of FEAx-COF. (b) FTIR spectrum of FEAx-COF showing the presence of carbonyl and imine bands as well as the absence of an aldehyde band.

^{13}C solid-state nuclear magnetic resonance (ssNMR) further proved the successful condensation by an absence of aldehyde carbonyl ^{13}C resonances at ~190 ppm in the COF and the appearance of the imine ^{13}C signal at 157 ppm (Figure 3-2a).[54] The distinct triazine carbon signal at 170 ppm, the signals from the ethyl groups at 12 and 37 ppm, together with the 1678 cm^{-1} and 1724 cm^{-1} bands in the FTIR spectra corresponding to the carbonyl groups of the alloxazine heterocycle prove the retention of the molecular structure of both FEAx and TAPT in the framework (Figure S3-8). Quantum-chemical

calculations on the B97-2/pcsSeg-2//PBE0-D3/def2-TZVP level of theory corroborate the ^{13}C NMR assignments (Figure S3-36).[55–60] The ^{1}H ssNMR spectrum of FEAx-COF shows aromatic protons around 7.6 ppm and two distinct aliphatic signals at 3.6 and 1.2 ppm corresponding to methylene and methyl groups, respectively (Figure S3-8). To understand the structural details and morphology of FEAx-COF, X-ray powder diffraction (XRPD), gas sorption, scanning electron microscopy (SEM), and transmission electron microscopy (TEM) analyses were performed. The XRPD pattern (Figure 3-2b) shows an intense reflection at $2\vartheta = 1.98°$, assigned to the 100 plane (space group P-3). In addition, a number of distinct reflections at $2\vartheta = 3.41°$ (110), 3.93° (200), 5.20° (210), and 6.81° (220) are visible, together with a broad stacking reflection at 24.3°. Based on the geometrical considerations of the starting materials and their expected connectivity in the framework, a unit cell with the space group P-3 was constructed, with cell parameters closely matching those obtained from Pawley refinement of the powder pattern (R_{wp} 8.0%). The obtained refined unit cell parameters are $a = b = 51.84$ Å, $c = 7.06$ Å, $\alpha = \beta = 90°$, $\gamma = 120°$. An eclipsed stacking model accounting for only minimal relative layer offsets gave best fits between experimental and simulated data (Figure S3-6).
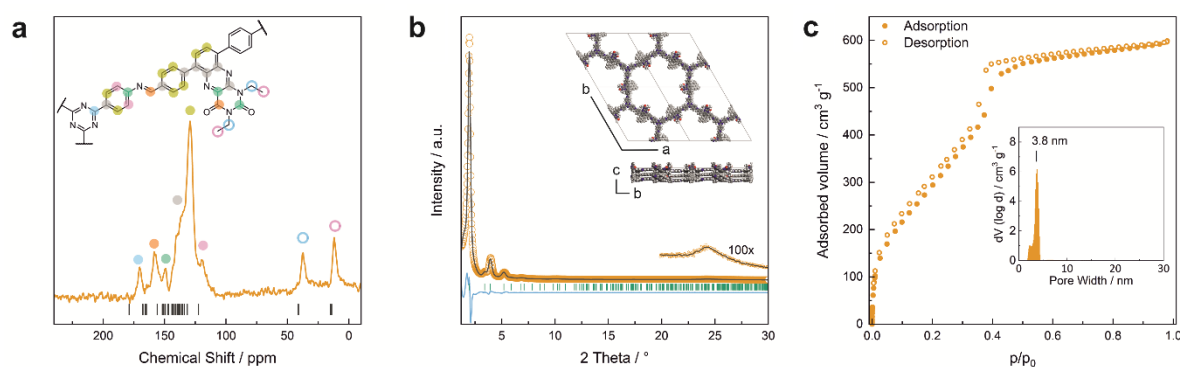
Figure 3-2 a) 13C ssNMR spectrum of FEAx-COF together with the corresponding assignments and calculated shifts. (b) XRPD pattern of FEAx-COF and illustration of the structural model used for refinement. The second COF layer is depicted in grey for better visualization. Experimental data shown in orange, Pawley refinement in grey, difference in blue, and peak positions in green. (c) Argon sorption isotherm of FEAx-COF at 87 K. Filled and open symbols represent the adsorption and the desorption branches, respectively. The inset shows the pore size distribution obtained from a QSDFT kernel for cylindrical pores.

Argon sorption analysis of FEAx-COF carried out at 87 K shows a type IV isotherm, which is typical for mesoporous materials (Figure 3-2c).[61] The Brunauer–Emmett–Teller (BET) surface area and pore volume were determined to be 1139 m^2g^{-1} and 0.76 cm^3g^{-1}, respectively. A pore size distribution (PSD) was calculated from the sorption isotherm using the quenched solid density functional theory (QSDFT) kernel for Argon at 87 K on carbon with cylindrical pores. The PSD shows a maximum at 3.8 nm, in agreement with the calculated pore size of 3.7 nm. PSD analysis thus further excludes the possibility of AB- (calculated pore size = 1.5 nm) and ABC-stacking (calculated pore size = 0.8 nm) of the layers (Figure S3-6).

SEM images of FEAx-COF show micrometer-sized, agglomerated spherical particles (Figure S3-10). TEM images visualize the hexagonal pores of the COF structure when viewed along the [001] zone axis (Figure S3-11) and Fast-Fourier Transform (FFT) analysis indicates a periodicity of 3.6 nm, in accordance with the experimental sorption and XRPD data.

With the synthesized COF in hand, we probed its activity as a sustainable catalyst for the selective photocatalytic oxidation of alcohols to aldehydes under aerobic, aqueous conditions. To determine if the COF is principally capable of such a reaction, the redox properties of FEAx-COF were investigated using cyclic voltammetry. The voltammogram of a COF-modified FTO working electrode shows an irreversible reduction peak with an onset potential ($E_{red, onset}$) ≈ -0.73 V (Figure S3-4) *vs.* saturated calomel electrode (SCE). Using the experimentally obtained optical band gap ($E_{g,opt}$) of 2.25 eV (Figure S3-12) the position of the conduction band (E_{CB}) and the valence band (E_{VB}) edges were estimated to be -3.97 eV and -6.22 eV *vs.* vacuum, respectively, following the empirical equations $E_{CB} = -(E_{red,onset}$ *vs.* SCE + 4.7) eV and $E_{VB} = E_{CB} - E_{g,opt}$.[62–64] Thus, both electron transfer to molecular oxygen ($E^0(O_2/O_2^{\bullet-})$ = -0.33V *vs.* NHE $\triangleq$ -0.57 *vs.* SCE)[65], and oxidation of electron-rich organic substrates such as 4-methoxybenzyl alcohol (MBA, E_{ox} = 1.48 V *vs.* SCE) – a model reaction in flavin research[36,37,66,67] – is thermodynamically feasible with FEAx-COF (E_{VB} 1.52 V *vs.* SCE).[68]

Indeed, irradiating the reaction mixture containing MBA and FEAx-COF in oxygenated acetonitrile/water with blue light (λ_{max} = 463 nm) for 17 h selectively oxidized MBA to 4-methoxybenzaldehyde (MBAld) with a yield of 44% (Table 3-1, entry 1).

Interestingly, the photooxidation reaction proceeds with a high selectivity of 96% for MBAld, suggesting the capability of FEAx-COF as a selective photocatalyst. Notably, only 4- methoxybenzoic acid (MBAcid) was detected as the minor side product (Figure S3-15). Control experiments additionally confirmed that the presence of COF and irradiation of the reaction mixture are essential for the reaction to proceed (Table 3-1, entries 2 and 3). The presence of oxygen was also observed to be necessary for the reaction, indicating that O_2 acts as a sacrificial electron acceptor (Table 3-1, entry 4).

Table 3-1: Photocatalytic oxidation of MBA by FEAx-COF

Entry	Variation from standard conditions[a]	Yield (%)[b]
1	-	44
2	No FEAx-COF	Traces
3	No irradiation	Traces
4	Under Argon atmosphere	3
5	In water	22
6	In acetonitrile	70
7	Additional N(EtOH)$_3$	17
8	Additional DABCO[c]	Traces
9	Additional *t*-BuOH	69

[a] Standard reaction conditions: 20 mM MBA, 1.5 mg FEAx-COF, 463 nm LEDs, MeCN/water (1 mL, 1:1), 45 °C, O_2, stirring. [b] Yield after 17 h determined *via* HPLC-MS. [c] 1,4-Diazabicyclo[2.2.2]octan.

We then tried to optimize the reaction yield of the photocatalytic system. The use of pure water and acetonitrile as solvents led to yields of 22% and 70%, respectively (Table 3-1, entries 5 and 6), which we attribute to the enhanced dispersibility of the rather hydrophobic COF in organic media, potentially enhancing the availability of active sites.

To gain mechanistic insights into the photocatalytic oxidation by FEAx-COF, a range of additional experiments was conducted. The addition of triethanolamine – $N(EtOH)_3$ – or DABCO as competing electron donors drastically reduced the yield (Table 3-1, entries 7 and 8), hinting at direct oxidation of the benzylic alcohol by the photoexcited COF. As the presence of molecular oxygen is necessary for the reaction to proceed (*vide supra*), we tried to probe the possible formation and participation of the different reactive oxygen species, namely, singlet oxygen, hydroxyl or superoxide radicals in the photocatalytic transformation.[69] Since neither the addition of hydroxyl radical scavenger *tert*-butanol (Table 3-1, entry 9), nor the absence of water (Table 3-1, entry 6) reduced the yield of MBAld, we expect hydroxyl radicals to only play a non-productive – if any – role in the catalytic cycle.

In order to detect possible singlet oxygen and superoxide species, we carried out electron paramagnetic resonance (EPR) spectroscopic measurements. When illuminating FEAx-COF in the presence of 5,5-dimethyl-1-pyrroline N-oxide (DMPO) as a spin-trap for the superoxide ion ($O_2^{\bullet-}$), we observed a 1:2:2:1 signal typical for the DMPO-OH adduct, formed by the decomposition of unstable DMPO-OOH, proving the presence and hence the formation of $O_2^{\bullet-}$ during the catalytic cycle (Figure S3-16).[70]

When using 2,2,6,6-tetramethylpiperidine (TEMP) as the spin trapping agent for the detection of singlet oxygen, a 1:1:1 signal characteristic for (2,2,6,6-tetramethylpiperidin-1-yl)oxyl (TEMPO) was observed.[71] Compared to the control measurement without illumination, the intensity of this signal increased after irradiation with blue light, suggesting that $^1O_2$ is also generated alongside $O_2^{\bullet-}$. Since TEMPO can also be formed in an alternative electron transfer reaction, we further corroborated the generation of singlet oxygen by oxidizing α-terpinene in the presence of FEAx-COF photocatalytically (Figure S3-17).[72,73] The formation of ascaridole clearly proves the presence of singlet oxygen, and in accordance with the oxidative power of FEAx-COF we also detected *p*-cymene and other products of electron transfer reactions.

The productive role of singlet oxygen in the oxidation of MBA was tested by using deuterated solvents for the photocatalysis experiment with FEAx-COF. We could observe a slightly increased yield of 55% (*vs.* 44%) compared to standard reaction conditions when using a mixture of acetonitrile-d_3 and D_2O (Table S

3-2, entry 10), which we attribute to the prolonged lifetime of $^1O_2$ in deuterated solvents.[74,75] On the other hand, a decreased yield of 27% is observed in the presence of singlet oxygen scavenging sodium azide (Table S3-2, entry 11). The retention of photocatalytic activity in the presence of a $^1O_2$ scavenger also demonstrates that singlet oxygen is not the sole active oxygen species. This indicates the coexistence of $O_2^{\bullet-}$ and $^1O_2$, which is also known for flavin[76] and covalent triazine framework photocatalysts in aerobic oxidations, for example.[77–79] However, we consider the generation of $^1O_2$ *via*

energy transfer from photoexcited FEAx-COF to be negligible, since we did not encounter photooxidation of furfuryl alcohol even though furans are known for their reactivity towards $^1O_2$ (Table S3-3, entry 6).[80] Instead, it is proposed that a second, but minor pathway for the oxidation of MBA to MBAld by singlet oxygen is enabled through electron transfer reactions with superoxide radicals, namely reoxidation of $O_2^{\bullet-}$ to $^1O_2$ by electron holes, or disproportionation of $O_2^{\bullet-}$ to $^1O_2$ and H_2O_2 (Figure S3-18).[20,81,82]

Based on these results and literature reports on aerobic photocatalysis with flavins,[67] a plausible mechanism for the photooxidation of MBA by FEAx-COF can be compiled (Figure 3-3a). The benzyl alcohol substrate is proposed to be oxidized by the photoexcited state of FEAx-COF, with the resulting radical anionic COF species reducing dioxygen to a superoxide radical. Through subsequent electron and proton transfers, $O_2^{\bullet-}$ and the substrate radical cation MBA$^{\bullet+}$ eventually give the final products H_2O_2 and MBAld. Indeed, H_2O_2 was detected in the reaction filtrate using titanyl sulfate as the reagent, which led to the immediate formation of orange peroxotitanyl species (Figure S3-28).[83,84]
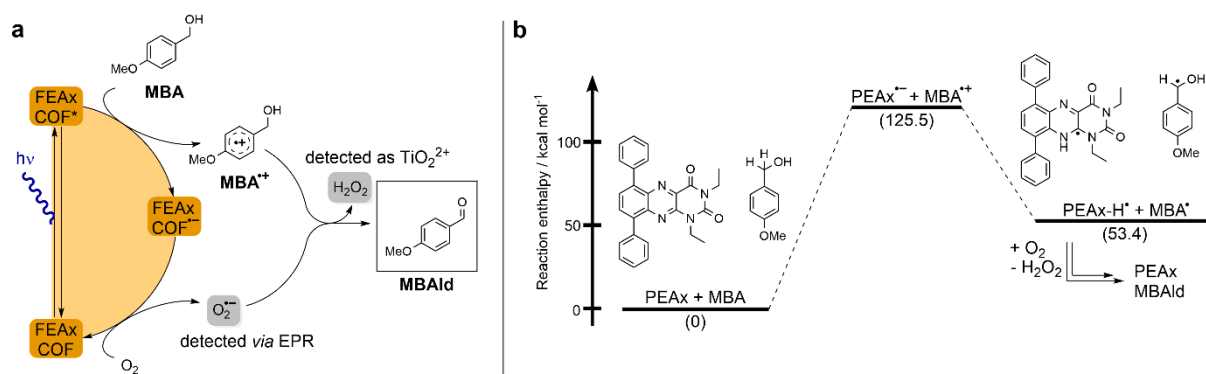
Figure 3-3: (a) Proposed mechanism for the photocatalytic oxidation of MBA by FEAx-COF. (b) Calculated reaction enthalpies for a possible pathway in the oxidation of MBA by model compound PEAx.

The reductive quenching of FEAx-COF in the mechanism elaborated above is in line with mechanistic investigations on MBA photooxidation by flavins.[66,67] In addition, quantum-chemical calculations on PEAx (1,3-diethyl-6,9-diphenylalloxazine) as a molecular model system representative of the extended COF structure corroborate the proposed mechanism. The comparison of stabilization energies for the anionic and cationic state on the PBE0 D3/def2 TZVP level of theory (Table S3-4) show the destabilization of the radical cation and the stabilization of the anion in the gas phase by +173.6 kcal mol^{-1} and -34.7 kcal mol^{-1}, respectively. This indicates a reductive quenching of FEAx-COF to FEAx-COF$^{\bullet-}$ as the more likely step than the oxidative quenching to FEAx-COF$^{\bullet+}$.[85,86]

Furthermore, the reaction enthalpy for the photooxidation of MBA by FEAx-COF was estimated on the PBE0-D3/def2-TZVP level of theory with solvation effects being considered using the implicit solvation model COSMO with a value of 36.64 as the dielectric constant to represent acetonitrile (Table S3-5).[87] Following the mechanism proposed for FEAx-COF, PEAx is believed to be reduced to the radical anion PEAx$^{\bullet-}$ after photoexcitation, while MBA is oxidized to MBA$^{\bullet+}$ in return (Figure 3-3b). The energy gained from the reduction is not enough to compensate for the formation of MBA$^{\bullet+}$, rendering this single electron transfer endothermic by +125.5 kcal mol^{-1}. Thus, considering the energy of the incident photons of 463 nm ≈ 62 kcal mol^{-1}, a proton-coupled electron transfer (PCET) leading to PEAx-H$^{\bullet}$ and

MBA$^\bullet$, with an associated reaction enthalpy of +53.4 kcal mol^{-1}, seems more probable. Given the aerobic reaction conditions, it is expected that MBA$^\bullet$ is further oxidized to MBAld either by a second photoexcited PEAx molecule, or by $O_2^{\bullet-}$, the latter of which results from reoxidation of the intermediate semiquinone radical anion PEAx$^{\bullet-}$ by dioxygen.[67]

The photocatalytic activity of FEAx-COF in the oxidation of MBA was then compared to three different molecular alloxazine model systems – 1,3-diethylalloxazine HEAx, PEAx, and the FEAx linker (Figure 3-4a). One important distinctive feature in the FEAx-COF system is the enhanced conjugation, which broadens its absorption profile and extends it up to 650 nm, with an absorption edge around 550 nm (Figure 3-4b). On the contrary, the light absorption of neither of the mentioned molecular alloxazines extends beyond the blue region of the visible spectrum.
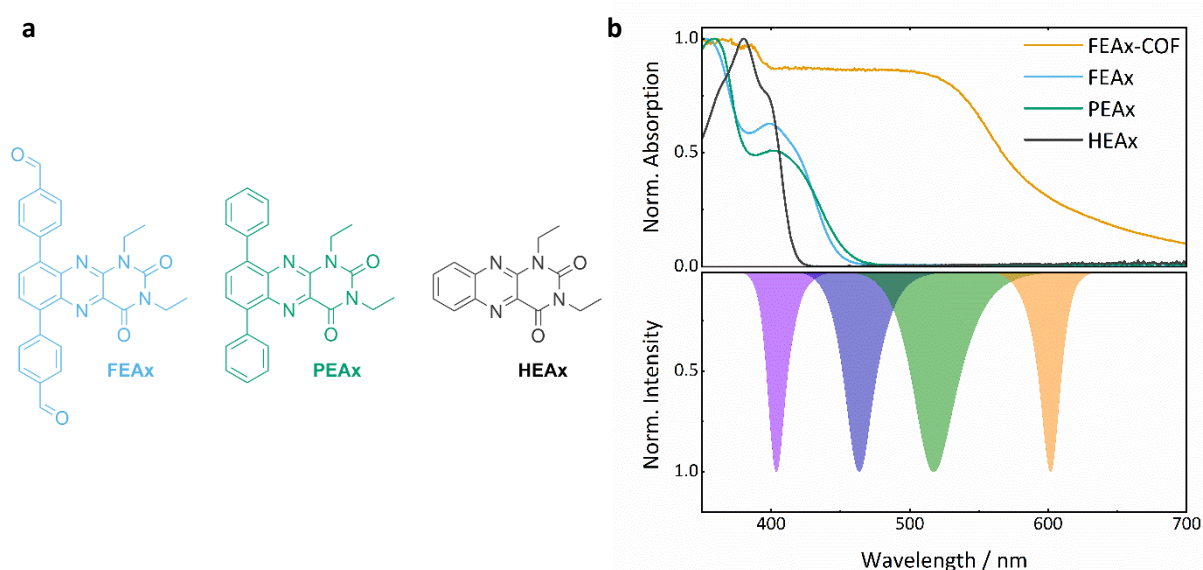
Figure 3-4: (a) Molecular structures of alloxazine model compounds. (b) UV-Vis spectra of model compounds and FEAx-COF (top) in comparison to LED emission spectra (bottom).

Consequently, FEAx-COF surpasses the activity of the molecular compounds when illuminated with blue LEDs of 463 nm – especially when using acetonitrile as the solvent (Figure S3-22). In a 1:1 mixture of acetonitrile and water, HEAx and FEAx-COF perform similarly (Figure S3-22). However, when using low energy green light (517 nm), the reaction yield still remains at 20% with FEAx-COF, while no product formation is observed with HEAx, PEAx, or FEAx (Figure S3-21). Under illumination with orange LEDs, no oxidation takes place in either case.

To allow for sufficient light absorption by all four photocatalysts, this comparative study was conducted with violet LEDs (λ_{max} = 404 nm). The dissolved alloxazines HEAx, PEAx, and FEAx, gave yields of 78%, 39%, and 87% after 17 h, respectively (Table 3-2), which is either lower or in the range of the heterogeneous catalyst FEAx-COF (79%). To investigate possible photodegradation effects of the catalysts under prolonged illumination, we repeated this experiment after illuminating the oxygenated

reaction mixtures for 72 hours prior to substrate addition.[*] Interestingly, pre-illuminated HEAx and FEAx show clearly decreased yields of 40% and 55%, respectively, whereas PEAx (45%) and FEAx-COF (73%) do not show significant signs of lower activity (Table 3-2). This hints to higher photostability in the latter cases. In fact, UV-Vis spectroscopy indicates more pronounced bleaching of the molecular alloxazines compared to FEAx-COF (Figure S3-23).

Table 3-2: Photocatalytic efficiency and photostability of FEAx-COF and model compounds in the oxidation of MBA under irradiation with violet light.

Entry	Catalyst	Yield (%)[a]	Yield (%) after preillumination[a,b]
1	HEAx	78	40
2	PEAx	39	45
3	FEAx	87	55
4	FEAx-COF	79	73

Reaction conditions: 20 mM MBA, 1.5 mg FEAx-COF or 2 mM model compound, 404 nm LEDs, MeCN (1 mL), O_2. [a] Yield after 17 h determined via HPLC-MS. [b] Samples illuminated prior to photocatalysis experiments (72 h, 404 nm, MeCN, O_2).

When further assessing the photocatalytic activities of the molecular alloxazines under illumination with violet LEDs but in different solvents, we get significantly diverging reaction courses. For HEAx, we find higher turnover in a 1:1 acetonitrile/water mixture compared to pure acetonitrile, whereas FEAx and PEAx show decreased activity (Figure S3-31).

Inspired by these findings, we performed pulsed-field-gradient NMR experiments to determine the relative diffusion coefficients for FEAx and HEAx as a measure for their aggregation behaviour. According to the Stokes-Einstein equation, the diffusion coefficient is reciprocally related to the hydrodynamic radius of a diffusing species, which changes upon self-aggregation of the molecules.[88] We find that HEAx exhibits a higher degree of aggregation in pure acetonitrile compared to a 1:1 acetonitrile/water mixture (Figure S3-32). On the contrary, FEAx shows higher aggregation in the aqueous solvent mixture. Although both molecular catalysts apparently show opposite aggregation behaviour in the respective solvents, a comparison with the photocatalytic yields of MBAld indicates an inverse correlation between aggregation and photocatalytic efficacy for both catalysts (Figure S3-32). In this regard, both FEAX and HEAX follow the behaviour of structurally related flavins as reported earlier by Feldmeier *et. al.* and Dadová *et. al.*[37,67] Notably, this effect strongly reduces the yield of MBAld with the molecular catalysts FEAx (water) and HEAx (MeCN) to < 5% when using blue LEDs, while FEAx-COF affords > 20% of MBAld in either case (Figure S3-22). Incorporation of the alloxazine unit in the COF thus provides two benefits: suppressing solvent-induced aggregation while maintaining the accessibility of the active sites within the ordered porous structure.

---

[*] This "preillumination" experiment aims at simulating repeated photocatalytic cycles with the photocatalysts under investigation. Since the molecular alloxazines are homogeneous catalysts, actual cycling including catalyst recovery is impractical. To assess the remaining activity of the catalysts, we add MBA after 72 h – otherwise, it would have been completely oxidized to MBAld or even MBAcid.

The photocatalytic activity of FEAx-COF was further compared to a COF not comprising alloxazine chromophores. By using a terphenyl linker instead of FEAx for the construction of this reference material, we were able to obtain a COF with similar characteristics such as crystallinity, pore size, and surface area (Figure S3-30). However, the absence of alloxazine chromophores in the terphenyl COF leads to a hypsochromic shift of about 100 nm. After illumination with blue light for 24 h, FEAx-COF afforded 67% of MBAld, which is significantly higher compared to the terphenyl COF (15%). These results nicely illustrate that the photocatalytic activity of FEAx-COF mainly arises from the incorporation of alloxazine units.

After photocatalysis, the FEAx-COF sample was fully characterized to check for possible decomposition. As seen from the XRPD pattern, the framework crystallinity is largely, yet not completely retained, in line with the strongly oxidizing conditions during catalysis (Figure S3-24). Sorption analysis evidences the preservation of mesopores but reveals a significantly diminished surface area which we attribute to a partial amorphization of FEAx-COF. The FTIR and ssNMR data show the appearance of weak aldehyde signals which point to slight degradation effects, while the overall molecular connectivity and hence the structure of the framework remains largely unchanged (Figure S3-25). Further, SEM imaging illustrates the retention of the morphology of FEAx-COF (Figure S3-26). In addition to its applicability for MBA photooxidation in different solvents and under varying irradiation wavelengths, FEAx-COF can also be used as a photocatalyst for an extended substrate scope. Since the reaction mechanism is based on an electron transfer from the substrate to the electron hole of FEAx-COF (*vide supra*), the scope is limited to substrates with oxidation potentials below E_{vb} (1.52 vs. SCE). Consequently, electron-poor alcohols such as 4-nitrobenzyl alcohol (E_{ox} = 2.84 *vs*. SCE), unsubstituted benzylic alcohol (E_{ox} = 1.94 *vs*. SCE), or furfuryl alcohol (E_{ox} = 1.73 *vs*. SCE) are not oxidized to the respective aldehydes in significant amounts (Table S3-3, entries 1-6). On the other hand, FEAx-COF oxidizes 2-thiophenemethanol (E_{ox} = 0.72 *vs*. SCE) with yields similar to MBA (Table S3-3, entries 5 and 7). Further, the photocatalytic activity of FEAx-COF is not limited to aromatic alcohols. Indeed, we could demonstrate the applicability of FEAx-COF also as a photocatalyst for the sulfoxidation of 2-methoxythioanisol (Table S3-3, entry 10) and for the C-H oxidation of substrates such as xanthene and 4-methylanisol (Table S3-3, entries 8 and 9).

Conclusions

We report the first COF composed of photoactive, yet photostable alloxazine building blocks that can be used efficiently as a photocatalyst in aerobic oxidations. By virtue of not only anchoring alloxazines to, but rather incorporating them into the heterogeneous support, we obtain a COF that strongly absorbs visible light. Consequently, the photocatalytic efficacy of FEAx-COF equals or even exceeds the performance of a series of comparable molecular alloxazine photocatalysts, while simultaneously proving more stable. Notably, FEAx-COF catalyzes the oxidation of MBA even under illumination with low energy green light. More generally, its heterogeneous nature prevents disadvantageous aggregation of catalytic sites and allows for better product-catalyst separation and recycling. Overall, the construction of alloxazine COFs nicely illustrates the synthetic possibilities of the underlying reticular chemistry and broadens the scope of bio-inspired, metal-free heterogeneous photocatalysis.

3.4 References

1   T. Banerjee, K. Gottschling, G. Savasci, C. Ochsenfeld, B. V. Lotsch, *ACS Energy Lett.* **2018**, *3*, 400–409.

2   X. Wang, L. Chen, S. Y. Chong, M. A. Little, Y. Wu, W.-H. Zhu, R. Clowes, Y. Yan, M. A. Zwijnenburg, R. S. Sprick, A. I. Cooper, *Nat. Chem.* **2018**, *10*, 1180–1189.

3   Z. Fu, X. Wang, A. M. Gardner, X. Wang, S. Y. Chong, G. Neri, A. J. Cowan, L. Liu, X. Li, A. Vogel, R. Clowes, M. Bilton, L. Chen, R. S. Sprick, A. I. Cooper, *Chem. Sci.* **2020**, *11*, 543–550.

4   C. Krishnaraj, H. Sekhar Jena, L. Bourda, A. Laemont, P. Pachfule, J. Roeser, C. V. Chandran, S. Borgmans, S. M. J. Rogge, K. Leus, C. V. Stevens, J. A. Martens, V. van Speybroeck, E. Breynaert, A. Thomas, P. van der Voort, *J. Am. Chem. Soc.* **2020**, *142*, 20107–20116.

5   Y. Zhi, Z. Li, X. Feng, H. Xia, Y. Zhang, Z. Shi, Y. Mu, X. Liu, *J. Mater. Chem. A* **2017** *5*, 22933–22938.

6   Z. Li, S. Han, C. Li, P. Shao, H. Xia, H. Li, X. Chen, X. Feng, X. Liu, *J. Mater. Chem. A* **2020**, *8*, 8706–8715.

7   S. Liu, M. Tian, X. Bu, H. Tian, X. Yang, *Chem. Eur. J.* **2021**, *27*, 7738–7744.

8   A. Jiménez-Almarza, A. López-Magano, L. Marzo, S. Cabrera, R. Mas-Ballesté, J. Alemán, *ChemCatChem* **2019**, *11*, 4916–4922.

9   M. Liu, J. Liu, K. Zhou, J. Chen, Q. Sun, Z. Bao, Q. Yang, Y. Yang, Q. Ren, Z. Zhang, *Adv. Sci.* **2021**, *8*, 2100631.

10   K. Feng, H. Hao, F. Huang, X. Lang, C. Wang, *Mater. Chem. Front.* **2021**, *5*, 2255–2260.

11   R. Chen, J.-L. Shi, Y. Ma, G. Lin, X. Lang, C. Wang, *Angew. Chem. Int. Ed.* **2019**, *58*, 6430–6434.

12   L. Ascherl, T. Sick, J. T. Margraf, S. H. Lapidus, M. Calik, C. Hettstedt, K. Karaghiosoff, M. Döblinger, T. Clark, K. W. Chapman, F. Auras, T. Bein, *Nat. Chem.* **2016**, *8*, 310–316.

13   V. S. Vyas, F. Haase, L. Stegbauer, G. Savasci, F. Podjaski, C. Ochsenfeld, B. V. Lotsch, *Nat. Commun.* **2015**, *6*, 8508.

14   L.-K. Wang, J.-J. Zhou, Y.-B. Lan, S.-Y. Ding, W. Yu, W. Wang, *Angew. Chem. Int. Ed.* **2019**, *58*, 9443–9447.

15   E. Vitaku, C. N. Gannett, K. L. Carpenter, L. Shen, H. D. Abruña, W. R. Dichtel, *J. Am. Chem. Soc.* **2020**, *142*, 16–20.

16   M. Reckenthäler, A. G. Griesbeck, *Adv. Synth. Catal.* **2013**, *355*, 2727–2744.

17   J. M. R. Narayanam, C. R. J. Stephenson, *Chem. Soc. Rev.* **2011**, *40*, 102–113.

18   C. K. Prier, D. A. Rankic, D. W. C. MacMillan, *Chem. Rev.* **2013**, *113*, 5322–5363.

19   F. Lima, U. K. Sharma, L. Grunenberg, D. Saha, S. Johannsen, J. Sedelmeier, E. V. van der Eycken, S. V. Ley, *Angew. Chem. Int. Ed.* **2017**, *56*, 15136–15140.

20   W. Schilling, D. Riemer, Y. Zhang, N. Hatami, S. Das, *ACS Catal.*, 2018, *8*, 5425–5430.

21   H. Kotani, K. Ohkubo, S. Fukuzumi, *J. Am. Chem. Soc.* **2004**, *126*, 15999–16006.

22   F. Lima, L. Grunenberg, H. B. A. Rahman, R. Labes, J. Sedelmeier, S. V. Ley, *Chem. Commun.* **2018**, *54*, 5606–5609.

23   D. P. Hari, B. König, *Chem. Commun.* **2014**, *50*, 6688–6699.

24   M. März, M. Kohout, T. Neveselý, J. Chudoba, D. Prukała, S. Niziński, M. Sikorski, G. Burdziński, R. Cibulka, *Org. Biomol. Chem.* **2018**, *16*, 6809–6817.

25   Y. Imada, T. Kitagawa, T. Ohno, H. Iida, T. Naota, *Org. Lett.* **2010**, *12*, 32–35.

26   Y. Imada, H. Iida, S. Ono, Y. Masui, S. Murahashi, *Chem. Asian J.* **2006**, *1*, 136–147.

27   Y. Imada, H. Iida, S. Ono, S. Murahashi, *J. Am. Chem. Soc.* **2003**, *125*, 2868–2869.

28   S. Ball, T. C. Bruice, *J. Am. Chem. Soc.* **1979**, *101*, 4017–4019.

29   A. A. Lindén, L. Krüger, J.-E. Bäckvall, *J. Org. Chem.* **2003**, *68*, 5890–5896.

30   A. E. Miller, J. J. Bischoff, C. Bizub, P. Luminoso, S. Smiley, *J. Am. Chem. Soc.* **1986**, *108*, 7773–7778.

31   V. Mojr, M. Buděšínský, R. Cibulka, T. Kraus, *Org. Biomol. Chem.* **2011**, *9*, 7318–7326.

32   M. Kurfiřt, J. Špačková, E. Svobodová, R. Cibulka, *Monatsh. Chem.* **2018**, *149*, 863–869.

33   P. Dongare, I. MacKenzie, D. Wang, D. A. Nicewicz, T. J. Meyer, *Proc. Natl. Acad. Sci. U.S.A.* **2017**, *114*, 9279–9283.

34   H. Schmaderer, P. Hilgers, R. Lechner, B. König, *Adv. Synth. Catal.* **2009**, *351*, 163–174.

35   J. Svoboda, H. Schmaderer, B. König, *Chem. Eur. J.* **2008**, *14*, 1854–1865.

36   R. Cibulka, R. Vasold, B. König, *Chem. Eur. J.* **2004**, *10*, 6224–6231.

37   J. Dadová, S. Kümmel, C. Feldmeier, J. Cibulková, R. Pažout, J. Maixner, R. M. Gschwind, B. König, R. Cibulka, *Chem. Eur. J.* **2013**, *19*, 1066–1075.

38   R. Lechner, S. Kümmel, B. König, *Photochem. Photobiol. Sci.* **2010**, *9*, 1367–1377.

39   K. A. Korvinson, G. N. Hargenrader, J. Stevanovic, Y. Xie, J. Joseph, V. Maslak, C. M. Hadad, K. D. Glusac, *J. Phys. Chem. A* **2016**, *120*, 7294–7300.

40   A. H. Tolba, F. Vávra, J. Chudoba, R. Cibulka, *Eur. J. Org. Chem.* **2020**, 1579–1585.

41   G. P. Moss, P. A. S. Smith, D. Tavernier, *Pure Appl. Chem.* **1995**, *67*, 1307–1375.

42   E. Sikorska, M. Sikorski, R. P. Steer, F. Wilkinson, D. R. Worrall, *J. Chem. Soc. Faraday Trans.* **1998**, *94*, 2347–2353.

43   V. Mojr, E. Svobodová, K. Straková, T. Neveselý, J. Chudoba, H. Dvořáková, R. Cibulka, *Chem. Commun.* **2015**, *51*, 12036–12039.

44   V. Mojr, G. Pitrová, K. Straková, D. Prukała, S. Brazevic, E. Svobodová, I. Hoskovcová, G. Burdziński, T. Slanina, M. Sikorski, R. Cibulka, *ChemCatChem* **2018**, *10*, 849–858.

45   K. Tatsumi, H. Ichikawa, S. Wada, *J. Contam. Hydrol.* **1992**, *9*, 207–219.

46   J. Špačková, E. Svobodová, T. Hartman, I. Stibor, J. Kopecká, J. Cibulková, J. Chudoba, R. Cibulka, *ChemCatChem* **2017**, *9*, 1177–1181.

47   M. Pandiri, N. Shaham-Waldmann, M. S. Hossain, F. W. Foss, K. Rajeshwar, Y. Paz, *Phys. Chem. Chem. Phys.* **2016**, *18*, 18575–18583.

48   M. Rochkind, M. Pandiri, M. S. Hossain, F. W. Foss, K. Rajeshwar, Y. Paz, *J. Phys. Chem. C* **2016**, *120*, 16069–16079.

49   L. Crocker, P. Koehler, P. Bernhard, A. Kerbs, T. Euser, L. Fruk, *Nanoscale Horiz.* **2019**, *4*, 1318–1325.

50   G. Lu, X. Huang, Z. Wu, Y. Li, L. Xing, H. Gao, W. Dong, G. Wang, *Appl. Surf. Sci.* **2019**, *493*, 551–560.

51   K. Zhang, G. Lu, Z. Xi, Y. Li, Q. Luan, X. Huang, *Chin. Chem. Lett.* **2021**, *32*, 2207–2211.

52   P. Hemmerich, *Helv. Chim. Acta* **1964**, *47*, 464-475.

53   Pill-Soon Song, Ming Sun, Anna Koziolowa, Jacek Koziol, *J. Am. Chem. Soc.* **1973**, *96*, 4319-4323.

54   A. M. Pütz, M. W. Terban, S. Bette, F. Haase, R. E. Dinnebier, B. V. Lotsch *Chem. Sci.* **2020**, *11*, 12647–12654.

55   P. J. Wilson, T. J. Bradley, D. J. Tozer, *J. Chem. Phys.* **2001**, *115*, 9233–9242.

56   F. Jensen, *J. Chem. Theory Comput.* **2015**, *11*, 132–138.

57   C. Adamo, V. Barone, *J. Chem. Phys.* **1999**, *110*, 6158–6170.

58   M. Ernzerhof, G. E. Scuseria, *J. Chem. Phys.* **1999**, *110*, 5029–5036.

59   S. Grimme, J. Antony, S. Ehrlich, H. Krieg, *J. Chem. Phys.* **2010**, *132*, 154104.

60   A. Schäfer, C. Huber, R. Ahlrichs, *J. Chem. Phys.* **1994**, *100*, 5829–5835.

61   M. Thommes, K. Kaneko, A. V. Neimark, J. P. Olivier, F. Rodriguez-Reinoso, J. Rouquerol, K. S. Sing, *Pure Appl. Chem.* **2015**, *87*, 1051–1069.

62   C. M. Cardona, W. Li, A. E. Kaifer, D. Stockdale, G. C. Bazan, *Adv. Mater.* **2011**, *23*, 2367–2371.

63   M. Calik, F. Auras, L. M. Salonen, K. Bader, I. Grill, M. Handloser, D. D. Medina, M. Dogru, F. Löbermann, D. Trauner, A. Hartschuh, T. Bein, *J. Am. Chem. Soc.* **2014**, *136*, 17802–17807.

64   B. P. Biswal, H. A. Vignolo-González, T. Banerjee, L. Grunenberg, G. Savasci, K. Gottschling, J. Nuss, C. Ochsenfeld, B. V. Lotsch, *J. Am. Chem. Soc.* **2019**, *141*, 11082–11092.

65   P. M. Wood, *Biochem. J.* **1988**, *253*, 287–289.

66 U. Megerle, M. Wenninger, R.-J. Kutta, R. Lechner, B. König, B. Dick, E. Riedle, *Phys. Chem. Chem. Phys.* **2011**, *13*, 8869–8880.

67 C. Feldmeier, H. Bartling, K. Magerl, R. M. Gschwind, *Angew. Chem. Int. Ed.* **2015**, *54*, 1347–1351.

68 C. Zeng, N. Zhang, C. M. Lam, R. D. Little, *Org. Lett.* **2012**, *14*, 1314–1317.

69 J. A. Badwey, M. L. Karnovsky, *Ann. Rev. Biochem.* **1980**, *49*, 695–726.

70 E. Finkelstein, G. M. Rosen, E. J. Rauckman, J. Paxton, *Mol. Pharmacol.* **1979**, *16*, 676–685.

71 Y. Lion, M. Delmelle, A. van de Vorst, *Nature* **1976**, *263*, 442–443.

72 G. Nardi, I. Manet, S. Monti, M. A. Miranda, V. Lhiaubet-Vallet, *Free Radic. Biol. Med.* **2014**, *77*, 64–70.

73 Y.-Z. Chen, Z. U. Wang, H. Wang, J. Lu, S.-H. Yu, H.-L. Jiang, *J. Am. Chem. Soc.* **2017**, *139*, 2035–2044.

74 P. R. Ogilby, C. S. Foote, *J. Am. Chem. Soc.* **1983**, *105*, 3423–3430.

75 P. B. Merkel, R. Nilsson, D. R. Kearns, *J. Am. Chem. Soc.* **1972**, *94*, 1031-1030.

76 T. Neveselý, E. Svobodová, J. Chudoba, M. Sikorski, R. Cibulka, *Adv. Synth. Catal.* **2016** *358*, 1654–1663**.**

77 W. Huang, B. C. Ma, H. Lu, R. Li, L. Wang, K. Landfester, K. A. I. Zhang, *ACS Catal.* **2017** *7*, 5438–5442.

78 C. Ayed, W. Huang, G. Kizilsavas, K. Landfester, K. A. I. Zhang, *ChemPhotoChem* **2020** *4,* 571–576.

79 L. Liao, D. Ditz, F. Zeng, M. Alves Favaro, A. Iemhoff, K. Gupta, H. Hartmann, C. Szczuka, P. Jakes, P. J. C. Hausoul, J. Artz, R. Palkovits, *ChemistrySelect* **2020** *5*, 14438–14446.

80 T. Montagnon, D. Kalaitzakis, M. Triantafyllakis, M. Stratakis, G. Vassilikogiannakis, *Chem. Commun.* **2014**, *50*, 15480–15498.

81 W. H. Koppenol, *Nature* **1976**, *262*, 420–421.

82 Y. Nosaka, A. Y. Nosaka, *Chem. Rev.* **2017**, *117*, 11302–11336.

83 G. M. Eisenberg, *Ind. Eng. Chem. Anal. Ed.* **1943**, *15*, 327–328.

84 M. Mori, M. Shibata, E. Kyuno, S. Ito, *Bull. Chem. Soc. Jpn.* **1956**, *29*, 904–907.

85 D. Ravelli, M. Fagnoni, A. Albini, *Chem. Soc. Rev.* **2013**, *42*, 97–113.

86 H. G. Roth, N. A. Romero, D. A. Nicewicz, *Synlett* **2016**, *27*, 714–723.

87 A. Klamt, G. Schüürmann, *J. Chem. Soc., Perkin Trans. 2* **1993**, 799–805.

88 A. Macchioni, G. Ciancaleoni, C. Zuccaccia, D. Zuccaccia, *Chem. Soc. Rev.* **2008**, *37*, 479–489.

4 Iridium-loaded Covalent Organic Frameworks for Water-Gas Shift Catalysis

Unpublished results

4.1 Introduction

In order to tackle the current environmental crisis and reduce carbon dioxide emissions, increasing effort is being put into solar power, battery-electric technologies, and energy storage systems. Hydrogen gas has a special role in the emerging paradigmatic sector coupling concept as it can be easily produced *via* photocatalytic or electrocatalytic water splitting, and subsequently used for energy storage and transformation. A detailed discussion on this aspect is given in chapter 1 of this thesis.

Today, however, the role of green hydrogen is still marginal. In 2021, less than 1% of H_2 came from environmentally friendly sources.[1] As of today, the main sources of H_2 are natural gas (62%), and coal (19%), both of which are labelled "grey hydrogen".[1,2] The reason for the still insignificant role of green hydrogen in this mixture is based not only on its non-competitive price,[*] but also on the sheer dimension of the hydrogen market. Dihydrogen is an indispensable reactant in oil refinement, methanol production, and the Haber-Bosch process – i.e., ammonia production – highlighting its economic importance.[3]

Hydrogen production from methane, for example, can be accomplished by steam reforming. In this process, CH_4 is partially oxidized with water to carbon monoxide and three equivalents of dihydrogen according to eq. 4-1.[4] Industrially, this net yield can be increased to four parts H_2 through integration of a water-gas shift reactor (eq. 4-2). There, the carbon monoxide obtained from steam reforming is converted with another equivalent of water to ultimately yield CO_2 and H_2 in the so-called water-gas shift reaction (WGS, eq. 4-3).[4] Furthermore, the removal of CO leads to purer hydrogen product streams.[5] Altogether, the WGS reaction is a useful tool in maximizing the hydrogen output from fossil fuels, bridging the time until carbon-neutral hydrogen generation techniques mature and can keep up with growing H_2 demand.

$$CH_4 + H_2O \ \rightarrow \ CO + 3\,H_2 \qquad \text{(eq. 4-1)}$$

$$CH_4 + 2\,H_2O \ \rightarrow \ CO_2 + 4H_2 \qquad \text{(eq. 4-2)}$$

$$CO + H_2O \ \rightarrow \ CO_2 + H_2 \qquad \text{(eq. 4-3)}$$

$$CO_2 + H_2 \ \rightarrow \ CO + H_2O \qquad \text{(eq. 4-4)}$$

---
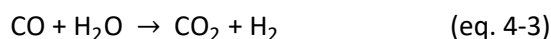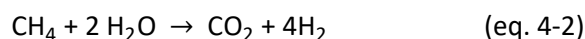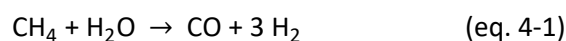
[*] Whereas grey hydrogen production costs roughly 1-2 US\$ kg^{-1}, the production of green hydrogen is currently in the range of 3-8 US\$ kg^{-1}. Source: *Int. J. Hydrog. Energy* **2022**, *47*, 24136–24154.

Industrial heterogeneous WGS catalysts are usually grouped into "high-temperature shift" iron/chromium oxide or "low-temperature shift" zinc/copper oxide catalysts, which are operated at temperatures of 350-450 °C and 190-250 °C, respectively.[6] The WGS reaction is in a chemical equilibrium with its back reaction, i.e., the reverse water-gas shift reaction (RWGS, eq. 4-4), and can thus be controlled accordingly. The forward reaction is mildly exothermic (ΔH = -41 kJ mol^{-1}), so that the equilibrium shifts towards the products (H_2 and CO_2) with decreasing temperatures, according to LE CHATELIER's principle.[7] However, since the reaction rate is higher at elevated temperatures, WGS reactors are operated at elevated temperatures as stated above, despite the less favorable chemical equilibrium.[7]

Homogeneous WGS catalysts on the other hand were found to work efficiently at temperatures lower than that required for commonly used heterogeneous systems.[8] [Ir(COD)L$_2$] complexes (COD = cyclooctadiene), for example, reportedly catalyze the WGS at 140 °C with rates comparable to other metal complexes.[9,10] It was proposed that the catalytically active species is formed through replacement of COD by CO. Over the cause of the catalysis, iridium-bound CO is supposedly attacked by water and subsequently released in the form of CO_2. SAUVAGE and co-workers later revealed that the final hydrogen release *via* reductive H_2 elimination is the rate-determining step in this scheme.[10] Coincidently, this exact step – and thus the whole WGS process under iridium catalysis – can be facilitated through irradiation with visible light. Ultimately, this allows for room temperature WGS catalysis with a related Ir complex, namely [Cp*Ir(bpy)Cl]Cl.

The underlying mechanism for photo-assisted WGS catalysis by [Cp*Ir(bpy)Cl]Cl and derivatives has been elaborated by ZIESSEL since 1988 (Scheme 4-1). It was found that the role of both the chloride ligand and the counterion is negligible, and that they are interchangeable for example with water (or hydroxide) in aqueous media.[11,12] The loss of the chloride ligand from **Ir-1** provides a free coordination sites viable for catalytic applications.[13] In the case of photo-assisted WGS catalysis, the Cl$^-$ ligand is replaced with CO in the first step, yielding a formally 2+ charged iridium complex **Ir-2** (Scheme 4-1). Nucleophilic attack of water on the carbonyl carbon and subsequent deprotonation gives the Ir-COOH species **Ir-3**.[14] In the rate determining step, CO_2 is released, leaving behind the Ir(I) species **Ir-4**. Due to being coordinatively unsaturated, this highly reactive species can only be isolated at high pH as a purple solid.[15,16] At pH 7 and below, however, **Ir-4** is readily protonated to its yellow conjugated acid **Ir-5**.[17] Neutral conditions also proved to be optimal for WGS catalysis with [Cp*Ir(bpy)Cl]Cl as CO_2 and H_2 formation are contrarily favored in basic and acidic media, respectively.[18] H_2 release does not only constitute the final step of the catalytic cycle, it is also the only part that relies on light absorption, rendering the whole process light-assisted. It can be best described as reaction of the hydride **Ir-5*** with a weak acid such as water in this case.[19] In the dark, hydride transfer is significantly slower as the ground state **Ir-5** is a weak hydride donor.[20] The underlying photo-induced hydricity increase was identified to be caused by metal-to-ligand charge-transfer (MLCT) from iridium to bpy, and/or ligand-to-ligand charge-transfer (LLCT) from bpy to hydrogen.[15,20] Even in the absence of a proton source, **Ir-5*** can release hydrogen through interaction with non-excited **Ir-5** *via* self-quenching.[21]
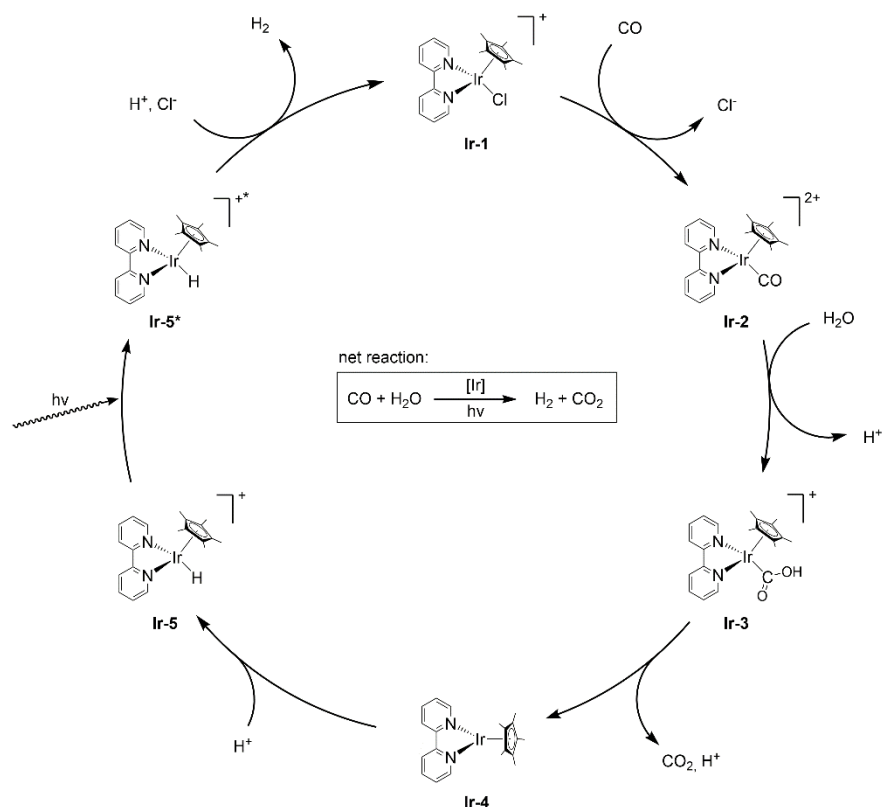
Scheme 4-1: Catalytic cycle for the photo-assisted water-gas shift reaction with [Cp*Ir(bpy)Cl]Cl. Modified from [14]. Copyright © 1991 WILEY-VCH Verlag GmbH & Co. KGaA, Weinheim.

Consequently, the hydricity of $[Cp^*Ir(bpy)H]^+$ and related compounds was also utilized for numerous hydrogenations reactions including ketones,[22] aldehydes,[23,24] and olefins.[25] In the context of C1 economy and CO_2 utilization, Cp^*Ir species were also found promising candidates for the hydrogenation of CO_2 to formic acid and/or formate (eq. 4-5).[26–28] It was even found that $[Cp^*Ir(bpy)Cl]Cl$ can catalyze the formation of methanol from formic acid – and thus ultimately from carbon dioxide – through disproportionation.[29–32]

$$CO_2 + H_2 \rightarrow HCOOH \qquad \text{(eq. 4-5)}$$

With such wide and promising catalytic properties for homogeneous catalysis with $[Cp^*Ir(bpy)Cl]Cl$ and its derivatives, it is not surprising that numerous heterogenization approaches have been made in the last years, given that heterogeneous catalysis allows for easy product/catalyst separation in contrast to homogeneous catalysis. $[Cp^*Ir(bpy)Cl]Cl$ is prepared from dimeric $[Cp^*IrCl_2]_2$ upon reaction with bipyridine at room temperature and without the need of additional reagents.[33] Therefore, basically any heterogeneous material exhibiting accessible bpy sites can be charged with mononuclear, defined iridium complexes. Examples for such supports include covalent triazine frameworks (CTFs),[34–38] metal-organic frameworks (MOFs),[39] and porous organic polymers (POPs).[40,41] Our group has extended this scope to covalent organic frameworks (COFs), which are crystalline, porous polymers constructed from organic building blocks in a target-oriented approach. Making use of the practically unlimited library of linkers, we devised COFs based on bipyridine units and tested them for water oxidation catalysis with the above mentioned $[Cp^*Ir(bpy)Cl]$-like complexes (see chapter 2 of this thesis). In a separate follow-up master thesis,[42] our group successfully exploited iridium-loaded COFs for both CO_2

hydrogenation as well as methanol formation. Though the retention of catalytic activity was confirmed after binding iridium to the COF supports, the imine bonds underlying the framework proved to be prone to hydrolysis and/or reduction under the acidic and alkaline conditions used for formic acid disproportionation and CO_2 hydrogenation, respectively.[42,43]

Herein, we demonstrate the applicability of iridium-loaded COFs for yet another catalytic application, i.e., the photo-assisted WGS reaction. To the best of our knowledge, COFs have not yet been reported as heterogeneous catalysts in this context. In a brief interlude, we introduce reductive reactions catalyzed by COF-supported iridium complexes in the form of transfer hydrogenations. The reduction of organic aldehydes using either formic acid or sodium formate as hydrogen source is successfully conducted with various iridium-loaded COF catalysts. Mechanistically, both WGS catalysis and transfer hydrogenations elapse *via* the same iridium hydride species. Therefore, also the WGS reaction could be catalyzed with a series of COFs after anchoring molecularly defined iridium species. Finally, we discuss the factors limiting WGS catalysis with heterogenized compared to homogeneous species.

4.2   Results and Discussion

A series of three isoreticular COFs was chosen to support iridium for heterogeneous WGS catalysis (Scheme 4-2). Of these, TAPB-BPY COF and its loading with the Cp*Ir moiety has been extensively studied in chapter 2 of this thesis (Cp* = pentamethylcyclopentadienyl). An analogous COF featuring triazine instead of benzene nodes (TT-BPY COF) will be exemplarily examined in more detail within this chapter. Both TAPB-BPY COF and TT-BPY COF feature bipyridine units covering the pore walls, which can bind Ir(III) as a cationic species similar to the molecular [Cp*Ir(bpy)Cl]Cl archetype (bpy = bipyridine), i.e., with both a chloride ligand and counterion. On the contrary, TAPB-PPY COF is constructed from 1,3,5-tris-(4-aminophenyl)benzene (TAPB) and a phenylpyridine-based dialdehyde. In contrast to bpy, phenylpyridine (ppy) binds the target iridium complex as a formal anion after cycloiridiation. Consequently, a base is required during the synthesis to achieve the C-H deprotonation, and the resulting Ir complex carries neither charge nor a Cl⁻ counterion. Synthetic details and characterization for TAPB-PPY COF and its iridium-loaded counterpart (Ir@TAPB-PPY COF) are given in the supporting information (chapter 6.4).
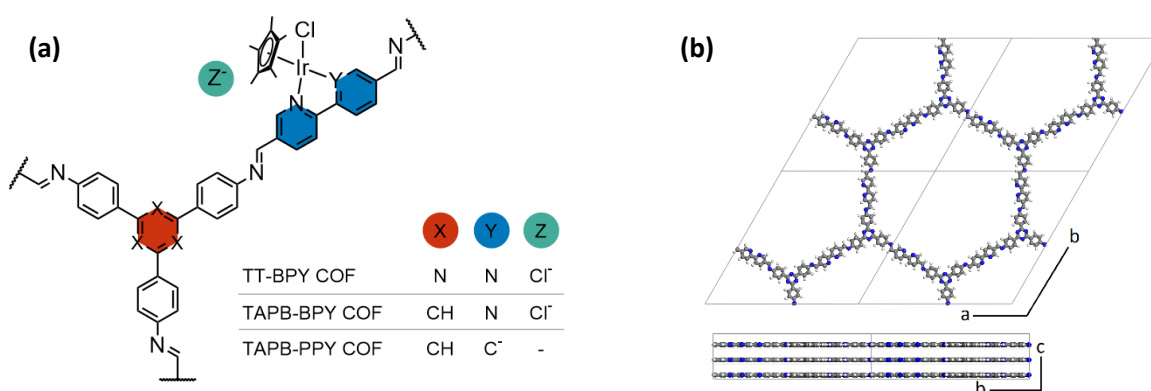
Scheme 4-2: (a) Molecular structures of a series of isoreticular iridium-loaded COFs used for WGS catalysis. (b) Illustration of the structural model for TT-BPY COF (color coding: C = grey; N = blue, H = white).

TT-BPY COF was obtained through standard acid-catalyzed condensation of 2,4,6-tris(4-aminophenyl)-1,3,5-triazine (TT) with 2,2'-bipyridine-5,5'-dicarbaldehyde (BPY) under solvothermal conditions (see supporting information, chapter 6.4). Fourier transform infrared (FTIR) spectroscopy gives evidence for this condensation in the form of an imine stretching vibration $v_{C=N}$ at 1625 cm^{-1} for the obtained solid (Figure S4-7). Both the prominent amine stretching vibrations of the TT linker (v_{N-H} = 3200 – 3500 cm^{-1}) and the aldehyde band of BPY ($v_{C=O}$ = 1696 cm^{-1}) are absent in TT-BPY COF, hinting to complete condensation. Furthermore, X-ray powder diffraction (XRPD) illustrates the crystallinity of the resulting material (Figure 4-1). TT-BPY COF exhibits sharp reflections at 2Θ = 2.35, 4.10, 4.74, 6.31, and 8.32°, and a broad stacking reflection around 25.5°. Using Pawley refinement, these signals could be assigned to the (100), (110), (200), (210), (220), and (001) planes of a *P*-6 unit cell with the cell parameters $a = b$ = 42.20 Å, c = 3.49 Å, $\alpha = \beta$ = 90°, and γ = 120° (R$_{wp}$ 8.48%, Figure S4-2).

The experimental data suggests that the COF layers in TT-BPY COF are stacked in a (nearly) eclipsed (AA) rather than a staggered (AB) fashion, further confirming the proposed structural model (Figure S4-3). Porosity assessment *via* argon sorption further corroborates this idea. TT-BPY COF exhibits a type IV isotherm characteristic of mesoporous materials.[44] The derived pore-size distribution features a distinct signal around 3.81 nm in accordance with the expected pore diameter of 3.8 nm (Figure S4-3, Figure S4-8). The BET surface area and the pore volume were determined to be 1386 m^2 g^{-1} and 1.080 cm^3 g^{-1}, respectively.

The as-synthesized TT-BPY COF was subsequently reacted with [Cp*IrCl$_2$]$_2$ in order to bind the targeted Cp*Ir motifs to the bpy units decorating the COF backbone, yielding Ir@TT-BPY COF. When using a large excess of Ir precursor in a suspension of TT-BPY COF in DMF, a maximal iridium content of around 15 wt% could be achieved as revealed *via* inductively coupled plasma (ICP) spectroscopy. 15 wt% Ir correspond to roughly half occupation of bipyridine units when assuming the attachment of [Cp*IrCl]Cl fragments. Lower iridium contents can also be achieved by adjusting the amount of reactants in the postsynthetic loading process (Table S4-1). Solid-state nuclear magnetic resonance (ssNMR) spectroscopy clearly confirms the presence of Cp* units, given the strong signals at 90 and 9 ppm, which can be assigned to the aromatic carbons and the connected methyl groups, respectively (Figure 4-1a). The underlying framework signals for triazine and imine carbons at 169 and 155 ppm, respectively, as well as the spectrum of other aromatic species remains unaltered, hinting at the conservation of the COF backbone during metalation. Also, ^{1}H ssNMR confirms the preservation of aromatic protons alongside the appearance of aliphatic protons around 1.5 ppm supposedly stemming from methyl groups (Figure S4-13). XRPD and sorption analysis reveal a decrease in long range order as well as a complete loss of mesoporosity after iridium loading (Figure 4-1b + c). However, it is possible to counter such effects using pre-metalated linkers for the synthesis of Ir@TT-BPY COF (Figure S4-4). This concept is further outlined in chapter 2, and only postsynthetic loading of COFs with iridium will be covered in the following.

Scanning electron microscopy (SEM) corroborates the proposed preservation of the TT-BPY COF structure after loading with Cp*Ir, as no changes in morphology are apparent (Figure S4-17-19, Figure

S4-21-23). Elemental mapping reveals the even distribution of both Ir and Cl over the COF particles, suggesting deposition of iridium in a molecular fashion. In addition, formation of iridium-containing nanoparticles is not observed in transmission electron microscopy (TEM) images (Figure S4-20, Figure S4-24). However, whereas metal-free TT-BPY COF exhibits visible pore channels, we could not find pores or other crystalline features for Ir@TT-BPY COF.
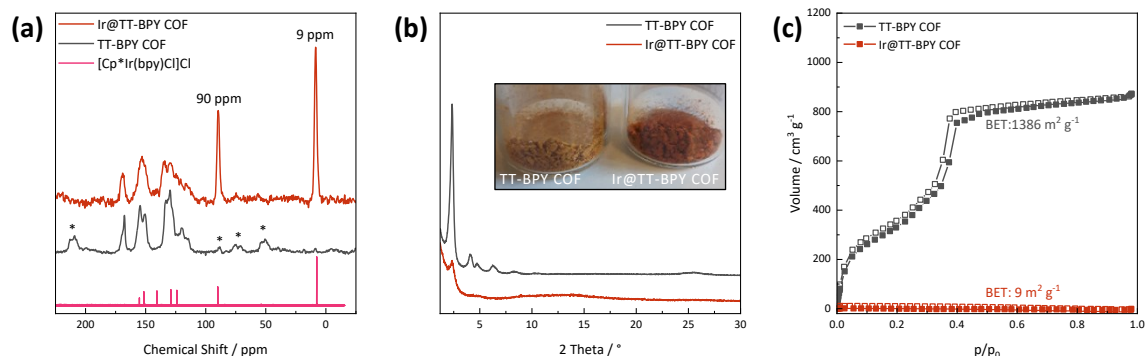
Figure 4-1: ^{13}C ssNMR spectra (a) (left), XRPD patterns (b), and Ar sorption isotherms (c) for TT-BPY COF before and after postsynthetic treatment with [Cp*IrCl$_2$]$_2$. NMR spectrum of [Cp*Ir(bpy)Cl]Cl dissolved in D$_2$O given for comparison. Asterisks mark spinning side bands. Inset shows photographic image of TT-BPY COF before and after metalation.

Finally, X-ray photoelectron spectroscopy (XPS) was used to confirm the binding of the targeted iridium complex to the COF support. Ir@TT-BPY COF exhibits a Ir 4f$_{7/2}$ peak with a binding energy of 62.65 eV, which is in good agreement with [Cp*Ir(bpy)Cl]Cl (62.21 eV, Figure S4-14), suggesting that Ir is bound to the COF in a manner comparable to the molecular Ir(III) complex. This finding is corroborated by the respective nitrogen XPS signals. Metal-free TT-BPY COF exhibits only one distinct N 1s signal centered around 398.96 eV, which comprises triazine, bipyridine, and imine nitrogen species alike (Figure 4-2).[45–49] After metalation, a new signal at 400.31 eV appears, which is ascribed to bipyridine nitrogen atoms binding to iridium. For molecular [Cp*Ir(bpy)Cl]Cl we found a similar value of 400.03 eV.
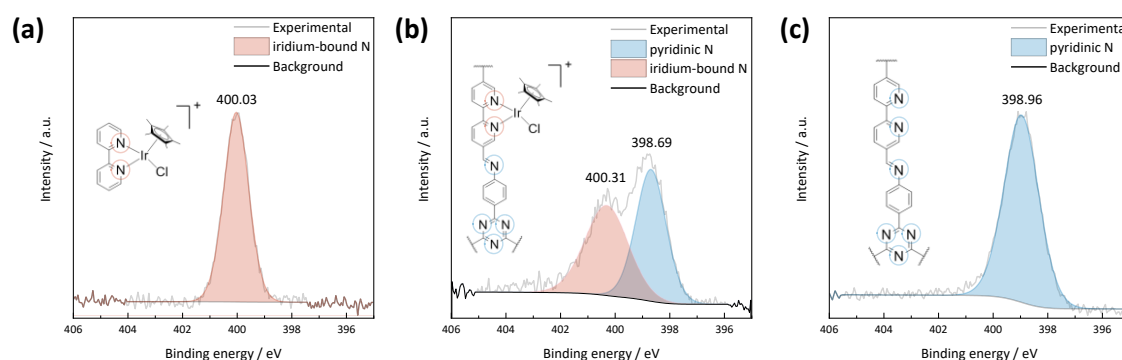
Figure 4-2: Nitrogen 1s XPS spectra for [Cp*Ir(bpy)Cl]Cl (a), Ir@TT-BPY COF (b), and parent TT-BPY COF (c).

Due to the high amount of iridium complexes bound to the COF, it is even possible to detect and distinguish the corresponding chlorine species *via* XPS. Ir@TT-BPY exhibits two sets of Cl 2p signals with 2p$_{3/2}$ peaks around 196.65 and 198.07 eV, which can be assigned to the chloride counterion and the iridium-bound Cl$^-$ ligand, respectively (Figure S4-15).[50,51] Deconvolution and integration revealed an estimate counterion/ligand ratio of 1:2.6 for Ir@TT-BPY COF, but 1:1.3 for molecular

[Cp*Ir(bpy)Cl]Cl. It is presumed that during synthesis the Cl^- counterion is partially replaced by, for example, OH^-.

In order to provide evidence not only for the targeted metal complex composition, but also for its retained catalytic activity, we performed transfer hydrogenation reactions with the isoreticular series Ir@TT-BPY COF, Ir@TAPB-BPY COF, and Ir@TAPB-PPY COF (Scheme 4-2). Iridium compounds including [Cp*Ir(bpy)Cl]Cl have been shown to efficiently reduce both aromatic and aliphatic aldehydes at low catalysts loadings, and with high turnover frequencies (TOFs).[23] This reaction can be conducted in water at 80 °C and with formic acid as the hydrogen source, which means that organic solvents can be avoided and CO_2 is the only side product. On top of that, the use of iridium-loaded heterogeneous catalysts such as COFs would further simplify this reaction by facilitating product-catalyst separation.

Table 4-1: Transfer hydrogenation experiments with Ir-loaded COFs.
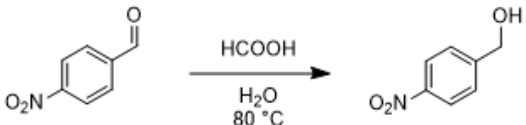
Entry	Catalyst[a]	Yield[b]	TOF[b]
1	Ir@TAPB-BPY	62%	1273 h^{-1}
2	Ir@TAPB-PPY COF	29%	595 h^{-1}
3	Ir@TT-BPY COF	6%	130 h^{-1}
4	[Cp*Ir(bpy)Cl]Cl	71%	1024 h^{-1}

[a]: iridium loading 2-3 wt%. See supporting information for details. [b]: after two hours
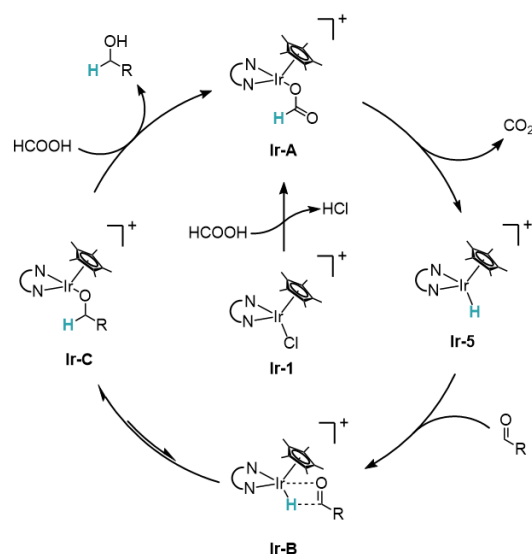
Scheme 4-3: Mechanistic proposal for transfer hydrogenations with Cp*Ir complexes. Adapted from [23] with permission. Copyright © 1999 Royal Society of Chemistry.

We chose 4-nitrobenzaldehyde as the substrate to probe the catalytic activity of our iridium-loaded COFs as it can be easily quantified via NMR spectroscopy and at the same time is sufficiently soluble under the reaction conditions.[*] We found that Ir@TAPB-BPY COF and Ir@TAPB-PPY COF show high conversion, judging from their TOFs of 1273 h^{-1} and 595 h^{-1} after two hours of reaction, respectively (Table 4-1, entries 1+2). Ir@TT-BPY COF exhibited a lower activity with a TOF of 130 h^{-1} after 2 h (Table 4-1, entry 3). Almost complete conversion is observed after 19 hours with Ir@TAPB-BPY COF, and no organic side product apart from 4-Nitrobenzyl alcohol was observed (Figure S4-25). The long reaction times can be ascribed to the low catalyst content of 0.025 mol% with regards to the substrate. Such high substrate/catalyst ratios allegedly suppress the formation of hydrogen gas by formic acid decomposition (Scheme 4-3). Intuitively, conversion rates can also be tuned by varying the loading of iridium to the respective COF. For Ir@TAPB-BPY COF with 14 wt% and Ir@TT-BPY COF with 15 wt%, we

---

[*] Other *para*-substituted benzaldehydes (R = H, Me, OMe) proved to be not completely soluble at 80 °C in water and needed addition of organic co-solvents for dissolution.

found complete conversion already after two and four hours of reaction time, respectively (Figure S4-26). Metal-free TAPB-BPY COF, on the other hand, does not catalyze the reduction of 4-Nitrobenzaldehyde, and no product formation was observed.

Interestingly, [Cp*Ir(bpy)Cl]Cl as a molecular reference showed a TOF of 1024 h^{-1}, which indicates lower catalytic activity compared to Ir@TAPB-BPY COF (Table 4-1, entry 4). However, [Cp*Ir(bpy)Cl]Cl already exhibited a TOF of 2714 h^{-1} after a reaction time of 40 minutes (Figure S4-27). Detailed kinetic studies are beyond the scope of this thesis, though.

In additional test reactions, sodium formate was employed as an alternative reactant in the transfer hydrogenation reaction. However, all tested iridium-loaded COFs show lower reaction yields with sodium formate compared to formic acid (Figure S4-25).

More interestingly, the choice of hydrogen donor has drastic effects on the COF support. FTIR spectroscopy reveals signs of imine hydrolysis when using formate, as indicated by a presumable aldehyde band at $v_{C=O}$ = 1697 cm^{-1} (Figure S4-28). Given the elevated reaction temperature and the aqueous medium, partial hydrolysis is not surprising. However, no aldehyde band is detected in Ir@TAPB-BPY after catalysis with formic acid under identical conditions. Instead, we note the complete disappearance of the imine band at $v_{C=N}$ = 1624 cm^{-1}. Together with a very weak amine vibration around 3412 cm^{-1}, this suggests the reduction of the framework's imine bonds to amine species. These observations are in line with our group's recent work on postsynthetic conversion of COF linkages, where also imine bonds were transformed into amines using formic acid.[43] Regardless of the hydrogen donor, however, Ir@TAPB-BPY COF does lose its crystallinity during catalysis judging from XRPD data (Figure S4-29).

After proving that the heterogenized iridium motifs retained their catalytic activity for reductive catalysis, we further test their applicability in the photo-assisted WGS reaction. To this end, we suspended iridium-loaded COFs in phosphate buffer in a gas-tight photoreactor and subsequently replaced the atmosphere with CO (Figure S4-30). Indeed, upon illumination with AM1.5-filtered simulated sunlight we could detect significant amounts of hydrogen in the photoreactor's headspace, which supposedly stem from WGS catalysis (Figure 4-3). In the dark, hydrogen evolution could not be observed (Figure S4-31). Ir@TT-BPY COF showed hydrogen evolution rates of about 1.36 µmol H_2 h^{-1} (221.14 µmol g^{-1} h^{-1}), which corresponds to a turnover number (TON) of 1.28 after three hours (Table 4-2, entry 1). The hydrogen evolution proceeds continuously with neither induction period nor obvious deactivation after several hours of illumination. Ir@TAPB-BPY COF shows a slightly lower activity with a TON of 1.12 (Table 4-2, entry 2). Ir@TAPB-PPY COF on the other hand shows a very low activity of 0.02 turnovers within three hours (Table 4-2, entry 3; Figure S4-31). This finding will be discussed later in this chapter.

A control experiment with metal-free TT-BPY COF shows no hydrogen evolution, indicating that anchoring of iridium species indeed induces the catalytic activity observed for Ir@TT-BPY COF (Table 4-2, entry 4). ICP analysis of the reaction mixtures after catalysis reveals that only small amounts of iridium in the range of 1% detached from the metalated COFs (Figure S4-32). Even though the

leached-out iridium species were not characterized further, it can be hypothesized that their eventual catalytic activity does not fully account for the TONs observed for Ir-loaded COFs. As shown by ZIESSEL, chelating ligands such as bpy are a prerequisite for light-assisted WGS catalysis with Cp*Ir species.[18] Assuming detachment of iridium centers from the bpy sites covering the COF pore walls, such species are thus expected to show little catalytic activity. The COFs retained their ordered structure, judging from preserved (100) reflections (Figure S4-35).

For the control experiment with homogeneous iridium species, we found activities one order of magnitude higher than in the heterogeneous systems (Table 4-2, entry 5). [Cp*Ir(bpy)Cl]Cl showed a TON of 11.46 after three hours, and 8.39 after two hours. Within the latter period, literature values for [Cp*Ir(bpy)Cl]Cl state a comparable TON of 6.[11] The small deviation can be explained by varying reaction conditions such as the lower CO pressure of only 1 atm for the literature experiment *vs.* 1.5 bar in our case.
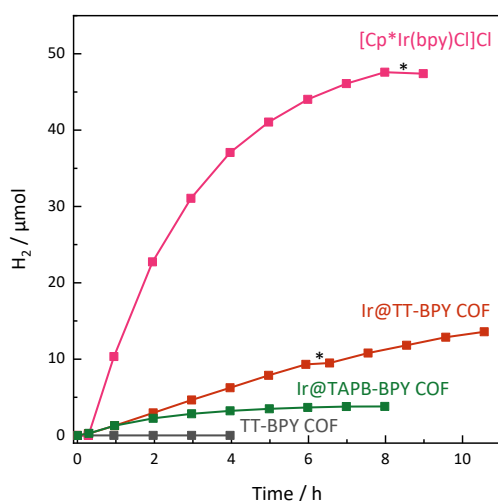
Table 4-2: Photo-assisted WGS catalysis with Ir-loaded COFs.

entry	catalyst	n(Ir) / μmol	TON [a]
1	Ir@TT-BPY COF	3.64	1.28
2	Ir@TAPB-BPY COF	2.55	1.12
3[b]	Ir@TB-PPY COF	0.62	0.02
4	TT-BPY COF	0.00	-
5[c]	[Cp*Ir(bpy)Cl]Cl	2.71	11.46

[a]: after 3 h   [b]: for the H_2 trace, see Figure S4-31 [c]: after 2 h, the TON was 8.39

Figure 4-3: Hydrogen evolution traces during photo-assisted WGS catalysis with homogeneous and heterogenized Cp*Ir species. Asterisk marks brief interruption of illumination.

Interestingly, we found that the iridium-catalyzed WGS reaction leads to visible color changes of the reaction mixture. Whereas during setup and degassing Ir@TT-BPY COF suspensions appear orange, they quickly turn blue upon increasing the CO pressure inside the photoreactor (Figure 4-4). In line with literature reports, we ascribe this color change to the reduction of Ir(III) to Ir(I) species, which are expected intermediates during WGS catalysis and show characteristic light absorption in the range of 600 – 750 nm (Scheme 4-1).[10,17,25]
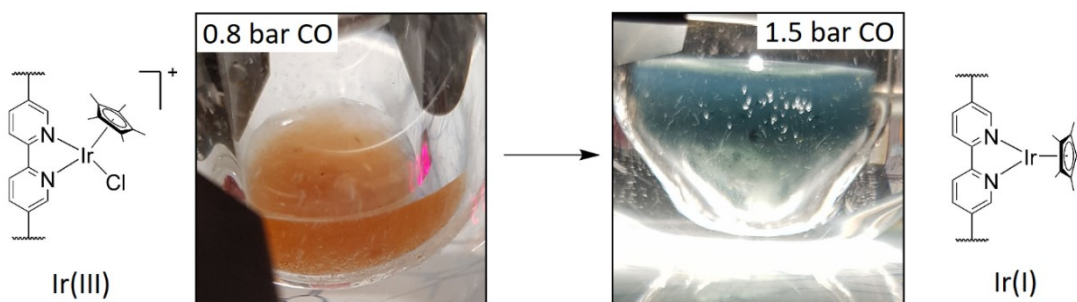
Figure 4-4: Photograph of an Ir@TT-BPY COF suspension before (left) and during (right) WGS catalysis together with the proposed molecular structures of iridium motifs under the given conditions.

Strikingly, the observed color changes are concomitant with catalytic activity. Whereas reaction mixtures of Ir@TT-BPY COF, Ir@TAPB-BPY COF, as well as molecular [Cp*Ir(bpy)Cl]Cl turn blue or green, suspensions of metal-free TT-BPY COF and Ir@TAPB-PPY COF stay yellow or orange after exposure to carbon monoxide (Table S4-12). Apparently, reduction of cyclometalated Ir(III) does not take place under the given conditions. Literature reports state the requirement for elevated temperatures and strong reductants such as $NaBH_4$ or sodium bis(2-methoxyethoxy)aluminum hydride (Red-Al) in order to reduce [Cp*Ir(ppy)Cl], which is the homogeneous analogue to Ir@TAPB-PPY COF.[52]

Another factor that comes into play when trying to explain varying catalytic activities is hydrophilicity. We note that iridium-loaded COF only turned blue in suspension, whereas residual COF particles in the "dry" parts of the photoreactor remained visually unchanged (Figure S4-30). This can be explained mechanistically, since nucleophilic attack of a water molecule on iridium-bound CO is a vital step in the catalytic WGS cycle that leads to blue Ir(I) motifs (Scheme 4-1). We further examined the water-dependent color change of iridium-loaded COFs upon reduction in a custom-built microscope setup. The COF sample was placed inside a sealable steel chamber equipped with quartz glass windows for simultaneous inspection via an optical microscope and a connected spectrophotometer (Figure S4-33). The chamber's gas inlet was connected to a set of washing bottles which provide streams of humidified gas (Ar or CO), allowing for dynamic exposure of the sample. In accordance with the observations made during actual WGS experiments, "dry" Ir@TAPB-BPY COF does not show visible color changes, even in a stream of humid CO (Figure 4-5). This indicates that either liquid water is required to drive iridium reduction with CO, or that the relative humidity of the CO stream was too low.
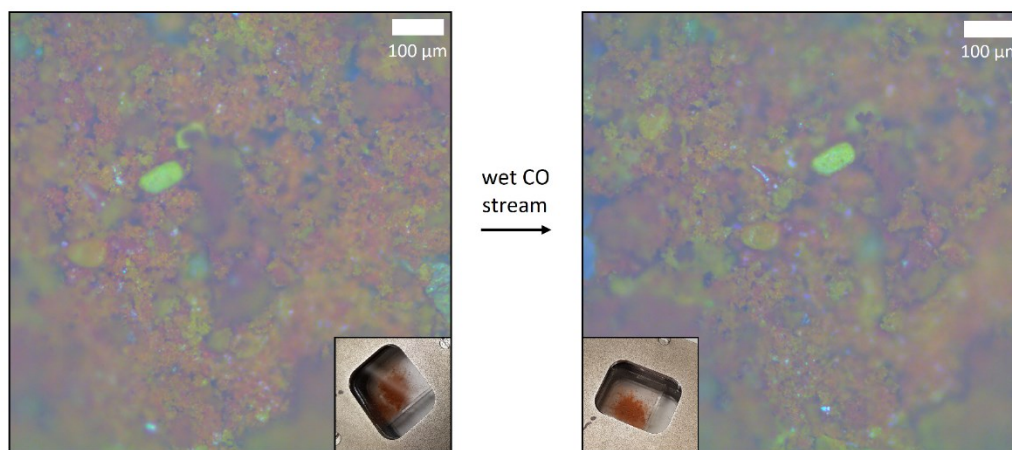
Figure 4-5: Optical microscope image of Ir@TAPB-BPY COF powder before (left) and during (right) exposure to a stream of humid CO. Sample illuminated from above. Insets show photographic images of the sample.

We thus examined the water sorption isotherms for our isoreticular series of COFs, which reflect the respective underlying hydrophilicity. All three COFs exhibit isotherms characteristic of rather hydrophobic sorbents, with slow uptake of water vapor at low relative pressures (p/p_0) and only mediocre uptakes at p/p_0 values >0.6 (Figure S4-5, Figure S4-6).[53] Given their construction from aromatic linkers without appreciable polar functionalities, this finding is not too surprising. We note, however, that Ir@TT-BPY COF and Ir@TAPB-BPY COF show somewhat higher hydrophilicity compared to Ir@TAPB-PPY COF, which is reflected in higher water uptake at high relative pressures and steeper linear adsorption at low relative pressures. This trend could be explained by the deviating electronics

of iridium species with either bipyridine (bpy) or phenylpyridine (ppy) ligands. Since the cyclometallated [Cp*Ir(ppy)Cl] motif is uncharged, it enables less interactions with the polar sorptive (i.e., water) compared to cationic [Cp*Ir(bpy)Cl]$^+$ species.

Unfortunately, actual values for the relative humidity of the used CO stream could not be obtained due to instrumental limitation.[*] Therefore, water sorption isotherms cannot be correlated to the microscopic evaluation of the response of Ir@TAPB-BPY COF to humidified CO streams. Pragmatically, we circumvent this issue by suspending the COF in phosphate buffer inside the measurement chamber. As in the WGS experiments, color changes upon CO exposure were apparent, though a distinct blue color could not be observed (Figure 4-6).
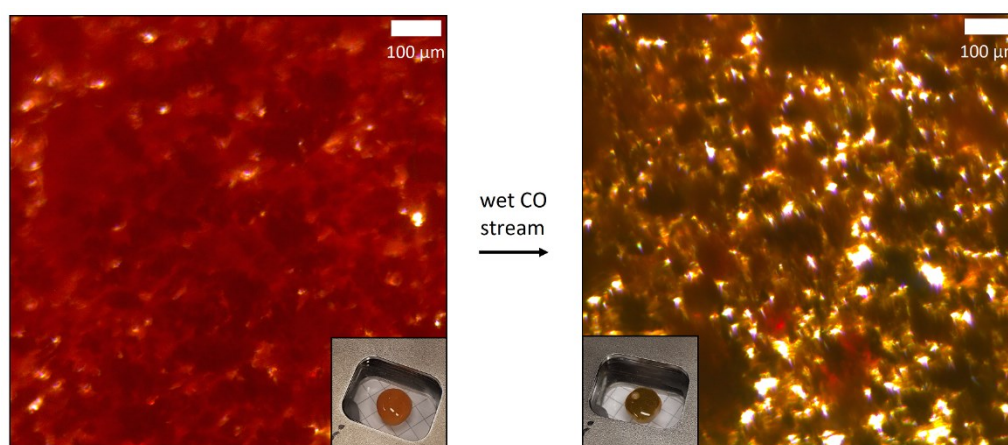
Figure 4-6: Optical microscope image of Ir@TAPB-BPY COF suspended in phosphate buffer (pH 7) before (left) and during (right) exposure to a stream of humid CO. Sample illuminated from below. Insets show photographic images of the sample.

We attribute this deviation to lower CO pressures (ca. 1.0 bar *vs.* 1.5 bar) or to lower mass transfer of CO within the unstirred drop of COF suspension. Nevertheless, it was possible to measure a change in absorbance upon exposure of suspended Ir@TAPB-BPY COF to CO, using *in-situ* UV-Vis spectroscopy. The appearance of a broad feature around 700 nm is in line with literature reports on Cp*Ir(I) complexes (Figure S4-34).[17,25] Due to the sensitivity of this species, trials to isolate a COF with bound Ir(I) species failed, though.[16,54] Upon removal of the solvent under Schlenk conditions, we could only recover a dark orange solid with no optical indication of blue Ir(I) species (Figure S4-37). The FTIR spectrum of this product indicates the preservation of the COF backbone, but showed only additional features attributable to phosphate counterions (Figure S4-38). A band around 2040 cm^{-1}, expected for iridium hydride species after protonation of Ir(I), was also not detected.[13,54]

Conclusion

In conclusion, we successfully made use of an isoreticular series of iridium-loaded COFs for photo-assisted WGS catalysis. To the best of our knowledge, no comparable study in this field has been reported. Careful analysis of the heterogeneous catalysts revealed the correct composition as well as the correct binding of the targeted iridium species to the COF support. Furthermore, the retention of

---

[*] A control experiment using nitrogen as carrier gas indicated relative humidities in the range of 95%.

catalytic activity was briefly illustrated in hydrogen transfer reactions on organic substrates, where first structure-property relationships came to light. In comparison, iridium-equipped COFs based on bipyridine linkers proved to be more active than Ir@TAPB-PPY COF, which is based on phenylpyridine units. We hypothesize the charge neutrality of the Cp*Ir(ppy) species to be disadvantageous for catalysis in aqueous media.

This trend continued in WGS experiments. Here, Ir@TAPB-PPY COF showed almost no activity. On the other hand, Ir@TT-BPY COF and Ir@TAPB-BPY showed decent TOFs of 0.43 and 0.37 h^{-1}, respectively, which is only one order of magnitude lower than the homogenous reference.

In a subsequent spectroscopic study, we found hints to the presence of intermediate Ir(I) species, which supports the proposed underlying mechanistic cycle. We identified the associated color change as a useful tool to quickly assess the catalytic potential of other iridium species. On that note, we found that our series of iridium-loaded COFs only shows this feature in suspension, but not in CO streams. Given that WGS catalysis with metalated COFs occurs at the solid-liquid interface, a more hydrophilic COF should benefit from better interaction with water and the carbon monoxide dissolved therein.[55,56] With very hydrophilic iridium-loaded catalysts, WGS catalysis might also be achieved at the gas-solid interface.[57,58] Luckily, the construction principle of COFs allows for almost limitless tunabililty so that suitable systems can easily be envisaged and synthesized. The foundation for such optimizations has been laid with this work.

Author Contributions

4.3   References

1   International Energy Agency (IEA), *Global Hydrogen Review 2022*, Paris **2022,** (accessed 24 May 2023).

2   A. Ajanovic, M. Sayer, R. Haas, *Int. J. Hydrog. Energy* **2022**, *47*, 24136–24154.

3   E. B. Agyekum, C. Nutakor, A. M. Agwa, S. Kamel, *Membranes* **2022**, *12*, 173.

4   T. L. LeValley, A. R. Richard, M. Fan, *Int. J. Hydrog. Energy* **2014**, *39*, 16983–17000.

5   P. Wolf, C. R. Wick, J. Mehler, D. Blaumeiser, S. Schötz, T. Bauer, J. Libuda, D. Smith, A.-S. Smith, M. Haumann, *ACS Catal.* **2022**, *12*, 5661–5672.

6   C. Ratnasamy, J. P. Wagner, *Catal. Rev.* **2009**, *51*, 325–440.

7   D. S. Newsome, *Catal. Rev. - Sci. Eng.* **1980**, *21*, 275–318.

8   R. M. Laine, E. J. Crawford, *J. Mol. Catal.* **1988**, *44*, 357–387.

9   J. Kaspar, R. Spogliarich, G. Mestroni, M. Graziani, *J. Organomet. Chem.* **1981**, *208*, C15-C17.

10   J. P. Collin, R. Ruppert, J. P. Sauvage, *Nouv. J. Chim.* **1985**, *9*, 395–404.

11   R. Ziessel, *J. Am. Chem. Soc.* **1993**, *115*, 118–127.

12   C. L. Pitman, A. J. M. Miller, *ACS Catal.* **2014**, *4*, 2727–2733.

13   M.-T. Youinou, R. Ziessel, *J. Organomet. Chem.* **1989**, *363*, 197–208.

14   R. Ziessel, *Angew. Chem.* **1991**, *103*, 863–866.

15   M. Ladwig, W. Kaim, *J. Organomet. Chem.* **1992**, *439*, 79–90.

16   C. L. Pitman, K. R. Brereton, A. J. M. Miller, *J. Am. Chem. Soc.* **2016**, *138*, 2252–2260.

17   K. R. Brereton, A. G. Bonn, A. J. M. Miller, *ACS Energy Lett.* **2018**, *3*, 1128–1136.

18   R. Ziessel, *J. Chem. Soc., Chem. Commun.* **1988**, 16–17.

19   S. M. Barrett, S. A. Slattery, A. J. M. Miller, *ACS Catal.* **2015**, *5*, 6320–6327.

20   S. M. Barrett, C. L. Pitman, A. G. Walden, A. J. M. Miller, *J. Am. Chem. Soc.* **2014**, *136*, 14718–14721.

21   M. B. Chambers, D. A. Kurtz, C. L. Pitman, M. K. Brennaman, A. J. M. Miller, *J. Am. Chem. Soc.* **2016**, *138*, 13509–13512.

22   C. S. Letko, Z. M. Heiden, T. B. Rauchfuss, *Eur. J. Inorg. Chem.* **2009**, *33*, 4927–4930.

23   Z. Yang, Z. Zhu, R. Luo, X. Qiu, J. Liu, J.-K. Yang, W. Tang, *Green Chem.* **2017**, *19*, 3296–3301.

24   A. H. Ngo, M. Ibañez, L. H. Do, *ACS Catal.* **2016**, *6*, 2637–2641.

25   M. R. Schreier, B. Pfund, X. Guo, O. S. Wenger, *Chem. Sci.* **2020**, *11*, 8582–8594.

26   Y. Himeda, N. Onozawa-Komatsuzaki, H. Sugihara, H. Arakawa, K. Kasuga, *Organometallics* **2004**, *23*, 1480–1483.

27   W.-H. Wang, J. F. Hull, J. T. Muckerman, E. Fujita, Y. Himeda, *Energy Environ. Sci.* **2012**, *5*, 7923.

28   G. H. Gunasekar, Y. Yoon, I.-H. Baek, S. Yoon, *RSC Adv.* **2018**, *8*, 1346–1350.

29   A. J. M. Miller, D. M. Heinekey, J. M. Mayer, K. I. Goldberg, *Angew. Chem. Int. Ed.* **2013**, *52*, 3981–3984.

30   A. F. Sasayama, C. E. Moore, C. P. Kubiak, *Dalton Trans.* **2016**, *45*, 2436–2439.

31   K. Sordakis, A. Tsurusaki, M. Iguchi, H. Kawanami, Y. Himeda, G. Laurenczy, *Green Chem.* **2017**, *19*, 2371–2378.

32   K. Sordakis, A. Tsurusaki, M. Iguchi, H. Kawanami, Y. Himeda, G. Laurenczy, *Chem. Eur. J.* **2016**, *22*, 15605–15608.

33   F. D. Sypaseuth, C. Matlachowski, M. Weber, M. Schwalbe, C. C. Tzschucke, *Chem. Eur. J.* **2015**, *21*, 6564–6571.

34   P. Sudakar, G. H. Gunasekar, I. H. Baek, S. Yoon, *Green Chem.* **2016**, *18*, 6456–6461.

35   K. Park, G. H. Gunasekar, N. Prakash, K.-D. Jung, S. Yoon, *ChemSusChem* **2015**, *8*, 3410–3413.

36   G. H. Gunasekar, H. Kim, S. Yoon, *Sustain. Energy Fuels* **2019**, *3*, 1042–1047.

37   G. Gunasekar, K. Park, H. Jeong, K.-D. Jung, K. Park, S. Yoon, *Catalysts* **2018**, *8*, 295.

38   J. J. Corral-Pérez, A. Billings, D. Stoian, A. Urakawa, *ChemCatChem* **2019**, *11*, 4725–4730.

39   B. An, L. Zeng, M. Jia, Z. Li, Z. Lin, Y. Song, Y. Zhou, J. Cheng, C. Wang, W. Lin, *J. Am. Chem. Soc.* **2017**, *139*, 17747–17750.

40   N. R. Bennedsen, D. B. Christensen, R. L. Mortensen, B. Wang, R. Wang, S. Kramer, S. Kegnæs, *ChemCatChem* **2021**, *13*, 1781–1786.

41   G. H. Gunasekar, S. Yoon, *J. Mater. Chem. A* **2019**, *7*, 14019–14026.

42   J. Rauh, Master Thesis, **2021**, Ludwig-Maximilians-Universität München, München.

43   L. Grunenberg, G. Savasci, M. W. Terban, V. Duppel, I. Moudrakovski, M. Etter, R. E. Dinnebier, C. Ochsenfeld, B. V. Lotsch, *J. Am. Chem. Soc.* **2021**, *143*, 3430–3438.

44   M. Thommes, K. Kaneko, A. V. Neimark, J. P. Olivier, F. Rodriguez-Reinoso, J. Rouquerol, K. S. Sing, *Pure Appl. Chem.* **2015**, *87*, 1051–1069.

45   J. Chen, X. Tao, C. Li, Y. Ma, L. Tao, D. Zheng, J. Zhu, H. Li, R. Li, Q. Yang, *Appl. Catal. B* **2020**, *262*, 118271.

46   J. Xu, C. Yang, S. Bi, W. Wang, Y. He, D. Wu, Q. Liang, X. Wang, F. Zhang, *Angew. Chem. Int. Ed.* **2020**, *59*, 23845–23853.

47   J. Xu, Y. He, S. Bi, M. Wang, P. Yang, D. Wu, J. Wang, F. Zhang, *Angew. Chem.* **2019**, *131*, 12193–12197.

48   G. Zhao, H. Li, Z. Gao, L. Xu, Z. Mei, S. Cai, T. Liu, X. Yang, H. Guo, X. Sun, *Adv. Funct. Mater.* **2021**, *31*, 2101019.

49   R. Bu, L. Zhang, X.-Y. Liu, S.-L. Yang, G. Li, E.-Q. Gao, *ACS Appl. Mater. Interfaces* **2021**, *13*, 26431–26440.

50   H. Takehira, M. R. Karim, Y. Shudo, M. Fukuda, T. Mashimo, S. Hayami, *Sci. Rep.* **2018**, *8*, 17392.

51   M. Wilson, R. Kore, A. W. Ritchie, R. C. Fraser, S. K. Beaumont, R. Srivastava, J. P. S. Badyal, *Colloids Surf. A* **2018**, *545*, 78–85.

52   Y. Hu, L. Li, A. P. Shaw, J. R. Norton, W. Sattler, Y. Rong, *Organometallics* **2012**, *31*, 5058–5064.

53   E.-P. Ng, S. Mintova, *Microporous Mesoporous Mater.* **2008**, *114*, 1–26.

54   C. Caix, S. Chardon-Noblat, A. Deronzier, R. Ziessel, *J. Electroanal. Chem.* **1996**, *403*, 189–202.

55   X. Wang, L. Chen, S. Y. Chong, M. A. Little, Y. Wu, W.-H. Zhu, R. Clowes, Y. Yan, M. A. Zwijnenburg, R. S. Sprick, A. I. Cooper, *Nat. Chem.* **2018**, *10*, 1180–1189.

56   T. Banerjee, B. V. Lotsch, *Nat. Chem.* **2018**, *10*, 1175–1177.

57   S. Werner, N. Szesni, R. W. Fischer, M. Haumann, P. Wasserscheid, *Phys. Chem. Chem. Phys.* **2009**, *11*, 10817–10819.

58   S. Werner, N. Szesni, M. Kaiser, R. W. Fischer, M. Haumann, P. Wasserscheid, *ChemCatChem* **2010**, *2*, 1399–1402.

5 Conclusions and Outlook

In this thesis, the applicability of COFs for the photocatalytic oxygen evolution half-reaction has been explored. Motivated by the COFleaf ERC staring grant (Grant agreement ID: 639233) we wanted to build on previous experiments on hydrogen evolution with COFs and pave the way to full water splitting using visible light by tackling the oxidative half-reaction. The approach presented in chapter 2 focusses on iridium complexes heterogenized on COF supports *via* bipyridine sites covering the pore walls. Analogous molecular iridium species are well-established water oxidation catalysts, and the retained catalytic activity upon anchoring to TAPB-BPY COF was confirmed in chemical water oxidation experiments. By using strongly oxidizing cerium ammonium nitrate sacrificial electron acceptor, electron hole photogeneration by the potential COF photocatalyst is bypassed as required source of oxidation equivalents. In subsequent photocatalytic experiments, we first observed oxygen evolution with iridium-loaded COFs. Through careful control experiments, however, we could trace the catalytic activity back to contaminated glassware, highlighting the importance of both thorough cleaning protocols as well as thoughtful blank experiments. Ultimately, we could confirm the absence of photocatalytic activity towards the water oxidation half-reaction for Ir@TAPB-BPY COF despite exhibiting a sufficiently positive valence band position and thus a suitable thermodynamic driving force. Additional computational analysis revealed that the four electron transfer steps required for the oxidation of one water molecule are associated with highly varying free energy changes, some of which exceed the COF's redox potential and hint at a large overpotential for the overall reaction. Thus, we hypothesize that despite being thermodynamically capable of water oxidation, Ir@TAPB-BPY COF fails to do so because of kinetic limitations.

Following this narrative, a possible solution to tackle such challenging kinetic bottlenecks would be to design COFs with even lower valence bands, so that the photogenerated electron holes can drive each of the four oxidation steps. Also, in the long-term, replacement of scarce and expensive iridium WOCs with more abundant elements should be envisaged in order to achieve higher cost efficiency. Most COFs reported in the literature for photocatalytic water oxidation make use of cobalt co-catalysts, and other first-row transition metals such as manganese and iron can also be envisaged.[1] However, we found that a significant number of reports on cobalt-loaded COFs for oxygen evolution photocatalysis provide only scarce experimental details and rarely present essential blank measurements. In the case of two literature examples examined in our photocatalysis study, we could not reproduce the claimed oxygen evolution.

The potential use of COFs for oxidative photocatalysis has, however, been shown for aerobic oxidations of aromatic alcohols with FEAx-COF. Inspired by naturally occurring flavin-motifs, we designed and successfully synthesized an alloxazine building block using classical organic chemistry methods. It's incorporation into an ordered framework nicely illustrated the principles of the COF concept, i.e., the limitless library of accessible COFs based on variation of the underlying organic linkers. Furthermore, the use of FEAx-COF as a photocatalyst demonstrated that by using functional building blocks also the resulting COF exhibits similar functionalities – in this case, redox activity. The integration of the

alloxazine unit into an extended network even proved to lead to increased catalytic activity due to the increased conjugation and the higher light absorption associated therewith.

However, the use as photoredox catalyst does not exhaust the potential of FEAx-COF in particular, or alloxazine-COFs in general. Their ability to participate both in one- and two-electron redox reactions makes alloxazine-based COFs promising candidates for, for example, pseudocapacitive energy storage.
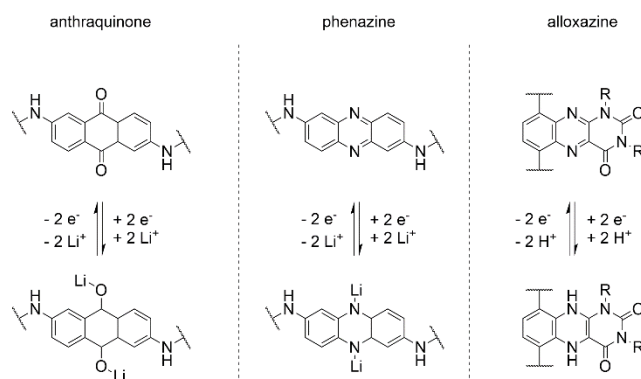
Scheme 5-1: Schematic representation of anthraquinone, phenazine, and alloxazine motifs in their oxidized (top) and reduced (bottom) state.

This field has already been explored by the DICHTEL group with their work on anthraquinone- and phenazine-based COFs which exhibit similar redox-activity due to their respective building blocks (Scheme 5-1).[2,3] Owing to their high surface areas and good chemical stability, such redox-active COFs can be used as pseudocapacitors with high power densitites.[4,5]

Alternatively, the scope of alloxazine-COFs could be extended by also synthesizing isoalloxazine analogues and thus actual flavin COFs. This might pave the way to metal-free water oxidation, given that flavinium species have been reported for electrocatalytic oxygen evolution without the need for co-catalytic species.[6] In a supervised student project which is not part of this thesis, we already synthesized a flavin derivate suitable for COF formation (Scheme 5-2), though we could not obtain crystalline polymers in first synthetic trials.[7]
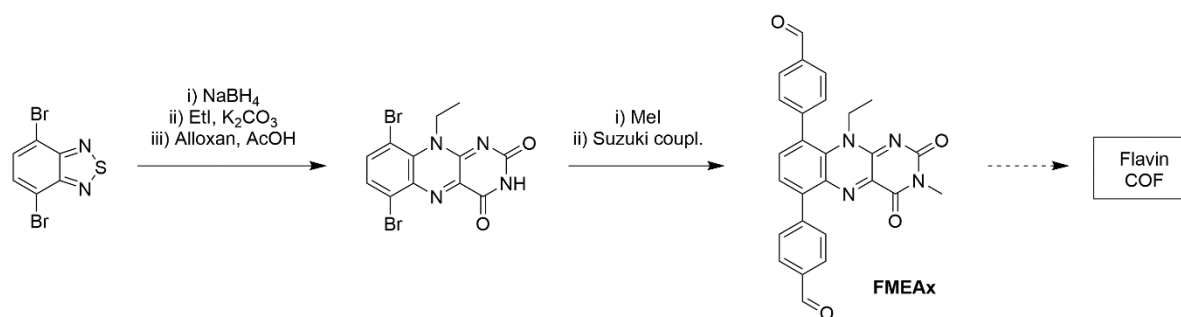
Scheme 5-2: Synthetic route to isoalloxazine linkers as potential building blocks for actual flavin COFs.

Lastly, we presented an alternative application for iridium-loaded COFs, highlighting their versatility beyond water oxidation. Despite using non-optimized experimental conditions, bipyridine-based COFs could catalyze the photo-assisted water-gas shift reaction after anchoring of Cp*Ir species. However, the intermediate reduction of Ir(III) to Ir(I) could only be observed for fully-suspended COFs particles

and not at the gas-solid interface of iridium-loaded COFs in humid gas streams. However, since COFs are highly tunable platforms, incorporating iridium motifs into highly hydrophilic frameworks could allow for photo-assisted WGS catalysis in gas streams. The postsynthetic modification of imine-COFs to nitrone-linked derivates has been demonstrated as a viable method to obtain COFs with high water vapor uptake even at low humidities.[8,9] Also, special photothermal flow reactors required to simultaneously illuminate large surfaces of a heterogeneous catalyst in humid gas streams have been reported lately.[10] Alternatively, the Ir-H species inherent to the catalytic WGS cycle could be used for organic reductions instead of hydrogen evolution.[11]

Besides OER and WGS catalysis, the Cp*Ir species covered within this thesis are also known to catalyze, for example, hydrogen evolution, alcohol oxidation, and CO_2 hydrogenations.[12,13] Although the application of iridium-loaded heterogeneous supports for these reactions has been reported in parts, further progress can still be achieved and innovative solutions can be found.[14–17] For example, the possibility to form iridium hydride species from [Cp*Ir(bpy)] motifs with dihydrogen allows for the construction of fuel cells.[18] In such a setting, the iridium species acts as the anode and oxidizes H_2 to H_2O – though it is proposed that the system could also be switched to photoelectrocatalytic water oxidation instead.[18] Given their high tunability, large surface areas, and long-range order, COFs provide just the right tools to explore the full potential of heterogenized metal complexes for such adventurous research.

5.1 References

1 M. D. Kärkäs, B. Åkermark, *Dalton Trans.* **2016**, *45*, 14421–14461.

2 C. R. DeBlase, K. E. Silberstein, T.-T. Truong, H. D. Abruña, W. R. Dichtel, *J. Am. Chem. Soc.* **2013**, *135*, 16821–16824.

3 E. Vitaku, C. N. Gannett, K. L. Carpenter, L. Shen, H. D. Abruña, W. R. Dichtel, *J. Am. Chem. Soc.* **2020**, *142*, 16–20.

4 C. R. DeBlase, K. Hernández-Burgos, K. E. Silberstein, G. G. Rodríguez-Calero, R. P. Bisbey, H. D. Abruña, W. R. Dichtel, *ACS nano* **2015**, *9*, 3178–3183.

5 X. Gao, Y. Dong, S. Li, J. Zhou, L. Wang, B. Wang, *Electrochem. Energ. Rev.* **2020**, *3*, 81–126.

6 E. Mirzakulova, R. Khatmullin, J. Walpita, T. Corrigan, N. M. Vargas-Barbosa, S. Vyas, S. Oottikkal, S. F. Manzer, C. M. Hadad, K. D. Glusac, *Nat. Chem.* **2012**, *4*, 794–801.

7 J. Schackmann, Internship report, LMU Munich **2019**.

8 L. Grunenberg, G. Savasci, S. T. Emmerling, F. Heck, S. Bette, A. Cima Bergesch, C. Ochsenfeld, B. V. Lotsch, *J. Am. Chem. Soc.* **2023**, *145*, 13241–13248.

9 D. Kurandina, B. Huang, W. Xu, N. Hanikel, A. Darù, G. D. Stroscio, K. Wang, L. Gagliardi, F. D. Toste, O. M. Yaghi, *Angew. Chem. Int. Ed.* **2023**, e202307674.

10 X. E. Cao, Y. Kaminer, T. Hong, P. Schein, T. Liu, T. Hanrath, D. Erickson, *iScience* **2020**, *23*, 101856.

11 A. Ambrosi, S. E. Denmark, *Angew. Chem. Int. Ed.* **2016**, *55*, 12164–12189.

12 K. R. Brereton, A. G. Bonn, A. J. M. Miller, *ACS Energy Lett.* **2018**, *3*, 1128–1136.

13   S. Abednatanzi, P. Gohari Derakhshandeh, P. Tack, F. Muniz-Miranda, Y.-Y. Liu, J. Everaert, M. Meledina, F. Vanden Bussche, L. Vincze, C. V. Stevens, V. van Speybroeck, H. Vrielinck, F. Callens, K. Leus, P. van der Voort, *Appl. Catal. B* **2020**, *269*, 118769.

14   L. Tensi, A. V. Yakimov, C. Trotta, C. Domestici, J. de Jesus Silva, S. R. Docherty, C. Zuccaccia, C. Copéret, A. Macchioni, *Inorg. Chem.* **2022**, *61*, 10575–10586.

15   N. R. Bennedsen, D. B. Christensen, R. L. Mortensen, B. Wang, R. Wang, S. Kramer, S. Kegnæs, *ChemCatChem* **2021**, *13*, 1781–1786.

16   J. J. Corral-Pérez, A. Billings, D. Stoian, A. Urakawa, *ChemCatChem* **2019**, *11*, 4725–4730.

17   K. Park, G. H. Gunasekar, N. Prakash, K.-D. Jung, S. Yoon, *ChemSusChem* **2015**, *8*, 3410–3413.

18   M. Kikkawa, T. Yatabe, T. Matsumoto, K.-S. Yoon, K. Suzuki, T. Enomoto, K. Kaneko, S. Ogo, *ChemCatChem* **2017**, *9*, 4024–4028.

6 Appendix

6.1 List of Abbreviations

ATP	adenosine triphosphate
BDBA	1,4-benzene diboronic acid
bdc	1,4-benzenedicarboxylate
BET	Brunauer-Emmett-Teller
BPDA	4,4'-biphenyldicarboxaldehyde
bpy	2,2'-bipyridine
CBM	conduction band minimum
CO_2RR	carbon dioxide reduction reaction
COF	covalent organic framework
CTF	covalent triazine framework
DCC	dynamic covalent chemistry
DCM	dichloromethane
DMF	*N,N*-dimethylformamide
DMSO	dimethyl sulfoxide
ETC	electron transport chain
FAx	6,9-bis-(4-formylphenyl)-alloxazine
FEAx	1,3-diethyl-6,9-bis-(4-formylphenyl)alloxazine
FTIR	Fourier transform infrared spectroscopy
GCC	graphite-conjugated catalyst
GHI	global horizontal irradiation
HEAx	1,3-diethyl-alloxazine
HER	hydrogen evolution reaction
HHTP	2,3,6,7,10,11-hexahydroxytriphenylene
HOMO	highest occupied molecular orbital
LLCT	ligand-to-ligand charge-transfer
LUMO	lowest unoccupied molecular orbital
MLCT	metal-to-ligand charge-transfer
MOF	metal-organic framework
$NADP^+$	nicotinamide adenine dinucleotide phosphate
OEC	oxygen evolution complex
OER	oxygen evolution reaction
PC	photocatalyst
PDAN	1,4-phenylenediacetonitrile
PEAx	1,3-diethyl-6,9-diphenyl-alloxazine
PEC	photoelectrocatalyst
POP	porous organic polymer
ppy	2-phenylpyridine
PRC	proton reduction catalyst
PS	photosensitizer
PS	photosystem
PtG	power-to-gas
PV	photovoltaic
RWGS	reversed water-gas shift
SEA	sacrificial electron acceptor
SED	sacrificial electron donor
SEM	scanning electron microscopy

STH	solar-to-hydrogen
TAPB	1,3,5-tris(4-aminophenyl)benzene
TAPP	5,10,15,20-tetrakis-(4-aminophenyl)-porphyrin
TAPT	2,4,6-tris(4-aminophenyl)-1,3,5-triazine
TEM	transmission electron microscopy
TFPPy	1,3,6,8-tetrakis-(4-formylphenyl)pyrene
TMT	2,4,6-trimethyl-1,3,5-triazine
TOF	turnover frequency
TON	turnover number
TTF	2,3,6,7-tetra (4formylphenyl)-tetrathiafulvalene
UV-Vis	ultraviolet–visible (spectroscopy)
VBM	valence band maximum
WGS	water-gas shift
WOC	water oxidation catalyst
XAS	X-ray absorption spectroscopy
XRPD	X-Ray powder diffraction

6.2   Supporting Information for Chapter 2

6.2.1   Materials and Methods

ICP-OES

ICP-OES spectroscopy was performed on a Varian Vista Pro and evaluated using the Agilent ICP Expert software. Samples were digested in concentrated nitric acid (65%) at 185 °C for 25 min with a CEM Discover SP-D.

Elemental analysis

Elemental analysis (C, H, N) was conducted on an ELEMENTAR vario EL using Helium as carrier gas.

Supercritical CO_2 drying

COF samples were kept soaked in ethanol prior to supercritical CO_2 extraction on a Leica EM CPD300 critical point dryer with ethanol as exchange liquid.

Nuclear magnetic resonance spectroscopy

Spectra of soluble samples were recorded using a Bruker AV400TR or a Jeol Eclipse 400+ spectrometer. Chemical shifts are denoted on the scale in parts per million (ppm), calibrated to residual non-deuterated solvent (^{1}H-NMR: 7.26 for $CDCl_3$, 2.50 for DMSO-d_6) or solvent carbon resonances (^{13}C-NMR: $CDCl_3$: 77.16 for $CDCl_3$, 39.52 for DMSO-d_6). Multiplicities are denoted as: s = singlet, d = duplet, t = triplet, q = quartet, m = multiplet, or as a combination thereof. Spectra were analyzed and processed using MestReNova version 10.0.2-15465.

Solid-state nuclear magnetic resonance experiments were performed on Bruker Neo 600 MHz instrument using a 4 mm outer diameter ZrO_2 rotor and a BL4 MAS double resonance probe at a spinning frequency of 14 kHz. The ^{13}C spectrum was acquired with ^{1}H cross-polarization.

X-ray photoelectron spectroscopy (XPS)

XPS measurements were conducted on Kratos Axis Ultra X-ray photoelectron spectrometer with a monochromatic Al Kα source and charge compensation. Binding energies were calibrated to the adventitious carbon 1s peak at 284.80 eV if not stated otherwise.[1,2] For postcatalytic samples, C 1s calibration was set to 284.5 eV.[3] The CasaXPS software 2.3.16 was used for data analysis. Powder samples were measured on indium foil.

Physisorption analysis

Argon and nitrogen sorption measurements at 87 K and 77 K, respectively, were performed with a Quantachrome Instruments Autosorb iQ MP. Samples of more than 20 mg were preheated *in vacuo* (10^{-7} mbar) at 120 °C for 12 h. ASiQwin Version 3.01 was used for data analysis. Pore size distributions were evaluated using the carbon QSDFT kernel for cylindrical pores for the adsorption branch if not stated otherwise. Expected pore sizes were derived from structural models in Materials Studio v6.0.0. Water sorption measurements were performed at the specified temperature using a water-jacketed water bath connected to a Julabo F12-ED thermostat.

Mass spectrometry

Experiments were performed on a Thermo Finnigan MAT 90 or MAT 95 mass spectrometer using electrospray ionization (ESI). m/z values were calculated using Perkin Elmer ChemDraw® Professional Version 16.0.0.82 (68).

Infrared spectroscopy

Infrared spectroscopy was conducted using a Perkin Elmer Spektrum BX II FT-IR equipped with an ATR unit (Smith Detection Dura-Sample IIR diamond). Background correction was done before sample measurements.

UV-Vis

Diffuse reflectance UV-Vis spectra were collected on a Cary 5000 spectrometer and referenced to barium sulfate. Absorption spectra were calculated from the reflectance data using the Kubelka-Munk function.

X-ray powder diffraction (XRPD)

XRPD patterns were collected at room temperature on a Bruker D8 Discovery with Ni-filtered Cu-Kα radiation (1.5406 Å) and a position-sensitive LynxEye detector in Bragg-Brentano geometry. Materials Studio v6.0.0 was used for structural modelling, XRD pattern simulations, and Pawley Refinement.

High angle measurements for the identification of different silver species were performed on a Stoe Stadi P powder diffractometer with Ge(111)-monochromated Cu-Kα$_1$ radiation (λ = 1.54051 Å) in Debye-Scherrer geometry. WinXPOW 3.0.2.1 was used for data analysis.

Electrochemistry

Cyclic voltammetry was conducted on a WaveDriver 200 EIS Bipotentiostat with COF-coated carbon paper working electrodes, a platinum wire counter electrode, and a non-aqueous Ag/Ag^+ reference electrode. Anhydrous acetonitrile with 0.1 M tetrabutylammonium hexafluorophosphate was used as electrolyte under Ar atmosphere. Prior to the measurement, the electrochemical cell was purged with argon for 10 min. Reduction onset potentials (E_{onset}) were extracted from the linear fits in the voltammograms according to a previous method.[4] Potentials *vs.* Fc/Fc^+ were converted to absolute energies according to equation S1:

$$E_{abs} = -(E_{(vs.\ Fc/Fc+)} + 5.1)\ eV \qquad\qquad (eq.\ S1)^{[5,6]}$$

The position of the conduction band (E_{CB}) was estimated from the valence band (E_{VB}) using the optical band gap $E_{g,opt}$ according to eq. S2:

$$E_{CB}\ (eV\ vs.\ vac) = E_{VB}\ (eV\ vs.\ vac) + E_{g,opt}\ (eV) \qquad\qquad (eq.\ S2)$$

The absolute energy for water oxidation at pH 7 was calculated according to eq. S3:

$$E_{abs} = -(4.5 + 1.23 - 0.059 \cdot pH)\ eV \qquad\qquad (eq.\ S3)^{[7]}$$

Electron paramagnetic resonance (EPR) spectroscopy

EPR spectra were measured with a BRUKER EMXnano. Experiments were conducted with degassed silver nitrate solutions (10, 100, or 1000 mM in water). Illumination was conducted with >420 nm similar to photocatalytic OER experiments (*vide infra*). DMPO was added either before or directly after the illumination in the form of a 0.3 M stock solution in order to trap $OH^\bullet$ in the form of $DMPO\text{-}OH^\bullet$. $[Ag^{II}(py)_4]S_2O_8$ was measured as a solid.

Catalytic Activity and Literature Comparison

TONs were calculated according to: $TON = \dfrac{n(O_2)}{n(metal)}$ TOFs were calculated from TONs through division by the underlying time periods. If stated, literature values were extracted from graphs using WebPlotDigitizer V4.6 by Ankit Rohatgi.

Photocatalytic Oxygen Evolution - Screening

If not stated otherwise, 5.0 mg COF were suspended in the respective aqueous reaction medium (5 mL) and sonicated for at least 10 minutes. The resulting suspension was transferred to a custom-made flow reactor (Figure S2-11) and the sacrificial electron acceptor was added. The reactor was closed and the reaction mixture was degassed in the dark with an argon flow of 40-60 NmL min^{-1} while stirring at 400 rpm. Once the system approached the baseline oxygen content, the flow was reduced to 20 NmL min^{-1} and the temperature of the water-jacketed reactor was kept at 25 °C using a JULABO FP50-ME thermostat. After adjusting the pressure to 1.10 – 1.25 bar, the baseline was measured for 30 minutes before starting the illumination from above through a quartz glass blind flange. The oxygen evolution rate was determined every three seconds using a PreSens flow-through cell with an integrated PSt-9

sensor spot connected to a Fibox 4 trace oxygen meter. The readout in ppm was baseline-corrected and subsequently converted to $\mu mol\ h^{-1}$ by applying a factor of $0.0749\ \mu mol\ h^{-1}\ ppm^{-1}$ (Figure S2-68). To prevent uncontrolled heating of the oxygen sensor during illumination, it was covered in wet paper towels together with the Pt100 temperature sensor. In between measurements, the reactor was cleaned with *aqua regia*, piranha solution, and copious amounts of water.

Photocatalytic Oxygen Evolution - GC

For more elaborate oxygen evolution experiments, we connected the flow reactor to a SHIMADZU GC-2030 with MS and BID detection in addition to the online PSt-9 detector. The pressure is kept stable at 1.15 bar using a pressure controller, and a flow of $5\ NmL\ min^{-1}$ helium is applied to increase the sensitivity of the oxygen detection (conversion factor $0.01338\ \mu mol\ h^{-1}\ ppm^{-1}$). Illumination was achieved with an AAA class Newport 94023A solar simulator.

Chemical Oxygen Evolution

If not stated otherwise, 5.0 mg COF were suspended in 4.6 mL 0.1 M HNO_3 and sonicated for 5 minutes. The resulting suspension was transferred to a custom-made flow reactor (Figure 2-3) and degassed in the dark with an argon flow of $40\text{-}60\ NmL\ min^{-1}$ while stirring at 400 rpm. Once the system approached the baseline oxygen content, the flow was reduced to $20\ NmL\ min^{-1}$ and the temperature of the water-jacketed reactor was kept at 25 °C. After adjusting the pressure to $1.10 - 1.25$ bar, the baseline was measured for 30 minutes before injecting a blank (0.1 M HNO_3, 0.2 mL) through a septum injector nut. After another 30 minutes, 0.2 mL of a CAN stock solution (1.95 M, in 0.1 M HNO_3) were injected, yielding a final CAN concentration of 78 mM. The oxygen evolution rate was determined every three seconds using a PreSens flow-through cell with an integrated PSt-6 or PSt-9 sensor spot connected to a Fibox 4 trace oxygen meter. The readout in ppm was converted to $\mu mol\ h^{-1}$ by applying a factor of $0.0749\ \mu mol\ h^{-1}\ ppm^{-1}$. For recycling and filtration experiments, either the filtrate or the residual COF were subjected to identical reaction conditions. In the latter case, the COF was washed with 0.1 M HNO_3, water, and acetone after the first catalytic experiment.

For reactions with a final CAN concentration of 10 mM, the blank and the CAN stock injection were done with a gastight HAMILTON® syringe (50 µL; final volume still 5 mL) in order to reduce the oxygen leakage.

For stability experiments, the amount of COF and reaction media were upscaled while mimicking catalysis conditions in round-bottom flasks. 50 mg COF were sonicated in aq. HNO_3 (50 mL, pH 1) for 10 minutes, and subsequently degassed by inert gas bubbling for 1 hour. Solid CAN (2.15 g, 3.91 mmol) was added, and the resulting suspensions were stirred under continuous inert gas bubbling for 90 minutes. The solid was filtered off, washed with HNO_3 (pH 1), water, DMF, acetone, and MeOH, prior to supercritical CO_2 drying and subsequent heating *in vacuo* (12 h, 120 °C).

Computational Chemistry

The ionisation potential (IP) and electron affinity (EA) of the polymers in water were predicted by ΔDFT calculations following a previously developed approach.[8,9] In this approach the COF is described as a

cluster model (see Figure S2-30) embedded in a continuum dielectric with the dielectric permittivity of the major component of the reaction mixture, here water (ε_r 80.1) or acetonitrile (ε_r 37.5). The use of a continuum solvation model allows for the description of the dielectric screening of charges in the low dielectric COF/polymer by the typically higher dielectric permittivity mixture of water sacrificial electron donor/acceptor mixture. Moreover, when using a dielectric permittivity value of 2 instead, roughly the value expected for an organic material, this approach reproduces IP and EA values measured experimentally[9,10] for conjugated polymers by photoelectron spectroscopy, in which the polymer particles/film is measured in vacuum and there is no solvent/reaction mixture present.

All predicted potentials were converted from the vacuum scale to the standard hydrogen electrode (SHE) scale by subtracting 4.44 V, the absolute value of the standard hydrogen electrode potential, of the vacuum scale value.

The free energy landscape of a step wise water oxidation mechanism for a cluster model of the Ir@TAPB-BPY COF and Co@TAPB-BPY COF was calculated using an approach adapted from a method originally developed by Norskov and co-workers for heterogeneous electrocatalysts.[11–13] This approach allows one to predict the overpotential required to drive water oxidation relative to the potential of the four-hole water oxidation reaction by the difference between the potential for the elementary redox step with the largest uphill free energy change and that of the four-hole water oxidation potential. In the calculations we equate the free energy of a proton and an electron with that of ½ H_2, the so-called computational hydrogen electrode approximation. The entropic contribution to the free energy was calculated by calculating the harmonic frequencies of all relevant cluster models, as well as molecular hydrogen and water. Because of the cost of the frequency calculations the cluster model used in these calculations is smaller than that used when calculating IP and EA (Figure S2-30). However, a calculation of only the enthalpic contribution to the free energy for the model in Figure S2-30 and the larger model in Figure S2-31 suggest that the effect of using such smaller models is small.

All DFT calculations used the B3LYP density functional[14–17] in combination with the DZP[18] (def2-SVP[19] in combination with a relativistic ECP[20] for Ir) basis-set and were performed using Turbomole 7.5[21,22] Solvation effects in the DFT calculations were described using the COSMO[23] implicit continuum solvation model and the water/acetonitrile dielectric permittivity value discussed above.

6.2.2   Synthetic Procedures

[Cp*IrCl$_2$]$_2$,[24] [Cp*Ir(bpy)Cl]Cl,[25] TTI-COF,[26] Co@TTI-COF, Co@TAPB-BPY COF,[27] RuO_2@WO_3,[28] and [Ag^{II}(py)$_4$]S$_2$O$_8$[29] were synthesized according to literature procedures.

Synthesis of iridium-loaded bipyridine linker **2**

Following a literature procedure[30] [Cp*IrCl$_2$]$_2$ (199 mg, 0.25 mmol) and 2,2'-bipyridiyl-5,5'-dialdehyde (108 mg, 0.5 mmol) were dissolved in DCM (6 mL) and stirred at rt for 42 h. The resulting orange solution was filtered through a 0.45 µm PTFE syringe filter and evaporated using a stream of nitrogen, yielding **2** as an orange solid (284.8 mg, 93%).

^{1}H NMR (400 MHz, Chloroform-*d*) δ 10.28 (s, 2H), 9.44 (d, *J* = 8.2 Hz, 2H), 9.25 (s, 2H), 8.68 (d, *J* = 8.1 Hz, 2H), 1.77 (s, 15H) ppm. ^{1}H NMR (400 MHz, Methanol-d_4, hydrate formation) δ 9.07 (d, *J* = 6.9 Hz, 2H), 8.60 (d, *J* = 9.9 Hz, 2H), 8.30 (d, *J* = 8.4 Hz, 2H), 5.81 (s, 2H), 1.71 (s, 15H). ^{13}C NMR (101 MHz, Methanol-d_4, hydrate formation) δ 156.0, 151.0, 144.0, 139.6, 124.8, 95.5, 91.0, 8.6 ppm. MS (ESI+): m/z calc. for $C_{22}H_{23}ClIrN_2O_2^+$ (M-Cl$^-$): 575.10718; found 575.10835. ICP: 33.49 wt% Ir; calc. 31.479 wt%)

Synthesis of TAPB-BPDA COF

A Biotage® 5 mL microwave vial was charged with TAPB (14.8 mg, 0.039 mmol, 2.0 eq.) and 4,4'-biphenyldicarboxaldehyde (BPDA, 12.9 mg, 0.060 mmol, 3.0 eq.). The vial was temporarily sealed with a rubber septum and flushed three times *via* vacuum/argon cycles. Mesitylene (1.33 mL) and 1,4-dioxane (0.66 mL) were added, and the reactants were suspended *via* sonication for 5 minutes. The suspension was degassed *via* three vacuum/argon cycles. Aqueous acetic acid (100 µL, 6M) was added, the vial was sealed with a crimp cap and heated to 130 °C for 3 d. After cooling to room temperature, the combined solids of two parallel reactions was filtered off and washed with $CHCl_3$ (3 x 15 mL), THF (3 x 10 mL), and acetone (3 x 10 mL). Drying in high vacuum at 120 °C for 12 h yielded TAPB-BPDA COF (35.2 mg, 73%) as an orange-brown solid. Elemental analysis calc. (%) for $C_{90}H_{60}N_6$: C 88.21, H 4.93, N 6.86; found: C 86.04, H 4.91, N 6.44.

Synthesis of TAPB-BPY COF

A Biotage® 20 mL microwave vial was charged with TAPB (92.3 mg, 0.252 mmol, 2.0 eq.) and 2,2'-bipyridyl-5,5'-dialdehyde (81.9 mg, 0.378 mmol, 3.0 eq.). The vial was temporarily sealed with a rubber septum and flushed three times *via* vacuum/argon cycles. Mesitylene (5.1 mL) and 1,4-dioxane (0.9 mL) were added, and the reactants were suspended *via* sonication for 5 minutes. The suspension was degassed *via* three vacuum/argon cycles. Aqueous acetic acid (600 µL, 6M) was added, the vial was sealed with a crimp cap and heated to 120 °C for 3 d. After cooling to room temperature, the solid was filtered off and washed with DMF (50 mL), THF (50 mL), acetone (50 mL), and MeOH (50 mL). Soxhlet extraction with MeOH overnight followed by supercritical CO_2 drying yielded TAPB-BPY COF (118 mg, 76%) as an ocre powder. Elemental analysis calc. (%) for $C_{84}H_{54}N_{12}$: C 81.93, H 4.42, N 13.65; found: C 79.38, H 4.59, N 12.72.

Synthesis of IrCp*@TAPB-BPY COF

IrCp*@TAPB-BPY COF was synthesized according to the procedure described for TAPB-BPY COF but with substitution of bipyridyl-5,5'-dialdehyde by the desired amount of iridium-loaded linker **2**.

Postsynthetic loading of TAPB-BPY COF with Iridium

A Biotage® 20 mL microwave vial was charged with TAPB-BPY COF (33.5 mg, 0.082 mmol bpy, 1.0 eq.) and [Cp*IrCl$_2$]$_2$ (33.7 mg, 0.042 mmol, 0.5 eq.). The vial was temporarily sealed with a rubber septum

and flushed three times *via* vacuum/argon cycles. Degassed methanol (5 mL) was added, and the suspension was stirred for two hours. The solid was filtered off and washed with MeOH (5 mL), water (5 mL), DMF (15 mL), EtOH (15 mL), THF (15 mL), acetone (50 mL), and MeOH (5 mL). Soxhlet extraction with MeOH overnight followed by supercritical CO_2 drying yielded Ir@TAPB-BPY COF (46.5 mg, 98 %) as an orange powder.

6.2.3 Additional Data
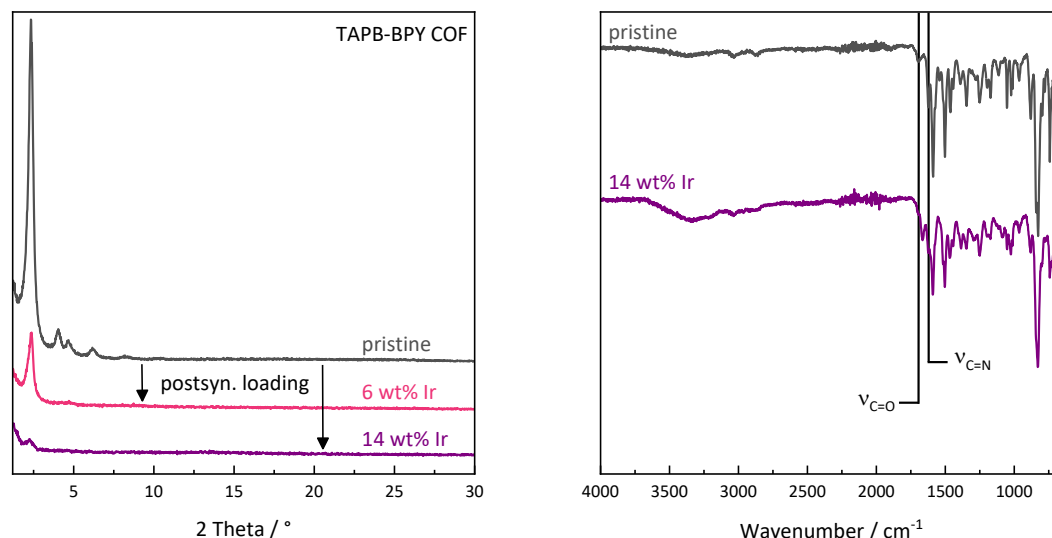
Figure S2-1: XRPD patterns (left) and FTIR spectra (right) for TAPB-COF before and after postsynthetic loading with varying amounts of [Cp*IrCl]. Annotations refer to the Ir content after loading as measured by ICP-OES.
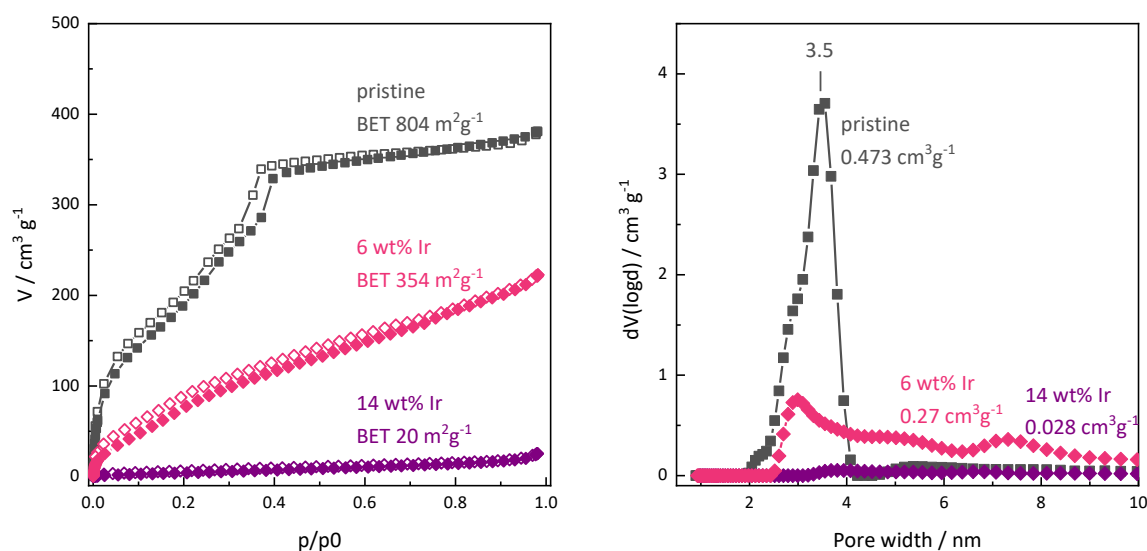
Figure S2-2: Argon sorption isotherm at 87 K (left) and pore size distribution (right) for TAPB-COF before and after postsynthetic loading with varying amounts of [Cp*IrCl₂]₂. Filled and open symbols represent the adsorption and the desorption branches, respectively. The pore size distribution was obtained from a QSDFT kernel for cylindrical pores (adsorption branch).
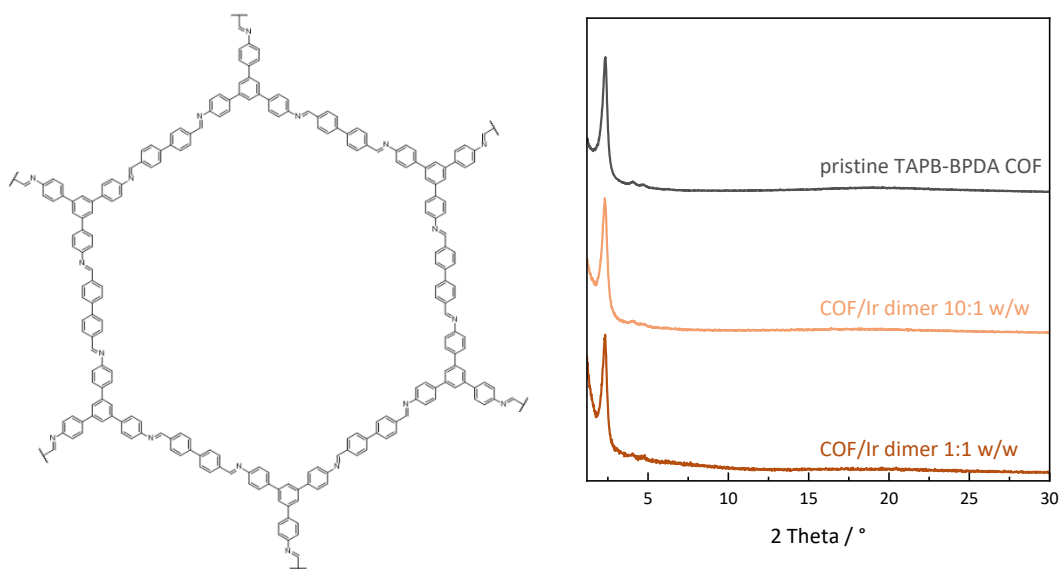
Figure S2-3: Molecular structure of TAPB-BPDA COF (left) and XRPD patterns for the attempted loading of TAPB-BPDA COF with the given amounts of [Cp*IrCl$_2$]$_2$ **1** (right). ICP analysis shows no sign of Ir in either case.
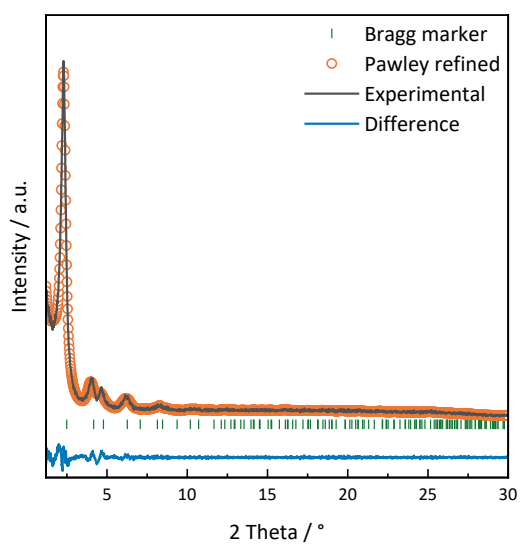
Figure S2-4: XRPD pattern and Pawley refinement for Ir@TAPB-BPY COF synthesized from Ir-loaded linker **2**.
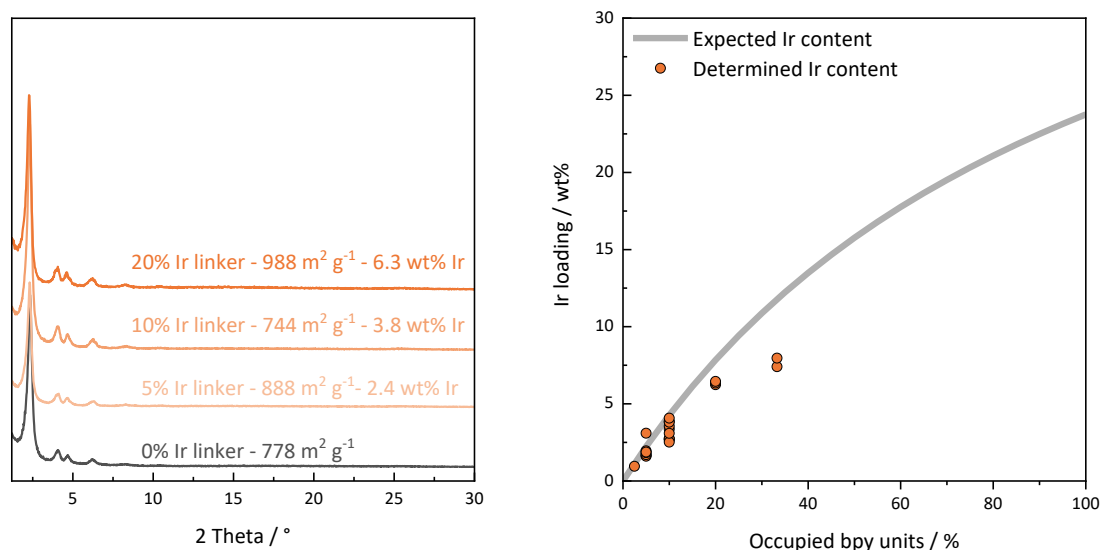
Figure S2-5: XRPD patterns for a series of TAPB-COF with varying amounts of iridium-loaded linker **2** (left). BET surface areas and Ir content (ICP-OES) given as annotations. Comparison of expected and determined iridium contents (right). Each data point represents one individual synthesis.

The expected iridium content w_{Ir} was calculated from the percentage x of employed iridium-loaded linker **2** according to:

$$w_{Ir}(x) = \frac{3 \cdot x \cdot M(Ir)}{M(COF) + 3 \cdot x \cdot \left(M(Ir) + M(Cp^*) + 2\,M(Cl)\right)} \cdot 100 \text{ wt\%}$$

Whereas M(COF) is the molecular weight of an ideal stoichiometric model of the COF containing three bipyridine units connected to two TAPB linkers *via* imine bonds.
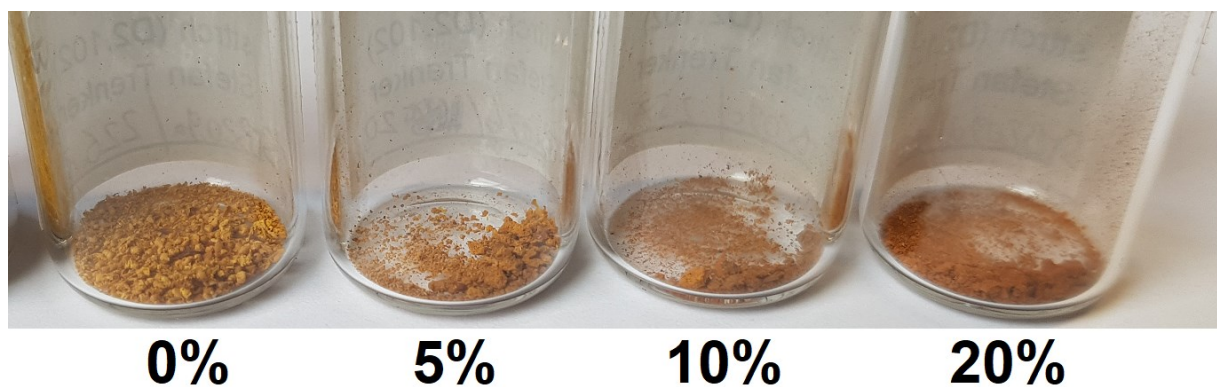
Figure S2-6: Photographic image of TAPB-BPY COF constructed from the specified amount of iridium-loaded linker **2**.
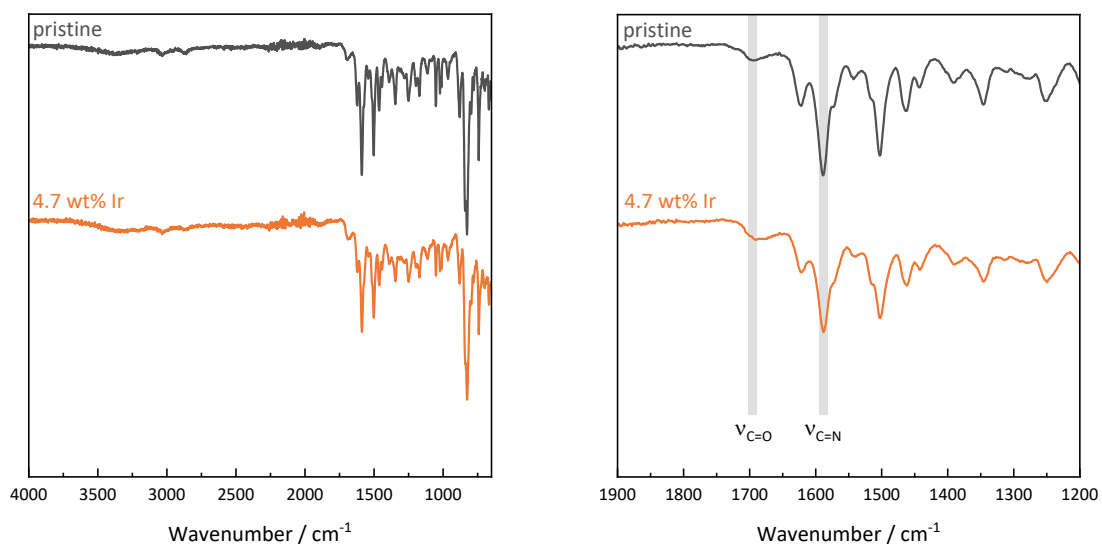
Figure S2-7: FTIR spectra of pristine and iridium-loaded TAPB-BPY COF. The stretching vibrations at 1693 cm^{-1} indicate residual aldehyde functionalities in both cases.
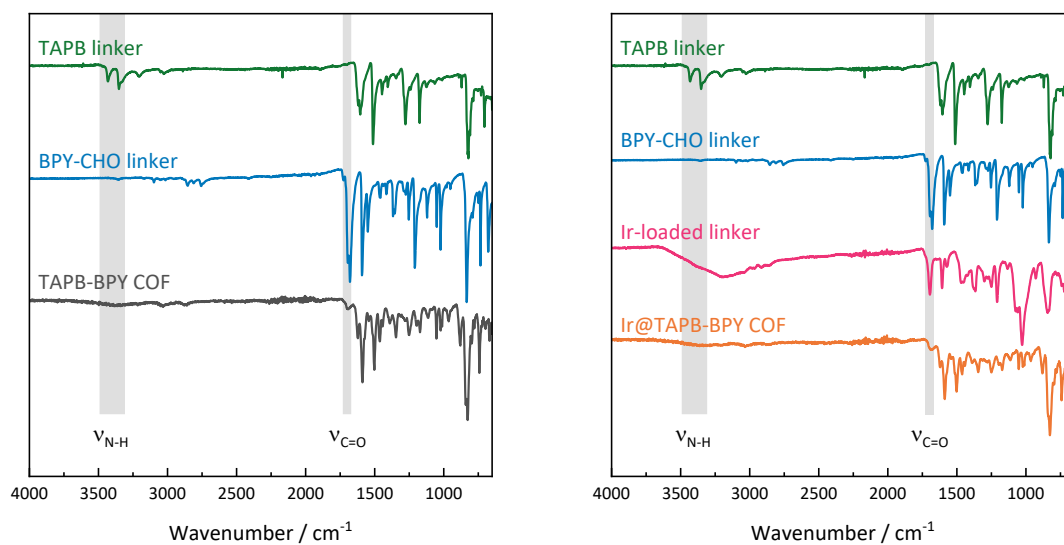
Figure S2-8: FTIR spectra of pristine TAPB-BPY COF (left) and Ir@TAPB-BPY COF (right) and their respective building blocks.
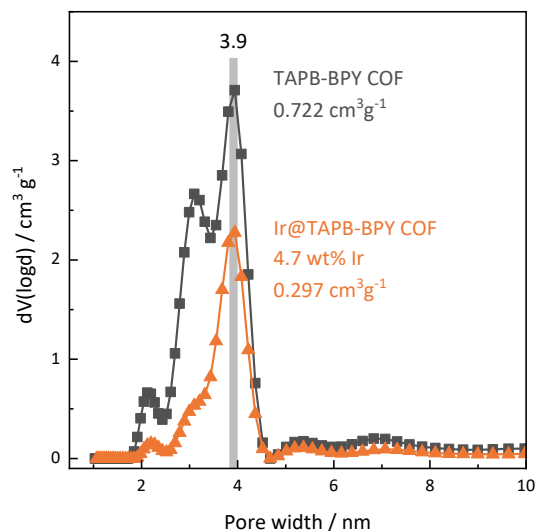
Figure S2-9: Pore size distribution and pore volumes for TAPB-BPY COF and Ir@TAPB-BPY COF constructed from iridium-loaded linker **2**. The PSD was calculated from the adsorption branch of the nitrogen sorption isotherms with a QSDFT kernel assuming cylindrical pores.
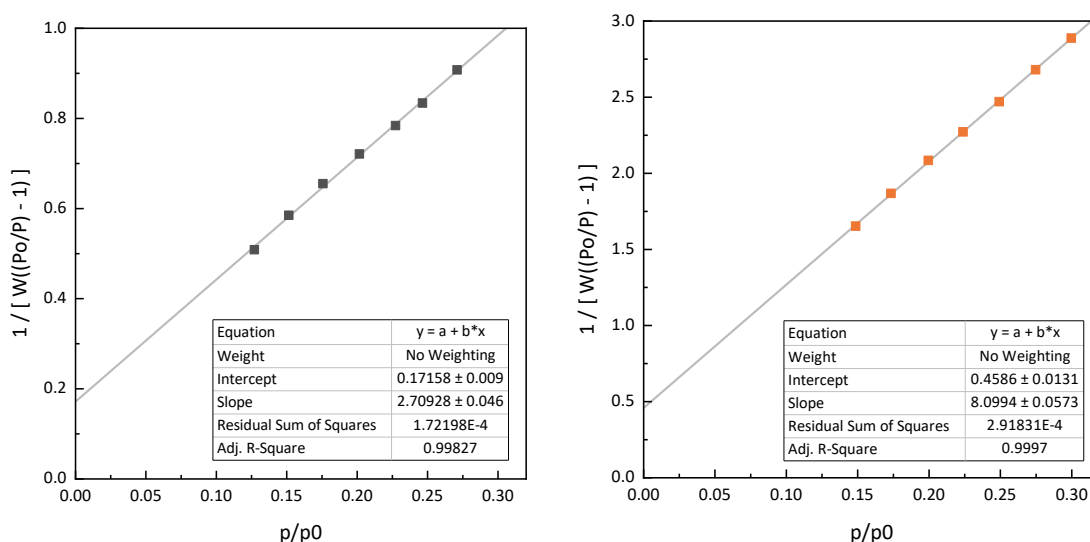
Figure S2-10: BET plots for TAPB-BPY COF (left) and Ir@TAPB-BPY COF constructed from iridium-loaded linker **2** (right).
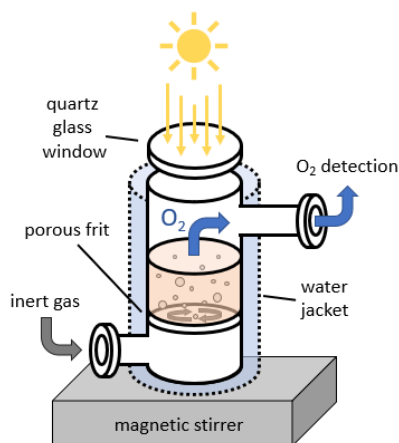
Figure S2-11: Flow reactor used for photocatalytic oxygen evolution experiments.
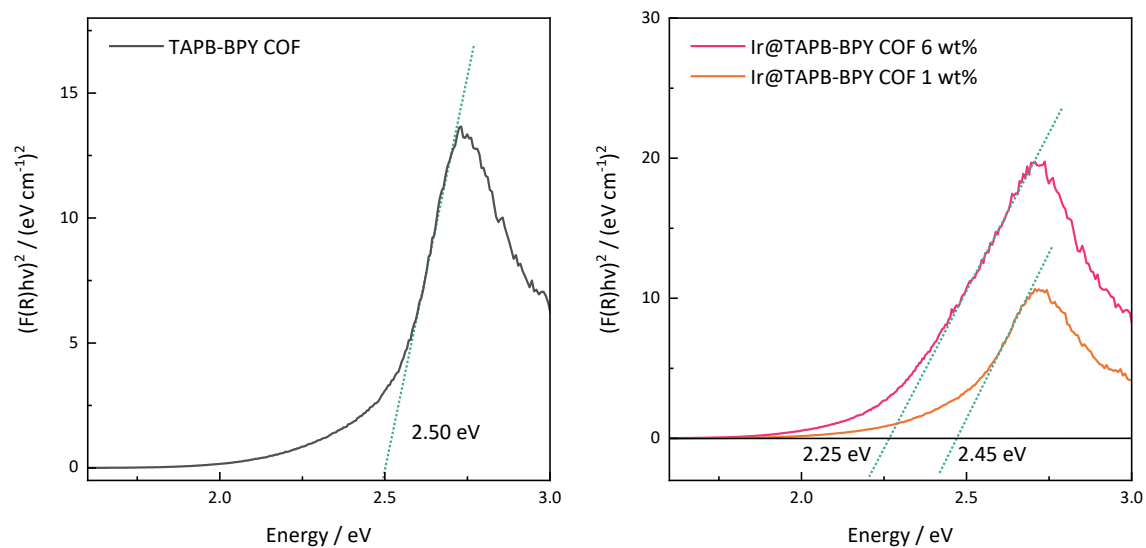
Figure S2-12: Tauc plot for TAB-BPY COF (left) and Ir@TAPB-BPY COF with varying Ir content (right). Annotations indicate the optical band gap.
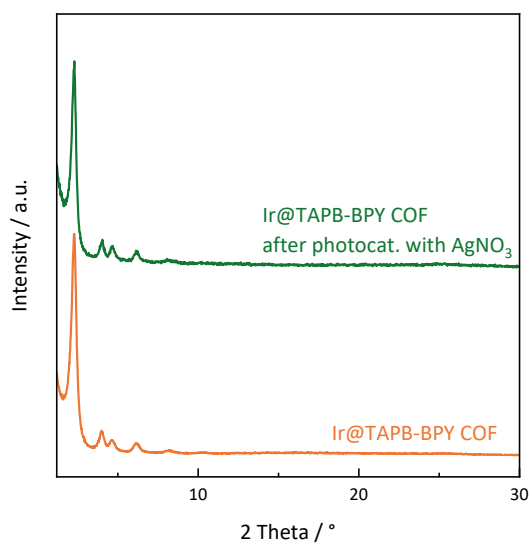
Figure S2-13: XRPD patterns for Ir@TAPB-BPY COF (1 wt% Ir) before and after photocatalysis in 10 mM AgNO$_3$ under visible light.
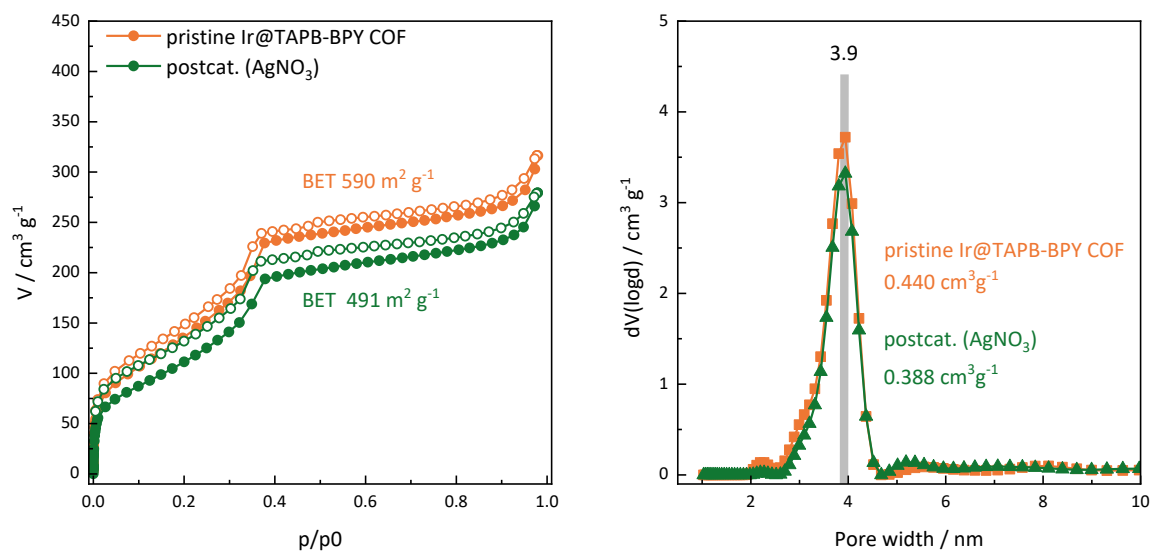
Figure S2-14: Nitrogen sorption isotherms at 77 K (left) and pore size distribution (right) for Ir@TAPB-BPY COF (1 wt% Ir) before and after photocatalytic oxygen evolution experiments with 10 mM AgNO$_3$. Filled and open symbols represent the adsorption and the desorption branches, respectively. The pore size distribution was obtained from a QSDFT kernel for cylindrical pores (adsorption branch).
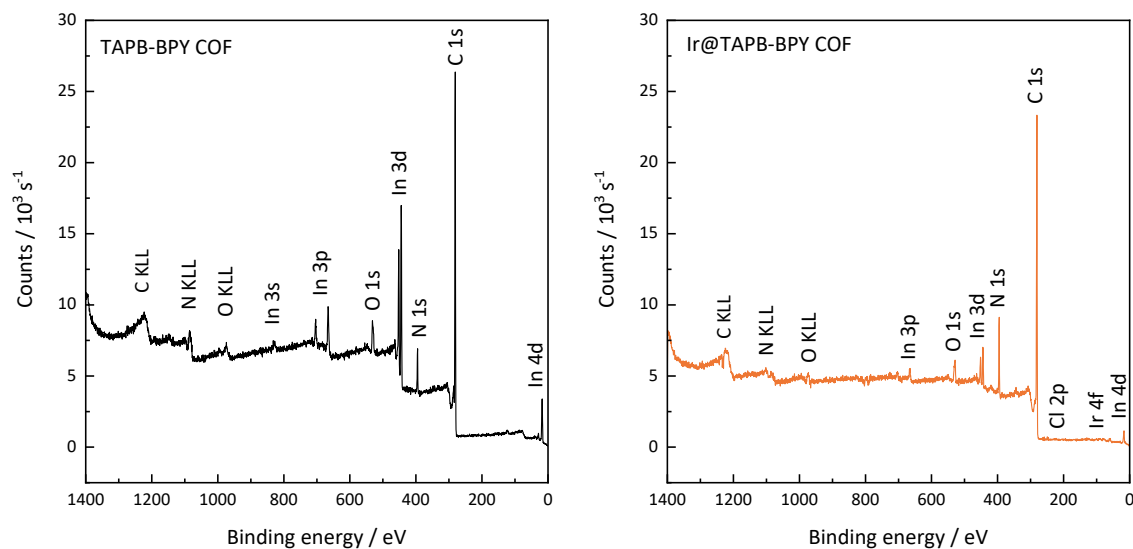
Figure S2-15: Survey X-ray photoelectron spectra of TAPB-BPY COF (left) and Ir@TAPB-BPY COF (right).
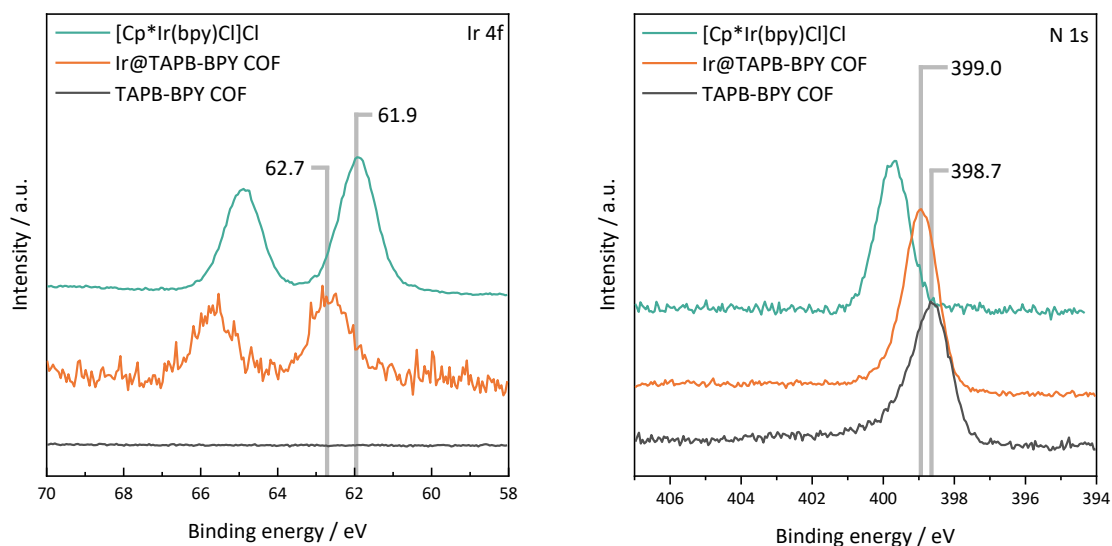
Figure S2-16: Ir 4f (left) and N 1s (right) XPS signals for Ir@TAPB-BPY COF, TAPB-BPY COF, and molecular Cp*Ir(bpy)Cl.
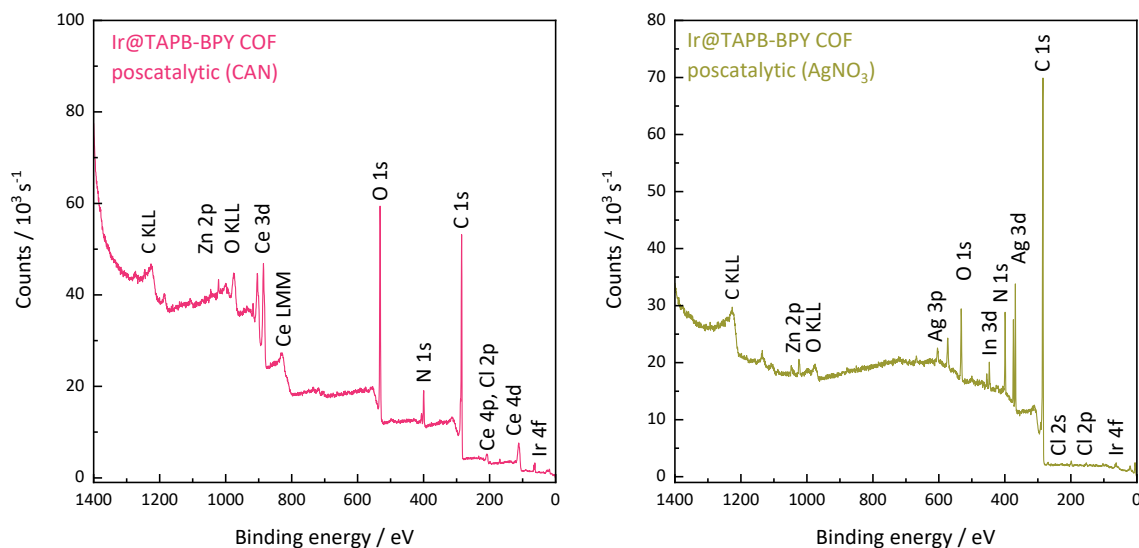
Figure S2-17: Survey X-ray photoelectron spectra of Ir@TAPB-BPY COF after oxygen evolution experiments with CAN (78 mM, left) and. AgNO$_3$ (10 mM, right)
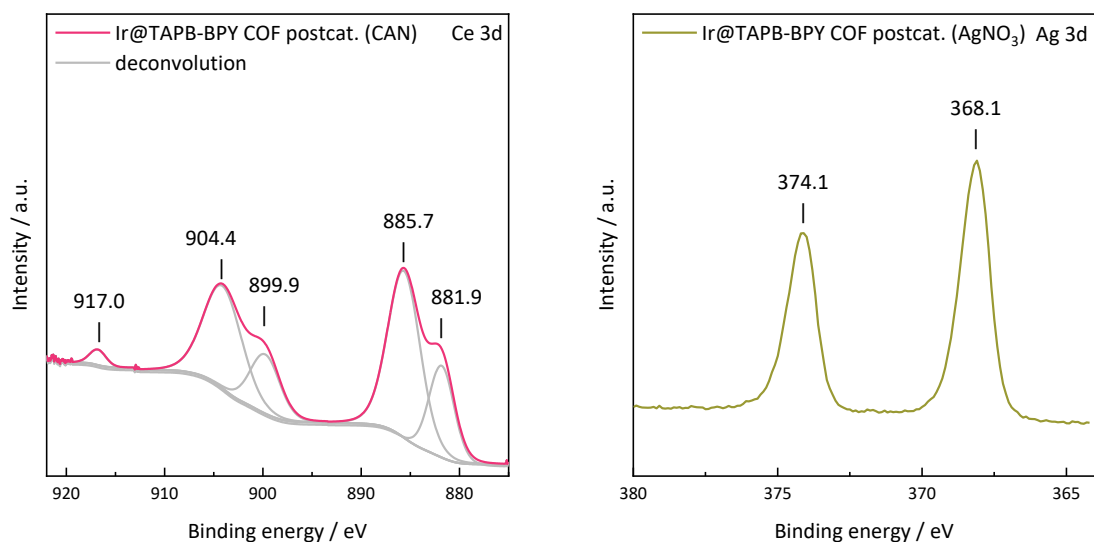
Figure S2-18: Selected XPS spectra for Ir@TAPB-BPY COF after oxygen evolution experiments with CAN (78 mM, left) and AgNO$_3$ (10 mM, right) and. The peak at 917.0 eV (Ce 3d) is ascribed to small amounts of Ce(IV), whereas the other peaks indicate the presence of Ce(III).[31–33] Since silver species are hardly distinguishable *via* XPS, so we refrain from an assignment here.[34]
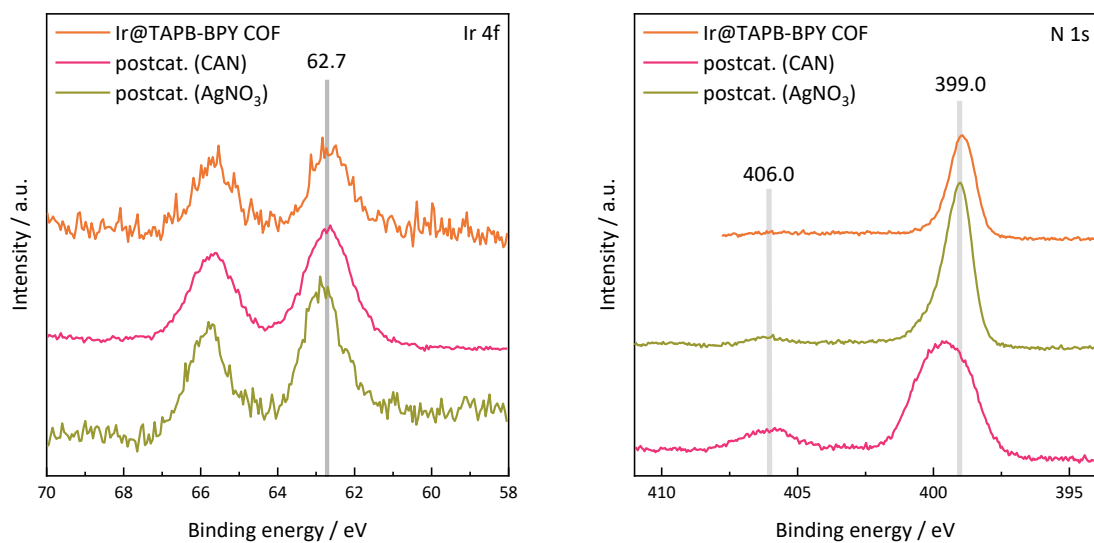
Figure S2-19: XPS spectra for Ir@TAPB-BPY COF after oxygen evolution experiments with AgNO$_3$ (10 mM) and CAN (78 mM) compared to pristine Ir@TAPB-BPY COF in the Ir 4f (left) and N 1s (right) ranges. The new signal at 406 eV and the broadening of the peak around 399 eV for the CAN-sample are ascribed to residual nitrate (counter-)ions and protonation and/or oxidation of imines, respectively.[35–38]
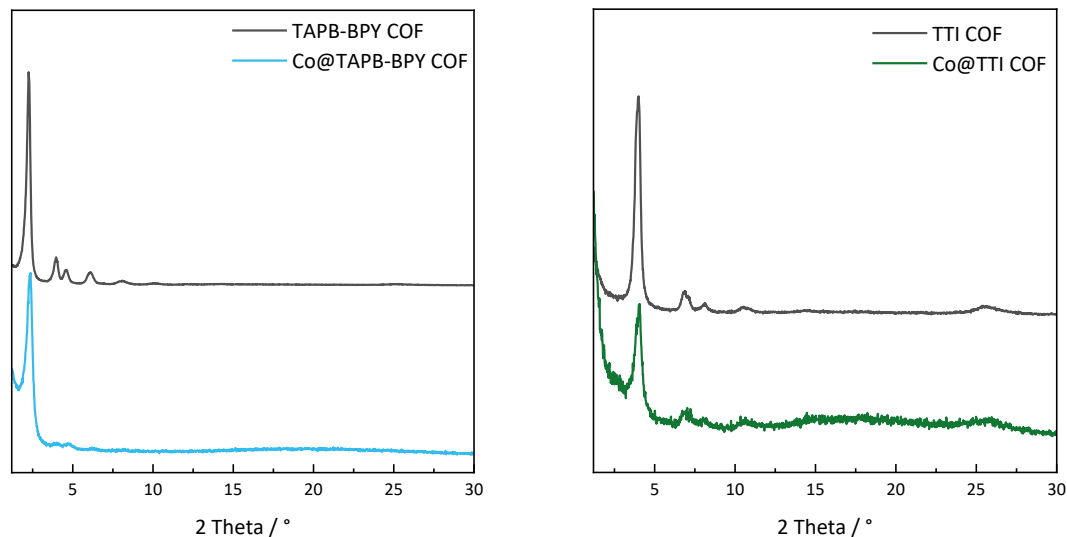
Figure S2-20: XRPD patterns for reproduced COFs Co@TAPB-BPY COF (left) and Co@TTI-COF (right) with the respective unmetalled COF.
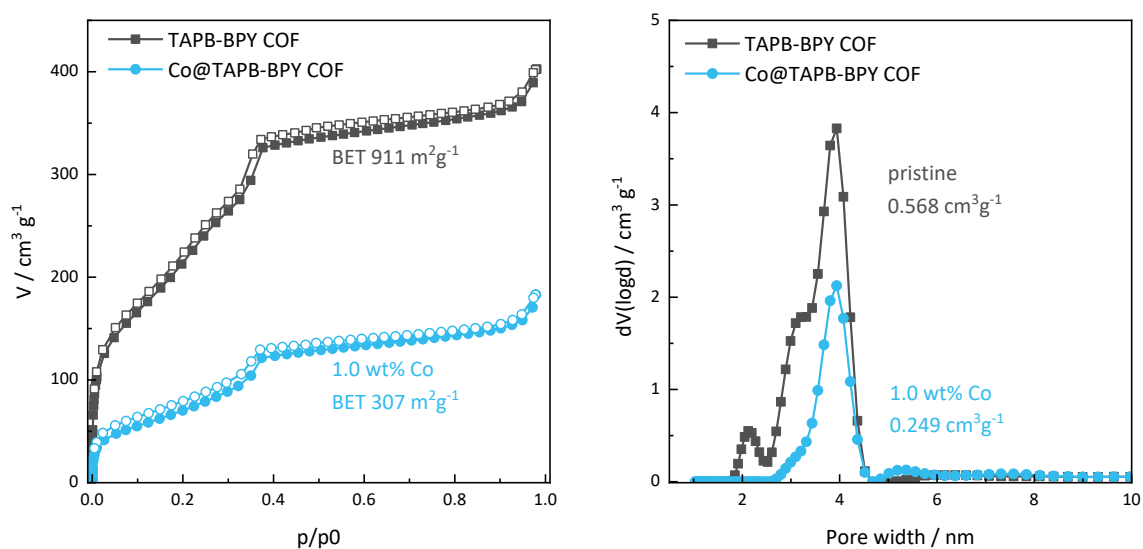
Figure S2-21: Nitrogen sorption isotherms at 77 K (left) and pore size distribution (right) for TAPB-BPY COF before and after postsynthetic loading with Co(NO$_3$)$_2$. Filled and open symbols represent the adsorption and the desorption branches, respectively. The pore size distribution was obtained from a QSDFT kernel for cylindrical pores (adsorption branch). The cobalt content was determined via ICP-OES.
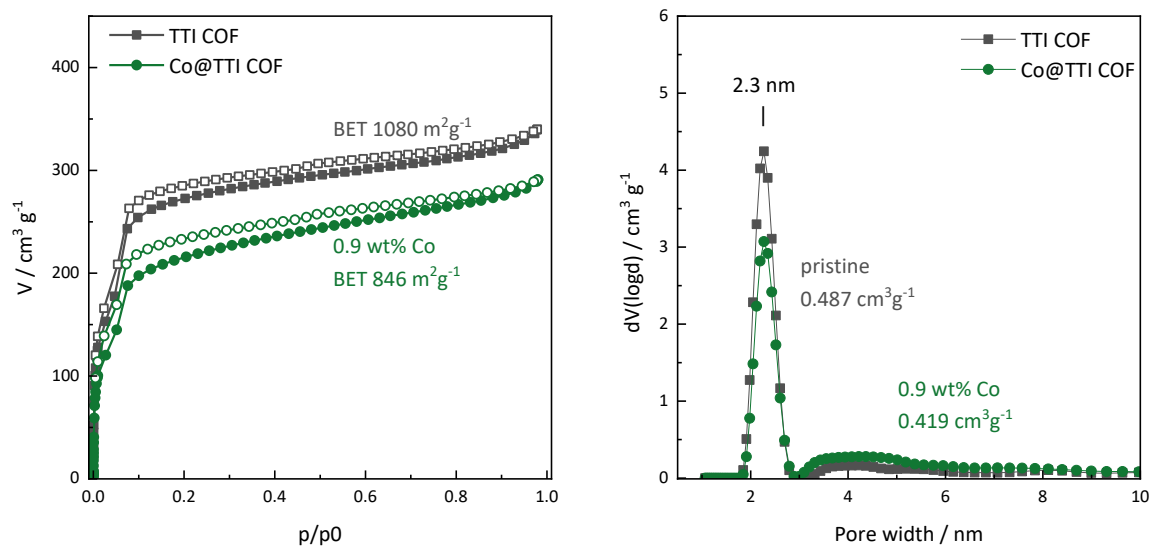
Figure S2-22: Nitrogen sorption isotherms at 77 K (left) and pore size distribution (right) for TTI-COF before and after postsynthetic loading with Co(NO$_3$)$_2$. Filled and open symbols represent the adsorption and the desorption branches, respectively. The pore size distribution was obtained from a QSDFT kernel for cylindrical pores (adsorption branch). The cobalt content was determined via ICP-OES.
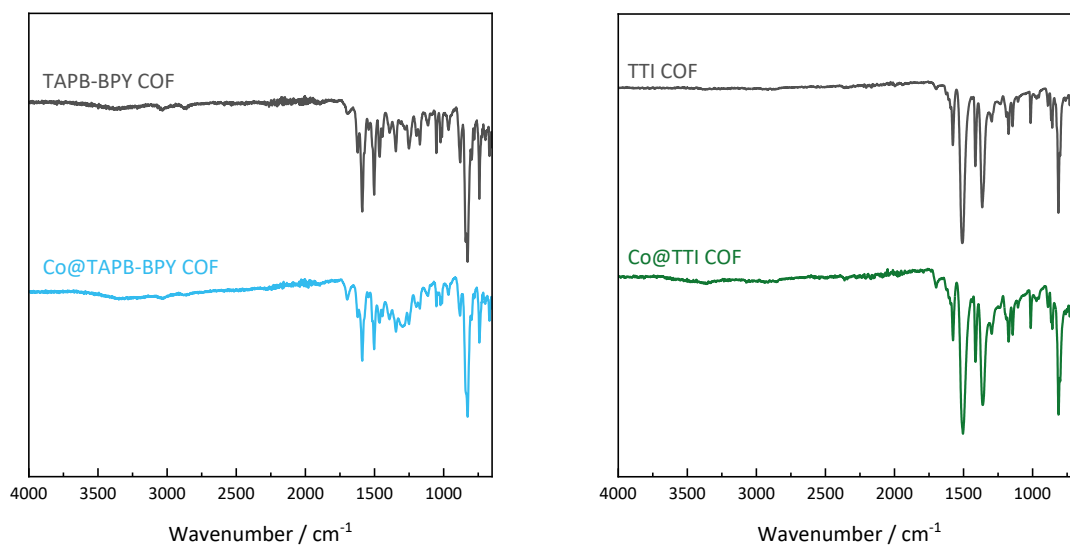
Figure S2-23: FTIR spectra of pristine and cobalt-loaded TAPB-BPY COF (left) and TTI-COF (right).
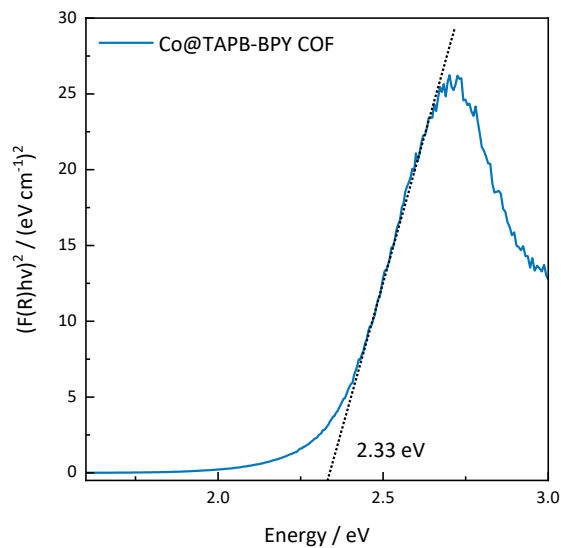
Figure S2-24: Tauc plot for Co@TAPB-BPY COF with 1.038 wt% Co content. The Annotation indicates the optical band gap.
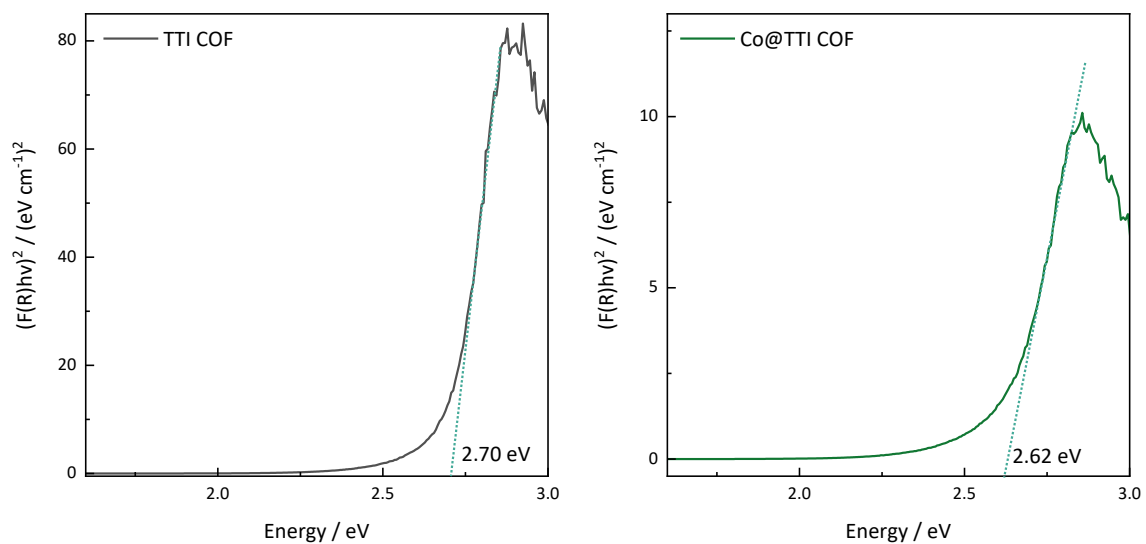
Figure S2-25: Tauc plot for TTI-COF (left) and Co@TTI-COF with 0.867 wt% Co content (right). Annotations indicate the optical band gap.
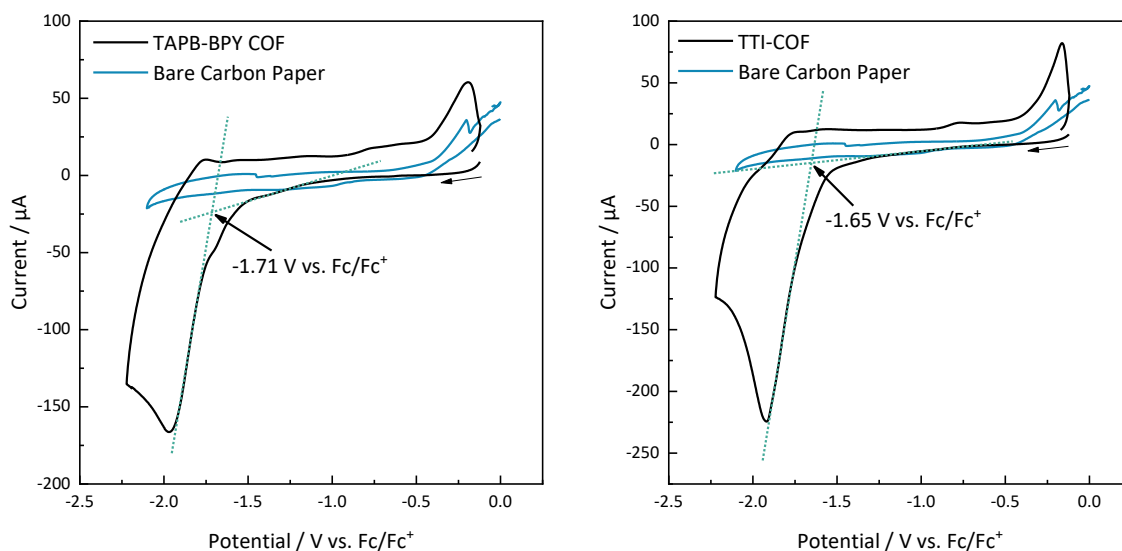
Figure S2-26: Cyclic voltammograms for TAPB-BPY COF, and TTI-COF. COFs measured after deposition on carbon paper working electrodes.
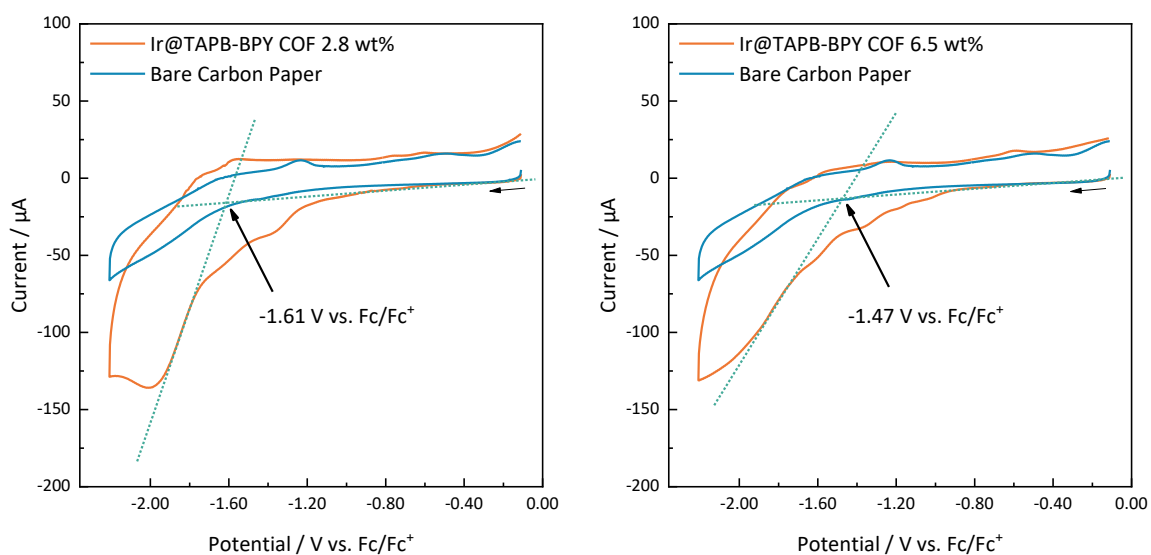
Figure S2-27: Cyclic voltammograms for Ir@TAPB-BPY COF samples of varying iridium contents. COFs measured after deposition on carbon paper working electrodes.
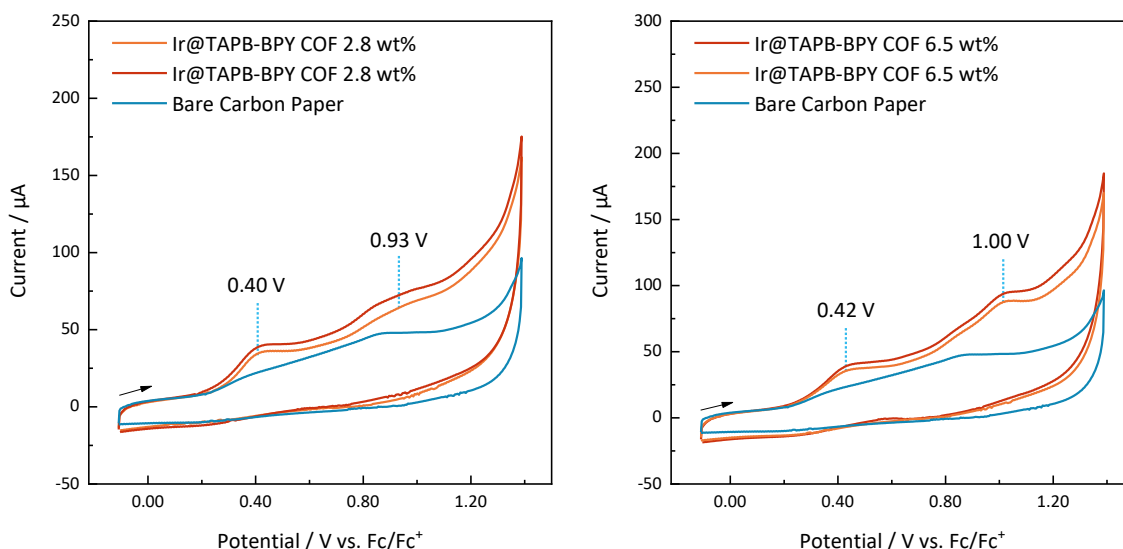
Figure S2-28: Cyclic voltammograms for Ir@TAPB-BPY COF samples of varying iridium contents. COFs measured after deposition on carbon paper working electrodes. Two separate Ir@TAPB-BPY COF electrodes are shown. Annotations mark yet unidentified processes.
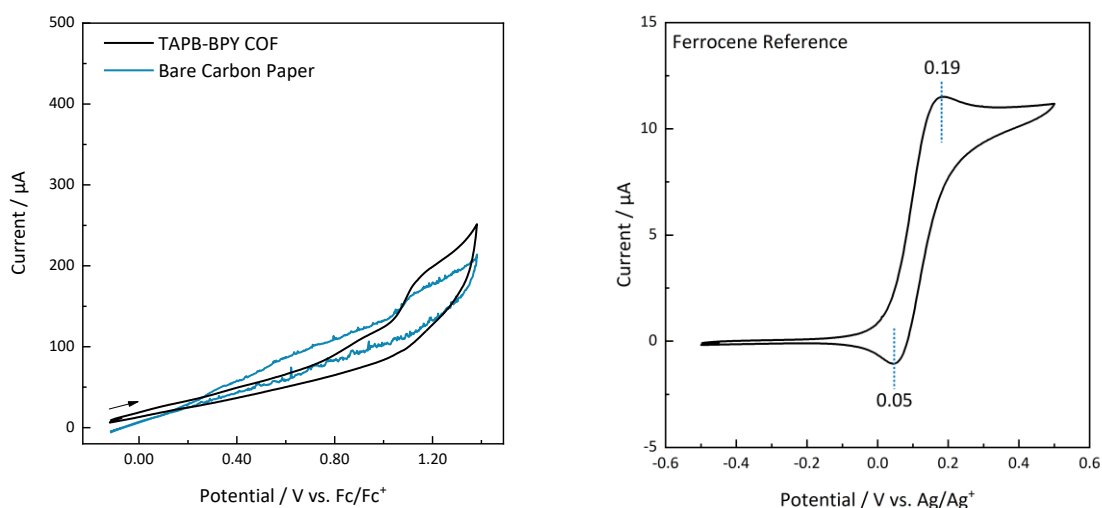
Figure S2-29: Cyclic voltammograms for TAPB-BPY COF (left) and the ferrocene reference (right).

Table S2-1: Comparison of band positions and related data for TAPB-BPY COF, TTI-COF, and respective literature examples.

COF	$E_{red, onset}$	E_{CB}	Opt. band gap	E_{VB}	Source
TAPB-BPY COF	-1.59 V vs. Ag/Ag$^+$ -1.71 V vs. Fc/Fc$^+$	-3.39 eV	2.50 eV	-5.89 eV	This work
TAPB-BPY COF ("Bp-COF")	-1.27 V vs. Ag/Ag$^+$ -1.34 V vs. Fc/Fc$^+$	-3.76 eV	2.41 eV	-6.17 eV	Ref. [27] [a]
TTI-COF	-1.65 V vs. Fc/Fc$^+$	-3.45 eV	2.70 eV	-6.15 eV	This work
TTI-COF ("I-TST")	-	-3.43 eV	2.93 eV	-6.27 eV	Ref. [39] [b]
Ir@TAPB-BPY COF (2.8 wt% Ir)	-1.50 V vs. Ag/Ag$^+$ -1.61 V vs. Fc/Fc$^+$	-3.49 eV	2.40 eV	-5.89 eV	This work
Ir@TAPB-BPY COF (6.5 wt% Ir)	-1.36 V vs. Ag/Ag$^+$ -1.47 V vs. Fc/Fc$^+$	-3.63 eV	2.25 eV	-5.89 eV	This work

Conversion of potentials done according to E(V vs. vac) = -(E(V vs. Fc/Fc+) + 5.1) eV   [a]: $E_{1/2}$(Fc/Fc$^+$) = 0.07 vs. Ag/Ag$^+$ extracted from reference measurement in the supporting information. [b]: Band positions not experimentally determined, but calculated.

Table S2-2: Ionisation potential (IP) and electron affinity (EA) values predicted for cluster models of the TAPB-BPY COF and TTI-COF in water and acetonitrile. All values are given in V vs. SHE.

	In acetonitrile		In water	
	IP	EA	IP	EA
TAPB-BPY COF	1.16	-1.57	1.13	-1.54
TTI-COF	1.37	-1.53	1.34	-1.50

Representative COF clusters used for the prediction are depicted in Figure S2-30.
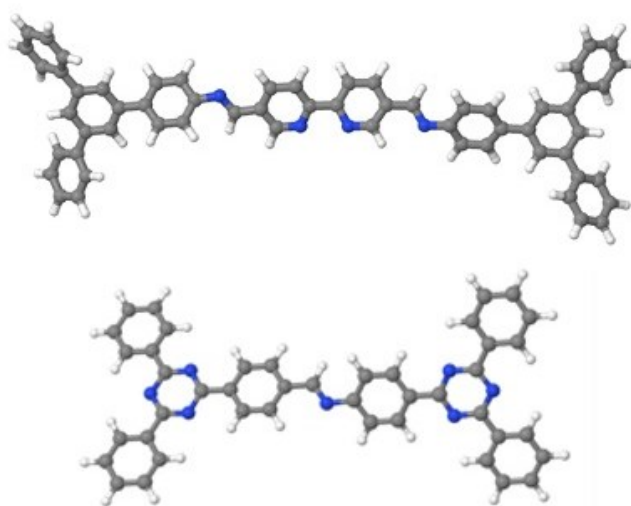
Figure S2-30: Cluster models used to calculate IP and EA of TAPB-BPY COF (top) and TTI-COF (bottom).
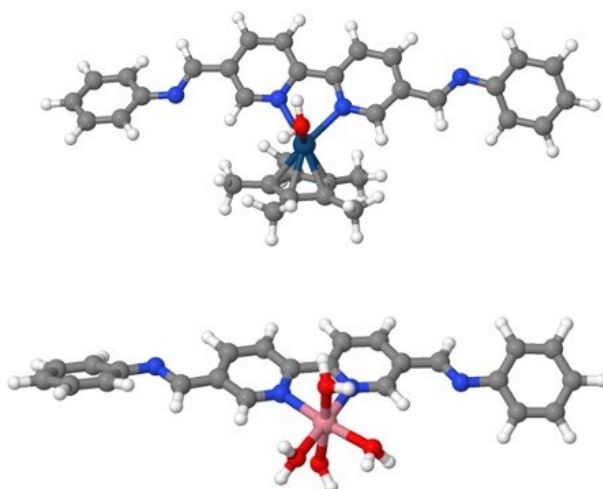
Figure S2-31: Cluster model of the Ir@TAPB-BPY COF (top) and Co@TAPB-BPY COF (bottom) used when calculating the free energy landscape of the water oxidation mechanism.

ΔG^0 at pH 0

(1)	(2)	(3)	(4)
1.57 eV	1.71 eV	1.01 eV	0.44 eV

$Ir(III)\text{-}H_2O$ $\xrightarrow{}$ $Ir(III)\text{-}OH^{\bullet}$ $\xrightarrow{}$ $Ir(III)\text{-}O(H)OH$ $\xrightarrow{}$ $Ir(III)\text{-}OOH$ $\xrightarrow{}$ $Ir(III)\text{-}H_2O$

- e⁻   - e⁻   - e⁻   - e⁻
- H⁺   - H⁺   - H⁺   - H⁺
          + H₂O   - O₂

- e⁻ | 0.84 eV   1.06 eV | + H₂O
- H⁺
        $Ir(III)\text{-}O$

Figure S2-32: Schematic reaction pathway for water oxidation on Ir@TAPB-BPY COF assuming redox-innocent Ir(III) centers according to the GCC principle. Changes in free energy given in eV at pH 0. Apart from PCET steps, the Ir(III)-O species (blue) is given for better comparison with Ir(V)=O species which are an important intermediate in the WNA mechanism of molecular Ir WOCs.

Figure S2-33: Free energy diagram for the oxidation of water for Ir@TAPB-BPY COF for different pH and applied potential values.

Figure S2-34: Free energy diagram for the oxidation of water for Co@TAPB-BPY COF for different pH and applied potential values.

Figure S2-35: Minimum energy structures for the Ir@TAPB-BPY COF cluster model with an OH group (top, left), an O atom (top, right), adsorbed H_2O_2 (bottom, left) and an OOH group (bottom, right).
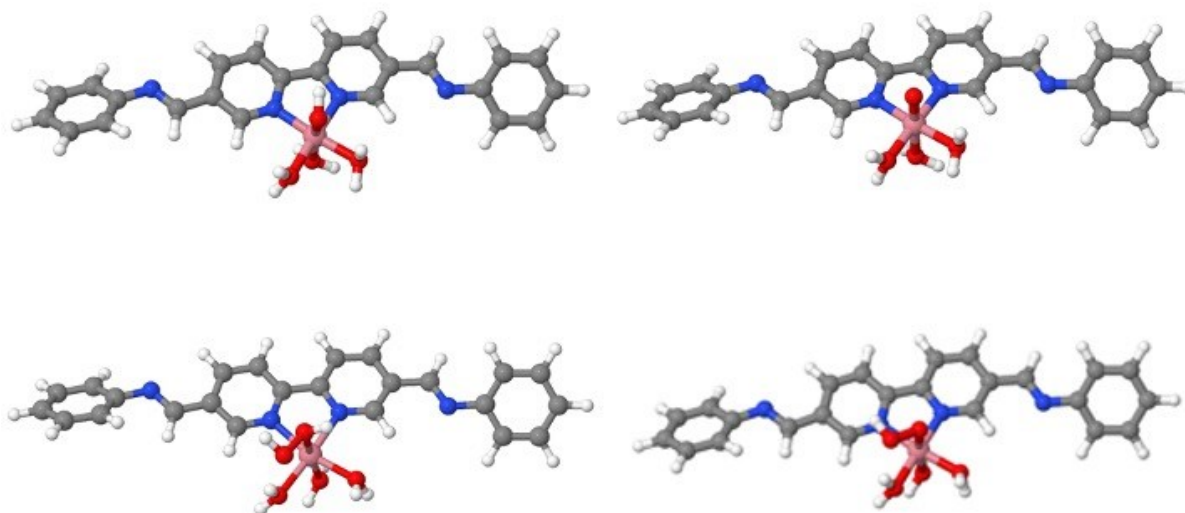
Figure S2-36: Minimum energy structures for the Co@TAPB-BPY COF cluster model with an OH group (top, left), an O atom (top, right), adsorbed H_2O_2 (bottom, left) and an OOH group (bottom, right).
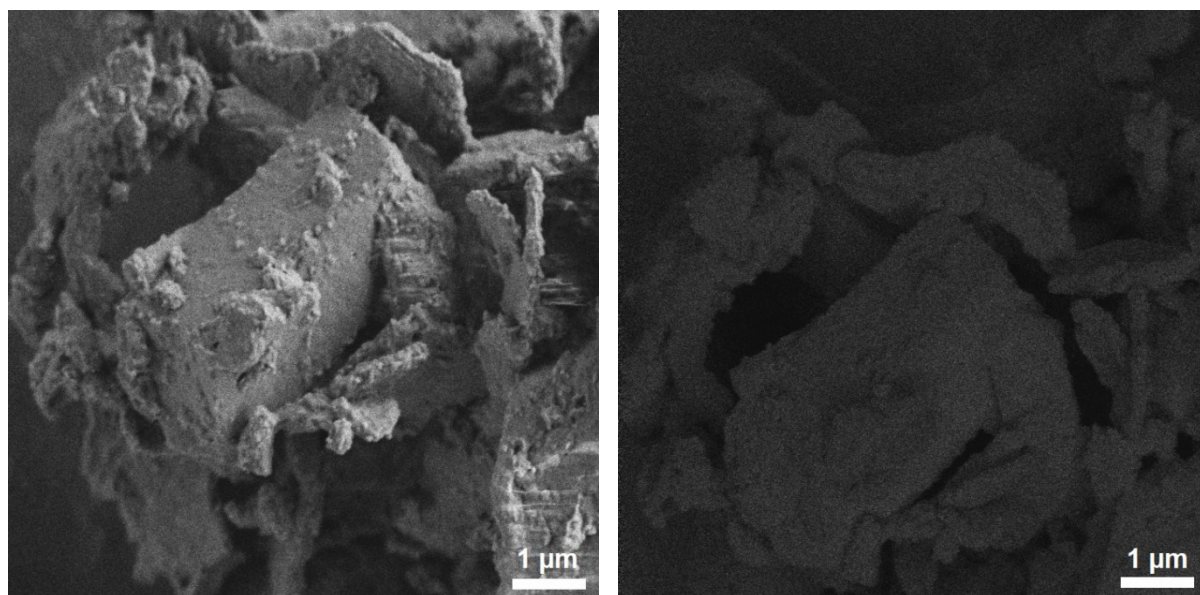
Figure S2-37: SEM images of TAPB-BPY COF with secondary electron detection (left) and energy selective backscattered electron detection (right).
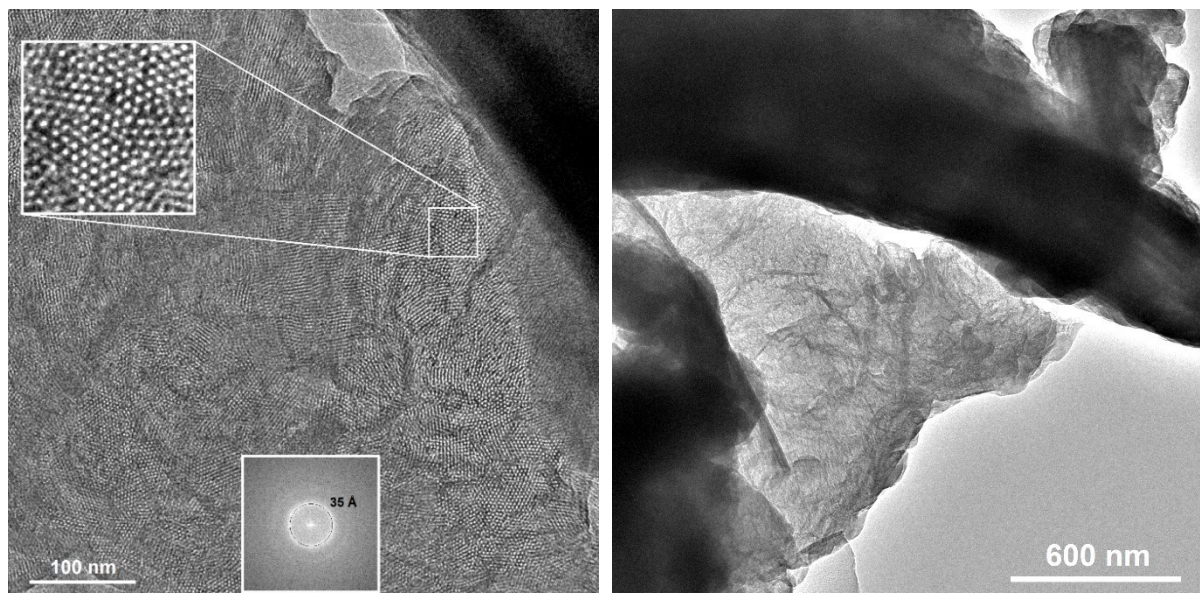
Figure S2-38: TEM images of TAPB-BPY COF. Magnified area highlights hexagonal arrangement of the pore. Inset shows FFT.
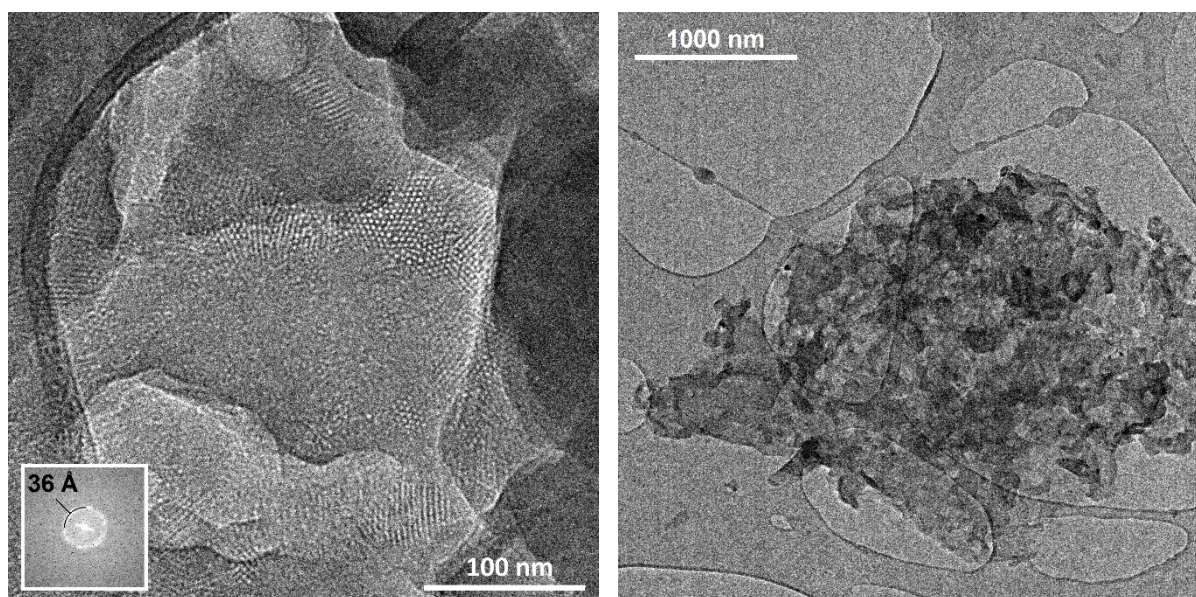
Figure S2-39: TEM images of Ir@TAPB-BPY COF constructed from iridium-loaded linker **2**. Inset shows FFT.
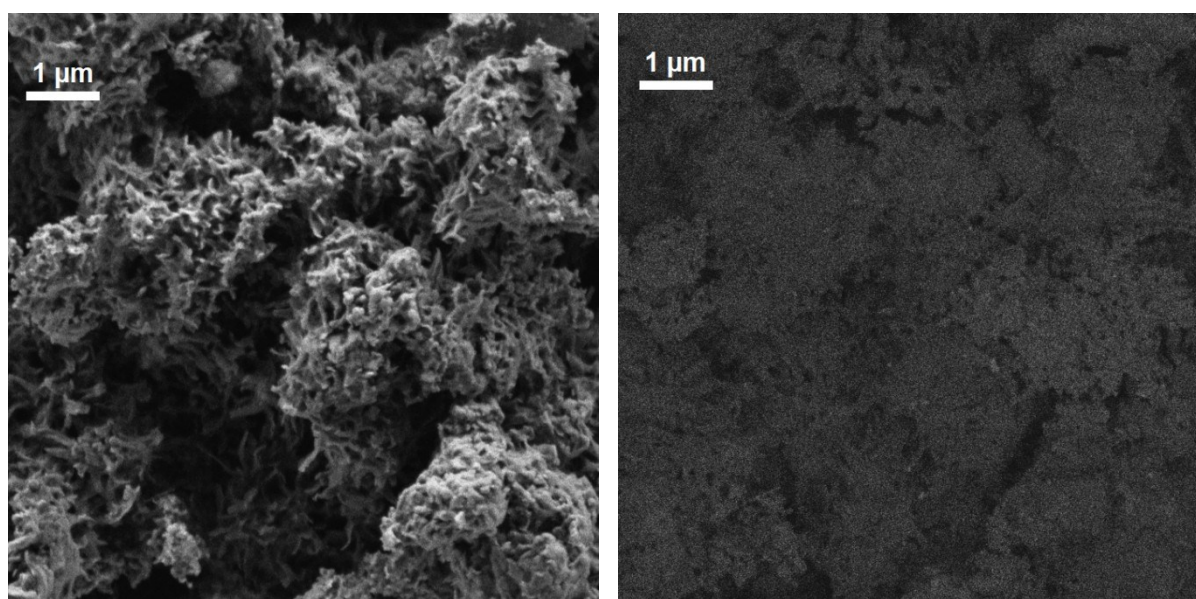
Figure S2-40: SEM images of Ir@TAPB-BPY COF constructed from iridium-loaded linker **2** with secondary electron detection (left) and energy selective backscattered electron detection (right).

Electron Image 12
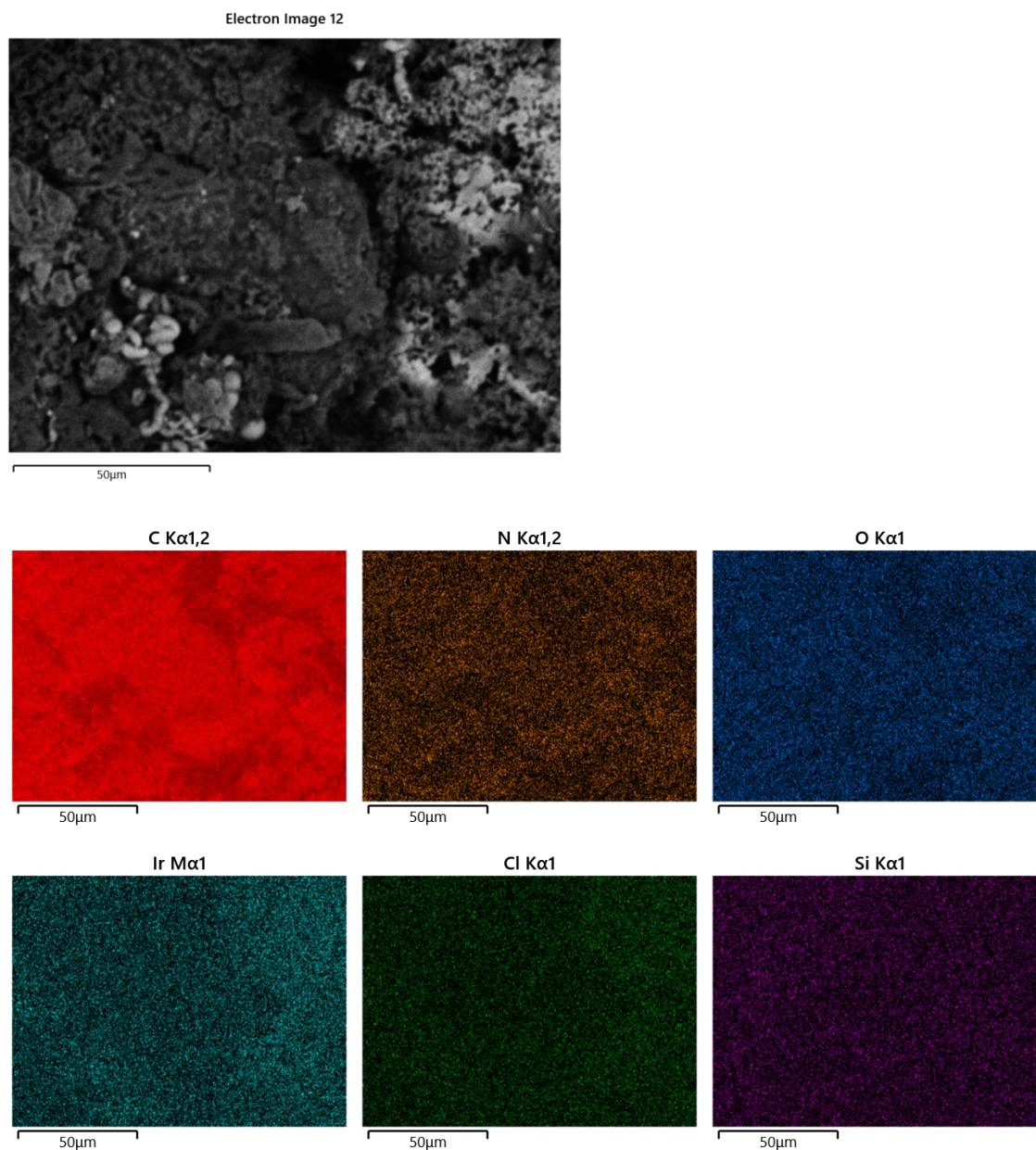
Figure S2-41: SEM elemental mapping of Ir@TAPB-BPY COF constructed from iridium-loaded linker **2**.
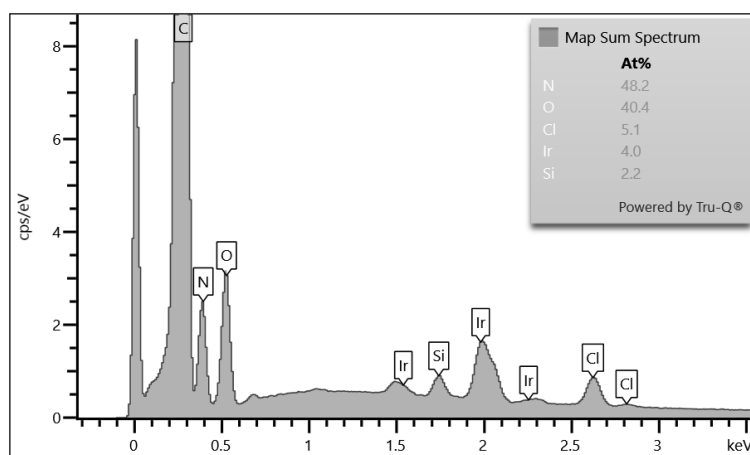
Figure S2-42: Summed-up EDX spectra for the elemental mapping of Ir@TAPB-BPY COF.
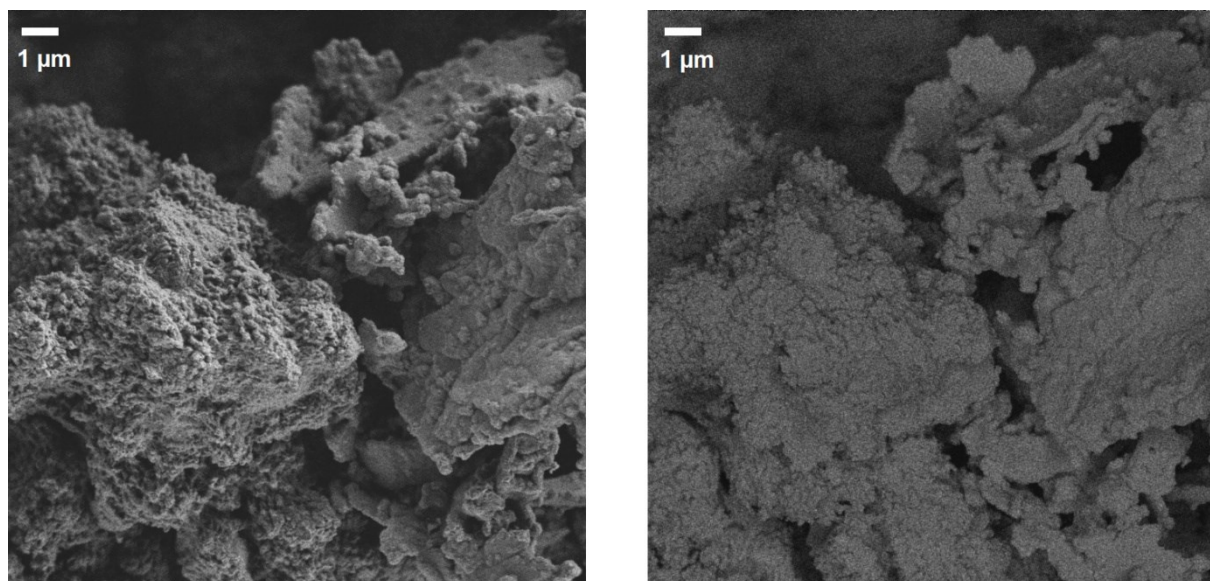
Figure S2-43: SEM imaging of TAPB-COF after postsynthetic loading with [Cp*IrCl]$_2$ with secondary electron detection (left) and energy selective backscattered electron detection (right).
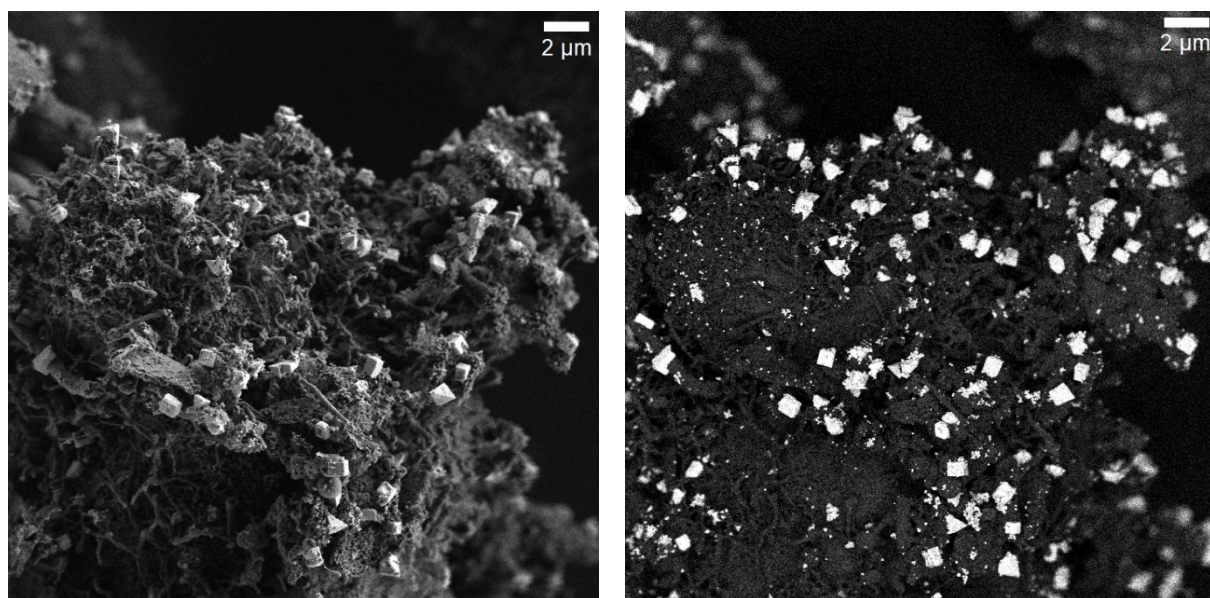
Figure S2-44: SEM images of Ir@TAPB-BPY COF after photocatalysis experiments with AgNO$_3$ with secondary electron detection (left) and energy selective backscattered electron detection (right).
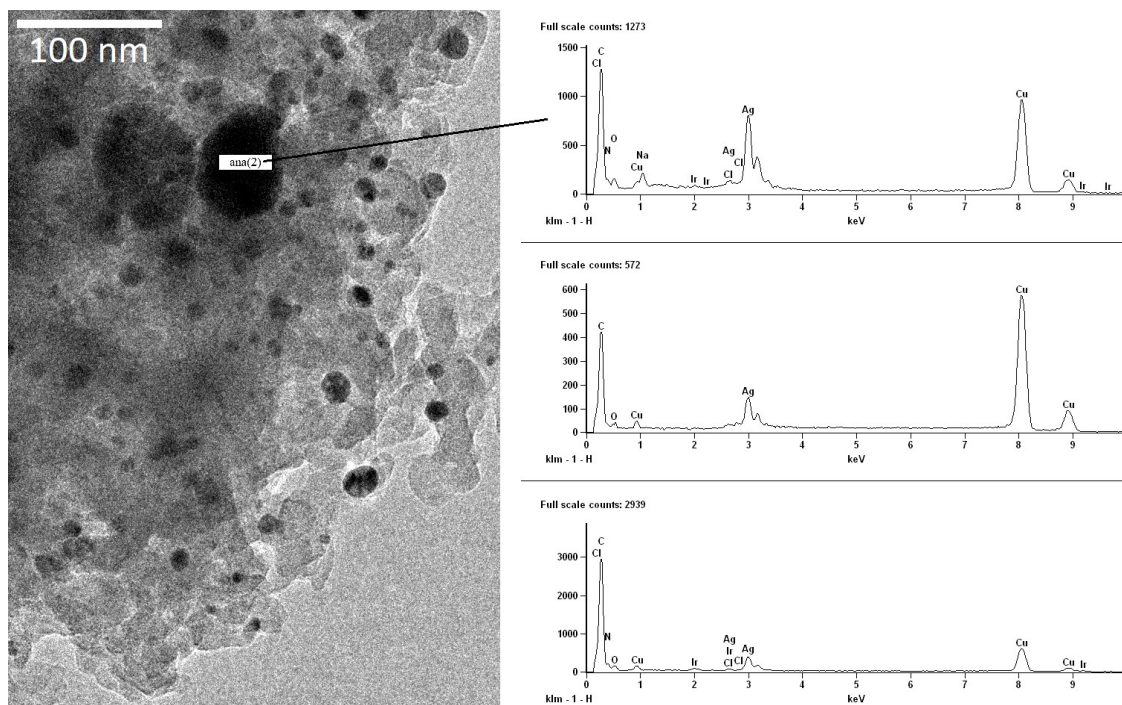
Figure S2-45: Overview TEM image of Ir@TAPB-BPY COF after photocatalysis experiments with AgNO$_3$ (left). EDX spectra (right) show the elemental composition at different positions on the COF, one of which is also present on the left image (top EDX spectrum).
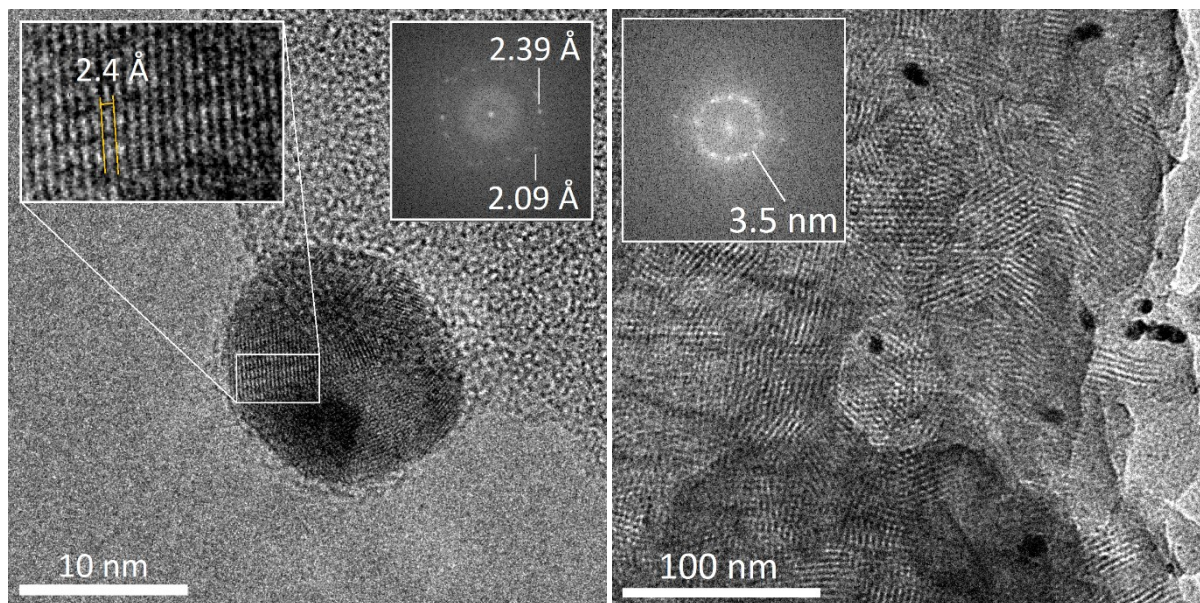
Figure S2-46: TEM images of Ir@TAPB-BPY COF after photocatalysis experiments with AgNO$_3$ showing the presence of crystalline nanoparticles (left) and the retained porosity of the COF (right). Insets show FFT or zoomed-in parts of the respective images.

Electron Image 8

C Kα1,2   N Kα1,2   O Kα1

Ag Lα1   Cl Kα1   Ir Mα1
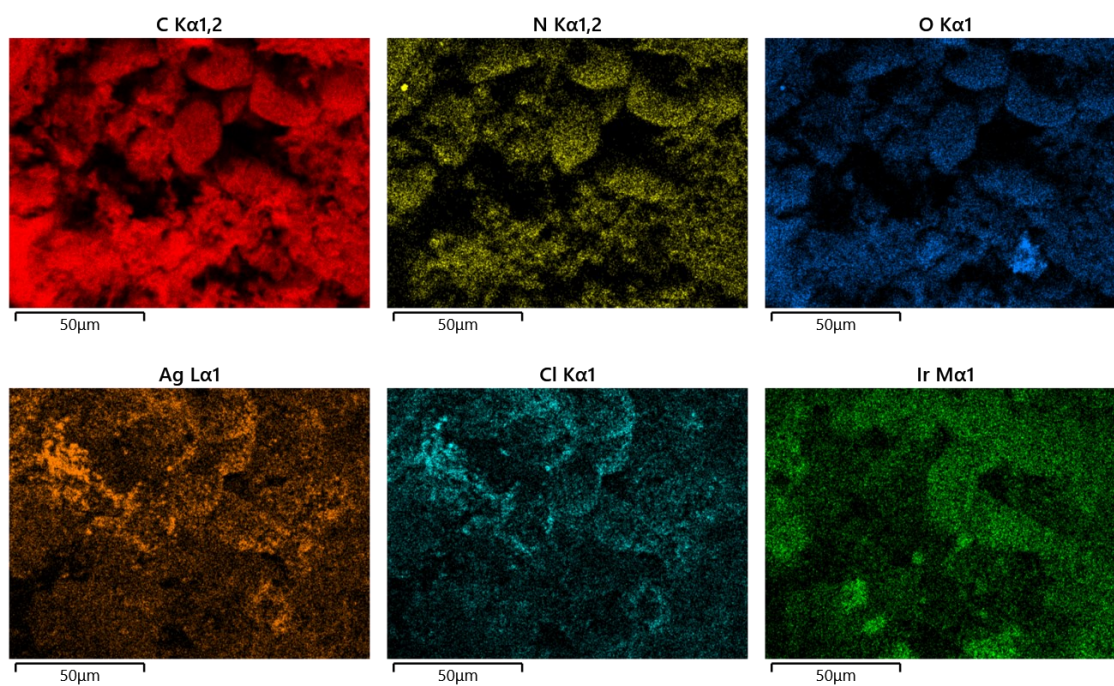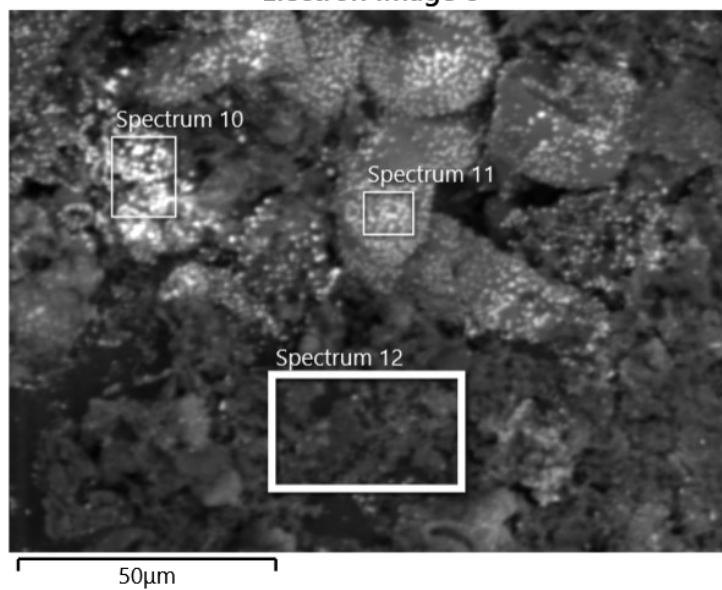
Figure S2-47: SEM elemental mapping of Ir@TAPB-BPY COF after photocatalysis experiments with AgNO$_3$.

Table S2-3: EDX analysis for Ir@TAPB-BPY COF after photocatalytic water oxidation experiments with AgNO$_3$. Values given in at%. EDX spectra measured at the positions specified in Figure S2-47.

Element	Spectrum 10	Spectrum 11	Spectrum 12
N	47.94	52.35	43.29
O	20.35	31.45	41.70
Ir	0.40	1.91	1.09
Cl	8.66	4.12	3.08
S	-	-	1.07
Ag	21.81	10.16	8.08
Na	-	-	1.07
Si	0.84	-	0.61
Total	100	100	100
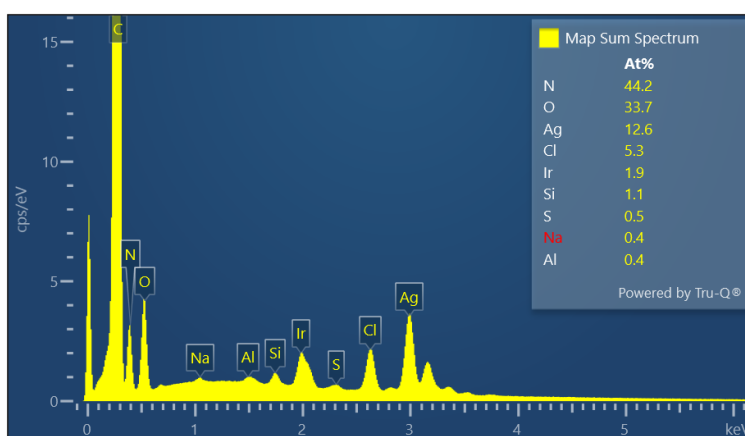
Figure S2-48: Summed-up EDX spectra for the elemental mapping of Ir@TAPB-BPY COF after photocatalysis experiments with AgNO$_3$.

Table S2-4: EDX analysis for Ir@TAPB-BPY COF before and after (photo-)catalytic water oxidation experiments with varying SEAs (map sum spectra). Values given in at%.

Element	pristine	Na$_2$S$_2$O$_8$[a]	AgNO$_3$[b]
N	47.88	36.54	44.21
O	39.53	50.31	33.66
Ir	4.05	3.47	1.93
Cl	6.25	2.26	5.32
Ce	-	-	-
S	0.41	3.70	0.51
Ag	-	-	12.55
Na	0.30	0.31	0.38
Al	0.55	0.47	0.37
Si	1.02	2.94	1.06
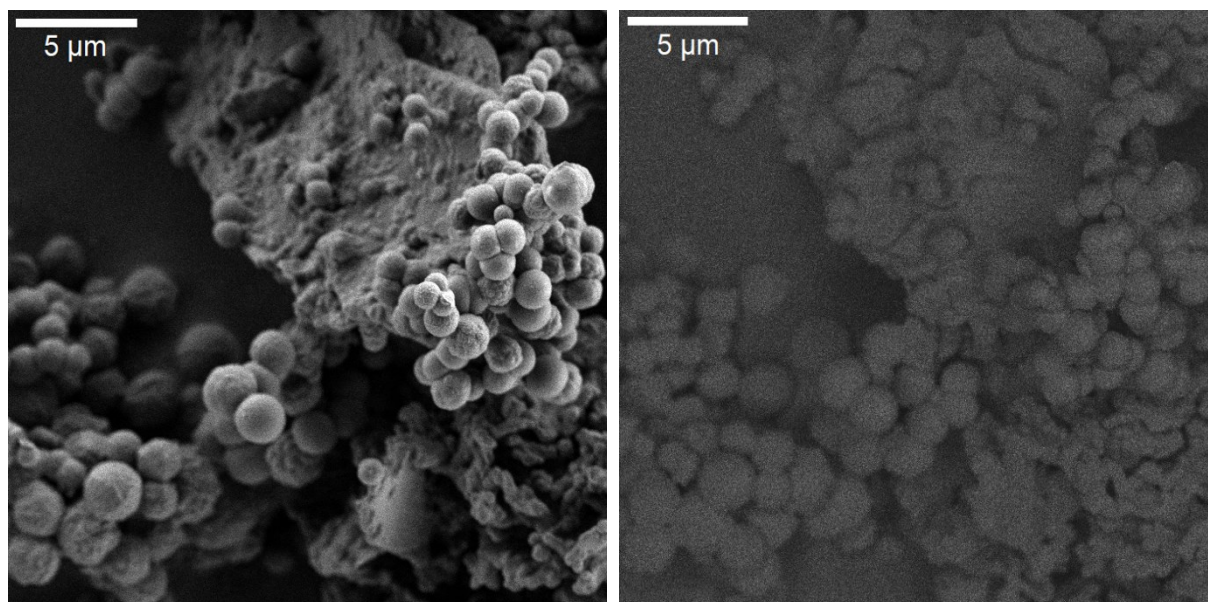
Figure S2-49: SEM images of Co@TAPB-BPY COF (1 wt% Co) with secondary electron detection (left) and energy selective backscattered electron detection for material contrast illustration (right).
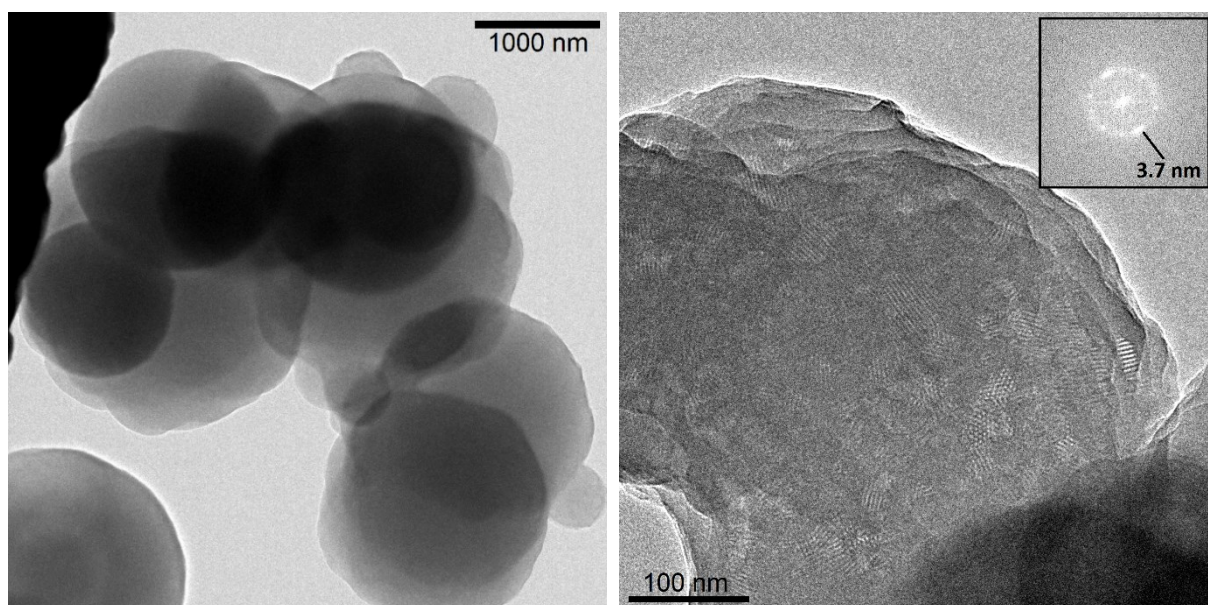
Figure S2-50: TEM images of Co@TAPB-BPY COF (1 wt%). Inset shows FFT.
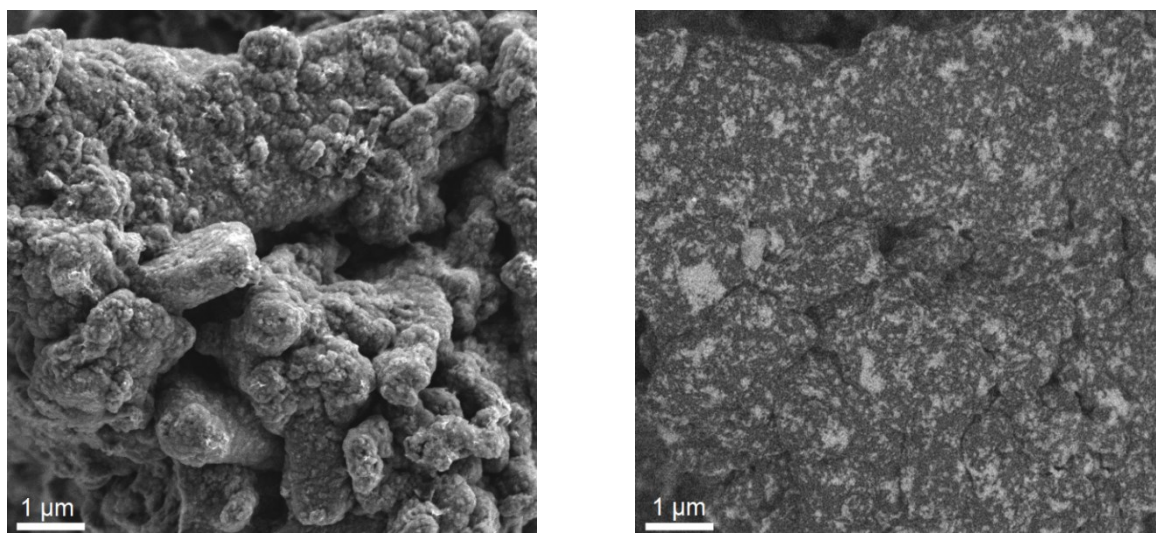
Figure S2-51: SEM images of Co@TTI-COF (0.9 wt% Co) with secondary electron detection (left) and energy selective backscattered electron detection for material contrast illustration (right).
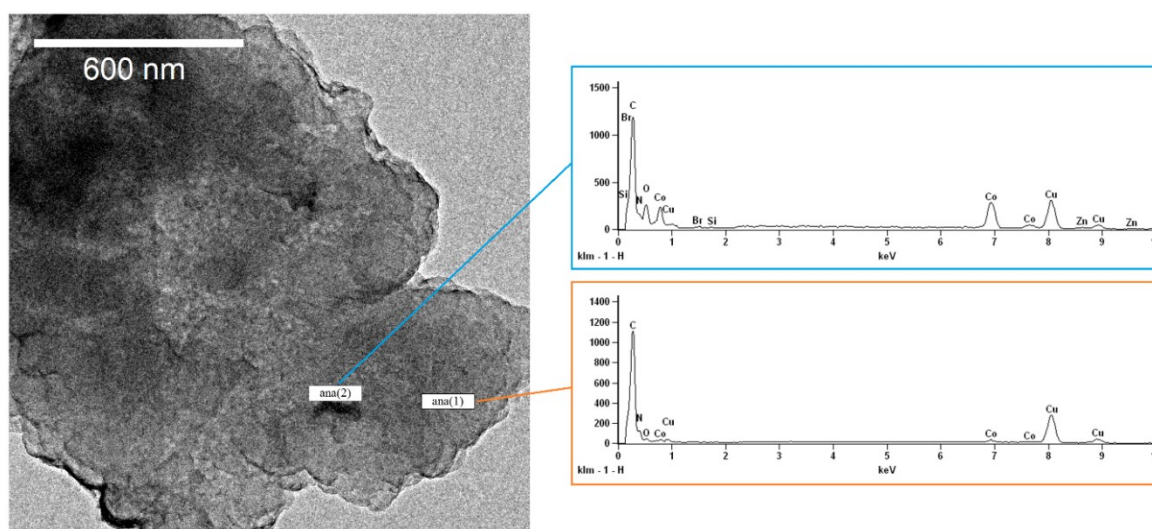
Figure S2-52: TEM image of Co@TTI-COF (0.9 wt% Co) and corresponding EDX spectra collected at the designated areas.
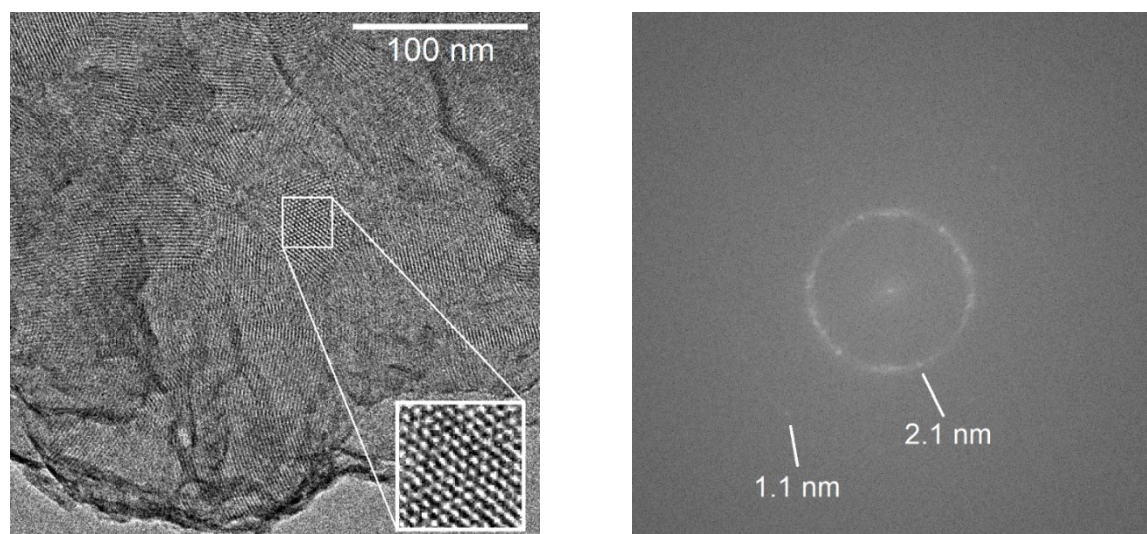
Figure S2-53: TEM image of Co@TTI-COF (0.9 wt% Co) and corresponding FFT.

Silver Nitrate Decomposition

As illustrated in the main text, we found apparent oxygen evolution from silver nitrate solutions without additional photosensitizer (Figure 2-5). We thus set out to understand this finding and elucidate the exact role of $AgNO_3$ as an SEA in the photocatalytic oxidation of water with heterogeneous photocatalysts. To this end, we repeated the illumination of a 10 mM $AgNO_3$ solution with complementary oxygen detection *via* gas chromatography (GC). For higher reproducibility and spectral match, we use a class AAA solar simulator with integrated AM1.5 filter. Overlapping data for both oxygen detection methods suggests that oxygen indeed evolves from silver nitrate solutions without an external photosensitizer (Figure S2-54). A duplicate experiment confirms the reproducibility.
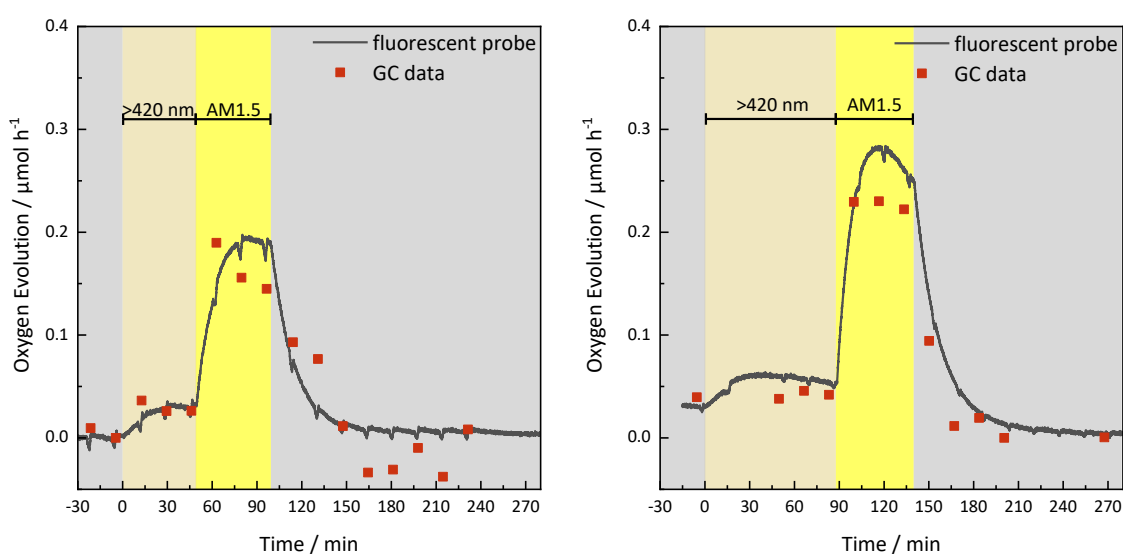
Figure S2-54: Oxygen evolution during irradiation of 10 mM $AgNO_3$ solutions with varying optical filters as annotated. Simultaneous measurement *via* gas chromatography and fluorescent sensors under flow conditions. Periodic peaks are due to pressure variations upon GC sampling.

Upon visual inspection, we could find grey deposits on the reactors glass frit and O-rings (Figure S2-56). To gain mechanistic insights, we analyzed a 10 mM $AgNO_3$ solution after illumination with visible light (>420 nm) for 90 minutes. TEM imaging of the precipitate after illumination shows the existence of particles with sizes in the range of $10 - 50$ nm (Figure S2-57). A scaled-up photolysis of 10 mM $AgNO_3$ with AM1.5 illumination and subsequent XRPD analysis reveals that the deposition consists of elemental silver (Figure S2-57).
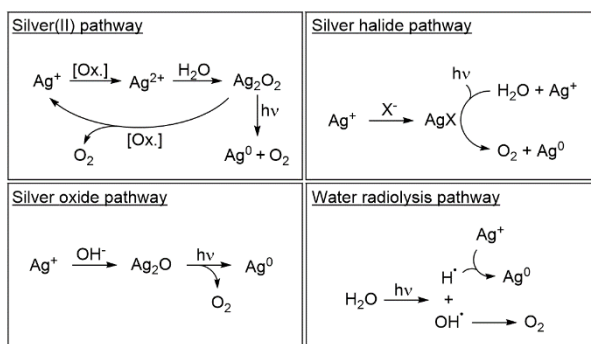
Figure S2-55: Potential pathways for oxygen evolution from silver(I) species.

There are several pathways that could explain both the observed oxygen evolution and the formation of metallic silver (Figure S2-55). BAHNEMANN *et al*. suggest silver peroxides as a source of oxygen during photocatalysis with Ag^+ species, which can form through undesired oxidation of Ag(I) to Ag(II) in aqueous solutions.[40,41] Subsequent oxygen evolution reactions *via* Ag^{3+} – formed through dismutation of Ag^{2+} – can also be envisaged.[42,43] However, given the high redox potential for the Ag(II)/Ag(I) couple (E^0 = 1.98 V), either a strong oxidizer or a low-valence band semiconductor would be needed to generate Ag^{2+} – both of which are missing in our experiment.[42] Nevertheless, we used electron paramagnetic resonance (EPR) spectroscopy to test for the presence of paramagnetic Ag^{2+} species, but neither *in-situ* nor *ex-situ* illumination of silver nitrate solutions in varying concentrations yielded the signals expected for Ag^{2+} (Figure S2-59).[42,44,45]

A special pathway for oxygen evolution from Ag^+ solutions arises in the presence of halides due to the formation of hardly soluble AgX salts. Recently, is has been shown by the MAEDA group that silver nitrate can act both as SEA and precursor to photosensitizing AgCl particles in one system. Upon reaction of $AgNO_3$ with $[Co(NH_3)_6]Cl_3$ silver chloride particles form, which act as photosensitizer for the oxygen evolution reaction with the remaining $[Co(NH_3)_6]^{3+}$ species as WOC.[46] Similarly, we also note the formation of AgCl particles when employing Ir@TAPB-BPY COF as photocatalyst with $AgNO_3$ as SEA due to the presence of chloride ligands and counterions (Figure S2-44). However, since the presence of chloride or other halides is detrimental for this OER pathway, it cannot explain the decomposition of silver nitrate solutions in ultrapure water in the absence of Ir@TAPB-BPY COF.

In addition, we considered Ag_2O as a potential intermediate in the photodecomposition of $AgNO_3$ (Figure S2-55).[42,47] We thus performed a control experiment with Ag_2O to assess its photostability and eventual accompanied oxygen evolution. In fact, upon illumination of a 5 mM suspension of Ag_2O in water, we were able to detect small amounts of oxygen with evolution rates around 0.05 μmol h^{-1} (AM1.5, Figure S2-58). In accordance with the proposed mechanism (Figure S2-55), we could detect traces of elemental silver after Ag_2O photolysis (Figure S2-58). However, the comparably small oxygen evolution rate even in the presence of pure Ag_2O suggests that its role as an intermediate in the investigated $AgNO_3$ decomposition pathway is negligible. Moreover, we regard the formation of significant amounts of Ag_2O from aqueous solutions of $AgNO_3$ at pH 7 to be unlikely, as this process usually requires more alkaline conditions.[42,47,48]

As a fourth pathway, we assessed the photoreduction of Ag$^+$ – and the accompanying water oxidation – as the cause of oxygen evolution from silver nitrate solutions. In fact, photolysis and radiolysis of silver(I) solutions has been established as a useful tool to synthesize silver nanoparticles, -clusters, and other silver structures.[49–53] Mechanistically, it is argued that excitation of H$_2$O leads to dissociation into reactive species such as OH$^•$, H$^•$, and e$_{aq}^-$, with the latter two being able to reduce Ag(I) to Ag(0).[53–55] The OH$^•$ radical on the other hand can subsequently lead to oxygen evolution, which was qualitatively confirmed by HADA *et al.* in 1976 when irradiating aqueous silver perchlorate solutions with 253.7 nm light.[56] However, we were not able to detect supposedly oxygen evolving OH$^•$ radicals *via* EPR spectroscopy with the spin trap 5,5-dimethyl-1-pyrroline-*N*-oxide (DMPO, Figure S2-59). In an indirect approach, we added isopropanol as hydroxyl radical scavenger to a 10 mM AgNO$_3$ solution and in fact detected less oxygen upon illumination, which hints to OH$^•$ radicals to play a role in the undesired oxygen evolution from AgNO$_3$, as proposed in the water radiolysis pathway (Figure S2-55, Figure S2-61).[57]

In wavelength-dependent literature studies it was found that longer wavelengths of up to 405 nm light can still photoreduce silver ions, though with slower kinetics.[58,59] Indeed, we also found higher oxygen evolution rates when illuminating a silver nitrate solution with shorter wavelength light (Figure S2-60). We pinned down the onset wavelength for this process to the range of 455-420 nm.

In summary, we could not find direct evidence that either of the four deceived AgNO$_3$ decomposition pathways underlies the significant oxygen evolution we observed (Figure S2-54). Ultimately we tried to rule out our flow setup itself (Figure 2-3) as the source of the OER. Surprisingly, when conducting AgNO$_3$ photolysis in a bulk photoreactor, we could not detect increased amounts of oxygen upon illumination (Figure S2-62). The addition of a loose glass frit to the bulk reactor did also not lead to oxygen evolution, ruling out the borosilicate frit material as unexpected photosensitizer and/or WOC. In follow-up experiments with a pristine flow reactor we could again not see significant oxygen evolution – in contrast to the usual "recycled" flow-through photoreactor (Figure S2-63). We thus deduced the photoreactor to be contaminated despite extensive cleaning after every experiment. Upon extraction of the top layer of the borosilicate frit and subsequent optical and electron microscopy we identified ruthenium-loaded tungsten oxide as the most likely reason for the observed photocatalytic oxygen evolution in some cases (Figure S2-64 - Figure S2-67).

Figure S2-56: Photographic image of a flow-reactor before (left) and after (right) photolysis of silver nitrate solutions (10 mM, AM1.5, 2 h).
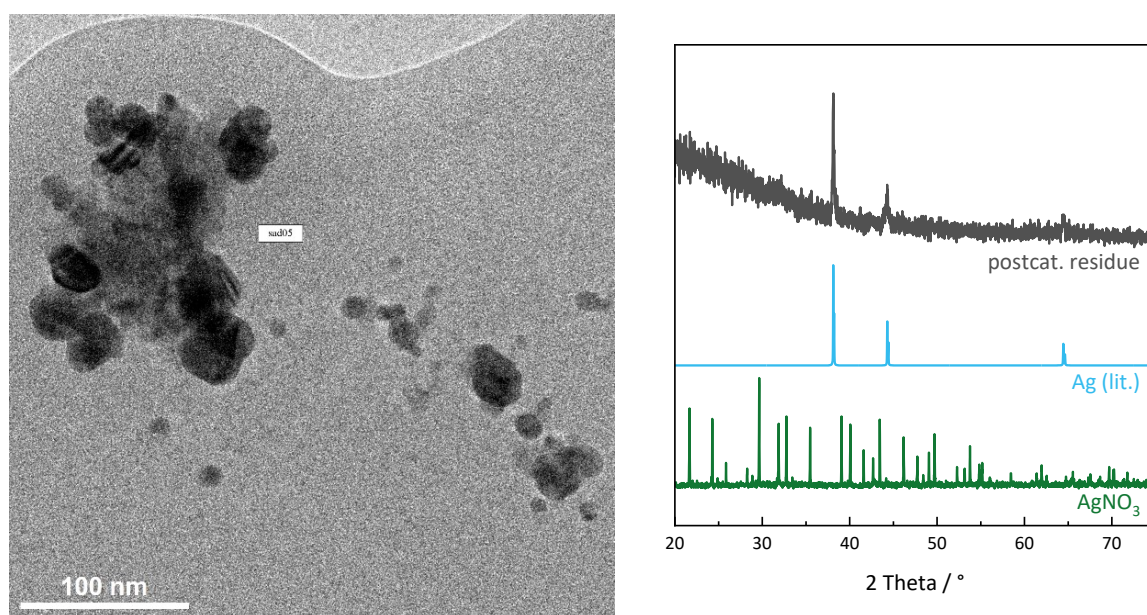
Figure S2-57: TEM images (left) and XRPD pattern (right) of particles obtained from $AgNO_3$ photolysis (10 mM). Silver reference: ICSD 64994, [60].
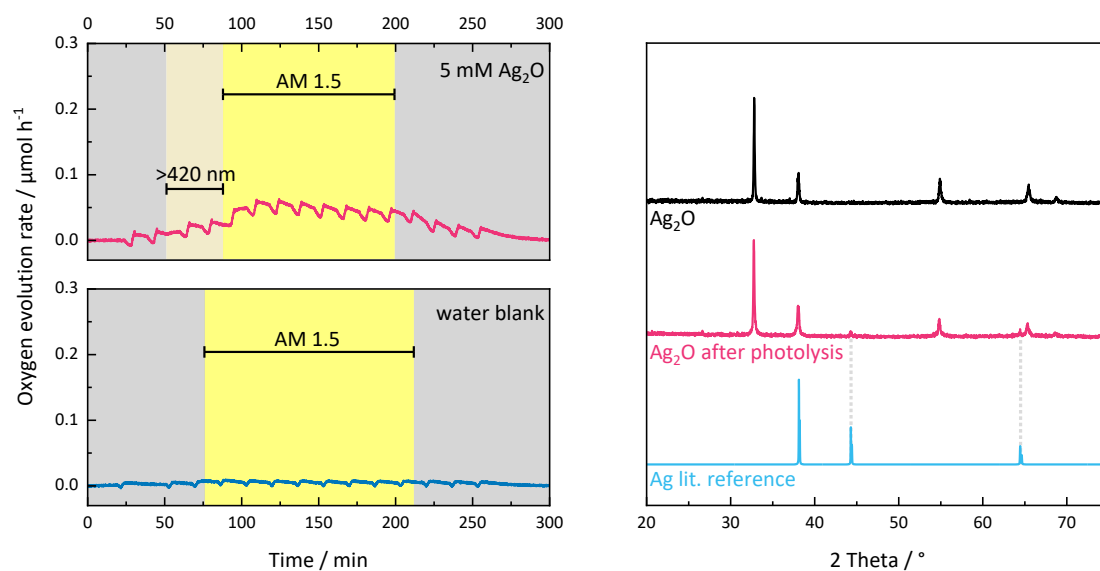
Figure S2-58: Oxygen evolution by an Ag_2O suspension (5 mM) (left) and XRPD pattern (right) of the remaining particles. Photolysis experiment for pure water shown for comparison. Periodic peaks are due to pressure variations upon GC sampling.
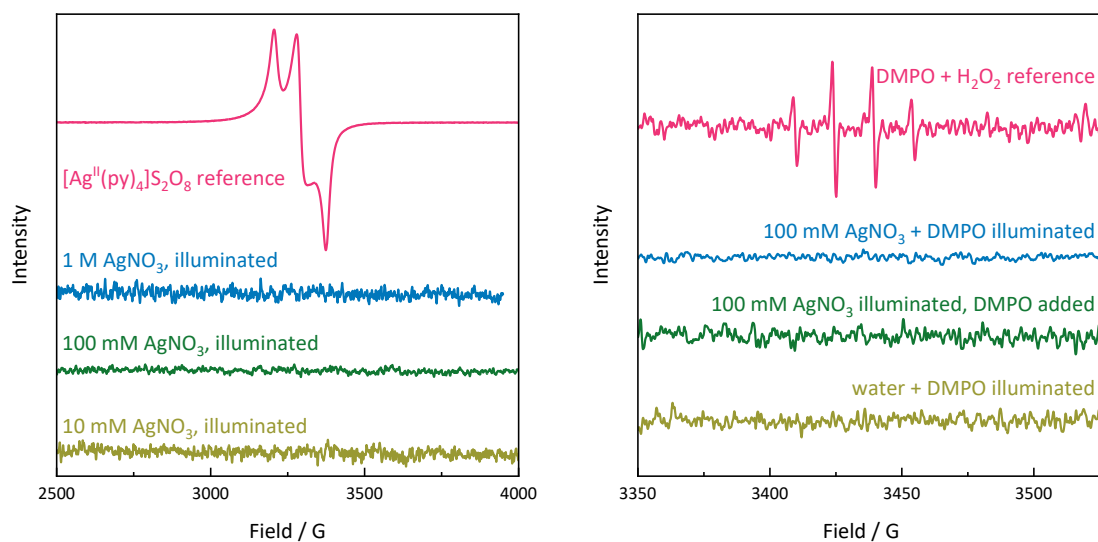
Figure S2-59: EPR spectra for the detection of paramagnetic metal species (left) and organic radicals (right).
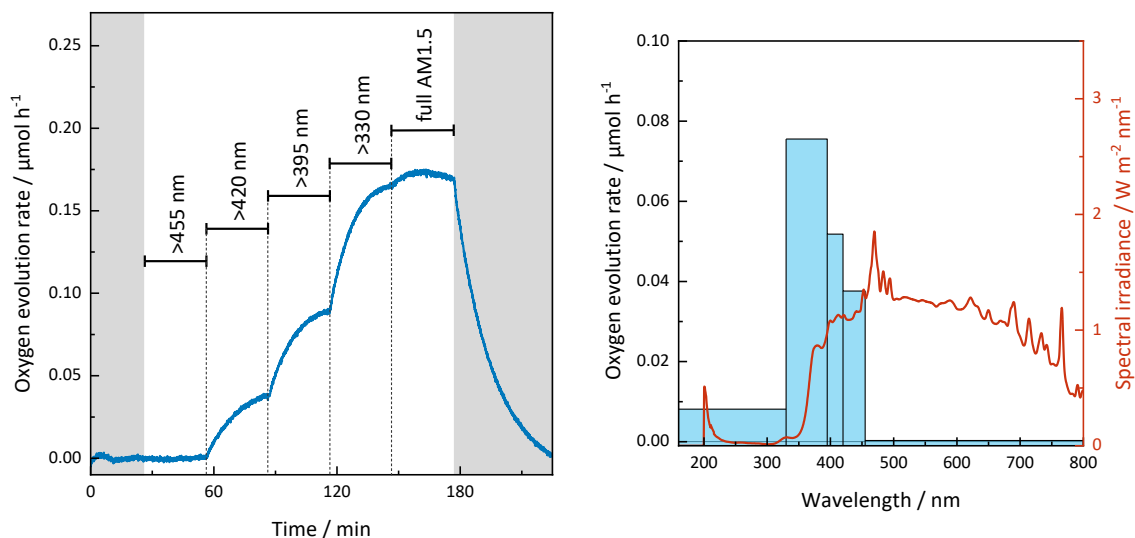
Figure S2-60: Wavelength-dependence of AgNO₃ photolysis measured during longpass-filtered illumination (solar simulator, 1 sun, AM1.5). Bar graph shows differential oxygen evolution, obtained by subtracting the oxygen evolution of longer wavelength illumination periods from the subsequent rate with shorter wavelength.
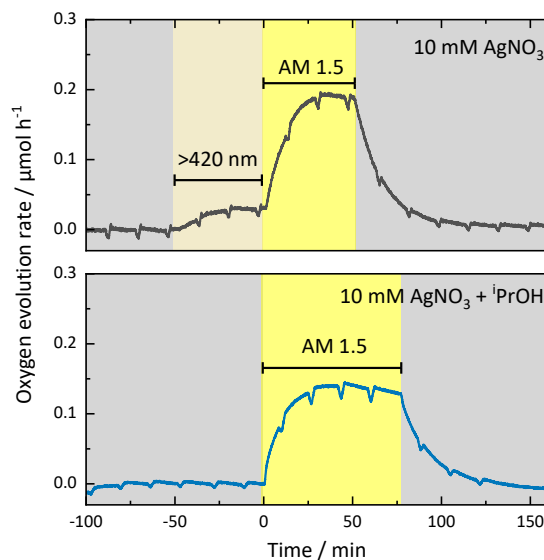
Figure S2-61: Photolysis of AgNO₃ (10 mM) in the absence (top) and presence (bottom) of isopropanol (0.2 M) as hydroxyl radical scavenger. Periodic peaks are due to pressure variations upon GC sampling.
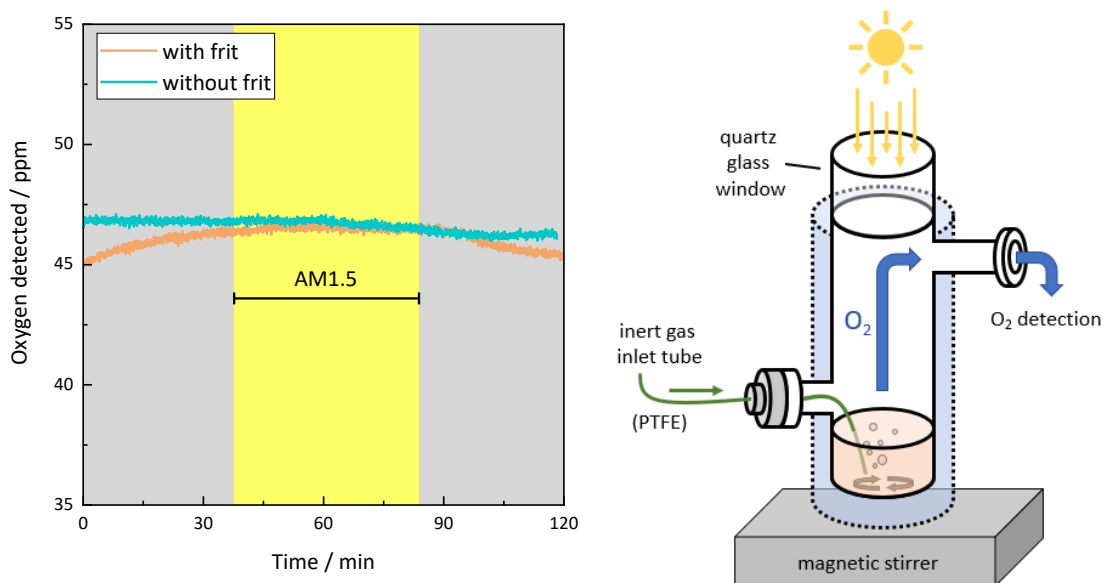
Figure S2-62: Control photolysis experiment with AgNO$_3$ (10 mM) in a bulk photoreactor with and without additional loose glass frit (borosilicate, por. 4, 20 mm diameter, 2.5 mm thick, pristine, left) submerged in the solution. Oxygen readouts are given on the original ppm scale. Schematic illustration of the experimental setup with the bulk photoreactor (right).
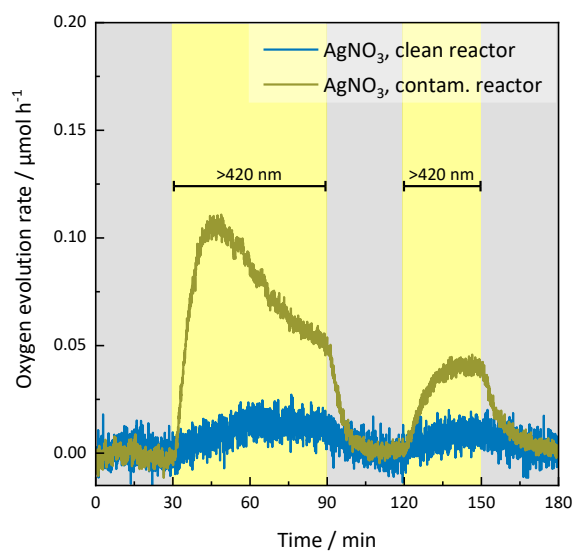
Figure S2-63: Comparison of AgNO$_3$ (10 mM) photolysis experiments in a contaminated (ocre) and a pristine flow photoreactor (blue). Reaction conditions: AgNO3 (10 mM, 5 mL), 300 W Xe lamp with installed >420 nm longpass filter. Grey areas represent dark reaction conditions.
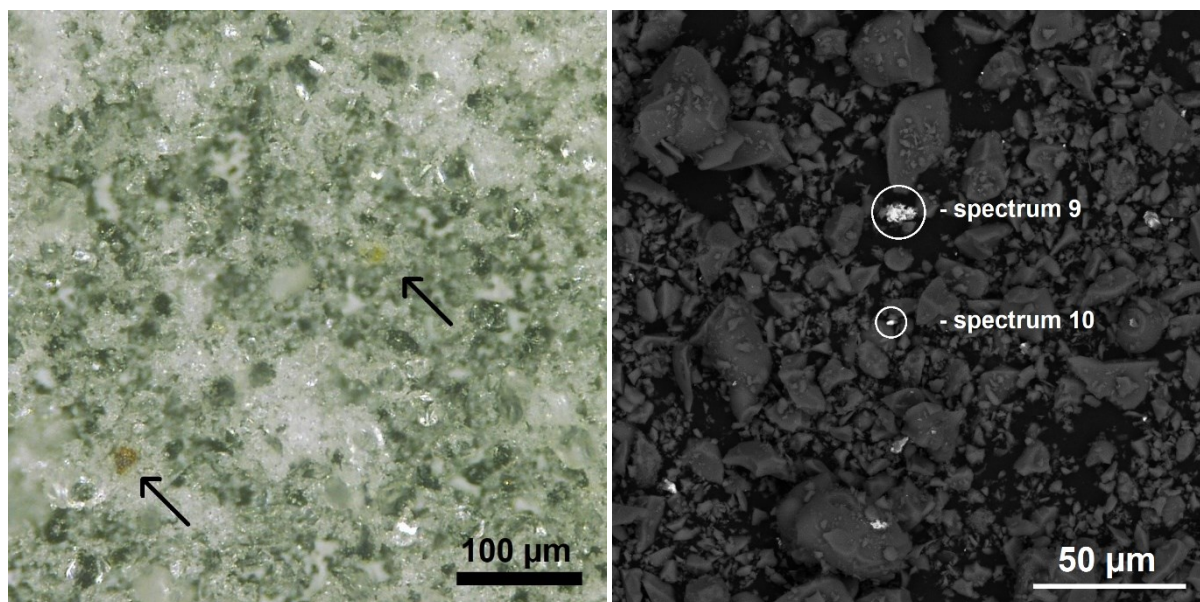
Figure S2-64: Microscopic (left) and SEM image with backscattered electron detection (right) of the flow reactor's drilled-out glass frit after several photocatalytic experiments and consecutive cleaning steps. The annotations refer to the EDX spectra summed up in Table S2-5 whereas the arrows highlight potential contaminations.

Table S2-5: Summary of EDX spectra measured on the flow reactor's drilled-out glass frit after several photocatalytic experiments and consecutive cleaning steps. Values given in at%.

Element	Spect.1	Spect. 2	Spect. 3	Spect. 4	Spect. 5	Spect. 6	Spect. 7	Spect. 8	Spect. 9	Spect. 10
O	56.55	40.29	43.61	27.18	78.67	67.48	31.78	37.37	47.81	78.13
F	1.73									
Na	2.53	2.21	3.09		0.56	2.39	1.01	0.93	1.97	1.43
Al	0.90	1.04	2.91	0.27		0.91	0.78	0.95	1.10	1.43
Si	24.49	26.06	14.09	6.15	4.83	28.90	11.30	10.42	14.91	10.19
S									0.24	
Cl			0.09							
K	0.23	0.23	0.10			0.32				0.10
Ca			0.09							
Ti			0.14							
Cr			6.66							
Mn			0.65							
Fe			23.90							
Ni			3.47							
Cu	12.27	28.65	0.70	58.09	0.52		50.52	43.73	30.46	0.33
Sr					1.68					
Mo			0.50							
Ru					0.66					
Ag	0.24	0.22		2.09			0.70	1.71	0.58	
Sn	1.06	1.30		6.21			3.91	4.89	2.92	
W					13.08					8.39
Total	100.00	100.00	100.00	100.00	100.00	100.00	100.00	100.00	100.00	100.00
Mater.	bronze	bronze	steel	bronze	WO_3	bare frit	bronze	bronze	bronze	WO_3

Mean for spectra 1,2,4,7,8,9: 90.2 at% Cu, 2.0 at% Ag, 7.8 at% Sn. These values suggest that Ag stems from a bronze rather than AgNO$_3$.
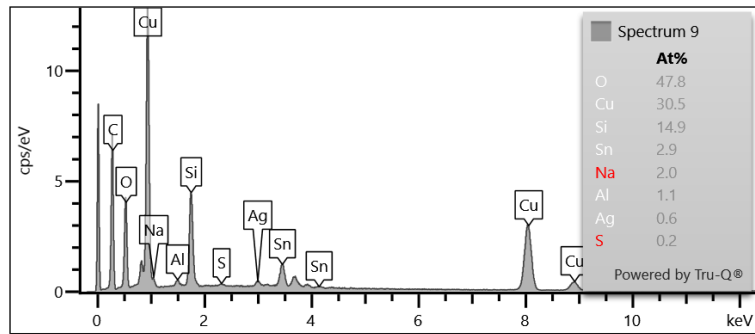
Figure S2-65: EDX spectrum of a contamination on the flow reactor's glass frit after several photocatalytic experiments and consecutive cleaning steps. Spectrum measured at position "9" marked in Figure S2-64.
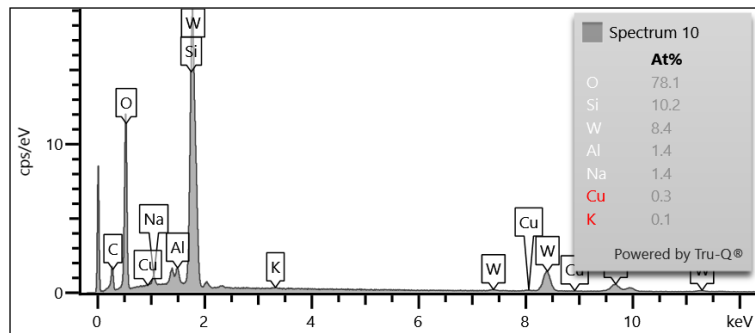
Figure S2-66: EDX spectrum of a contamination on the flow reactor's glass frit after several photocatalytic experiments and consecutive cleaning steps. Spectrum measured at position "10" marked in Figure S2-64.
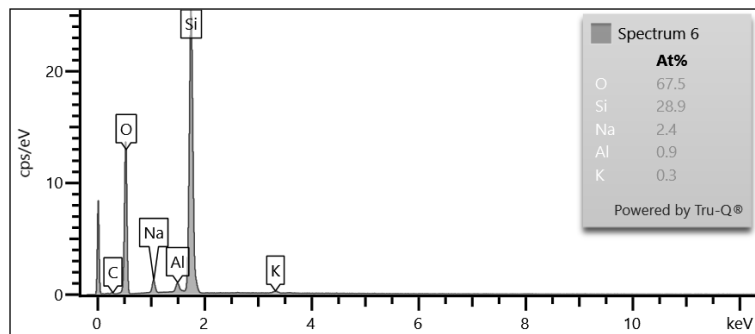
Figure S2-67: EDX spectrum of non-contaminated parts of the flow reactor's glass frit after several photocatalytic experiments and consecutive cleaning steps.
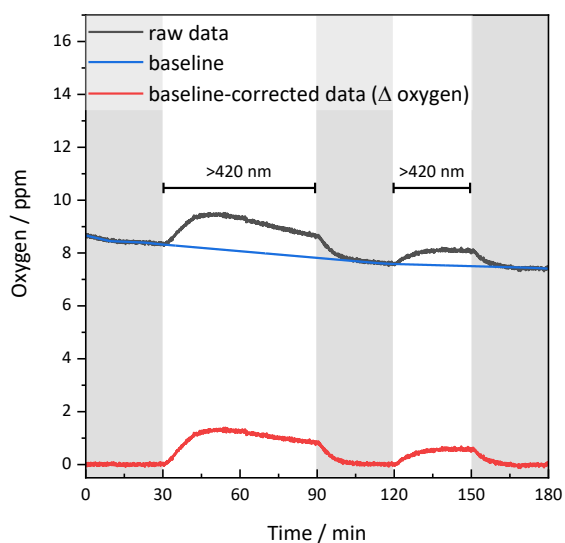
Figure S2-68: Exemplary representation of the background correction usually applied to raw oxygen readouts obtained from fluorescent sensor spots under flow conditions.
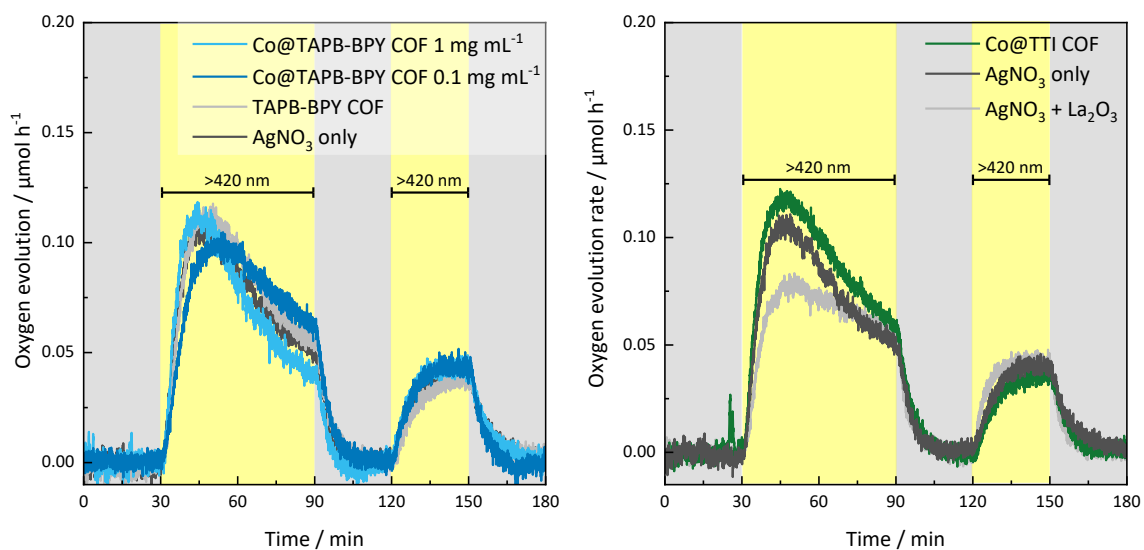
Figure S2-69: Photocatalytic oxygen evolution experiments with literature-known COFs. Reaction conditions: 5.0 mg COF (or 0.5 mg if stated), AgNO$_3$ (10 mM, 5 mL), 300 W Xenon lamp, >420 nm longpass filter. 10 mg La$_2$O$_3$ added as pH buffer for Co@TTI-COF.
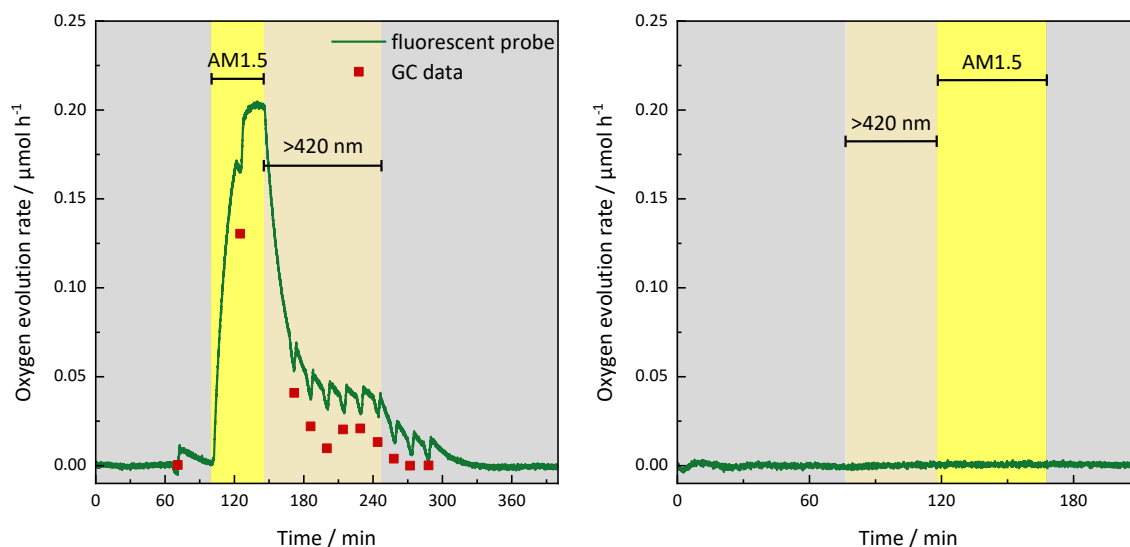
Figure S2-70: Oxygen evolution experiment with Co@TTI COF under literature-inspired conditions (1 mg COF with 0.867 wt% Co, 10 mg La$_2$O$_3$, 5 mL 10 mM AgNO$_3$). Illumination with a solar simulator as annotated (1 sun). Periodic peaks are due to pressure variations upon GC sampling. Reactions conducted in a contaminated (left) and a pristine photoreactor (right).
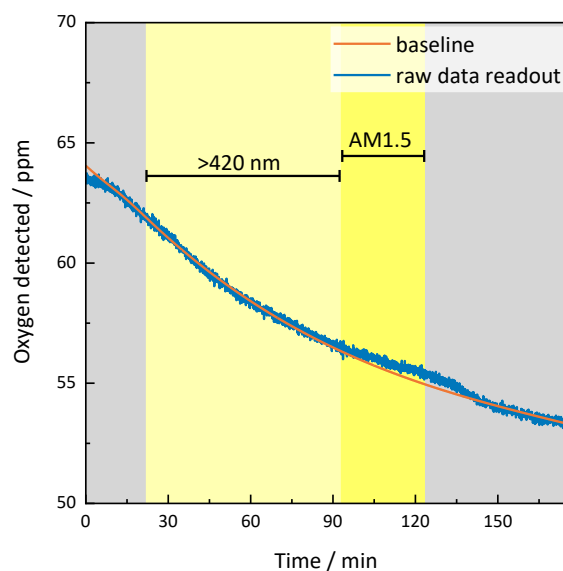
Figure S2-71: Raw data and derived baseline for the photocatalytic oxygen evolution experiment with Co@TAPB-BPY COF in a bulk photoreactor without glass frit (Figure S2-62). Reaction condition: 2 mg COF, 20 mL AgNO3, 5 mM. Illumination with an AAA sun simulator (1 sun) and optical filters as specified. Grey areas represent dark reaction conditions. The negative slope is due to ongoing degassing of the bulk/flow hybrid setup.
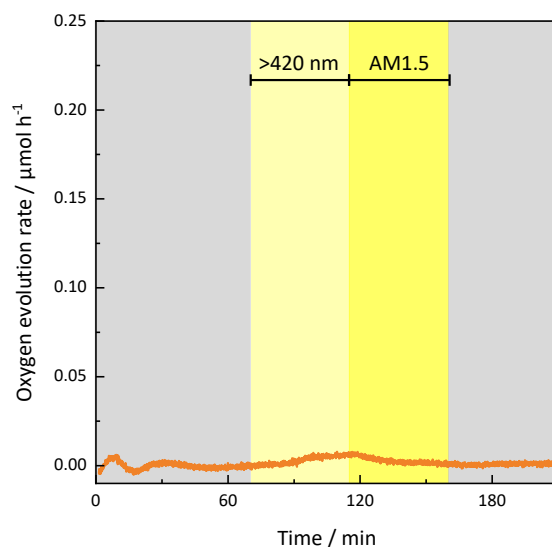
Figure S2-72: Photocatalytic oxygen evolution experiment with Ir@TAPB-BPY COF (1.9 wt% Ir) in a pristine flow reactor. Reaction condition: (5 mg COF, 10 mM AgNO$_3$, 5 mL). Illumination with 1 sun (AAA sun simulator) and optical filters as specified. Grey areas represent dark reaction conditions.
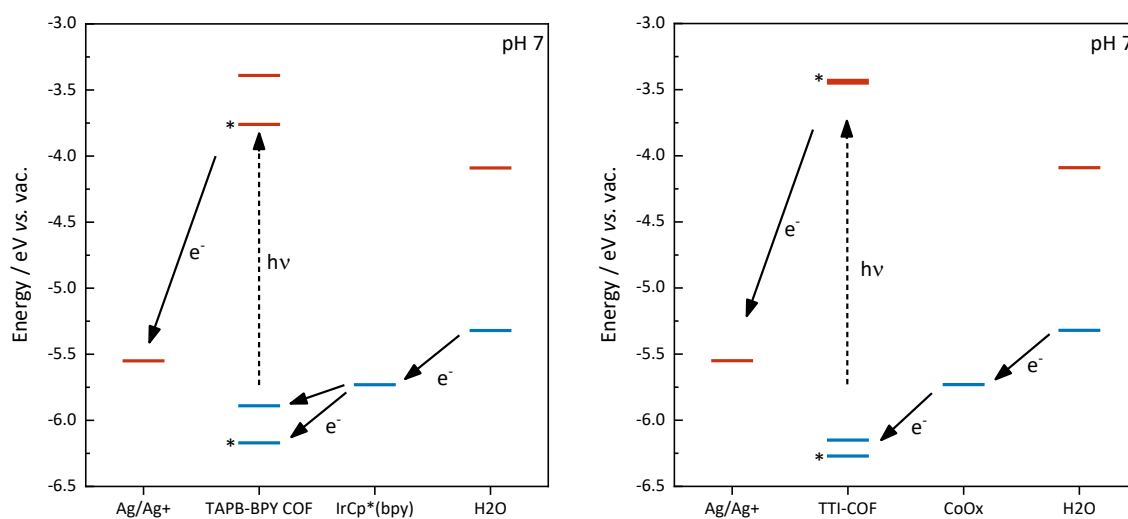
Figure S2-73: Schematic thermodynamics underlying photocatalytic water oxidation with TAPB-BPY COF and IrCp*(bpy) (left) and TTI-COF and cobalt oxide (right) as WOC. Literature values for COFs according to Table S2-1 marked with an asterisk. Values for IrCp*(bpy) and CoOx taken from literature reports and converted to E_{abs} according to $E_{vac} = -(E_{NHE} + 4.5)$.[71,72]

Table S2-6: Comparison of COFs and other systems reported for photocatalytic water oxidation.

Photosensitizer	Co-catalyst	Sarificial	OER	Optical filter	Source
BpCo-COF-0	None	5 mM AgNO$_3$	traces	>420 nm	Ref. [27]
BpCo-COF-1	Co 1.2 wt%	5 mM AgNO$_3$	152 µmol g^{-1} h^{-1}	>420 nm	Ref. [27]
g-C$_{40}$N$_3$-COF	None	10 mM AgNO$_3$, La$_2$O$_3$	1.6 µmol h^{-1} 32 µmol g^{-1} h^{-1}	>420 nm	Ref. [61]
g-C$_{40}$N$_3$-COF	Co 3.0 wt%	10 mM AgNO$_3$, La$_2$O$_3$	2.5 µmol h^{-1} 50 µmol g^{-1} h^{-1}	>420 nm	Ref. [61]
I-TST = TTI-COF	None	10 mM AgNO$_3$, La$_2$O$_3$	0.13 µmol h^{-1} 13 µmol g^{-1} h^{-1}	>420 nm	Ref. [39] [a]
I-TST = TTI-COF	Co(OH)$_2$	10 mM AgNO$_3$, La$_2$O$_3$	~0.4 µmol h^{-1} ~37 µmol g^{-1} h^{-1}	>420 nm	Ref. [39] [a]
sp^{2}c-COF	Co(NO$_3$)$_2$	10 mM AgNO$_3$, La$_2$O$_3$	1.1 µmol h^{-1} 22 µmol g^{-1} h^{-1}	>420 nm	Ref. [62]
g-C$_{52}$N$_6$-COF	Co(NO$_3$)$_2$ 3wt%	10 mM AgNO$_3$, La$_2$O$_3$	12.5 µmol g^{-1} h^{-1}	>420 nm	Ref. [63]
g-C$_{54}$N$_6$-COF	Co(NO$_3$)$_2$ 3wt%	10 mM AgNO$_3$, La$_2$O$_3$	51 µmol g^{-1} h^{-1}	>420 nm	Ref. [63]
N$_0$-COF	"CoNO$_3$"	10 mM AgNO$_3$, La$_2$O$_3$	390 µmol g^{-1} h^{-1}	>300 nm	Ref. [64]
TpBpy-NS	Pt ~1.2 wt%	10 mM AgNO$_3$, La$_2$O$_3$	3.18 µmol h^{-1} 212 µmol g^{-1} h^{-1}	>420 nm	Ref. [65]
TpBpy-2-NS	Pt ~1.2 wt%	10 mM AgNO$_3$, La$_2$O$_3$	1.36 µmol h^{-1} 91 µmol g^{-1} h^{-1}	>420 nm	Ref. [65]
BtB-COF	16 wt% Co(ClO$_4$)$_2$	0.1 mM AgNO$_3$ [b]	6.65 µmol h^{-1} 665 µmol g^{-1} h^{-1}	>420 nm	Ref. [66]
CTF-BPDCN	None	10 mM NaIO$_3$ La$_2$O$_3$	0.78 µmol h^{-1} 26 µmol g^{-1} h^{-1}	>420 nm	Ref. [67]
CTF-1	RuO$_2$	200 mM AgNO$_3$	7 µmol h^{-1} 140 µmol g^{-1} h^{-1}	>420 nm	Ref. [68]
CTF-1	None	50 mM AgNO$_3$	1.5 µmol h^{-1} 30 µmol g^{-1} h^{-1}	>420 nm	Ref. [68]
P10 – linear polymer	1 wt% Co predeposited	10 mM AgNO$_3$, 200 mg La$_2$O$_3$, 100 mL, 50 mg	16.6 µmol h^{-1} 332 µmol g^{-1} h^{-1}	Full arc	Ref. [69]
	Same	same	5.2 µmol h^{-1} 104 µmol g^{-1} h^{-1}	>420 nm	Ref. [69]

[a]: OER values extracted from graph. [b] The authors state [AgNO$_3$] as 0.1 mM and 1 mM at different sections of the respective supporting information.

Table S2-7: Comparison of background oxygen evolution measurements (sacrificial only) in selected publications.

SEA	conc., vol.	buffer/additive	OER	Illumination	Ref	Material
$AgNO_3$	10 mM, 100 mL	200 mg La_2O_3	not measured	300 W Xe lamp, >420 nm	[62]	sp^2c-COF
$AgNO_3$	5 mM, 100 mL	none	unclear "blank"	300 W Xe lamp, >420 nm	[27]	Bp-COF
$AgNO_3$	10 mM, 100 mL	200 mg La_2O_3	not measured	300 W Xe lamp, >420 nm	[61]	g-C40N3-COF
$AgNO_3$	10 mM, 50 mL	100 mg La_2O_3	not measured	300 W Xe lamp, >420 nm	[39]	I-TST = TTI-COF
$AgNO_3$	10 mM, 100 mL	200 mg La_2O_3	"no O_2 evolution detected"	300 W Xe lamp, >420 nm	[63]	$g\text{-}C_{52}N_6\text{-}$ COF / $g\text{-}C_{54}N_6\text{-}$ COF
$AgNO_3$	10 mM, 100 mL	200 mg La_2O_3	not measured	unknown, >300 nm	[64]	N_0-COF
$AgNO_3$	10 mM, 50 mL	100 mg La_2O_3	not measured	300 W Xe lamp, >420 nm	[65]	TpBpy-NS
$AgNO_3$	0.1 mM[a], 50 mL	none	not measured	300 W Xe lamp, >420 nm	[66]	BtB-COF
$NaIO_3$	unknown	none	not measured			
NaS_2O_8 (sic)	unknown	none	not measured			
$AgNO_3$	10 mM, 100 mL	200 mg La_2O_3	0 µmol h^{-1}	300 W, >420 nm	[69]	P10
$AgNO_3$	10 mM, 100 mL	none	ca. 3 µmol in 5 h	300 W, UV+vis	[70]	IrO_2
$NaIO_3$	10 mM, 50 mL	200 mg La_2O_3	Not measured	300 W, >420 nm 44.5 mWcm^{-2}	[67]	CTF-BPDCN
$Na_2S_2O_8$	20 mM, 10 mL	1 mM TSPP	0	150 mW cm-2 AM 1.5	[28]	TiO_2
KIO_3	10 mM, 10 mL	1 mM TSPP	Ca. 1.1	150 mW cm-2 AM 1.5	[28]	TiO_2

[a] The authors state 0.1 mM and 1 mM at different sections of the respective supporting information.

Table S2-8: Screening results for photocatalytic oxygen evolution experiments with Co@TAPB-BPY COF and comparison to literature results.

Co / wt%	c(AgNO$_3$)	COF / medium	reactor	illumination	OER rate μmol h^{-1}	OER rate μmol h^{-1} g^{-1}	Source
0					0	0 ("traces")	
1.2					1.52	152	
0.25	5 mM	10 mg COF in 100 mL water	Pyrex glass reaction cell	300 W Xe lamp >420 nm	~0.75	~75[a]	[27]
0.5					~0.92	~92[a]	
2.5					~1.30	~130[a]	
5.1					~0.71	~71[a]	
7.5					~0.70	~70[a]	
0	10 mM	No COF in 5 mL water		300 W Xe lamp >420 nm	0.1	-	This work
0	10 mM	5 mg COF in 5 mL water		300 W Xe lamp >420 nm	0.11	20	This work
1.223	10 mM	0.5 mg COF in 5 mL water	flow reactor, contaminated with RuOx@WO$_3$	300 W Xe lamp >420 nm	0.04	8.2	This work
1.688	10 mM	5 mg COF in 5 mL water		300 W Xe lamp >420 nm	0.1	20	This work
~1	10 mM	4 mg COF in 5 mL water		300 W Xe lamp full arc	0.24	60	This work
				AM1.5	0.18	45	
				>420	0.10	25	
1.223	10 mM	0.5 mg COF in 5 mL water		300 W Xe lamp >420 nm	0.1	196	This work
1.038	5 mM	2 mg COF in 20 mL water	bulk reactor	Solar simulator >420 nm	0	0	This work

[a]: value extracted from graph.

Table S2-9: Screening results for photocatalytic oxygen evolution experiments with Co@TTI-COF and comparison to literature results.

Co / wt%	c(AgNO$_3$)	COF / medium	reactor	illumination	OER rate μmol h^{-1}	OER rate μmol h^{-1} g^{-1}	Ref.
0	10 mM	10 mg COF 100 mg La$_2$O$_3$ in 50 mL water	quartz tube?	300 W Xe lamp >420 nm	~0.13	~12.5[a]	[39]
~2	10 mM	10 mg COF 100 mg La$_2$O$_3$ in 50 mL water		300 W Xe lamp >420 nm	~0.4	~37[a]	[39]
0.867	10 mM	1.0 mg COF 10 mg La$_2$O$_3$ in 5 mL water	flow reactor, contaminated	Solar simulator >420 nm	0.04	40	This work
				AM1.5	0.2	200	
0.324	10 mM	5.0 mg COF 10 mg La$_2$O$_3$ in 5 mL water		300 W Xe lamp >420 nm	0.12	24	This work
0.867	10 mM	1.0 mg COF 10 mg La$_2$O$_3$ in 5 mL water	flow reactor, pristine	Solar simulator AM1.5	0	0	This work
				>420 nm	0	0	

[a]: value extracted from graph.

Figure S2-74: Positive control experiments for photocatalytic oxygen evolution. Illumination with a 300 W Xe lamp and optical filters as annotated. Left: 0.1 mM [Cp*Ir(bpy)Cl]Cl, 1 mM Ru(bpy)$_3$, 20 mM Na$_2$S$_2$O$_8$, Right: 5.02 mg TiO$_2$ Aeroxid, RuCl$_3$ (50 µg Ru), 10 mM NaIO$_3$.

We found that irradiation of a persulfate solution leads to significant oxygen evolution under unfiltered illumination with a 300 W Xenon arc lamp (Figure S2-75). BAHNEMANN suggests that the sulfate radicals derived from persulfate reduction (eq. S4) subsequently oxidize water and release oxygen *via* hydroxyl radicals (eq. S5-6).[40,73] In our studies, oxygen evolution was most pronounced in the absence of both photosensitizer and eventual co-catalyst (Table S2-10, entry 1), implying primarily homolytic cleavage of S$_2$O$_8^{2-}$ (eq. S7) takes place rather than photoreduction.[74,75]
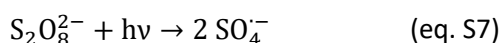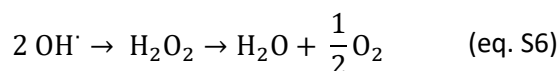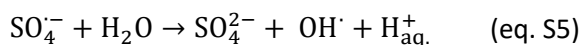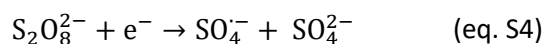
$$S_2O_8^{2-} + e^- \rightarrow SO_4^{\cdot-} + SO_4^{2-} \qquad \text{(eq. S4)}$$

$$SO_4^{\cdot-} + H_2O \rightarrow SO_4^{2-} + OH^\cdot + H_{aq.}^+ \qquad \text{(eq. S5)}$$

$$2\,OH^\cdot \rightarrow H_2O_2 \rightarrow H_2O + \tfrac{1}{2}O_2 \qquad \text{(eq. S6)}$$

$$S_2O_8^{2-} + h\nu \rightarrow 2\,SO_4^{\cdot-} \qquad \text{(eq. S7)}$$

On the contrary, we did not detect significant amounts of oxygen with metal-free TAPB-BPY COF in the presence of Na$_2$S$_2$O$_8$ (Table S2-10, entry 2). We presume that the COF quenches the decomposition pathway through reaction with the highly reactive sulfate radicals, which are known to oxidize organics.[76,77] Iridium-loaded TAPB-BPY COF, however, shows apparent oxygen evolution, even over the course of 14 hours (Table S2-10, entry 3, Figure S2-76). This opposing behavior for pristine and metalated TAPB-BPY COF points out the importance of adequate blank measurements – otherwise, the oxygen evolution in the case of Ir@TAPB-BPY COF might have been mistaken as the results of catalytic water oxidation, although it is presumably caused by decomposition of the SEA. However, in the case of S$_2$O$_8^{2-}$ such misinterpretations can easily be avoided through the use of 420 nm longpass filters since persulfate does not decompose when irradiated with visible light.

Table S2-10: Photocatalytic water oxidation experiments with persulfate under full arc illumination.

Entry	Persulfate	COF	Oxygen evolution, full arc	Oxygen evolution, AM 1.5
1	20 mM	-	1.5 µmol h^{-1}	0.1 µmol h^{-1}
2	20 mM	TAPB-BPY COF	0 µmol h^{-1}	0 µmol h^{-1}
3	20 mM	Ir@TAPB-BPY COF	0.7 µmol h^{-1}	0 µmol h^{-1}
4	-	Ir@TAPB-BPY COF	0 µmol h^{-1}	0 µmol h^{-1}

Reaction conditions: 5 mg COF, 5 mL total volume, 300 W Xenon lamp, unfiltered.
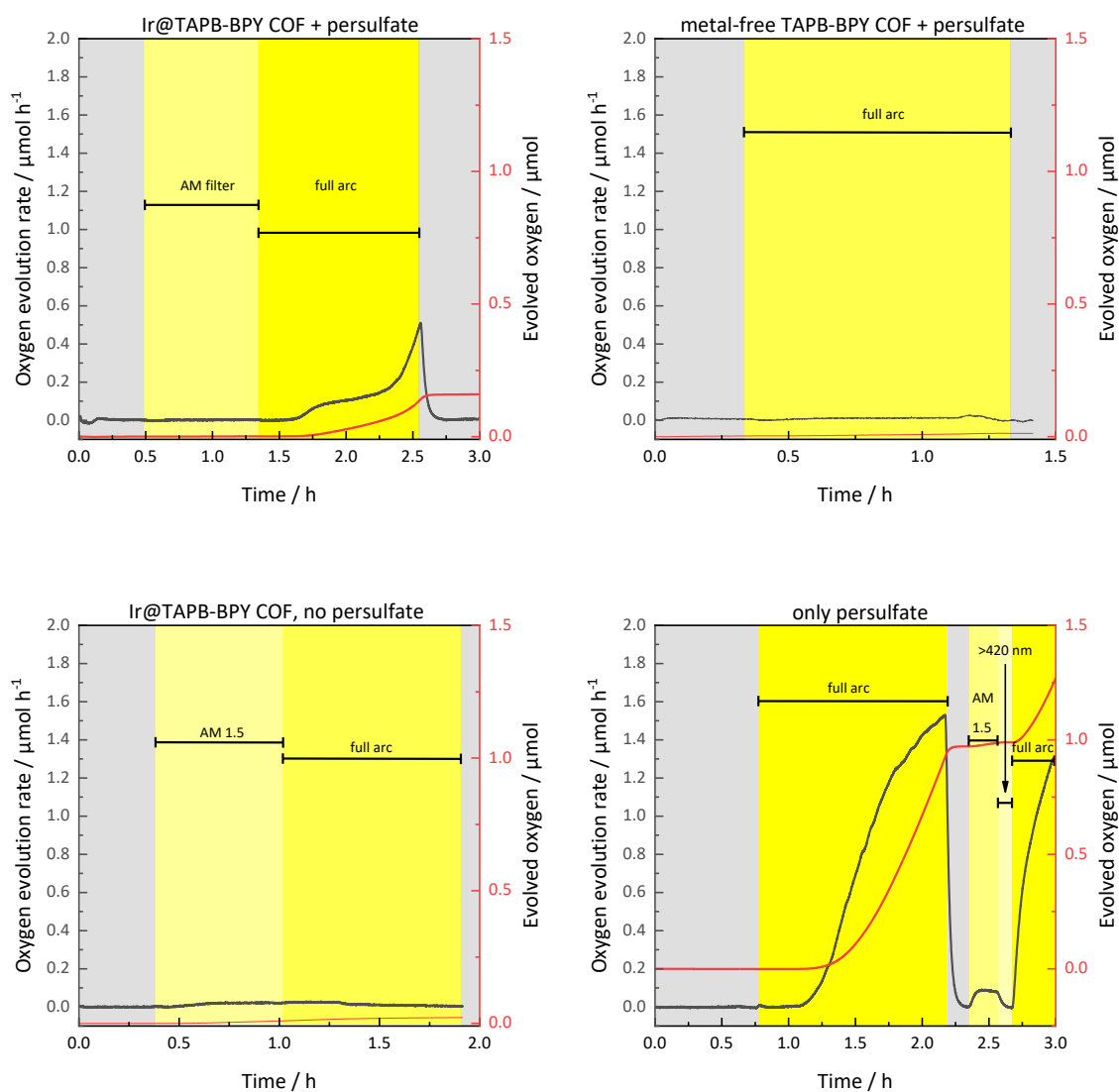
Figure S2-75: Oxygen evolution rates for photocatalytic reactions with persulfate. Reaction conditions: 5.0 mg COF, 5.0 mL 20 mM $Na_2S_2O_8$, 300 W Xenon lamp, filters as annotated.
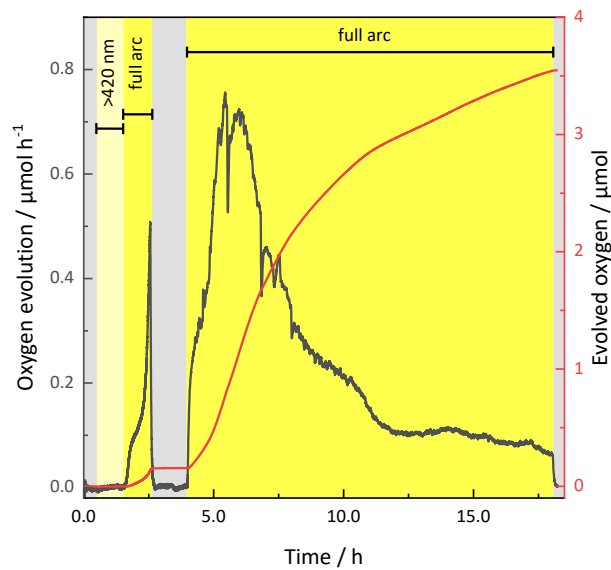
Figure S2-76: Long-time photocatalytic oxygen evolution experiment with Ir@TAPB-BPY COF. Reaction conditions: 5 mg COF, 5 mL 20 mM $Na_2S_2O_8$, 300 W Xenon lamp.
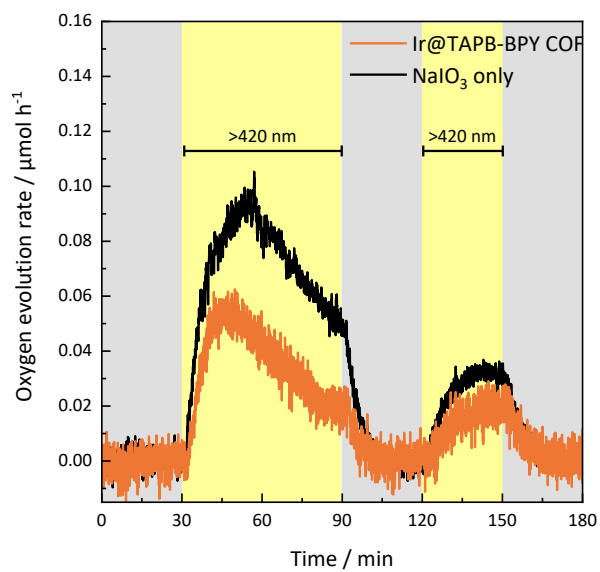
Figure S2-77: Photocatalytic oxygen evolution experiments with Ir@TAPB-BPY COF (1.9 wt%) and a $NaIO_3$ blank. Reaction conditions: 5.0 mg COF, $NaIO_3$ (10 mM, 5 mL), 300 W Xenon lamp, >420 nm longpass filter. As discussed for $AgNO_3$, impurities are proposed to cause the oxygen evolution in both cases.
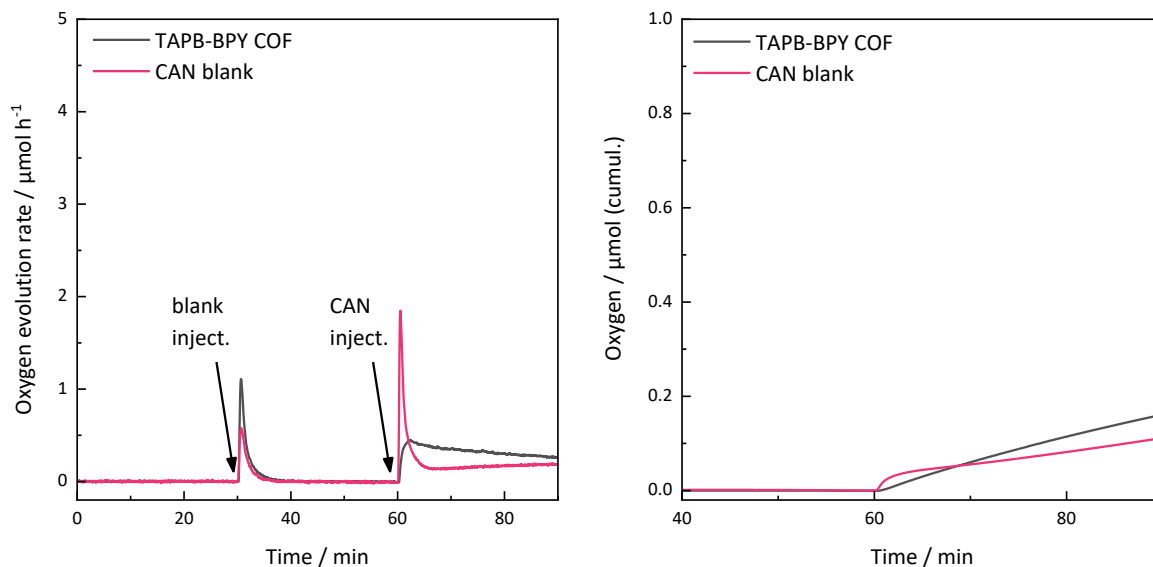
Figure S2-78: Blank experiments for the chemical water oxidation with CAN. Reaction condition: 5 mg TAPB-BPY COF (if stated), 78 mM CAN (final conc.) in 5 mL HNO_3 (pH 1).
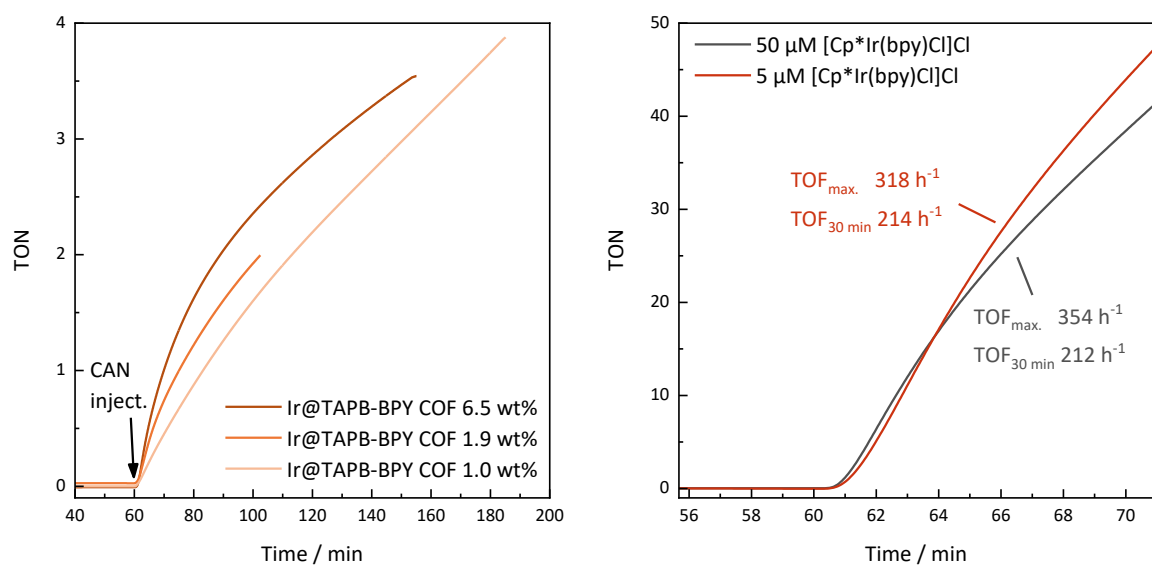
Figure S2-79: TON plot for chemical water oxidation experiments with Ir@TAPB-BPY COFs of varying iridium content as annotated (a). TON plot for chemical water oxidation experiments with molecular [Cp*Ir(bpy)Cl]Cl (b). Reaction conditions: 78 mM CAN in 5 mL HNO_3 (pH 1). WOC concentration as annotated.
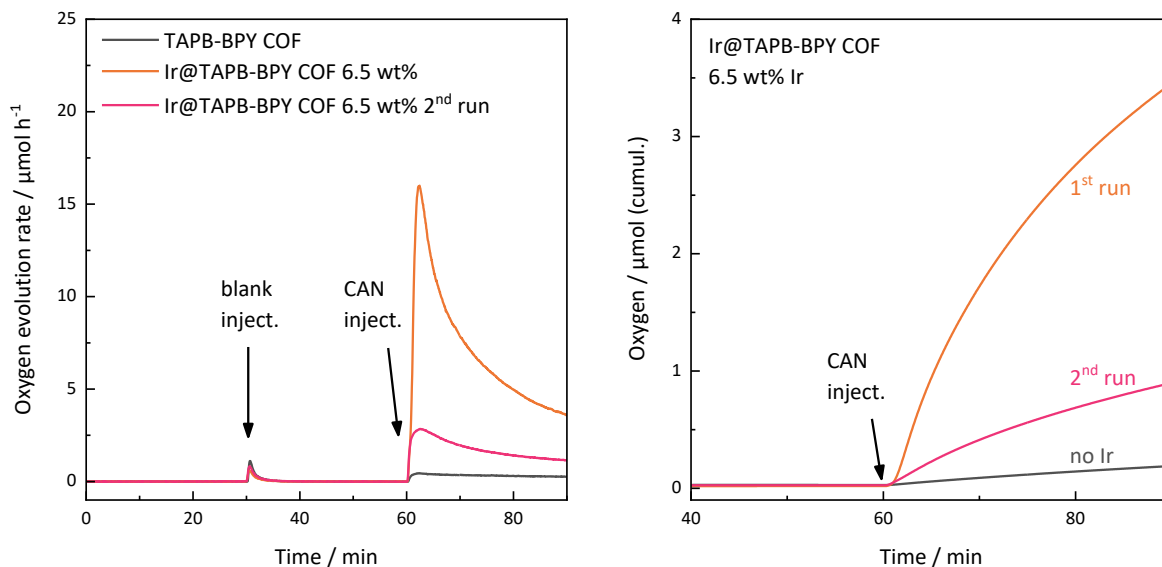
Figure S2-80: Consecutive chemical water oxidation experiments with Ir@TAPB-BPY COF. Iridium-free TAPB-BPY COF shown for comparison. Reaction conditions: 5.0 mg Ir@TAPB-BPY COF (1st run), 78 mM CAN (pH 1 in aq. HNO$_3$, final volume 5 mL). After the first run, the reaction mixture was filtered through the reactor glass frit, and the residual COF was washed with HNO$_3$ (pH 1), water, and acetone before conducting a second run under identical conditions.
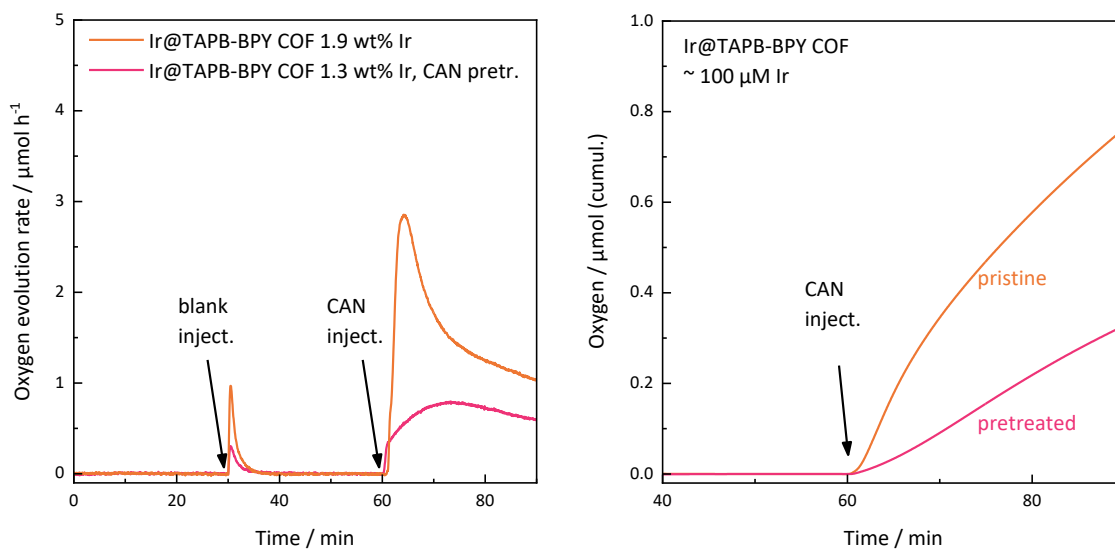
Figure S2-81: Chemical water oxidation experiments with Ir@TAPB-BPY COF with and without pretreatment in 78 mM CAN. Reaction conditions: 5.0 / 7.0 mg Ir@TAPB-BPY COF (pristine / pretreated) to yield ~100 µM Ir, 78 mM CAN (pH 1 in aq. HNO$_3$, final volume 5 mL).
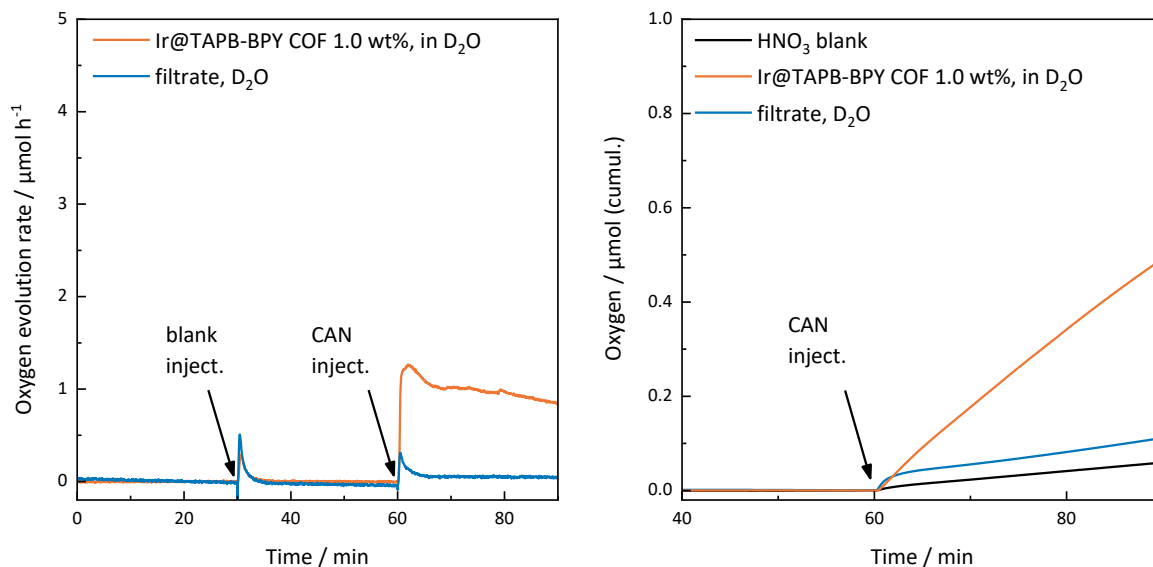
Figure S2-82: Filtration experiment for the chemical oxygen evolution with Ir@TAPB-BPY COF. After catalysis, the COF was separated by filtration, and the filtrate was subjected to a new run in order to assess the catalytic activity of the detached iridium species. Reaction conditions: 5 mg Ir@TAPB-BPY COF with 1.0 wt% Ir, 78 mM CAN (final conc.) in 5 mL DNO₃ (pH 1).
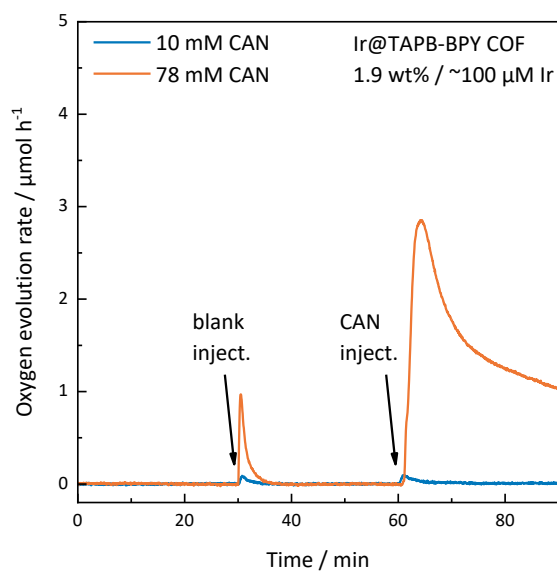
Figure S2-83: Chemical water oxidation experiments with Ir@TAPB-BPY COF and CAN concentrations of 78 mM (orange) and 10 mM (blue). Reaction conditions: 5.0 mg Ir@TAPB-BPY COF, 78 or 10 mM CAN (pH 1 in aq. HNO₃, final volume 5 mL). For the 10 mM experiment, the injection volume was reduced to 50 μL to mitigate background oxygen detection.
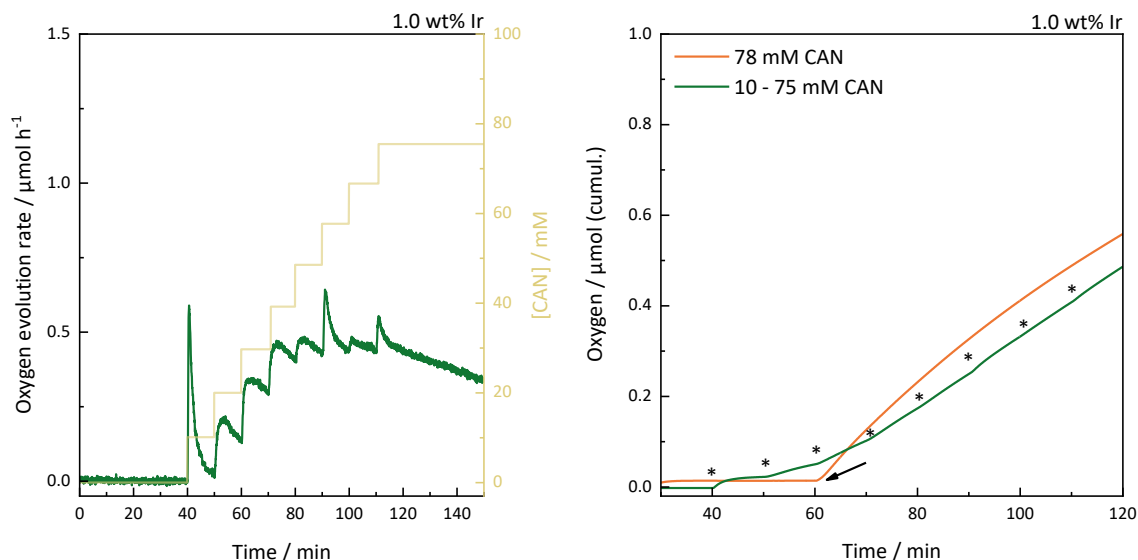
Figure S2-84: Left: Chemical water oxidation experiment with Ir@TAPB-BPY COF and subsequent addition of CAN aliquots. Quickly declining signal suggest that the detected oxygen is not of catalytic nature, but partly caused by insufficiently degassed stock solution and/or syringe. Right: Comparison of oxygen evolved during fixed-concentration and dosing experiments. Reaction conditions: 5.0 mg Ir@TAPB-BPY COF (1.0 wt% Ir), 78 or 10 mM CAN (pH 1 in aq. HNO_3, final volume 5 mL). Asterisks mark subsequent addition of CAN (50 µL of a 1 M stock solution), whereas the arrow marks the injection of a single portion CAN, yielding the stated final concentration.
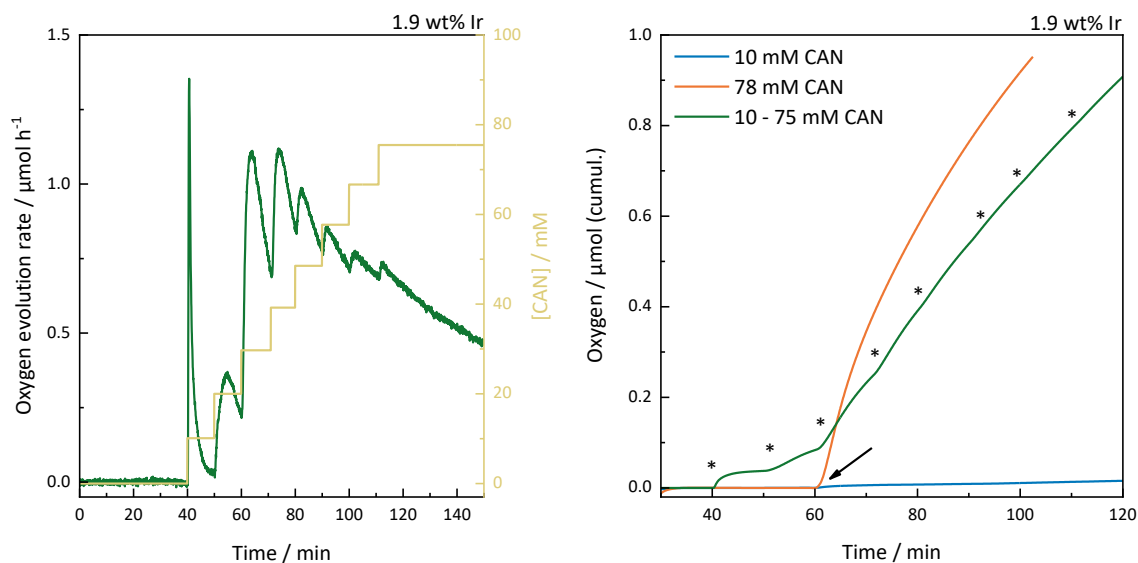
Figure S2-85: Left: Chemical water oxidation experiment with Ir@TAPB-BPY COF and subsequent addition of CAN aliquots. The first, quickly declining signal suggests that the detected oxygen after the first injection is not of catalytic nature, but caused by insufficiently degassed stock solution and/or syringe. Right: Comparison of oxygen evolved during fixed-concentration and dosing experiments. Reaction conditions: 5.0 mg Ir@TAPB-BPY COF (1.9 wt% Ir), 78 or 10 mM CAN (pH 1 in aq. HNO_3, final volume 5 mL). Asterisks mark subsequent addition of CAN (50 µL of a 1 M stock solution), whereas the arrow marks the injection of a single portion CAN, yielding the stated final concentration.
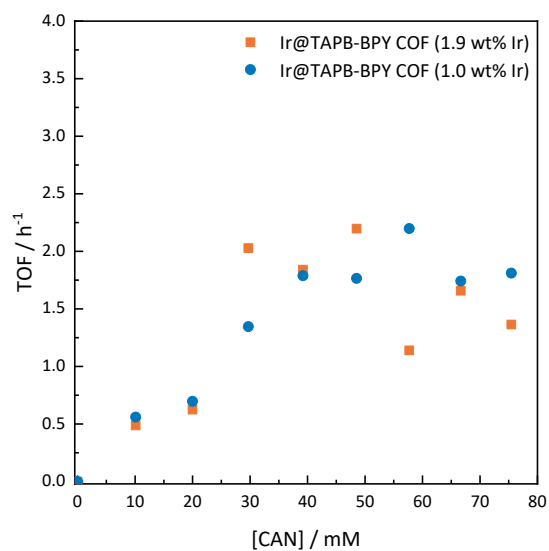
Figure S2-86: Dependance of the catalytic oxygen evolution by Ir@TAPB-BPY COF on the CAN concentration.
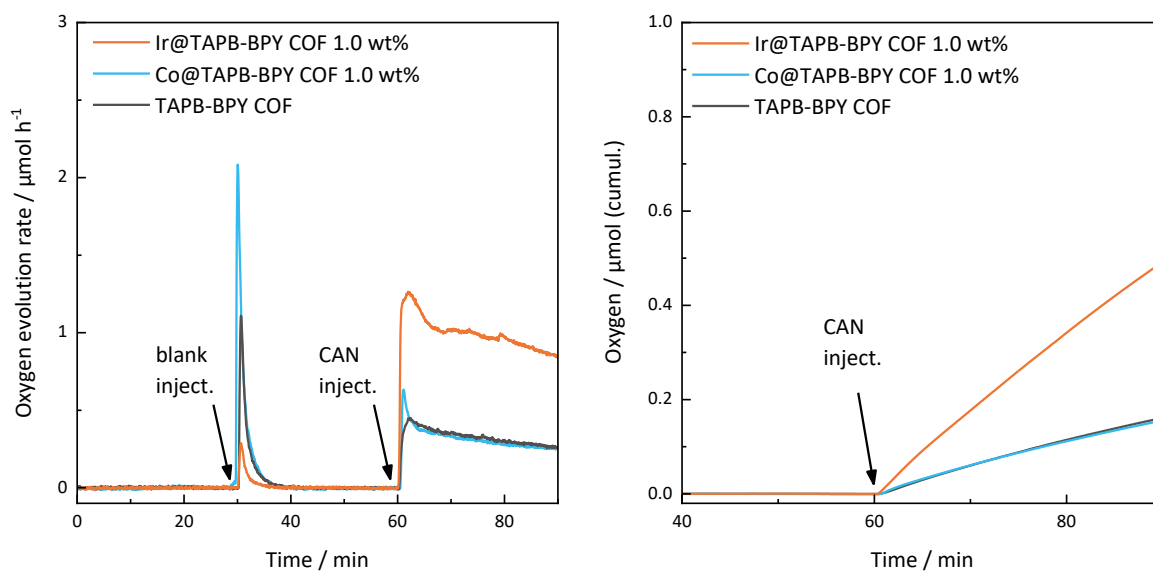
Figure S2-87: Chemical water oxidation experiment with Co@TAPB-BPY COF compared to Ir@TAPB-BPY COF and TAPB-BPY COF. Reaction conditions: 5.0 mg COF, 78 mM CAN (pH 1 in aq. HNO_3, final volume 5 mL).
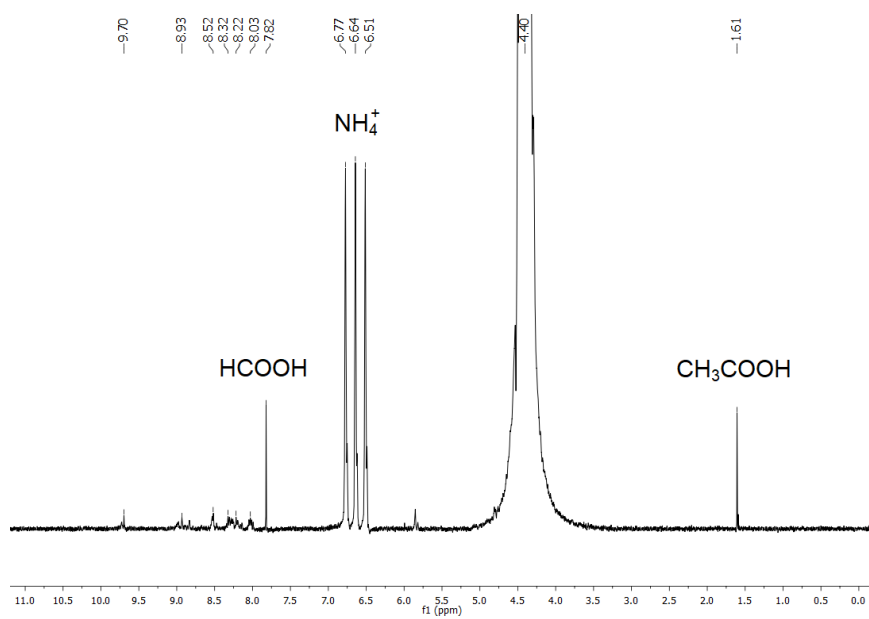
Figure S2-88: ^{1}H NMR spectrum of the filtrate of Ir@TAPB-BPY COF after chemical water oxidation reaction with CAN (78 mM in pH 1 D$_2$O, see Figure S2-82). Chemical shifts referenced to NH$_4^+$ according to literature values.[78]
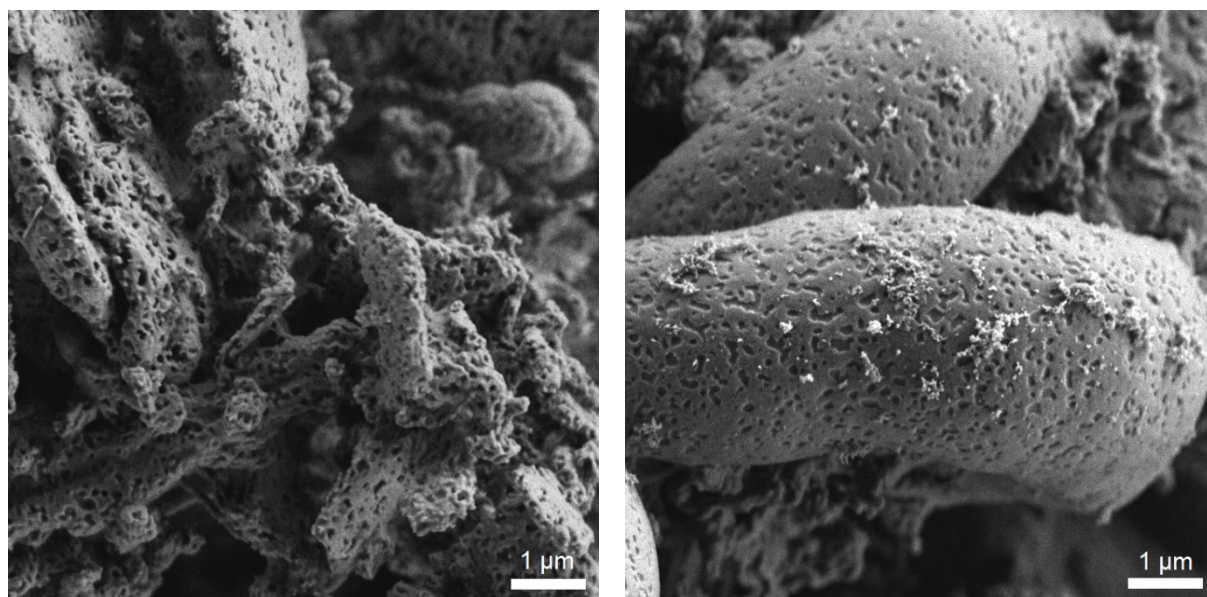
Figure S2-89: SEM images of Ir@TAPB-BPY COF before (left) and after (right) water oxidation catalysis experiments with CAN (78 mM).

Electron Image 2

C Kα1,2

O Kα1

N Kα1,2

Ir Mα1

Cl Kα1

Ce Mα
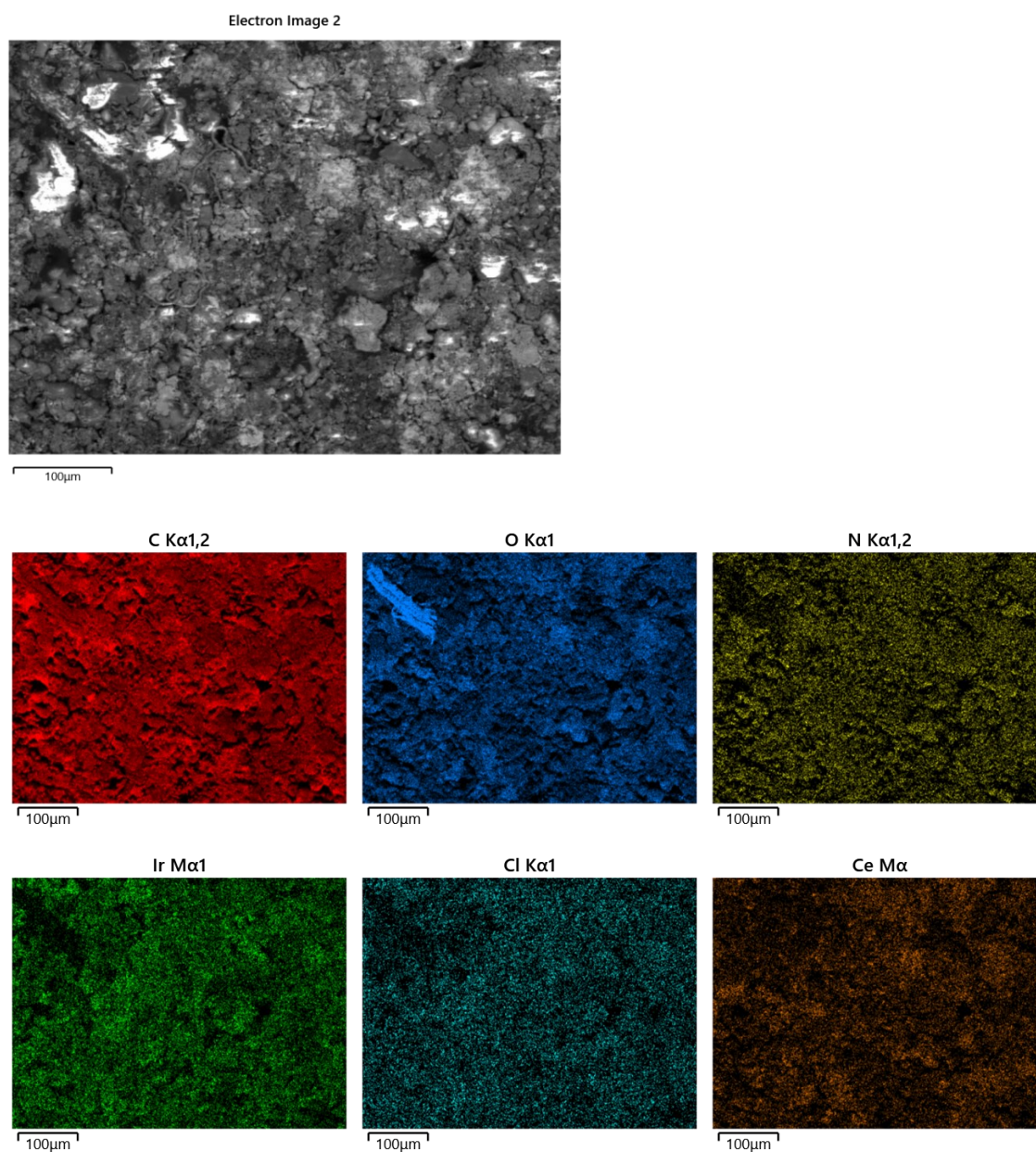
Figure S2-90: SEM elemental mapping of Ir@TAPB-BPY COF after water oxidation catalysis experiments with CAN (78 mM).
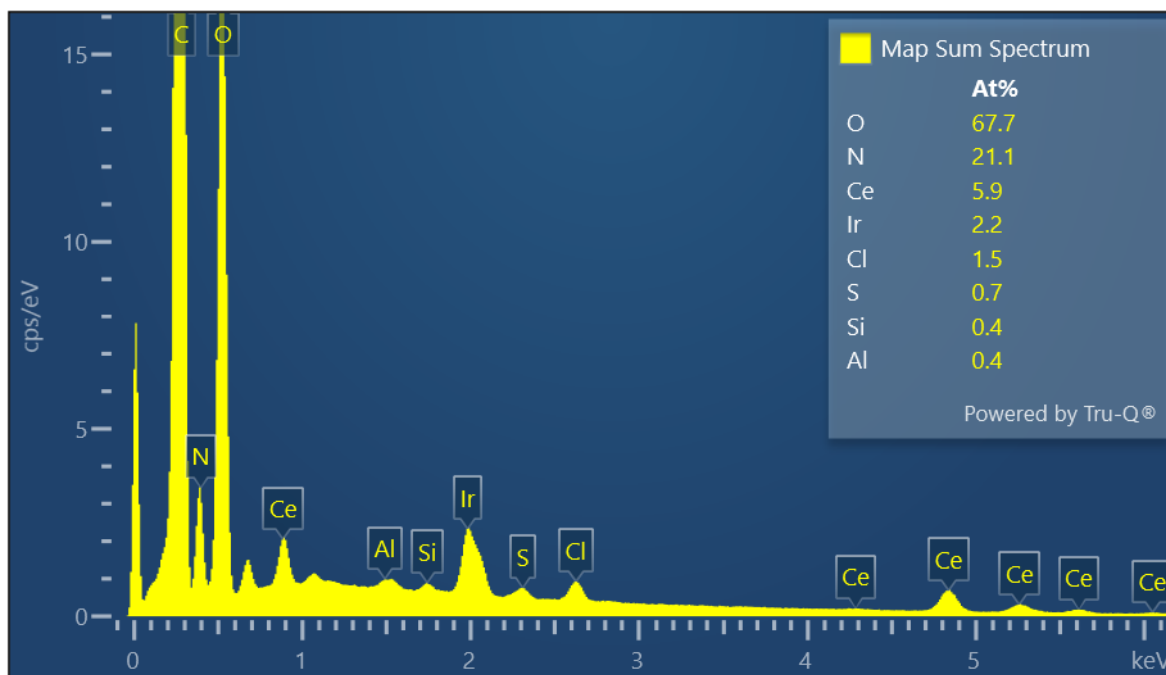
Figure S2-91: Summed-up EDX spectra for the elemental mapping of Ir@TAPB-BPY COF after chemical water oxidation catalysis with CAN (78 mM).
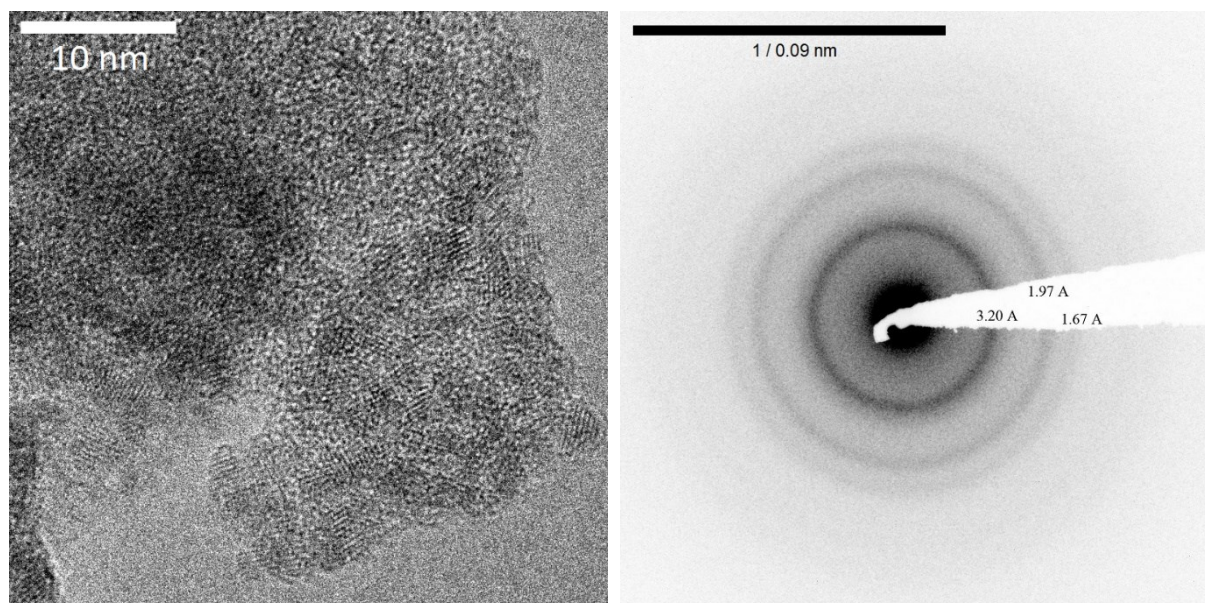
Figure S2-92: TEM image (left) and selected area diffraction pattern (right) of Ir@TAPB-BPY COF after oxygen evolution with 78 mM CAN.
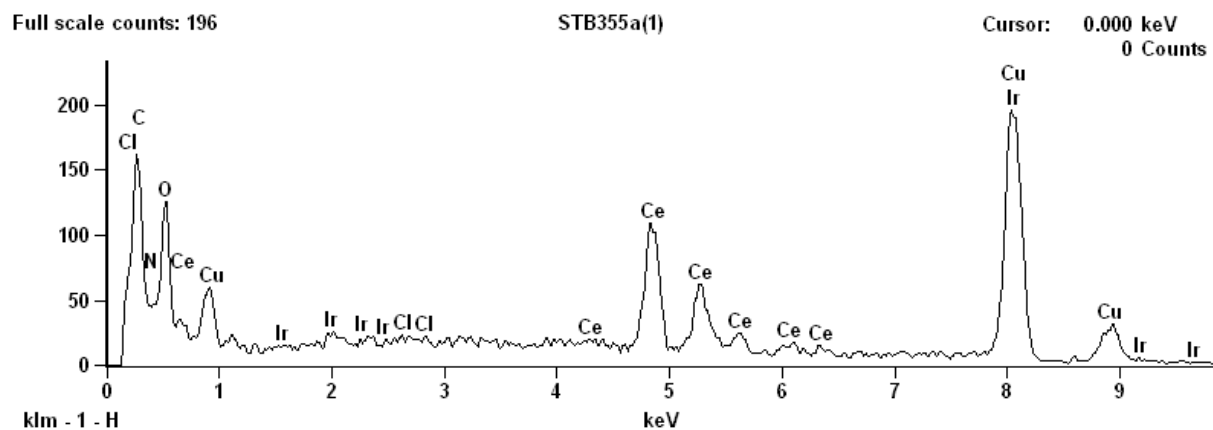
Figure S2-93: EDX data for TEM-examined Ir@TAPB-BPY COF after oxygen evolution with 78 mM CAN (Figure S2-92). The Ce/Ir/Cl ratio (at%) is 93.6/3.9/2.5.
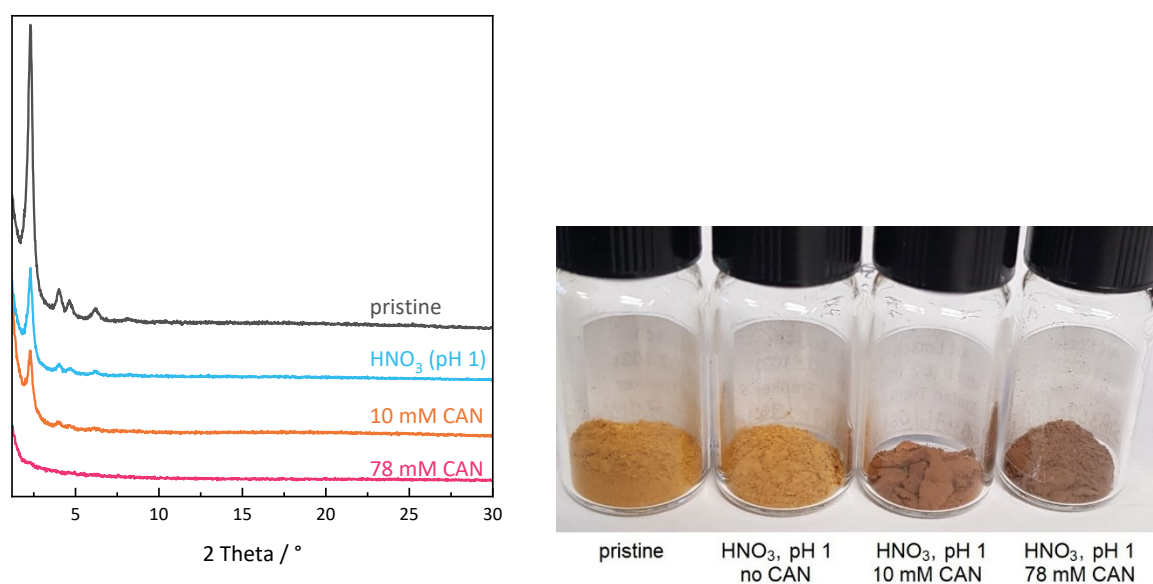
Figure S2-94: Left: XRPD data for Ir@TAPB-BPY COF before and after stability tests under the stated conditions. Right: Photographic image of Ir@TAPB-BPY COF (1.9 wt% Ir) before and after stability tests under the stated conditions. For details, see Table S2-11.
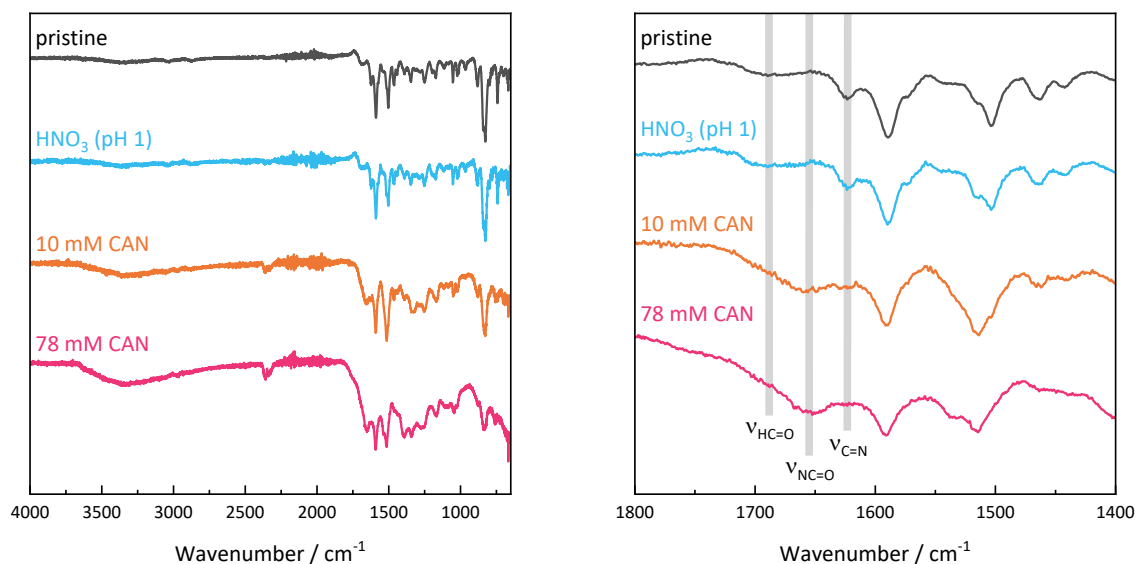
Figure S2-95: FTIR spectra of Ir@TAPB-BPY COF after chemical water oxidation with CAN in varying concentrations.
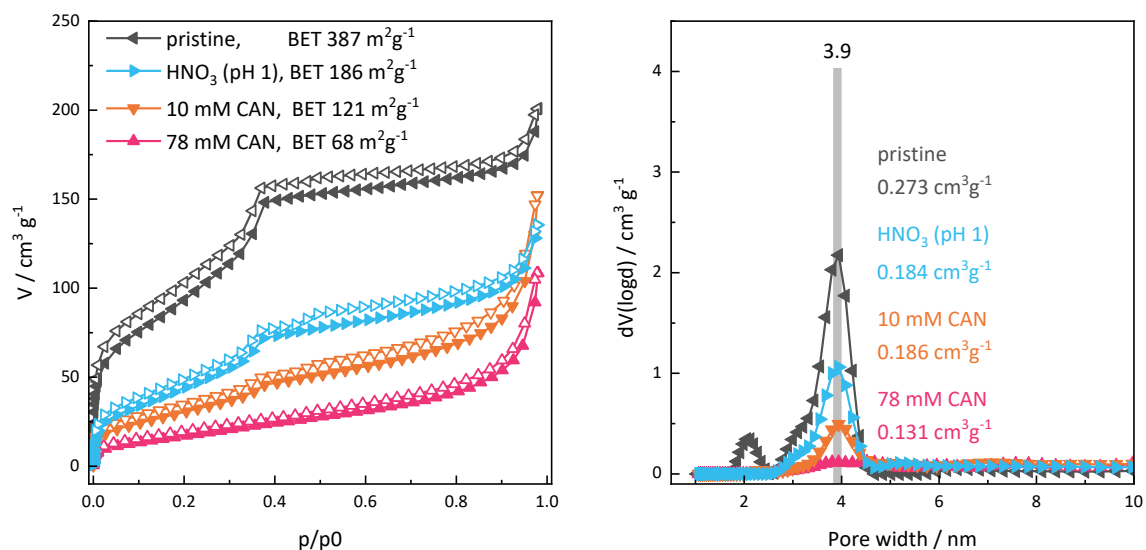
Figure S2-96: Nitrogen sorption isotherms for Ir@TAPB-BPY COF (1.8 wt% Ir) before and after stability tests under the stated conditions (left). The pore size distribution (right) was obtained from a QSDFT kernel for cylindrical pores (adsorption branch). Pore volumes given as annotation.
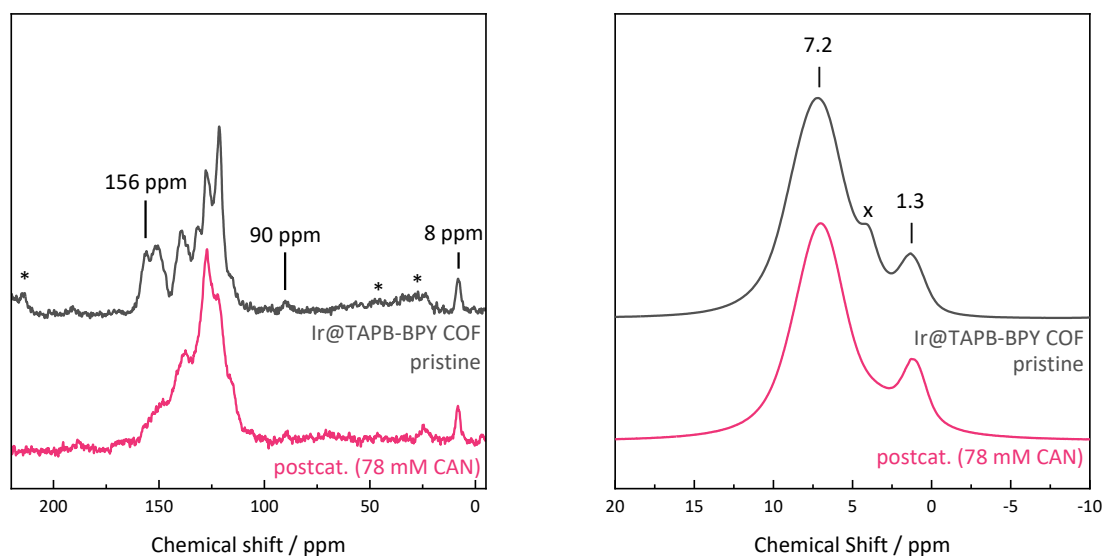
Figure S2-97: 13C (left) and 1H (right) ssNMR spectra of Ir@TAPB-COF (4.7 wt% Ir) before and after oxygen evolution experiments with CAN (78 mM, pH 1). Asterisks mark spinning side bands, cross marks residual water signal.

Table S2-11: ICP data for stability experiments with Ir@TAPB-BPY COF under chemical water oxidation conditions.

	pristine	No CAN	10 mM CAN	78 mM CAN
wt% Ir	1.8 wt%	2.0 wt%	1.7 wt%	1.3 wt%
Ir leakage	-	5-7%	10-12%	18-22%
Ce deposition	-	-	0.2 wt%	10.3 wt%

The statistic error of the ICP measurements was in the range of 0.1-0.2 wt% for the solids.
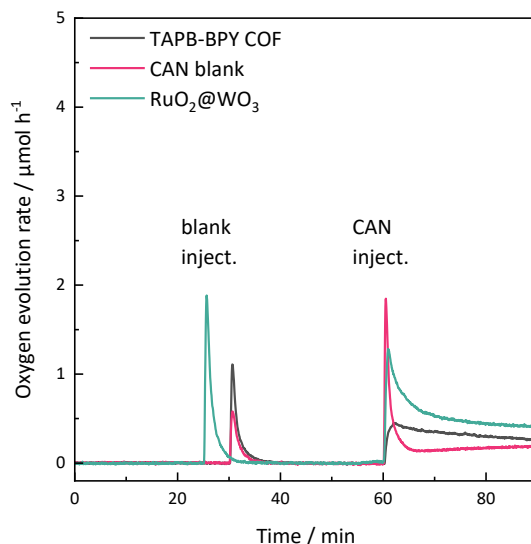
Figure S2-98: Control experiment for the chemical water oxidation with CAN as oxidant (78mM) and ruthenium-loaded tungsten oxide as WOC.
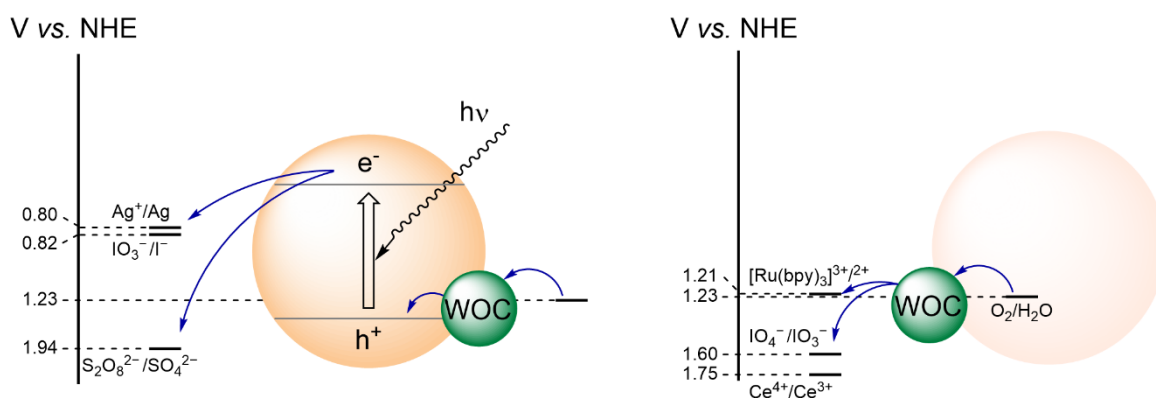
Figure S2-99: Schematic illustration of SEA redox potentials in water oxidation catalysis driven photocatalytically (left) and chemically (right). Not to scale.

6.2.4   References

1   P. Swift, *Surf. Interface Anal.* **1982**, *4*, 47–51.

2   T. L. Barr, S. Seal, *J. Vac. Sci. Technol. A* **1995**, *13*, 1239–1246.

3   M. C. Biesinger, *Appl. Surf. Sci.* **2022**, *597*, 153681.

4   B. P. Biswal, H. A. Vignolo-González, T. Banerjee, L. Grunenberg, G. Savasci, K. Gottschling, J. Nuss, C. Ochsenfeld, B. V. Lotsch, *J. Am. Chem. Soc.* **2019**, *141*, 11082–11092.

5   S. Trenker, L. Grunenberg, T. Banerjee, G. Savasci, L. M. Poller, K. I. M. Muggli, F. Haase, C. Ochsenfeld, B. V. Lotsch, *Chem. Sci.* **2021**, *12*, 15143–15150.

6   L. Yao, A. Rodríguez-Camargo, M. Xia, D. Mücke, R. Guntermann, Y. Liu, L. Grunenberg, A. Jiménez-Solano, S. T. Emmerling, V. Duppel, K. Sivula, T. Bein, H. Qi, U. Kaiser, M. Grätzel, B. V. Lotsch, *J. Am. Chem. Soc.* **2022**, *144*, 10291–10300.

7   T. Sick, A. G. Hufnagel, J. Kampmann, I. Kondofersky, M. Calik, J. M. Rotter, A. Evans, M. Döblinger, S. Herbert, K. Peters, D. Böhm, P. Knochel, D. D. Medina, D. Fattakhova-Rohlfing, T. Bein, *J. Am. Chem. Soc.* **2018**, *140*, 2085–2092.

8   P. Guiglion, C. Butchosa, M. A. Zwijnenburg, *J. Mater. Chem. A* **2014**, *2*, 11996–12004.

9   P. Guiglion, A. Monti, M. A. Zwijnenburg, *J. Phys. Chem. C* **2017**, *121*, 1498–1506.

10   D. J. Woods, S. A. J. Hillman, D. Pearce, L. Wilbraham, L. Q. Flagg, W. Duffy, I. McCulloch, J. R. Durrant, A. A. Y. Guilbert, M. A. Zwijnenburg, R. S. Sprick, J. Nelson, A. I. Cooper, *Energy Environ. Sci.* **2020**, *13*, 1843–1855.

11   J. K. Nørskov, J. Rossmeisl, A. Logadottir, L. Lindqvist, J. R. Kitchin, T. Bligaard, H. Jónsson, *J. Phys. Chem. B* **2004**, *108*, 17886–17892.

12   J. Rossmeisl, J. K. Nørskov, C. D. Taylor, M. J. Janik, M. Neurock, *J. Phys. Chem. B* **2006**, *110*, 21833–21839.

13   J. Rossmeisl, Z.-W. Qu, H. Zhu, G. J. Kroes, J. K. Nørskov, *J. Electroanal. Chem.,* **2007**, *607*, 83–89.

14   A. D. Becke, *J. Chem. Phys.* **1993**, *98*, 5648–5652.

15   C. Lee, W. Yang, R. G. Parr, *Phys. Rev. B* **1988**, *37*, 785–789.

16   S. H. Vosko, L. Wilk, M. Nusair, *Can. J. Phys.* **1980**, *58*, 1200–1211.

17   P. J. Stephens, F. J. Devlin, C. F. Chabalowski, M. J. Frisch, *J. Phys. Chem.* **1994**, *98*, 11623–11627.

18   A. Schäfer, H. Horn, R. Ahlrichs, *J. Chem. Phys.* **1992**, *97*, 2571–2577.

19   F. Weigend, R. Ahlrichs, *Phys. Chem. Chem. Phys.* **2005**, *7*, 3297–3305.

20   D. Andrae, U. Häußermann, M. Dolg, H. Stoll, H. Preuß, *Theor. Chim. Acta* **1990**, *77*, 123–141.

21   S. G. Balasubramani, G. P. Chen, S. Coriani, M. Diedenhofen, M. S. Frank, Y. J. Franzke, F. Furche, R. Grotjahn, M. E. Harding, C. Hättig, A. Hellweg, B. Helmich-Paris, C. Holzer, U. Huniar, M. Kaupp, A. Marefat Khah, S. Karbalaei Khani, T. Müller, F. Mack, B. D. Nguyen, S. M. Parker, E. Perlt, D. Rappoport, K. Reiter, S. Roy, M. Rückert, G. Schmitz, M. Sierka, E. Tapavicza, D. P. Tew, C. van Wüllen, V. K. Voora, F. Weigend, A. Wodyński, J. M. Yu, *J. Chem. Phys.* **2020**, *152*, 184107.

22   F. Furche, R. Ahlrichs, C. Hättig, W. Klopper, M. Sierka, F. Weigend, *Wiley Interdiscip. Rev. Comput. Mol. Sci.* **2014**, *4*, 91–100.

23   A. Klamt, G. Schüürmann, *J. Chem. Soc., Perkin Trans. 2* **1993**, 799–805.

24   M. Jakoobi, N. Halcovitch, G. F. S. Whitehead, A. G. Sergeev, *Angew. Chem.* **2017**, *129*, 3314–3317.

25   Z. Yang, Z. Zhu, R. Luo, X. Qiu, J. Liu, J.-K. Yang, W. Tang, *Green Chem.* **2017**, *19*, 3296–3301.

26   F. Haase, E. Troschke, G. Savasci, T. Banerjee, V. Duppel, S. Dörfler, M. M. J. Grundei, A. M. Burow, C. Ochsenfeld, S. Kaskel, B. V. Lotsch, *Nat. Commun.* **2018**, *9*, 2600.

27   J. Chen, X. Tao, C. Li, Y. Ma, L. Tao, D. Zheng, J. Zhu, H. Li, R. Li, Q. Yang, *Appl. Catal. B* **2020**, *262*, 118271.

28   H. A. Vignolo-González, S. Laha, A. Jiménez-Solano, T. Oshima, V. Duppel, P. Schützendübe, B. V. Lotsch, *Matter* **2020**, *3*, 464–486.

29   H. Firouzabadi, P. Salehi, A. R. Sardarian, M. Seddighi, *Synth. Commun.* **1991**, *21*, 1121–1127.

30   F. D. Sypaseuth, C. Matlachowski, M. Weber, M. Schwalbe, C. C. Tzschucke, *Chem. Eur. J.* **2015**, *21*, 6564–6571.

31   E. Bêche, P. Charvin, D. Perarnau, S. Abanades, G. Flamant, *Surf. Interface Anal.* **2008**, *40*, 264–267.

32   E. Paparazzo, G. M. Ingo, N. Zacchetti, *J. Vac. Sci. Technol. A* **1991**, *9*, 1416–1420.

33   D. R. Mullins, *Surf. Sci. Rep.* **2015**, *70*, 42–85.

34   V. K. Kaushik, J. Electron Spectrosc. Relat. Phenom. **1991**, 56, 273–277.

35   S. Golczak, A. Kanciurzewska, M. Fahlman, K. Langer, J. Langer, *Solid State Ionics* **2008**, *179*, 2234–2239.

36   F. Kapteijn, J. A. Moulijn, S. Matzner, H.-P. Boehm, *Carbon* **1999**, *37*, 1143–1150.

37   H. Wang, T. Maiyalagan, X. Wang, *ACS Catal.* **2012**, *2*, 781–794.

38   M. K. Rabchinskii, S. D. Saveliev, D. Y. Stolyarova, M. Brzhezinskaya, D. A. Kirilenko, M. V. Baidakova, S. A. Ryzhkov, V. V. Shnitov, V. V. Sysoev, P. N. Brunkov, *Carbon* **2021**, *182*, 593–604.

39   Y. Wan, L. Wang, H. Xu, X. Wu, J. Yang, *J. Am. Chem. Soc.* **2020**, *142*, 4508–4516.

40   J. Schneider, D. W. Bahnemann, *J. Phys. Chem. Lett.* **2013**, *4*, 3479–3483.

41   I. Ivanova, T. A. Kandiel, Y.-J. Cho, W. Choi, D. Bahnemann, *ACS Catal.* **2018**, *8*, 2313–2325.

42   T. H. Jeon, D. Monllor-Satoca, G.-H. Moon, W. Kim, H.-I. Kim, D. W. Bahnemann, H. Park, W. Choi, *Nat. Commun.* **2020**, *11*, 967.

43   H. N. Po, J. H. Swinehart, T. L. Allen, *Inorg. Chem.* **1968**, *7*, 244–249.

44   J. A. McMillan, B. Smaller, *J. Chem. Phys.* **1961**, *35*, 1698–1701.

45   T. Buch, *J. Chem. Phys.* **1965**, *43*, 761–762.

46   H. Mogi, M. Okazaki, S. Nishioka, K. Maeda, *Sustain. Energy Fuels* **2021**, *5*, 5694–5698.

47   X. Wang, S. Li, H. Yu, J. Yu, S. Liu, *Chem. Eur. J.* **2011**, *17*, 7777–7780.

48   F. Fathi, M. Schlitt, D. B. Pedersen, H.-B. Kraatz, *Langmuir* **2011**, *27*, 12098–12105.

49   J. P. Abid, A. W. Wark, P. F. Brevet, H. H. Girault, *Chem. Commun.* **2002**, 792–793.

50   H. A. Mahlmann, T. E. Willmarth, *Nature* **1964**, *202*, 590–591.

51   Y. Konishi, H. Saijo, H. Hada, M. Tamura, *Nature* **1977**, *268*.

52   Z. Shen, H. Duan, H. Frey, *Adv. Mater.* **2007**, *19*, 349–352.

53   J. Belloni, M. Mostafavi, H. Remita, J.-L. Marignier, M.-O. Delcourt, *New J. Chem.* **1998**, 1239–1255.

54   C. L. Thomsen, D. Madsen, S. R. Keiding, J. Tho/gersen, O. Christiansen, *J. Chem. Phys.* **1999**, *110*, 3453–3462.

55   V. Svoboda, R. Michiels, A. C. LaForge, J. Med, F. Stienkemeier, P. Slavíček, H. J. Wörner, *Sci. Adv.* **2020**, *6*, eaaz0385.

56   H. Hada, Y. Yonezawa, Y. Akio, A. Kurakake, *J. Phys. Chem.* **1976**, *80*, 2728–2731.

57   M. K. Temgire, S. S. Joshi, *Radiat. Phys. Chem.* **2004**, *71*, 1039–1044.

58   S. Ge, J. Zhao, G. Ma, *Langmuir* **2020**, *36*, 4088–4097.

59   F. Cataldo, O. Ursini, G. Angelini, *J. Radioanal. Nucl. Chem.* **2016**, *307*, 447–455.

60   E. A. Owen, G. I. Williams, *J. Sci. Instrum.* **1954**, *31*, 49–54.

61   S. Bi, C. Yang, W. Zhang, J. Xu, L. Liu, D. Wu, X. Wang, Y. Han, Q. Liang, F. Zhang, *Nat. Commun.* **2019**, *10*, 2467.

62   E. Jin, Z. Lan, Q. Jiang, K. Geng, G. Li, X. Wang, D. Jiang, *Chem* **2019**, *5*, 1632–1647.

63   J. Xu, C. Yang, S. Bi, W. Wang, Y. He, D. Wu, Q. Liang, X. Wang, F. Zhang, *Angew. Chem. Int. Ed.* **2020**, *59*, 23845–23853.

64   S. Chai, X. Chen, X. Zhang, Y. Fang, R. S. Sprick, X. Chen, *Environ. Sci. Nano* **2022**, *9*, 2464–2469.

65   Y. Yang, X. Chu, H.-Y. Zhang, R. Zhang, Y.-H. Liu, F.-M. Zhang, M. Lu, Z.-D. Yang, Y.-Q. Lan, *Nat. Commun.* **2023**, *14*, 593.

66   Y. He, G. Liu, Z. Liu, J. Bi, Y. Yu, L. Li, *ACS Energy Lett.* **2023**, *8*, 1857–1863.

67   L. Chen, L. Wang, Y. Wan, Y. Zhang, Z. Qi, X. Wu, H. Xu, *Adv. Mater.* **2020**, *32*, e1904433.

68   J. Xie, S. A. Shevlin, Q. Ruan, S. J. A. Moniz, Y. Liu, X. Liu, Y. Li, C. C. Lau, Z. X. Guo, J. Tang, *Energy Environ. Sci.* **2018**, *11*, 1617–1624.

69   R. S. Sprick, Z. Chen, A. J. Cowan, Y. Bai, C. M. Aitchison, Y. Fang, M. A. Zwijnenburg, A. I. Cooper, X. Wang, *Angew. Chem. Int. Ed.* **2020**, *59*, 18695–18700.

70   F. A. Frame, T. K. Townsend, R. L. Chamousis, E. M. Sabio, T. Dittrich, N. D. Browning, F. E. Osterloh, *J. Am. Chem. Soc.* **2011**, *133*, 7264–7267.

71   T. Zhang, K. E. deKrafft, J.-L. Wang, C. Wang, W. Lin, *Eur. J. Inorg. Chem.* **2014**, *2014*, 698–707.

72   J. T. Kirner, J. J. Stracke, B. A. Gregg, R. G. Finke, *ACS Appl. Mater. Interfaces* **2014**, *6*, 13367–13377.

73   A. Mills, M. A. Valenzuela, *J. Photochem. Photobiol. A* **2004**, *165*, 25–34.

74   I. A. Ike, K. G. Linden, J. D. Orbell, M. Duke, *Chem. Eng. J.* **2018**, *338*, 651–669.

75   S. Wacławek, H. V. Lutze, K. Grübel, V. V. Padil, M. Černík, D. Dionysiou, *Chem. Eng. J.* **2017**, *330*, 44–62.

76   H. Liu, T. A. Bruton, W. Li, J. van Buren, C. Prasse, F. M. Doyle, D. L. Sedlak, *Environ. Sci. Technol.* **2016**, *50*, 890–898.

77   P. D. Bartlett, J. D. Cotman, *J. Am. Chem. Soc.* **1949**, *71*, 1419–1422.

78   A. Savini, P. Belanzoni, G. Bellachioma, C. Zuccaccia, D. Zuccaccia, A. Macchioni, *Green Chem.* **2011**, *13*, 3360.

6.3   Supporting Information for Chapter 3

6.3.1   Materials and Methods

If not stated otherwise, all chemicals were obtained from commercial sources and used without further purification.

Physisorption analysis

Argon sorption measurements were performed at 87 K with a Quantachrome Instruments Autosorb iQ MP. Samples of about 20 mg were preheated in vacuo (10^{-7} mbar) at 120 °C for 12 h. ASiQwin Version 3.01 was used for data analysis. Pore size distributions were evaluated using the carbon QSDFT

kernel for cylindrical pores for both the adsorption and desorption branch. Expected pore sizes were derived from structural models in Materials Studio v6.0.0.

Mass spectrometry

Experiments were performed on a Thermo Finnigan MAT 90 or MAT 95 mass spectrometer using electrospray ionization (ESI). m/z values were calculated using Perkin Elmer ChemDraw® Professional Version 16.0.0.82 (68).

Infrared spectroscopy

Infrared spectroscopy was conducted using a Perkin Elmer Spektrum BX II FT-IR equipped with an ATR unit (Smith Detection Dura-Sample IIR diamond). Background correction was done before sample measurements. Depicted spectra are the mean of five scans.

Elemental analysis

Elemental analysis (C, H, N) was conducted on an Elementar vario EL using Helium as carrier gas.

UV-Vis

If not stated otherwise, UV-Vis spectra of molecular compounds were measured as solutions in acetonitrile on a Agilent Cary 60 UV-Vis spectrometer. Spectra of solid FEAx-COF were measured on a Jasco V-650 spectrophotometer.

Photoluminescence (PL)

Steady-state luminescence data was collected at RT using an Edinburgh FLS980 spectrometer. The samples were excited by a housed 450 W xenon lamp whose light passed through a single grating (1800 l/mm, 250 nm blaze) Czerny-Turner monochromator and finally a bandwidth slit. The sample emission was passed through a double grating (1200 l/mm, 500 nm blaze) Czerny-Turner monochromator and detected by a peltier-cooled Hamamatsu R928P photomultiplier tube.

X-ray powder diffraction (XRPD)

XRPD patterns were recorded at room temperature on a Bruker D8 Discovery with Ni-filtered CuKα-radiation (1.5406 Å) and a position-sensitive LynxEye detector. Materials Studio v6.0.0 was used for structural modelling, XRD pattern simulations, and Pawley Refinement.

Single-crystal X-ray diffraction

Single-crystal X-ray diffraction data were collected at room temperature on a Bruker D8 Venture diffractometer equipped with a rotating anode generator with Mo Kα radiation (λ = 0.71073 Å). The diffraction intensities were integrated using the SAINT software package and a multiscan absorption correction was applied with SADABS-2016/2 (Bruker, 2016/2). The crystal structure was solved using intrinsic phasing (SHELXT)[1] and refined against F2 by applying the full-matrix least-squares method (SHELXL)[2] using the software OLEX2.[3] Hydrogen atoms were inserted at idealized positions and refined using a riding model. All non-hydrogen atoms were refined anisotropically using full-matrix

least-squares. Illustration of molecular structures with thermal ellipsoids was done with ORTEP-3 Version 2014.1.

Thermogravimetric analysis (TGA)

For TGA, the samples were filled into corundum crucibles. Measurements were carried out using a Netzsch STA 449 F5 Jupiter with an argon flow of 20 mL/min in a temperature range between 20 and 900 °C and a heating rate of 5 K/min. Data handling was performed with the Netzsch Proteus® software package.

Scanning electron microscopy

Images were recorded on a Zeiss Merlin SEM with an EHT voltage of 1.2 kV.

Transmission electron microscopy

The sample was slightly ground and distributed onto a holey carbon/copper grid. TEM was performed with a Philips CM 30 ST microscope (300 kV, LaB_6 cathode).

Electron paramagnetic resonance (EPR)

EPR spectra were measured with a Bruker EMXnano. Experiments were conducted with 2.0 mg FEAx-COF in MeCN/water (1 mL, 1:1) after sonication for 5 min and oxygenation for 5 minutes. 0.1 mmol of the stated spin trap was added before illumination with blue LEDs (λ = 463 nm) for 5-15 minutes.

Supercritical CO2 drying

COF samples were kept soaked in ethanol prior to supercritical CO_2 extraction on a Leica EM CPD300 critical point dryer with ethanol as exchange liquid.

Nuclear magnetic resonance spectroscopy

Solid-state nuclear magnetic resonance experiments on pristine FEAx-COF were performed on Bruker Neo NMR spectrometer operating at a ^{1}H Larmor frequency of 700 MHz using a 1.3 mm triple-resonance MAS probe and a spinning frequency of 55.55 kHz. The ^{13}C spectrum was measured as a direct-polarization ^{13}C experiment with a total of 4096 scans and a delay of 25 s. The COF sample was dried at 60 °C in vacuo prior to measurement.

Solid-state nuclear magnetic resonance experiments on FEAx-COF after catalysis were performed on Bruker Neo 600 MHz instrument using a 3.2 mm outer diameter ZrO_2 rotor and a BL3.2 MAS double resonance probe at a spinning frequency between 20 and 24 kHz. The ^{13}C spectrum was acquired by direct excitation accompanied by high power proton decoupling in a total of 3320 scans, and was subjected to background subtraction.

Spectra of soluble samples were recorded using a Bruker AV400TR or a Jeol Eclipse 400+ spectrometer. Chemical shifts are denoted on the scale in parts per million (ppm), calibrated to residual non-deuterated solvent (^{1}H-NMR: 7.26 for $CDCl_3$, 2.50 for DMSO-d_6) or solvent carbon resonances (13C-

NMR: CDCl₃: 77.16 for $CDCl_3$, 39.52 for DMSO-d_6). Multiplicities are denoted as: s = singlet, d = duplet, t = triplet, q = quartet, m = multiplet, or as a combination thereof. Spectra were analyzed and processed using MestReNova version 10.0.2-15465.

Diffusion coefficient determination

The pulsed field gradient NMR technique (PFG NMR) was applied to determine the relative diffusion coefficients D_{TMS}/D_M for M = FEAx or HEAx in acetonitrile-d_3 and acetonitrile-d_3/water-d_2 1:1 as a measure for the aggregation behaviour, as shown in Eq. S3-1.[4] Eq. S3-1 contains the diffusion coefficient D_t, numerical correction factors $c\ f_s$ and the hydrodynamic radius r_H of the sample (sa) and a standard (st). Tetramethylsilane (TMS) served as an internal standard for viscosity and temperature. The measurements were performed in 5 mm tubes on a Bruker Avance III 400 MHz spectrometer at 300 K with a stimulated-echo sequence[5] and default spoiler gradient (*diff*Ste program, Bruker TopSpin). A gradient pulse with a lenght δ = 1 ms (opt shape) and a diffusion time Δ = 50 ms was applied. The gradient was varied linearly in 16 steps between 4.03 and 80.63 Gs/cm. Data processing was performed with the Bruker TopSpin 3.5 Dynamics module using automated peak picking and fitting of the signal Intensity vs. gradient *B* according to the Stejskal-Tanner equation (Eq. S3-2). Experiments were repeated at least three times with an appropriate number of scans (error bars represent the standard deviation).

$$\frac{D_t^{st}}{D_t^{sa}} = \frac{c^{sa} f_s^{sa} r_H^{sa}}{c^{st} f_s^{st} r_H^{st}} \qquad\text{(Eq. S3-1)}$$

$$\frac{I}{I_0} = e^{-BD} \qquad\text{(Eq. S3-2)}$$

Quantum-chemical calculations

Structures for all investigated molecular compounds were optimized on PBE0-D3/def2-TZVP level of theory.[6–9] Subsequent frequency calculations were performed on the same level of theory to ensure all minima to be true minima on the potential energy hypersurface. The same level of theory was used to calculate vertical radical stabilization energies as total energy differences between radical anionic, radical cationic, and neutral states of investigated model systems. Solvation effects have been considered using the implicit solvation model COSMO with a value of 36.64 as the dielectric constant to represent acetonitrile. Difference densities were calculated on the TD-PBE0/def2-TZVP//PBE0-D3/def2-TZVP level of theory, using the lowest vertical excitation. Calculations were performed using the Turbomole program package in version 7.3.[10]

NMR chemical shieldings were obtained on B97-2/pcsSeg-2 level of theory using the FermiONs++ program package.[11–13] NMR chemical shifts were obtained as differences of NMR chemical shieldings with respect to tetramethylsilane for carbon and hydrogen and nitromethane for nitrogen atoms on the same level of theory.

High pressure liquid chromatography with mass spectrometry (HPLC-MS)

High pressure liquid chromatography with mass spectrometry (HPLC-MS) was performed on an Agilent 1290 Infinity II LC system with an Agilent diode array detector (DAD; G7117B) connected to an AGILENT InfinityLab LC/MSD XT single quadrupole mass spectrometer (G6135B) with a multimode ESI-APCI ionization source. Analysis of the combined signals was performed in Agilent ChemStation software.

Chromatographic separation was achieved on an AGILENT Zorbax RRHD SB-C18 column (2.1x50 mm, 1.8 µm) at 40°C with mixtures of acetonitrile (MeCN), water and formic acid (FA), according to the solvent composition timetable (Table S3-1) and a total solvent flow of 0.7 mL/min. Absorption of the compounds was measured at 280±2 nm (reference: 325±10 nm) with DAD.

MS data was obtained using MM-APCI ionization (positive/negative 50:50) in scan mode for signals between 100-600 m/z.

Table S3-1: Solvent composition timetable (HPLC-MS).

Time / min	Water / %	Water+1% FA / %	MeCN / %	MeCN+1% FA / %
0	72	8	18	2
2.00	45	5	45	5
2.01	4.5	0.5	85.5	9.5
2.50	4.5	0.5	85.5	9.5

Sample preparation

For a typical measurement, 25 µL of the sample suspension were diluted with acetonitrile/water 8:2 (975 µL) and filtered through a 13 mm 0.2 µm WWPTFE PALL Aerodisc® MS Syringe Filter. 1 µL of the filtrate was then injected.

Calibration

Equation	y = a + b*x
Plot	MBA
Weight	No Weighting
Intercept	12.56574 ± 2.857
Slope	0.59593 ± 0.0035
Residual Sum of Square	108.3431
Pearson's r	0.99993
R-Square (COD)	0.99986
Adj. R-Square	0.99982
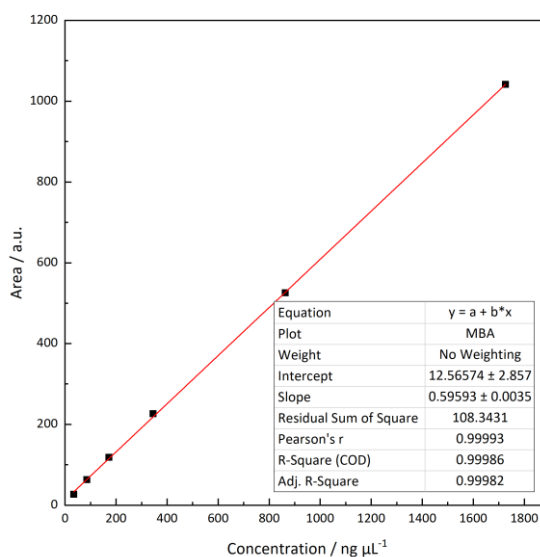
Figure S3-1: The calibration line for MBA shows a linear response. Area is obtained by peak integration acquired by DAD-detector absorption at 280±2 nm (Reference 325±10 nm).

Equation	y = a + b*x
Plot	MBAld
Weight	No Weighting
Intercept	5.42954 ± 10.830
Slope	9.73384 ± 0.0553
Residual Sum of Square	331.28268
Pearson's r	0.99997
R-Square (COD)	0.99994
Adj. R-Square	0.9999
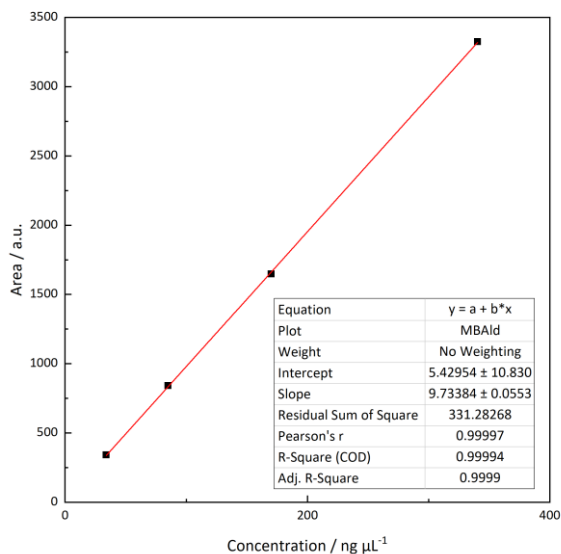
Figure S3-2: The calibration line for MBAld shows a linear response. Area is obtained by peak integration acquired by DAD-detector absorption at 280±2 nm (Reference 325±10 nm).

Equation	y = a + b*x
Plot	MBAcid
Weight	No Weighting
Intercept	37.85052 ± 16.41
Slope	1.66352 ± 0.0185
Residual Sum of Square	3575.07241
Pearson's r	0.99975
R-Square (COD)	0.9995
Adj. R-Square	0.99938
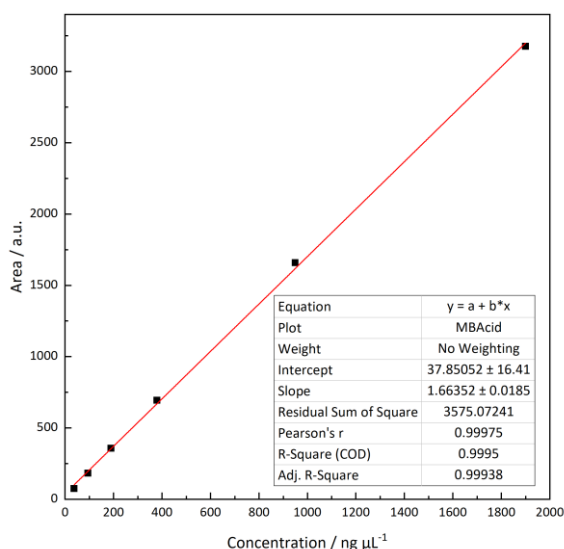
Figure S3-3: The calibration line for MBAcid shows a linear response. Area is obtained by peak integration acquired by DAD-detector absorption at 280±2 nm (Reference 325±10 nm).

Photooxidations

For a typical photocatalytic experiment, 1.50 mg of FEAx-COF was suspended in 1 mL solvent in a 0.5–2.0 mL Biotage® microwave reaction vial and sonicated for 5 minutes in a water bath. In the case of molecular alloxazine photocatalysts, 2.2 µmol were used instead, which matches the expected amount of alloxazine units in 1.50 mg FEAx-COF. The reaction mixtures were oxygenated by oxygen bubbling for five minutes before addition of substrate and additional reagent. For reactions under Argon, the reaction mixture was instead degassed by four freeze-pump-thaw cycles after addition of substrate.

If not stated otherwise, reaction mixtures were illuminated inside a closed metal cylinder (diameter 10 cm, height 14.5 cm) with one meter of LED strip wrapped around the inside (60 diodes, 14.4 W/m, 12 V, 120° emission angle; see Figure S3-27). The heat emission from the blue LEDs caused the reaction mixtures to heat up to 45 °C. In the case of differently colored LEDs, the photoreactors were cooled to room temperature using fans to account for potentially varying heat emission from the LEDs. If stated, this procedure was also applied to experiments with blue LEDs. Intensity measurements for every reactor were done at the same position central above the opening.

The yield and selectivity of the photocatalytic oxidation of 4-methoxybenzyl alcohol was determined *via* HPLC, using independent calibration curves for 4-methoxybenzyl alcohol, 4-methoxybenzaldehyde, and 4-methoxybenzoic acid (Figure S3-1- Figure S3-3). For other substrates (Table S3-3), the conversion was determined *via* NMR spectroscopy.

Electrochemistry

Non-aqueous cyclic voltammetry experiments for FEAx-COF were conducted on a METROHM Autolab PGSTAT302N potentiostat with a COF-coated FTO working, a platinum wire counter and a non-aqueous Ag/AgNO$_3$ (0.01 M) reference electrode, referenced to SCE using Ferrocene (Fc) as an internal standard ($E_{1/2,Fc}$ = 0.40 V vs. SCE).[14] COF films were grown solvothermally on FTO substrates (1 cm^2) by submersing them in the reaction mixture during solvothermal synthesis. Prior to the measurement, the electrochemical cell was purged with argon for 10 min.

Reduction onset potentials (E_{onset}) were extracted from the x-intercept of the linear fits in the voltammograms, according to a previous method.[15] Together with the optical bandgap ($E_{g,opt}$ = 2.25 eV) this value was used to estimate valence band (VB) and conduction band (CB) edges vs. the vacuum level[16] according to the following equations:

E_{CB} = -($E_{onset\ vs.\ SCE}$ - $E_{1/2,Fc}$ + 5.1) eV

E_{VB} = E_{CB} − $E_{g,opt}$

Energy levels of the material vs. vacuum level were calculated to E_{CB} = -3.97 eV and E_{VB} = -6.22 eV.
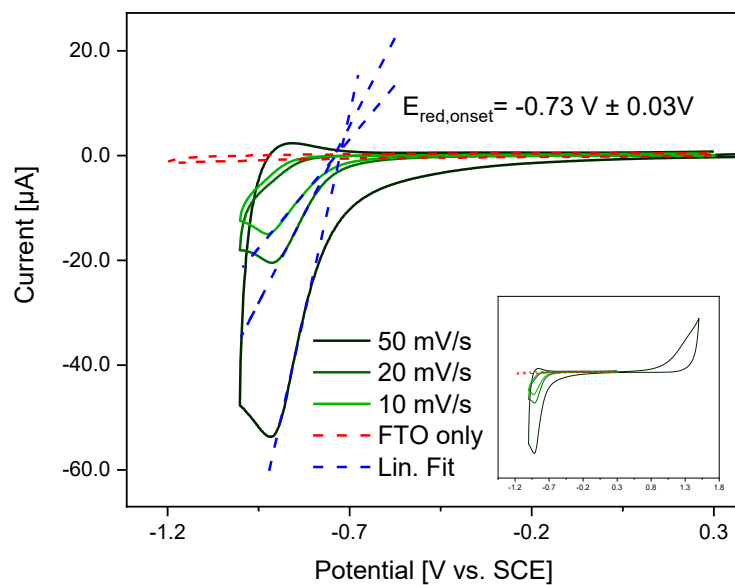
Figure S3-4: Cyclic voltammograms of a COF-coated FTO working electrode in 0.1M NBu$_4$PF$_6$ in anhydrous acetonitrile at different scan rates. Red line shows background measurement without COF. Inset showing extended potential range.

6.3.2 Synthetic Procedures
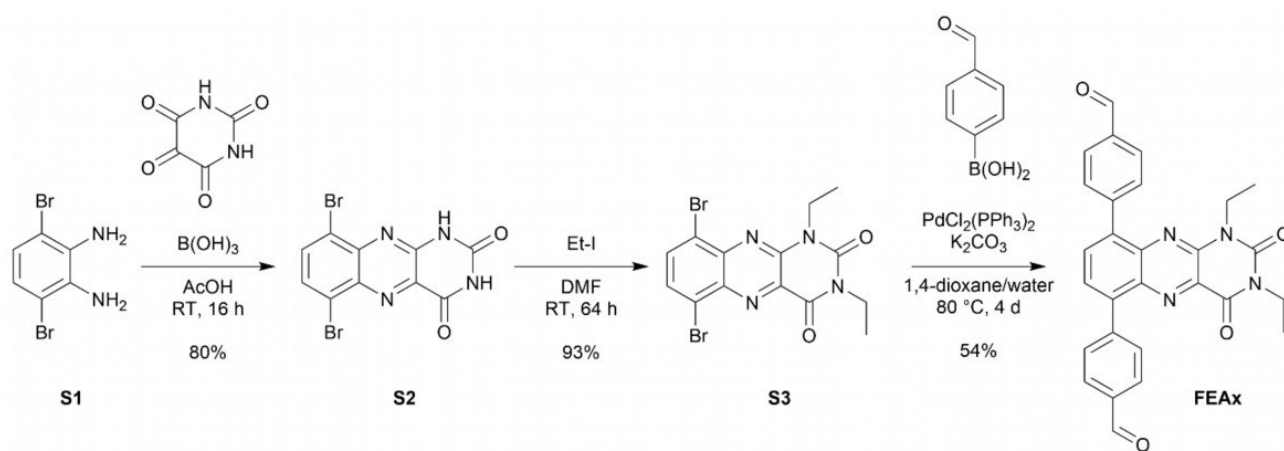
Scheme S3-1: Synthetic route to the FEAx linker.

2,4,6-tris(4-aminophenyl)-1,3,5-triazine (TAPT) was synthesized according to the literature.[17]

3,6-dibromobenzene-1,2-diamine **S1** was synthesized according to the literature.[18]

Alloxazine was synthesized according to the literature.[19]

[1,1':4',1''-Terphenyl]-4,4''-dicarbaldehyde was synthesized according to the literature.[20]

Synthesis of 6,9-dibromoalloxazine **S2**
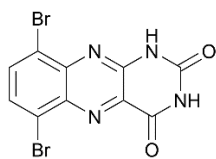
S2

Alloxan monohydrate (1.06 g, 6.50 mmol, 1.0 eq.) and boric acid (0.49 g, 7.80 mmol, 1.2 eq.) were dissolved in hot glacial acetic acid (48 mL). 3,6-Dibromobenzene-1,2-diamine **S1** (1.73 g, 6.50 mmol, 1.0 eq.) was dissolved in glacial acetic acid (12 mL) and added to the reaction mixture, resulting in a deep yellow solution. The mixture was stirred at room temperature for 16 h. The resulting solid was filtered off, washed with concentrated acetic acid (40 mL), and water (60 mL). Drying yielded 6,9-dibromoalloxazine **S2** (1.93 g, 5.18 mmol, 80%) as a yellow powder. ^{1}H NMR (400 MHz, DMSO-d_6) δ 12.27 (s, 1H), 11.89 (s, 1H), 8.17 (d, J = 8.2 Hz, 1H), 8.02 (d, J = 8.2 Hz, 1H) ppm. ^{13}C NMR (101 MHz, DMSO-d_6) δ 159.6, 149.9, 148.1, 141.1, 137.0, 136.2, 133.3, 131.6, 124.3, 120.5 ppm. MS (ESI-): m/z calc. for $C_{10}H_3Br_2N_4O_2^-$ (M-H$^+$): 370.86078; found: 370.86128. Elemental analysis calc. (%) for $C_{10}H_4Br_2N_4O_2$: C 32.29, H 1.08, N 15.06; found: C 32.32, H 1.20, N 14.86.

1,3-diethyl-6,9-dibromoalloxazine **S3**
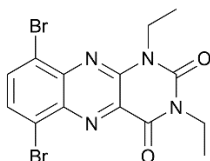
S3

6,9-dibromoalloxazine **S2** (0.69 g, 1.85 mmol, 1.0 eq.) and potassium carbonate (1.02 g, 7.40 mmol, 4.0 eq.) were suspended in anhydrous DMF (35 mL). Iodoethane (0.60 mL, 7.40 mmol, 4.0 eq.) was added dropwise and the reaction mixture was stirred at room temperature in the dark for 64 h. After slow addition of water (20 mL), the solvents were removed under reduced pressure. The residue was washed with water (30 mL) and dried *in vacuo* for 1 h, yielding 6,9-dibromo-1,3-diethylalloxazine **S3** (0.73 g, 1.71 mmol, 93%) as an ochre solid. ^{1}H-NMR (400 MHz, CDCl$_3$) δ 8.03 (d, J = 8.1 Hz, 1H, Ar-*H*), 7.91 (d, J = 8.1 Hz, 1H, Ar-*H*), 4.56 (q, J = 7.0 Hz, 2H, C*H$_2$*CH$_3$), 4.25 (q, J = 7.1 Hz, 2H, C*H$_2$*CH$_3$), 1.46 (t, J = 7.0 Hz, 3H, CH$_2$C*H$_3$*), 1.36 (t, J = 7.1 Hz, 3H, CH$_2$C*H$_3$*) ppm. ^{13}C-NMR (101 MHz, CDCl$_3$) δ 158.3, 149.7, 145.8, 142.0, 138.3, 136.7, 132.4, 130.9, 125.5, 122.0, 39.0, 38.2, 13.2, 12.7 ppm. MS (ESI+): m/z calc. for $C_{14}H_{13}Br_2N_4O_2^+$ (M+H$^+$): 428.93793; found: 428.93802. Elemental analysis calc. (%) for $C_{14}H_{12}Br_2N_4O_2$: C 39.28, H 2.83, N 13.09; found: C 37.71, H 2.36, N 13.21.

1,3-diethyl-6,9-bis-(4-formylphenyl)-alloxazine (FEAx)
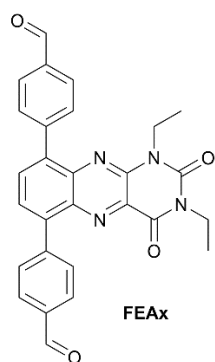
6,9-dibromo-1,3-diethylalloxazine **S3** (858 mg, 2.00 mmol, 1.0 eq.), 4-Formylphenylboronic acid (930 mg, 6.02 mmol, 3.0 eq.), and potassium carbonate (1.66 g, 12.0 mmol, 6.0 eq.) were suspended in a mixture of 1,4-dioxane (35 mL) and water (1.8 mL). Bis(triphenylphosphine)palladium(II) dichloride (49.4 mg, 0.07 mmol, 0.03 eq.) was added, and the reaction mixture was stirred at 80 °C for 4 d. After cooling to room temperature, the mixture was filtered through a pad of celite and concentrated under reduced pressure. Purification by automated flash column chromatography (n-hexane/EtOAc 2:3 to 1:1) yielded FEAx (518 mg, 1.08 mmol, 54%) as a yellow solid. ^{1}H NMR (400 MHz, CDCl$_3$) δ 10.15 (s, 1H), 10.13 (s, 1H), 8.10 − 7.90 (m, 10H), 4.32 (q, J = 7.0 Hz, 2H), 4.22 (q, J = 7.1 Hz, 2H), 1.33 (t, J = 7.1 Hz, 3H), 1.31 (t, J = 7.0 Hz, 3H) ppm. ^{13}C NMR (101 MHz, CDCl$_3$) δ 192.2, 192.1, 159.0, 149.9, 144.6, 143.8, 143.3, 141.4, 141.1, 138.3, 137.9, 136.1, 135.9, 133.8, 131.7, 131.2, 129.8, 129.7, 129.5, 129.3, 38.3, 38.0, 13.2, 13.0 ppm. MP: 227 °C. HRMS (ESI+): m/z calc. for C$_{28}$H$_{23}$N$_4$O$_4^+$ (M+H$^+$): 479.17138; found: 479.17120. Elemental analysis calc. (%) for C$_{28}$H$_{22}$N$_4$O$_4$: C 70.28, H 4.63, N 11.71; found: C 69.66, H 4.46, N 11.25.

1,3-diethyl-6,9-diphenyl-alloxazine PEAx
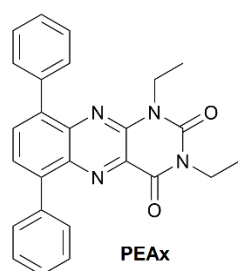
In a Biotage® 20 mL microwave vial, 6,9-dibromo-1,3-diethylalloxazine **S3** (219 mg, 0.51 mmol, 1.0 eq.), Phenylboronic acid (187 mg, 1.50 mmol, 3.0 eq.), and potassium carbonate (417 mg, 3.02 mmol, 6.0 eq.), were suspended in a mixture of 1,4-dioxane (10 mL) and water (0.5 mL). Bis(triphenylphosphine)palladium(II) dichloride (14.2 mg, 0.02 mmol, 0.04 eq.) was added, and the reaction mixture was stirred at 80 °C for 3 d, then the heat was decreased to 50 °C for additional 19 h. After cooling to room temperature, the mixture was filtered through a pad of celite and concentrated under reduced pressure. Purification by automated flash column chromatography (*n*-hexane/EtOAc 19:1 to 1:1) yielded PEAx (518 mg, 1.08 mmol, 54%) as a yellow solid. ^{1}H NMR (400 MHz, CDCl$_3$) δ 8.02 (d, J = 7.5 Hz, 1H), 7.90 (d, J = 7.5 Hz, 1H), 7.87 − 7.82 (m, 2H), 7.76 − 7.70 (m, 2H), 7.58 − 7.42 (m, 6H),

4.33 (q, J = 7.0 Hz, 2H), 4.22 (q, J = 7.0 Hz, 2H), 1.33 (2 t, J = 7.0 Hz, 6H). ^{13}C NMR (101 MHz, CDCl$_3$) δ 159.3, 150.1, 144.1, 141.6, 141.5, 138.7, 138.3, 137.9, 137.5, 133.8, 131.1, 130.6, 129.2, 129.1, 128.4, 128.4, 128.1, 128.0, 38.2, 37.9, 13.3, 13.0. MP: 239 °C. MS (ESI+): m/z calc. for C$_{26}$H$_{23}$N$_4$O$_2^+$ [M+H$^+$]: 423.18155; found 423.18193. Elemental analysis calc. (%) for C$_{26}$H$_{22}$N$_4$O$_2$: C 73.92, H 5.25, N 13.26; found: C 72.30, H 5.22, N 12.55. Single-crystals were grown by slowly evaporating solutions of PEAx in CHCl$_3$.

1,3-diethyl-alloxazine HEAx
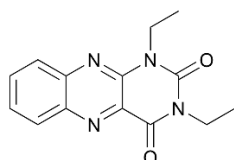
HEAx

To alloxazine (1.00 g, 4.70 mmol, 1 eq.) and potassium carbonate (2.60 g, 18.8 mmol, 4 eq.) in dry DMF (90 mL) was added iodoethane (1.52 mL, 18.8 mmol, 4 eq.). After stirring at room temperature in the dark for 18 h, the solvent was removed. The resulting solid was resuspended in water (60 mL), filtered off, and washed with water (2 x 40 mL). Drying *in vacou* yielded HEAx (1.16 g, 4.28 mmol, 91%) as a pale yellow powder. ^{1}H NMR (400 MHz, CDCl$_3$) δ 8.33 (d, J = 8.5 Hz, 1H), 8.03 (d, J = 8.6 Hz, 1H), 7.89 (t, J = 7.7 Hz, 1H), 7.75 (t, J = 7.7 Hz, 1H), 4.53 (q, J = 6.9 Hz, 2H), 4.26 (q, J = 7.0 Hz, 2H), 1.41 (t, J = 6.9 Hz, 3H), 1.36 (t, J = 7.0 Hz, 3H). ^{13}C NMR (101 MHz, CDCl$_3$) δ 159.6, 149.9, 145.0, 143.6, 140.1, 133.8, 131.0, 130.1, 129.1, 128.0, 38.2, 38.0, 13.3, 13.1 ppm. MP: 172 °C. MS (ESI+): m/z calc. for C$_{14}$H$_{15}$N$_4$O$_2^+$ (M+H$^+$): 271.11895; found: 271.11916. Elemental analysis calc. (%) for C$_{14}$H$_{14}$N$_4$O$_2$: C 62.21, H 5.22, N 20.73; found: C 62.12, H 5.00, N 20.43. Single-crystals were grown by slowly evaporating solutions of HEAx in CHCl$_3$.

6,9-bis-(4-formylphenyl)-alloxazine (FAx)

FAx
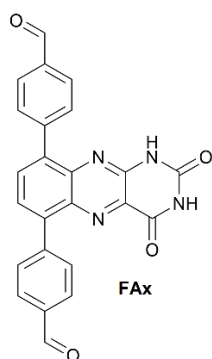
6,9-Dibromoalloxazine **S2** (0.40 g, 1.08 mmol, 1.0 eq.), 4-formylphenylboronic acid (0.50 g, 3.24 mmol, 3.0 eq.) and potassium carbonate (0.87 g, 6.48 mmol, 6.0 eq.) were suspended in 1,4-dioxane (28 mL) and degassed with three vacuum/argon cycles. Bis(triphenylphosphin)-palladium(II)chloride (38.3 mg, 0.054 mmol, 0.05 eq.) was added and the reaction mixture was heated to 80 °C for 21 h and subsequently to 90 °C for another 46 h under inert gas atmosphere. After cooling to ambient temperature, water (40 mL) was added and the solvent was removed. The product was filtered off, washed with water (100 mL), and dried in the desiccator overnight. 6,9-bis-(4-formylphenyl)-alloxazine (0.42 g, 0.99 mmol) was obtained as an impure brown solid. ^{1}H-NMR: (270 MHz, DMSO-d_6) δ 10.13 (s,

1H), 10.11 (s, 1H), 8.06-7.90 (m, ~15H), 7.72 (d, J = 7.5 Hz, 1H), 7.65 (d, J = 8.1 Hz, 1H) ppm. MS (ESI-): m/z calc. for $C_{24}H_{13}O_4N_4$ (M^-): 421.09423; found: 421.09457. Elemental analysis calc. (%) for $C_{24}H_{13}O_4N_4$: C 68.24, H 3.34, N 13.26; found: C 51.29, H 3.10, N 10.78.

FEAx-COF Synthesis

A Biotage® 5 mL microwave vial was charged with FEAx (27.0 mg, 0.056 mmol, 1.5 eq.) and TAPT (13.3 mg, 0.038 mmol, 1.0 eq.). The vial was temporarily sealed with a rubber septum and flushed three times *via* vacuum/argon cycles. 1,2-dichlorobenzene (1.8 mL) and ethanol (0.15 mL) were added, and the reactants were suspended *via* sonication for 5 minutes. The suspension was degassed *via* three vacuum/argon cycles. Aqueous acetic acid (100 µL, 6M) was added, the vial was sealed with a crimp cap and heated in a muffle furnace at 120 °C for 7 d. After cooling to room temperature, the combined solids of five parallelized batches were filtered off and washed with DMF (50 mL), THF (50 mL), DCM (30 mL), acetone (100 mL), and MeOH (30 mL). Soxhlet extraction with MeOH overnight followed by supercritical CO_2 drying yielded FEAx-COF (143 mg, 75%) as an orange powder. Elemental analysis calc. (%) for $C_{126}H_{90}N_{24}O_6$: C 74.32, H 4.45, N 16.51; found: C 68.82, H 4.37, N 14.92.

Syntheses in other solvent mixtures such as mesitylene/1,4-dioxane 7:2, 1,2-dichlorobenzene/2-propanol 7:6, and 1,2-dichlorobenzene/*n*-butanol 1:1, or in 1,2-dichlorobenzene/ethanol with varying acid concentrations gave less crystalline COF.

FAx-COF Synthesis

A Biotage® 5 mL microwave vial was charged with FAx (25.6 mg) and TAPT (10.8 mg). The vial was temporarily sealed with a rubber septum and flushed three times *via* vacuum/argon cycles. 1,2-dichlorobenzene (985 µL) and ethanol (85 µL) were added and the reactants were suspended *via* sonication for 3 minutes. The suspension was degassed *via* three vacuum/argon cycles. Aqueous acetic acid (30 µL, 6M) was added, the vial was sealed with a crimp cap and heated in a muffle furnace at 120 °C for 3 d. After cooling to room temperature, the solid was filtered off and washed with DMF (10 mL), THF (10 mL), DCM (10 mL). The product was dried in a desiccator overnight.

The BET surface area was determined to be 21.4 m^2g^{-1}. XRPD patterns for this batch of FAx-COF and samples synthesized in different solvents are shown in Figure S3-5.

Terphenyl-COF Synthesis

A Biotage® 5 mL microwave vial was charged with [1,1':4',1''-Terphenyl]-4,4''-dicarbaldehyde (16.1 mg, 0.056 mmol, 1.5 eq.) and TAPT (13.3 mg, 0.038 mmol, 1.0 eq.). The vial was temporarily sealed with a rubber septum and flushed three times *via* vacuum/argon cycles. 1,2-dichlorobenzene (1.8 mL) and ethanol (150 µL) were added and the reactants were suspended *via* sonication for 5 minutes. The suspension was degassed *via* three vacuum/argon cycles. Aqueous acetic acid (27 µL, 6M) was added, the vial was sealed with a crimp cap and heated in a muffle furnace at 120 °C for 7 d. After cooling to room temperature, the combined solids of three parallelized batches were filtered off and washed with DMF (30 mL), THF (20 mL), acetone (50 mL), and MeOH (20 mL). Soxhlet extraction with MeOH overnight followed by supercritical CO_2 drying yielded Terphenyl-COF (44.3 mg, 54%) as a yellow solid.

6.3.3 Additional Data
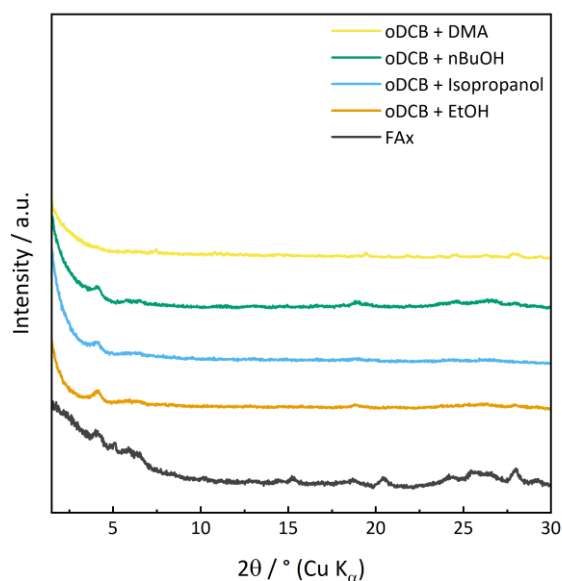
Figure S3-5: XRPD data for the synthesis of non-ethylated FAx-COF in various solvents in comparison to the FAx linker.
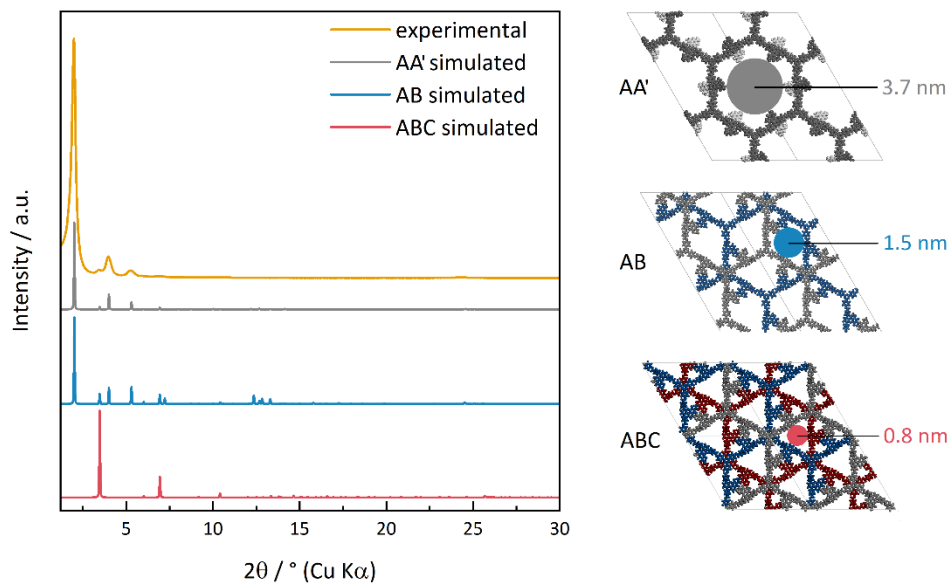
Figure S3-6: Experimental powder diffractogram of FEAx-COF in comparison to simulated patterns of different stacking models. Colored circles illustrate the expected pore size for each stacking model.
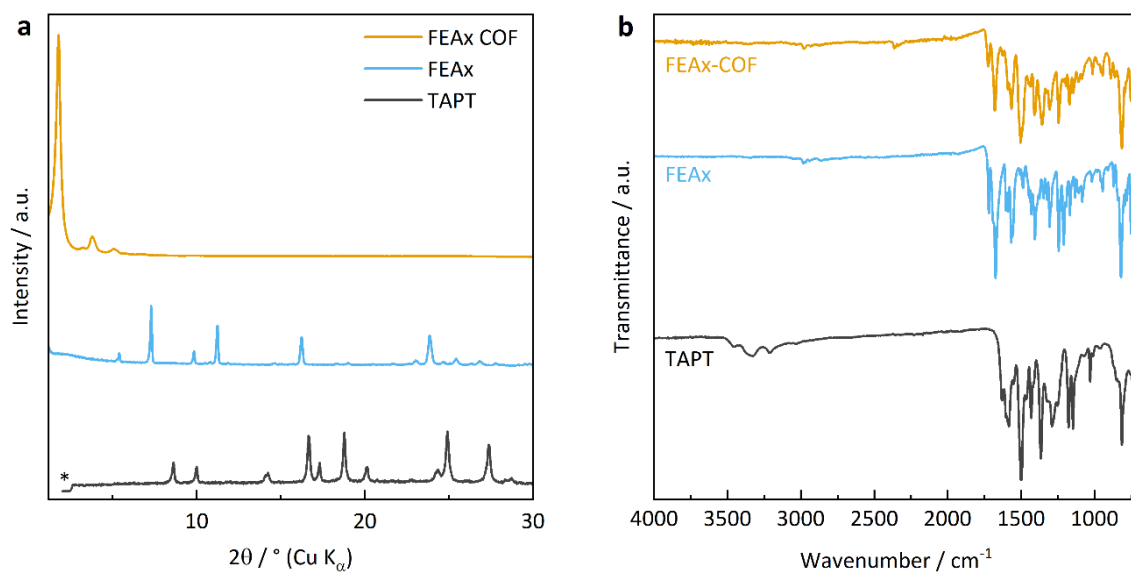
Figure S3-7: Powder diffractogram (a) and FTIR spectrum (b) of FEAx-COF in comparison with its molecular linkers. The asterisk indicates data collection blocked by a beam stop.
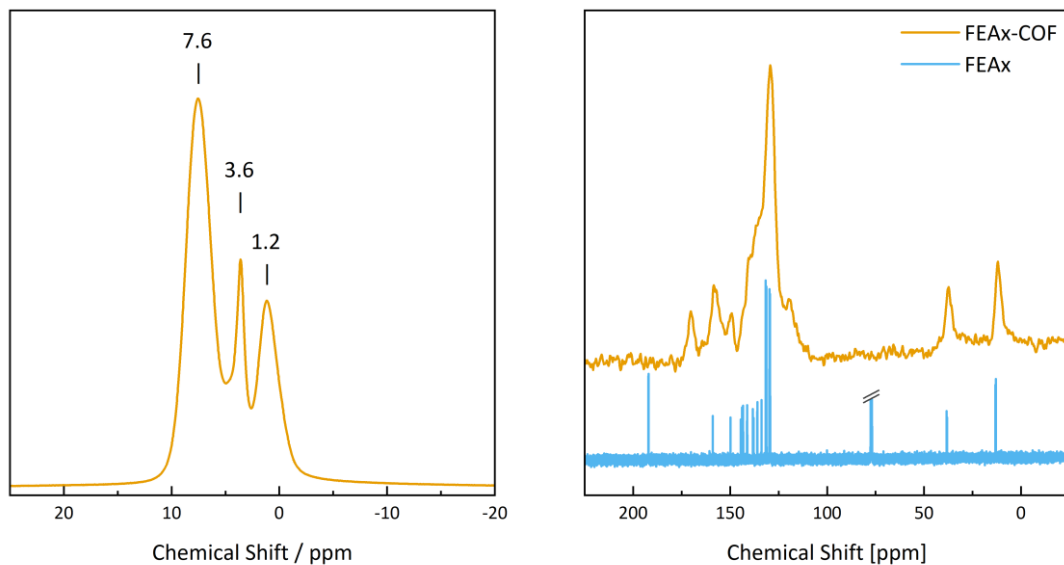
Figure S3-8: ^{1}H-ssNMR spectrum of FEAx-COF (left) and ^{13}C-NMR spectra of FEAx-COF in comparison to the FEAx linker (right). FEAx-COF measured as a solid, FEAx linker measured as a solution in $CDCl_3$. Residual solvent peak at 77.16 ppm abbreviated for clarity.

Equation	y = a + b*x
Weight	No Weighting
Intercept	0.1241 ± 0.00548
Slope	1.75598 ± 0.0264
Residual Sum of Squares	6.49837E-5
Adj. R-Square	0.99864

Equation	y = a + b*x
Weight	No Weighting
Intercept	6.87183 ± 1.16246E-1
Slope	93.28028 ± 5.54768E-
Residual Sum of Squa	5.94517E-26
Adj. R-Square	1
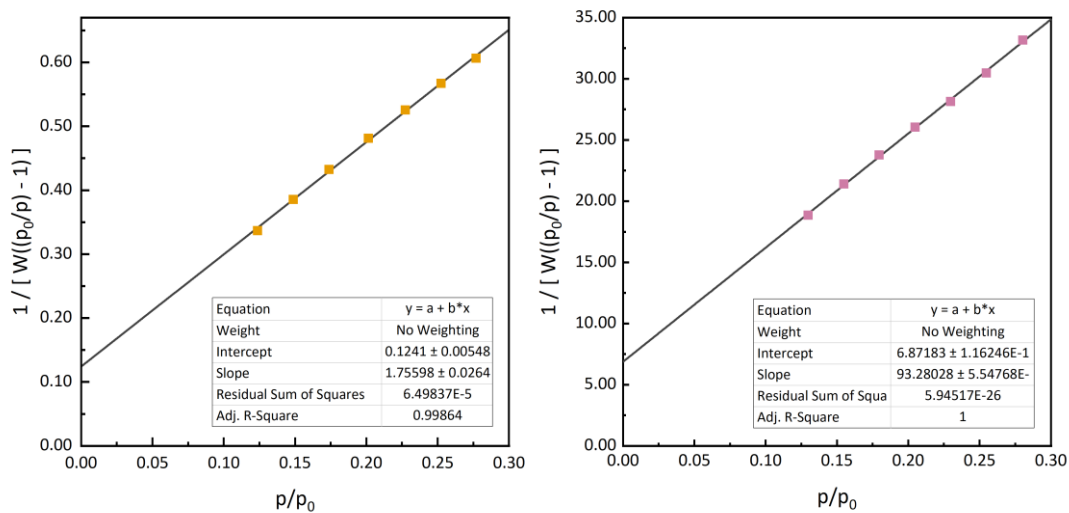
Figure S3-9: BET plot for FEAx-COF (left) and non-ethylated FAx-COF (right).
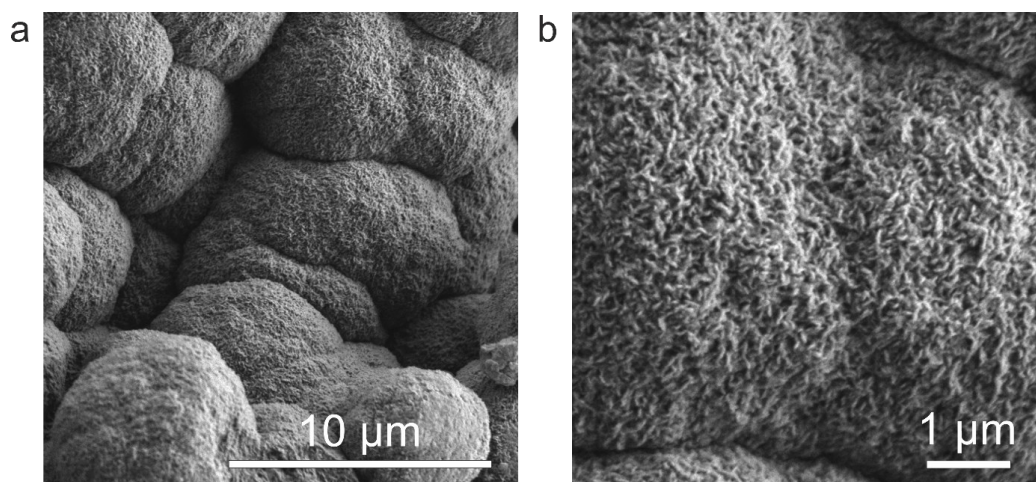
Figure S3-10: SEM images of FEAx-COF showing aggregated, micrometer-sized particles with fringed surfaces. Image (b) shows a zoom onto a particle shown in (a).
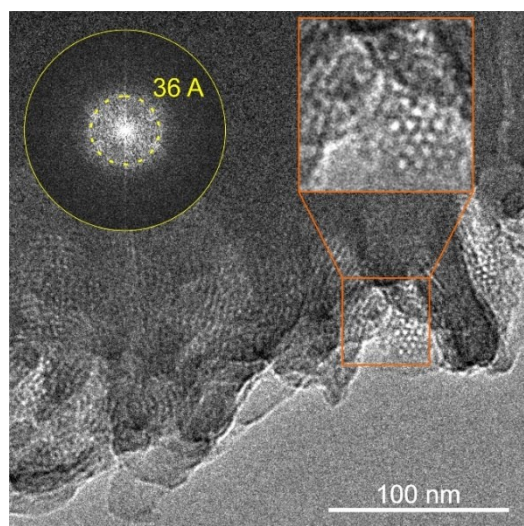
Figure S3-11: TEM image of FEAx-COF. The magnification illustrates the hexagonal arrangement of the mesopores. The FFT of the TEM image underlines the periodicity of 3.6 nm.
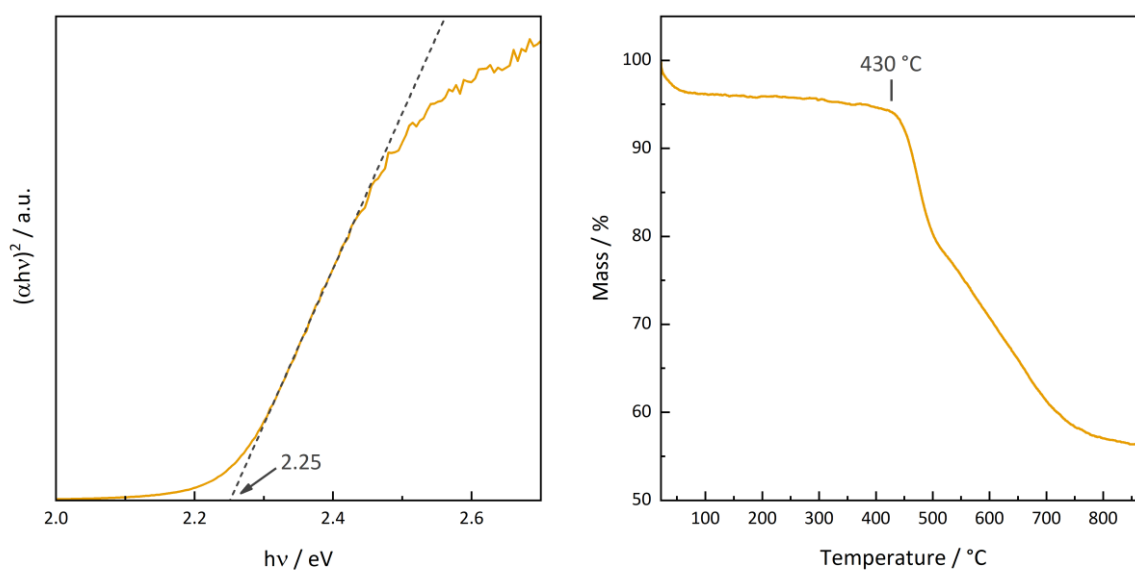
Figure S3-12: Tauc plot (left) and thermal analysis under argon (right) for FEAx-COF.
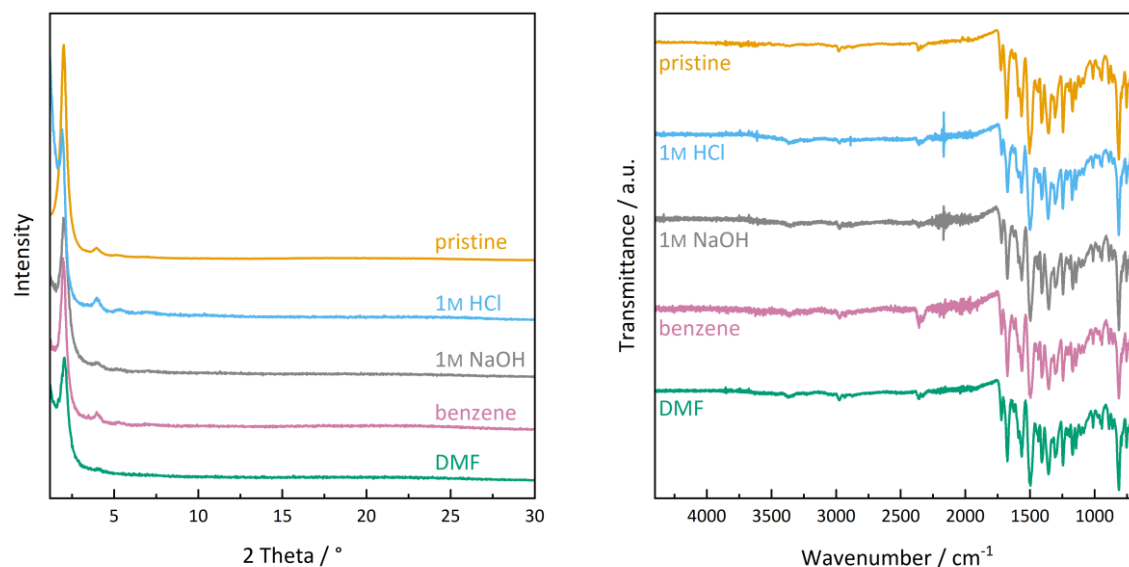
Figure S3-13: XRPD (left) and IR data (right) for stability tests with FEAx-COF. COF suspended in the stated solvent and stirred for 24 h on a platform shaker at 150 rpm, then washed and dried (scCO$_2$).

Table S3-2: Photocatalytic oxidation of MBA by FEAx-COF.

Entry	Variation from Standard Conditions[a]	Comment	17 h		24 h	
			Yield / %	Select. / %	Yield / %	Select. / %
1	none		44	97	67	96
2	no FEAx-COF		traces	100	traces	100
3	no irradiation		traces	100	traces	100
4	under Argon atmosphere		3	100	4	100
5	in water		22	94	25	93
6	in acetonitrile		70	94	84	92
7	additional N(EtOH)$_3$	competing e$^-$ donor	17	98	-[d]	-[d]
8	additional DABCO[b]	competing e$^-$ donor / $^1O_2$ scavenger	traces	100	1	100
9	additional t-BuOH	OH$^\bullet$ scavenger	69	96	-[d]	-[d]
10	in MeCN-d_3/D$_2$O	longer $^1O_2$ lifetime	55	99	79	99
11	additional NaN$_3$	$^1O_2$ scavenger	27	95	-[d]	-[d]
12	additional BQ[c]	O$_2^{\bullet-}$ scavenger	42	94	-[d]	-[d]
13	additional BQ,[c] no FEAx-COF	O$_2^{\bullet-}$ scavenger	54	84	56	85
14	additional CuCl$_2$	competing e$^-$ acceptor / O$_2^{\bullet-}$ scavenger	9	100	13	100

[a] Standard reaction conditions: 20 mM MBA, 1.5 mg FEAx-COF, 463 nm LEDs, MeCN/water (1 mL, 1:1), O$_2$, stirring. Additional reagent: 0.02 mmol. Yield and selectivity determined via HPLC-MS. [b] 1,4-Diazabicyclo[2.2.2]octan. [c] 1,4-Benzoquinone. [d] Not measured.

The addition of selective scavengers to reaction mixtures containing FEAx-COF and MBA was used to pinpoint the reaction mechanism, for example by identifying reactive oxygen species. In addition to

the experiments already discussed in the main text (Table S3-2, entries 1-11), we also employed a number of potential superoxide radical scavengers, namely 1,4-benzoquinone (BQ) and $CuCl_2$. When adding BQ to the reaction mixture, the yield of MBAld after 17 h remains unchanged compared to the standard conditions (Table S3-2, entries 1 and 12). However, even when illuminating a solution of BQ and MBA not containing FEAx-COF, we still get a yield of 54% (Table S3-2, entry 13). Closer inspection of the course of MBAld formation indicates that addition of BQ leads to undesired alcohol oxidation *via* pathways not involving FEAx-COF photocatalysis.[21] Therefore, scavenging experiments with BQ are not applicable to deduce the role of $O_2^{\bullet-}$ in our case. On the other hand, when using $CuCl_2$ as $O_2^{\bullet-}$ scavenger[22] / competing electron acceptor,[23] we see a clear decrease in activity for FEAx-COF, which we attribute to a reduced generation of $O_2^{\bullet-}$.
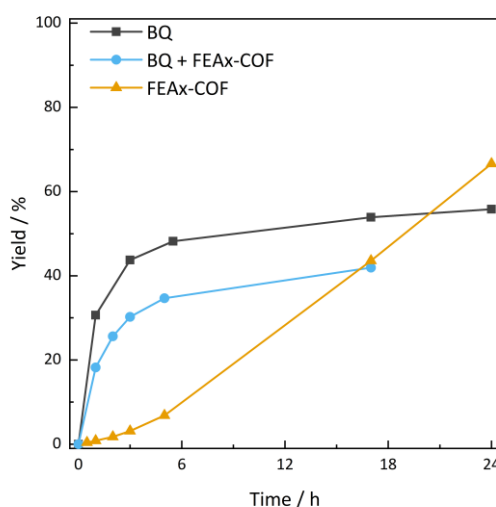
Figure S3-14: Photocatalytic oxidation of MBA with benzoquinone as superoxide scavenger. Reaction conditions: 20 mM MBA, 1.5 mg FEAx-COF, 0.02 mmol BQ, 463 nm LEDs, MeCN/water (1 mL, 1:1), O_2, stirring. Yield determined *via* HPLC-MS.
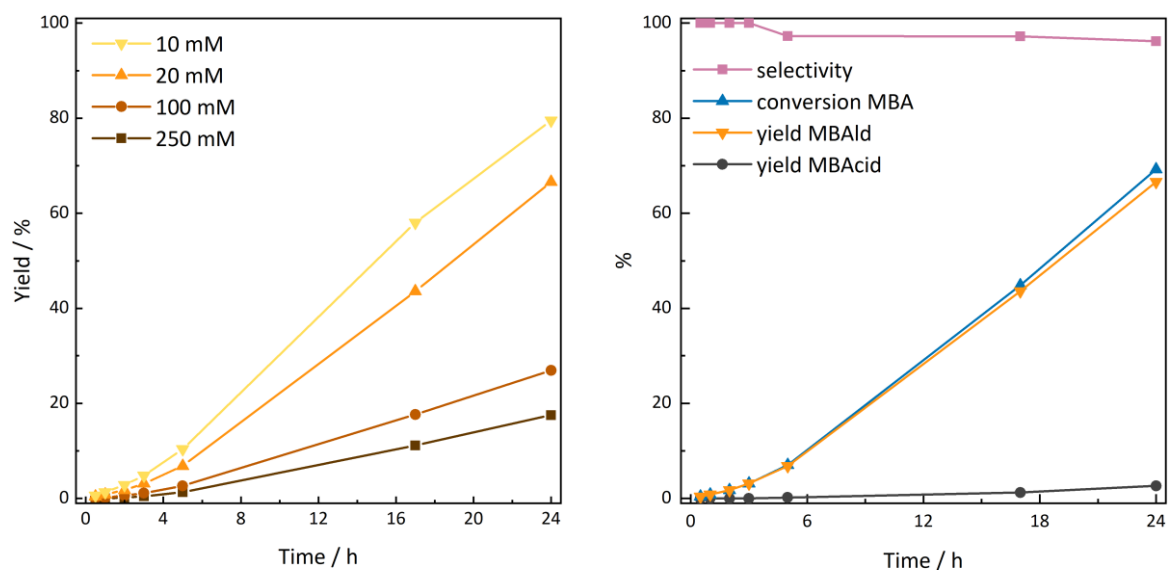
Figure S3-15: Photocatalytic activity of FEAx-COF in MBA solutions with varying concentrations (left). Detailed reaction course for the 20 mM experiment as an example for a typical photocatalytic experiment with FEAx-COF (right). Reaction conditions: 1.5 mg FEAx-COF, 463 nm LEDs, MeCN/water (1 mL, 1:1), O_2, stirring. Yield, selectivity, and conversion determined *via* HPLC-MS.
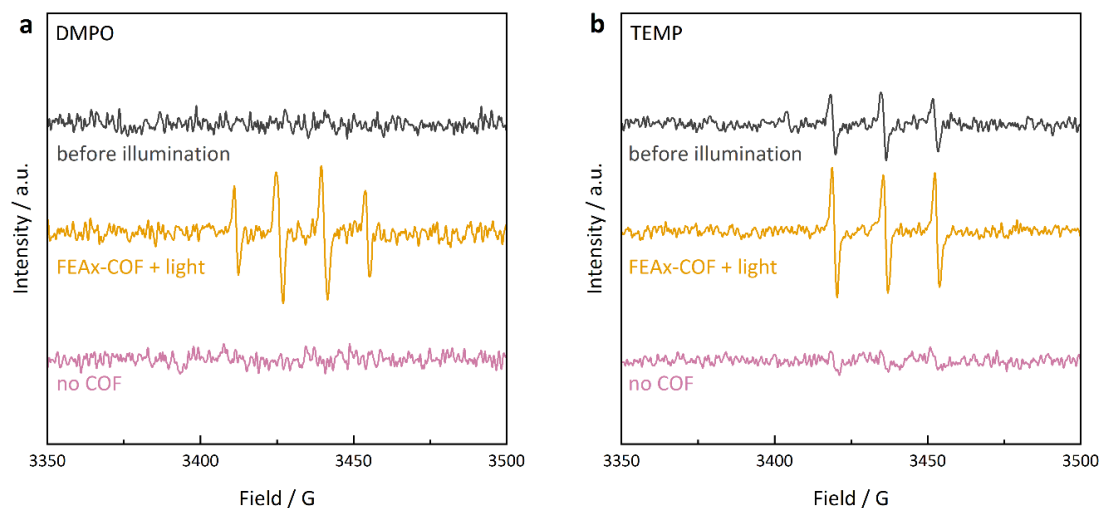
Figure S3-16: Detection of reactive oxygen species with EPR spin-traps DMPO for superoxide (a) and TEMP for $^1O_2$ (b), respectively.
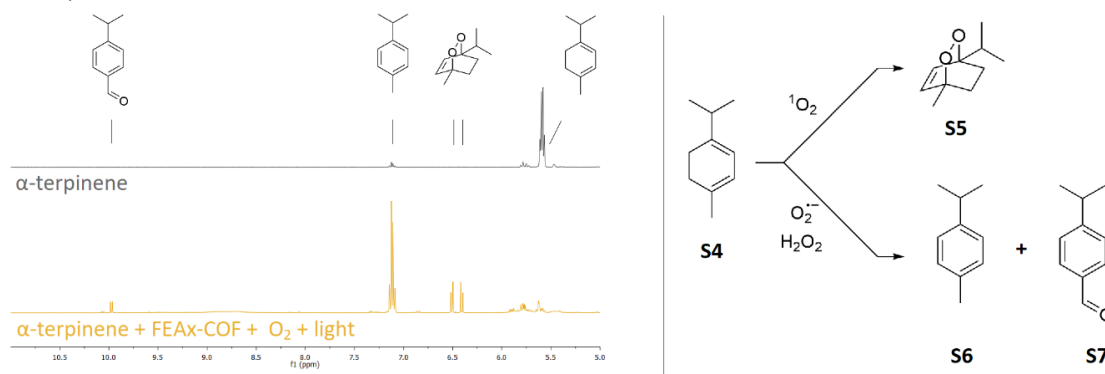
Figure S3-17: The oxidation of α-terpinene **S4** by FEAx-COF shows both ascaridole **S5** from reaction with $^1O_2$ as well as oxidation products *p*-cymene **S6** and aldehyde **S7**. Reaction conditions: 1.5 mg FEAx COF, 50 mM α-terpinene in MeCN-d_3, O_2, RT, 404 nm LED irradiation.
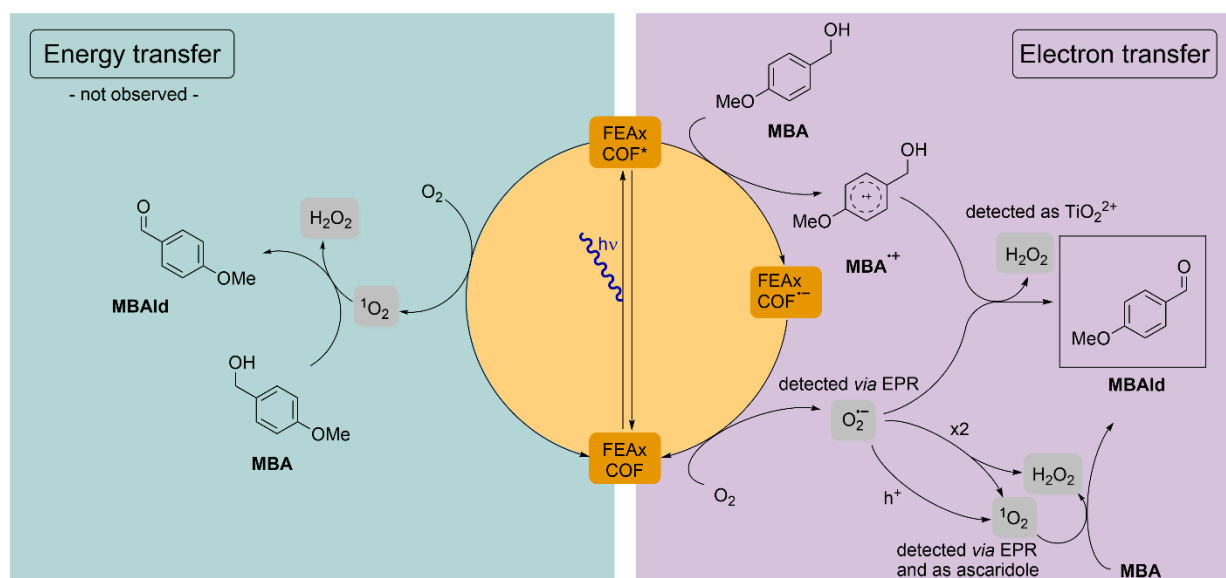
Figure S3-18: Possible catalytic cycles for the photooxidation of MBA by FEAx-COF ν *via* energy transfer (left) and electron transfer (right).
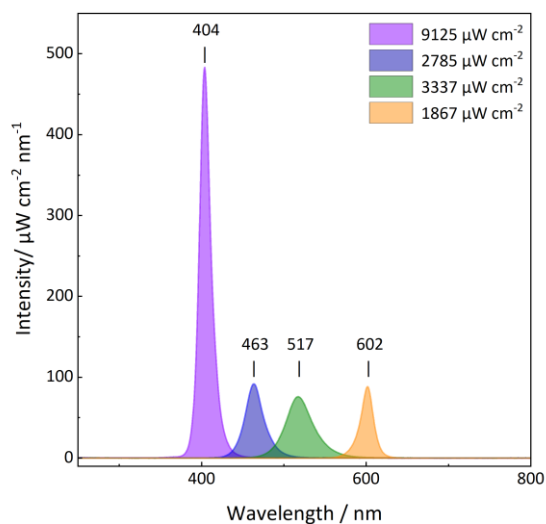
Figure S3-19: Emission spectra of LED photoreactors used in this study. The annotations and the legend correspond to λ_{max} and integrated intensity, respectively.
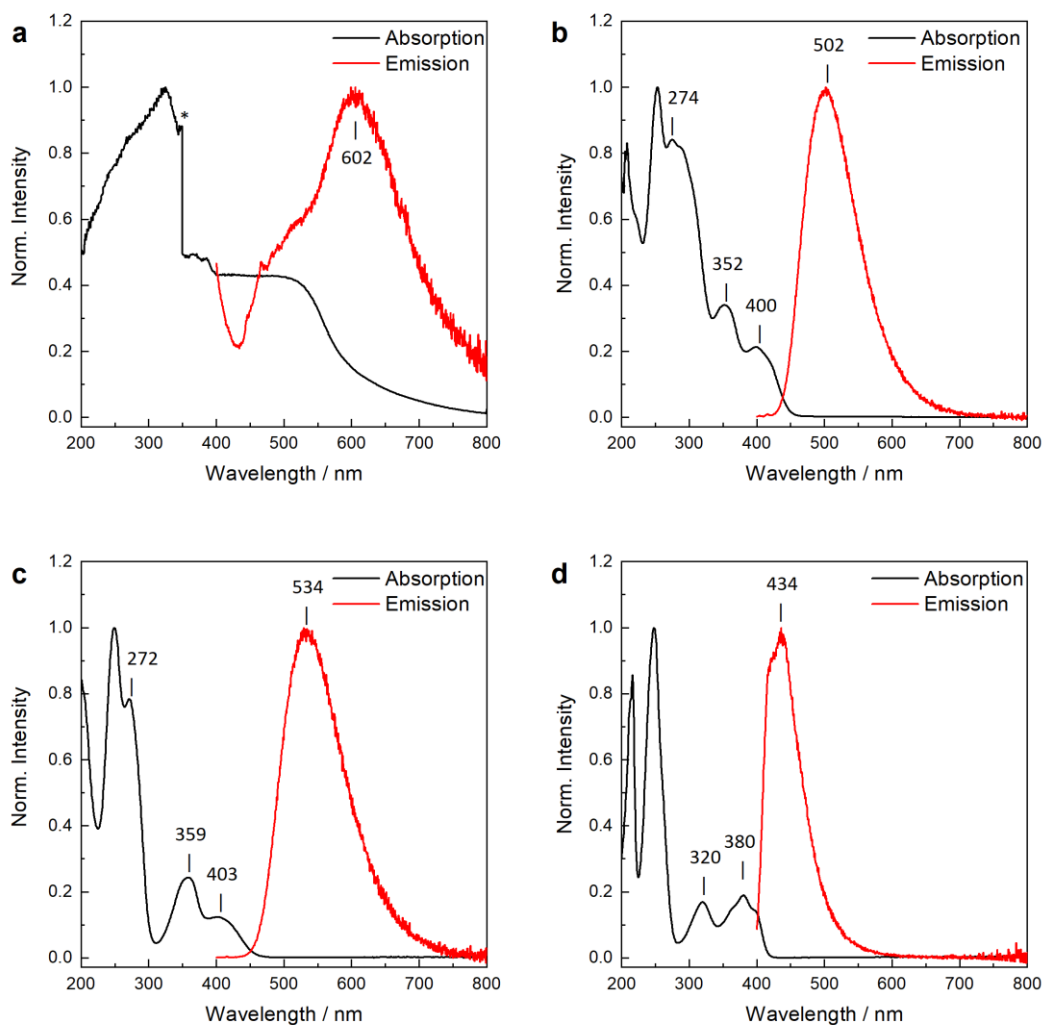
Figure S3-20: Absorption and emission spectra of FEAx-COF (a) and the model compounds FEAx (b), PEAx (c) and HEAx (d). Model compound spectra were measured after dissolution in acetonitrile. FEAx-COF spectra were measured as powder. Asterisk indicates lamp change during solid-state UV-Vis measurement.
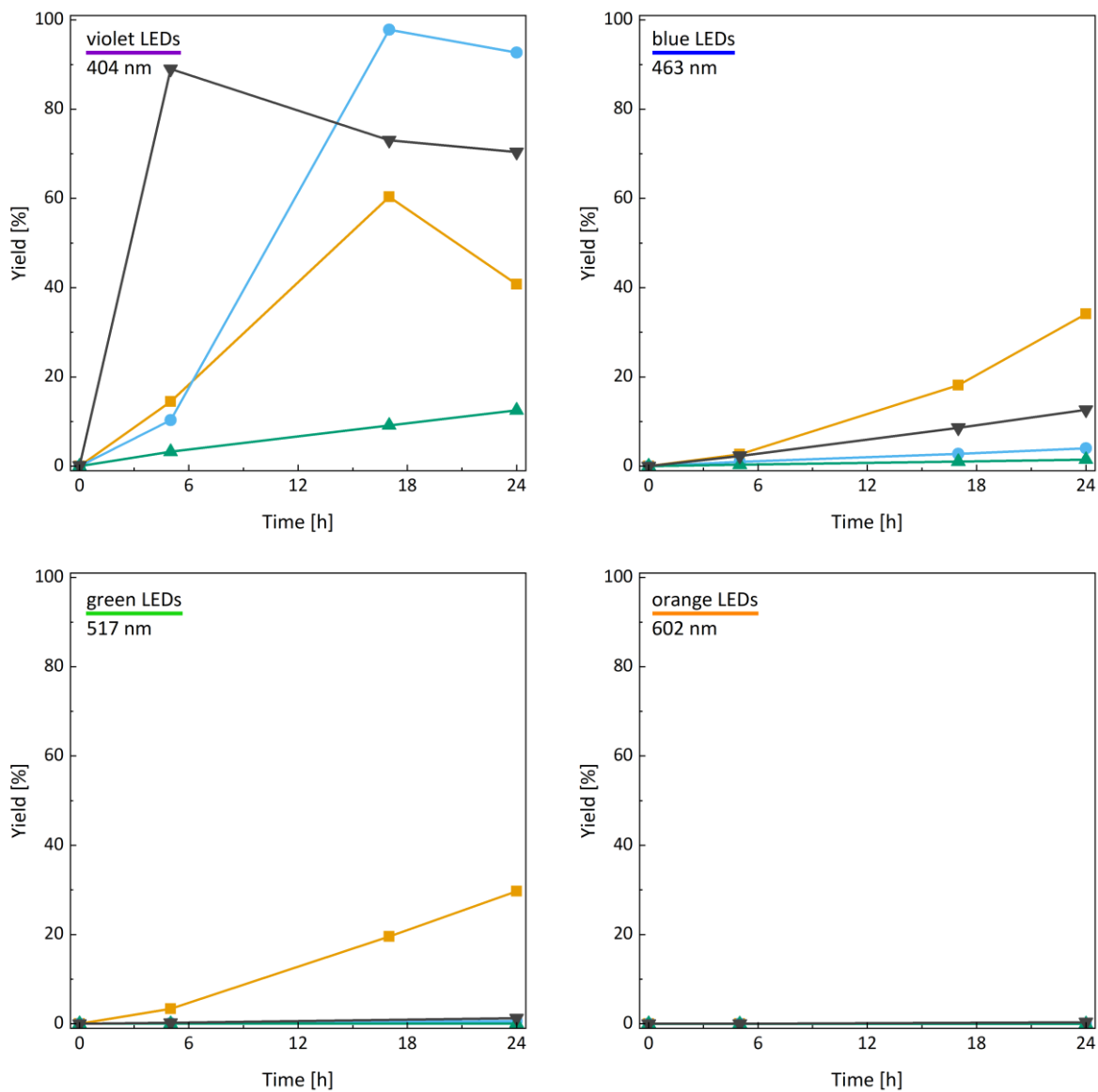
Figure S3-21: Wavelength-dependent photocatalysis with FEAx COF (orange) and model compounds FEAx (blue), PEAx (green), and HEAx (grey). 20 mM MBA in MeCN/water (1:1, 1 mL), 2 mM molecular alloxazine or 1.5 mg FEAx-COF, O_2., room temperature. Yield determined *via* HPLC. Reactions under violet light show yields decreasing with progressing reaction time due to overoxidation of MBAld to MBAacid. See Figure S3-19 for LED emission spectra.
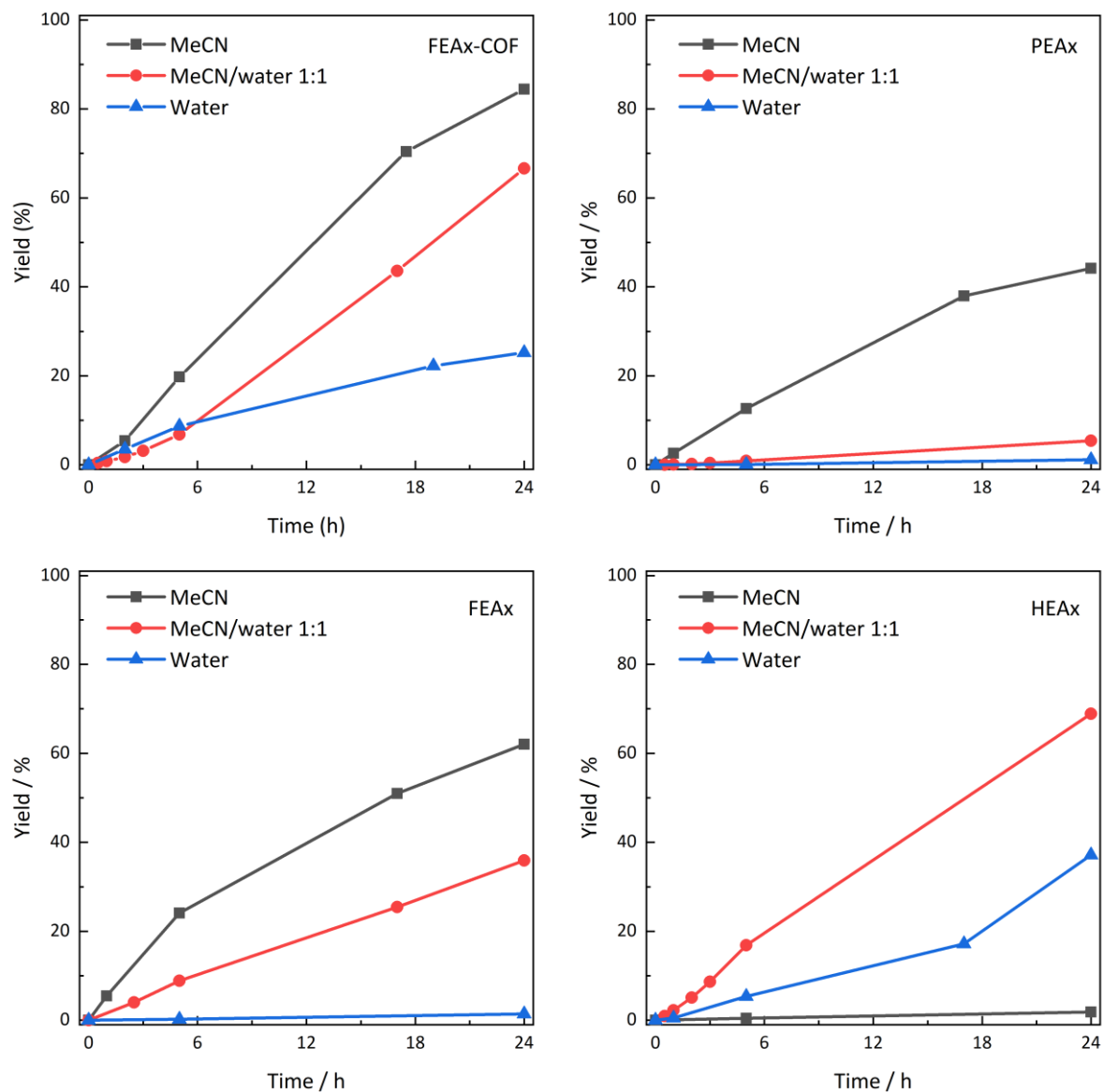
Figure S3-22: Comparison of photocatalytic yields of FEAx COF and the model compounds FEAx, PEAx, and HEAx in various solvents. Reaction conditions: 20 mM MBA in 1 mL solvent, 2 mM molecular alloxazine or 1.5 mg FEAx-COF, O_2, 463 nm LEDs, 45 °C.
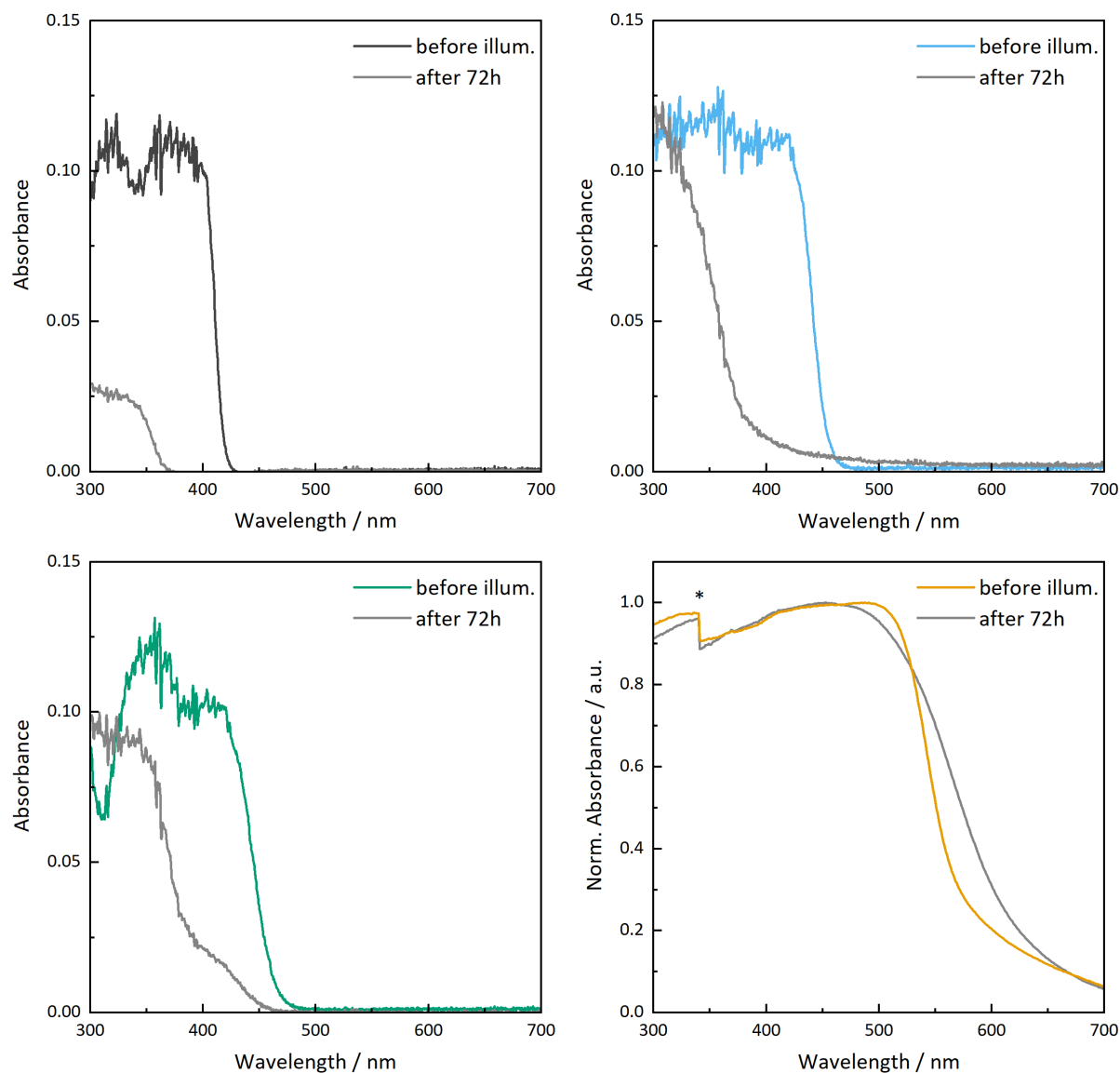
Figure S3-23: UV-Vis spectra of HEAx (dark grey), PEAx (green), FEAx (blue), and FEAx-COF (orange) before and after illumination with violet LEDs for 72 h. Reaction conditions: 2 mM molecular alloxazine or 1.5 mg FEAx-COF in MeCN (1 mL), O_2, RT. Spectra of molecular alloxazines measured as 0.2 mM solutions (in MeCN) on a Varian Cary 50 spectrophotometer, FEAx-COF measured after isolation as a solid. Asterisk indicates lamp change during solid state UV-Vis measurement. Note that the data for FEAx-COF is normalized to account for potentially varying amounts of probed powder.
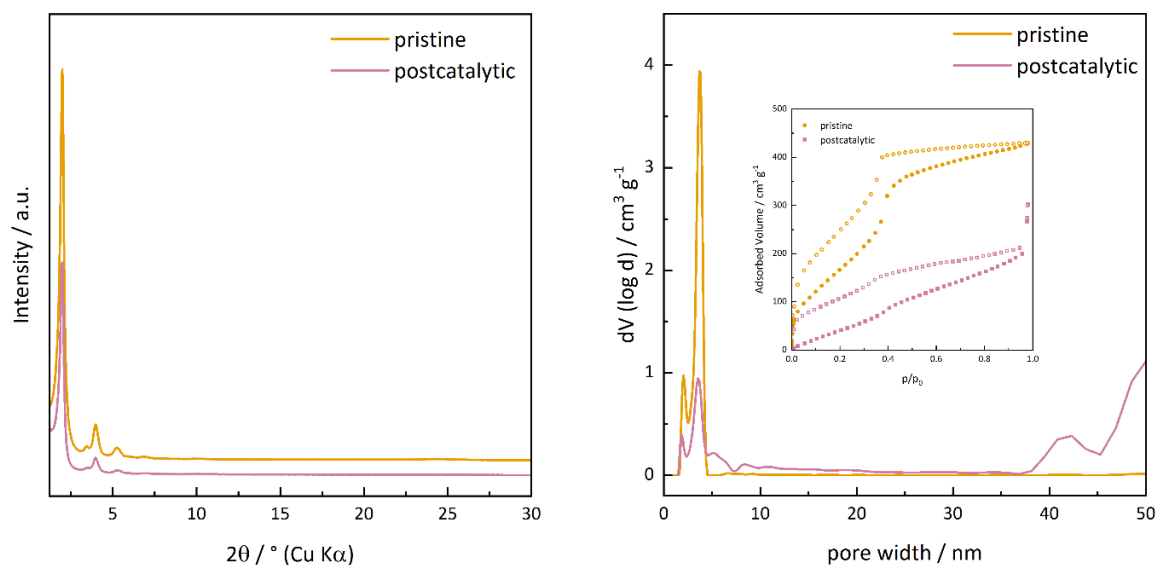
Figure S3-24: Post-catalytic characterization of FEAx-COF *via* XRPD (left) and pore size distribution (right) after reaction in MeCN/water with 463 nm irradiation for 24 h. Inset shows underlying sorption isotherms. The BET surface area of this batch of FEAx-COF before and after photocatalysis was determined to be 677.4 and 238.5 $m^2 g^{-1}$, respectively.
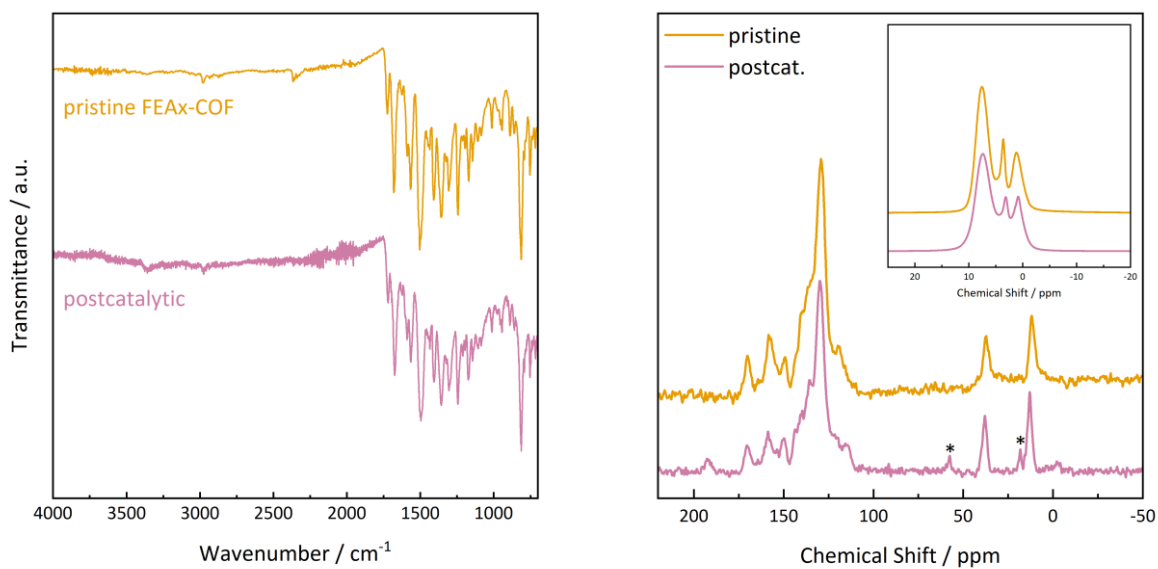
Figure S3-25: Post-catalytic characterization of FEAx-COF *via* FTIR (left) and ^{13}C ssNMR (right). Inset shows ^{1}H ssNMR spectra. Asterisks indicate signals of residual ethanol from the supercritical drying procedure.
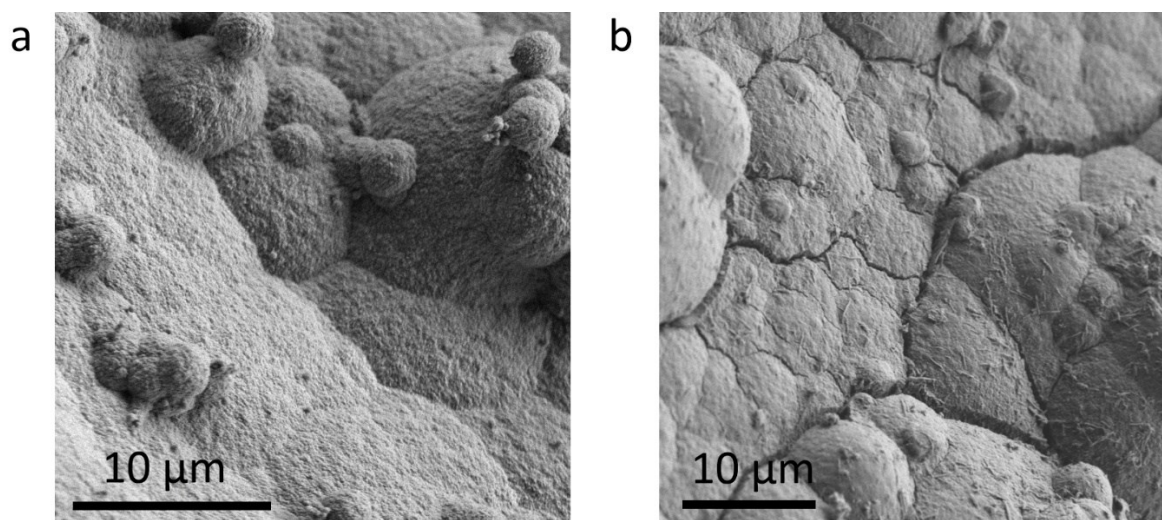
Figure S3-26: SEM images of FEAx before (a) and after (b) photocatalysis.
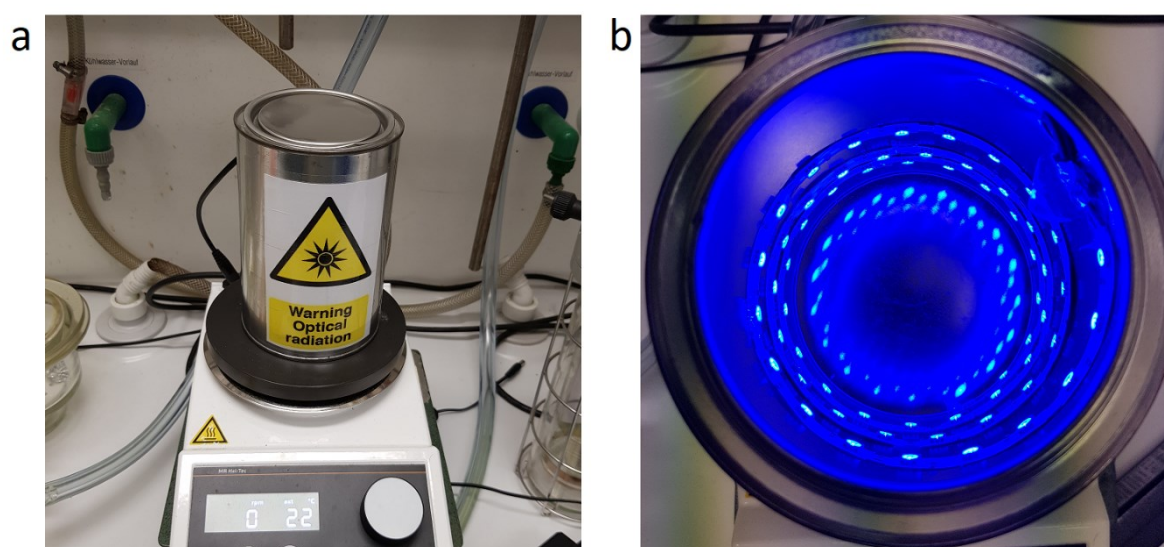
Figure S3-27: Photograph of a photoreactor used for the photooxidation reactions (a). Top view into the opened reactor with 463 nm LEDs (b).

| TiOSO$_4$ (stock) | water + TiOSO$_4$ | react. mixt. + TiOSO$_4$ | react. mixt. | H$_2$O$_2$ + TiOSO$_4$ |
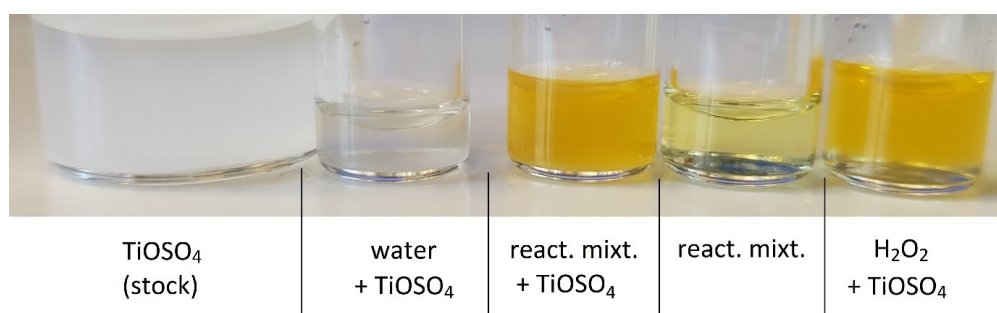
Figure S3-28: Photograph of peroxide detection experiments with titanyl sulfate.
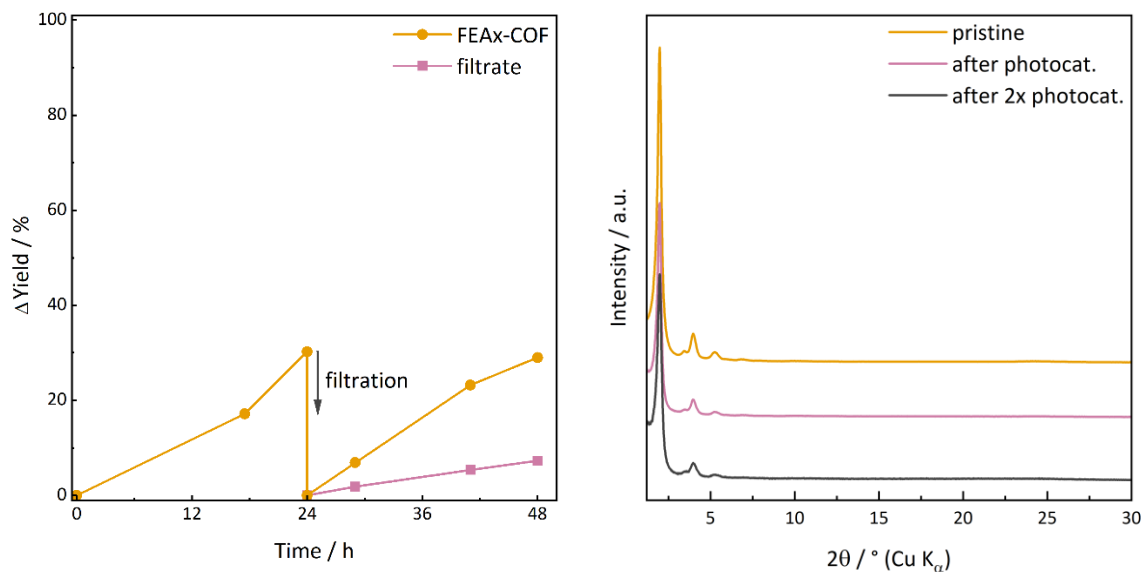
Figure S3-29: Left: Filtration and recycling photocatalysis experiments with FEAx-COF. Reaction conditions: 20 mM MBA in MeCN/water (1:1, 1 mL), 1.5 mg FEAx-COF, O_2, 463 nm LEDs, RT. After 24 h, the COF was separated by centrifugation, washed, and reused for photocatalysis under identical conditions. The selectivity was 98.4% and 98.8% in the first and second run, respectively. The filtrate was illuminated under the same conditions, showing only little residual activity which we assign to residual nanoparticular COF that could not be centrifuged off. For better visualization, the yield for the filtrate is corrected by the amount of product already formed before filtration. Right: XRPD patterns for FEAx-COF before and after consecutive photocatalysis experiments.
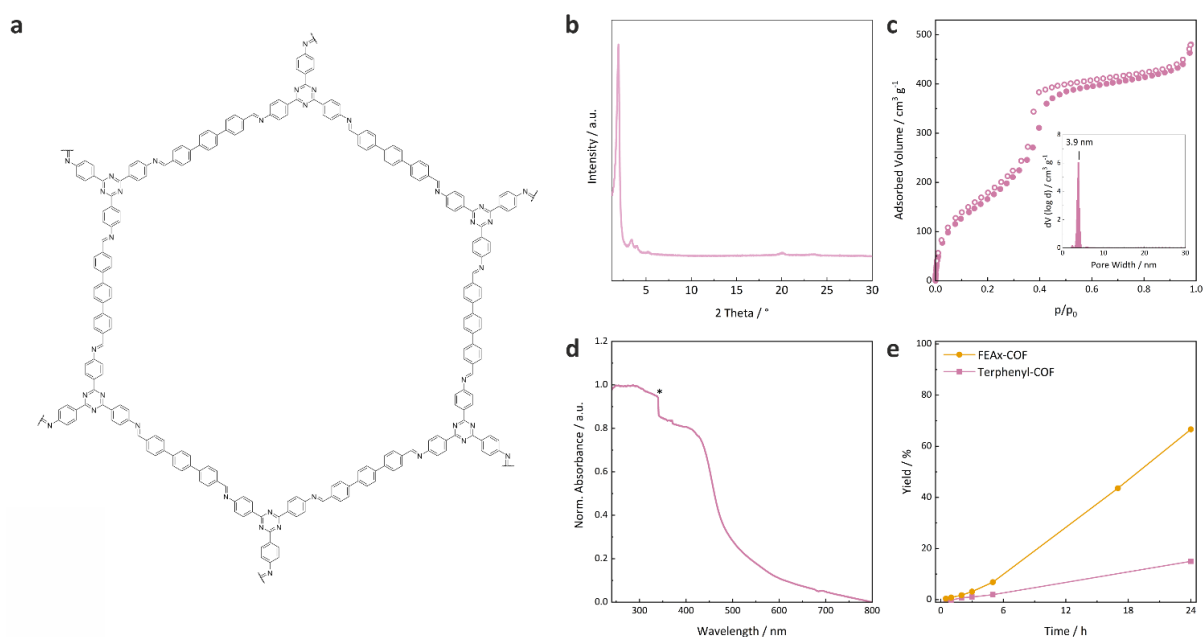
Figure S3-30: (a) Molecular structure of Terphenyl-COF. (b) XRPD pattern of Terphenyl-COF. (c) Argon sorption isotherm of Terphenyl-COF at 87 K. Filled and open symbols represent the adsorption and the desorption branches, respectively. The inset shows the pore size distribution obtained from a QSDFT kernel for cylindrical pores. The BET surface area was determined to be 645.9 m^2 g^{-1}. (d) Solid-state UV-Vis spectrum of Terphenyl-COF. Asterisk indicates lamp change. (e) Photocatalytic efficacy of Terphenyl-COF compared to FEAx-COF in the oxidation of MBA. Reaction conditions: 20 mM MBA in MeCN/water (1:1, 1 mL), 1.5 mg COF, 463 nm LEDs, O_2. Yield determined via HPLC.

Table S3-3: Photocatalytic oxidation of benzylic alcohols and other substrates by FEAx-COF.

Entry	Substrate	Product	Yield / %	E_{ox} / V [a]	Ref.
1	R = 4-NO$_2$		traces	2.84	[24]
2	R = 4-tBu		3	2.06	[25]
3	R = 4-H		0	1.94	[24]
4	R = 4-Me		2	1.84	[24]
5	R = 4-OMe		17[b]	1.48[c]	[26]
6			0	1.73	[27]
7			16	0.72[d]	[28]
8			15[e]	1.35-1.42	[29]
9			14	1.51	[30]
10			12	1.13	[30]
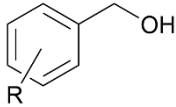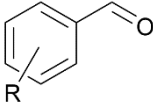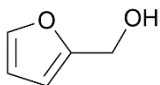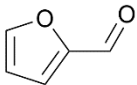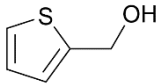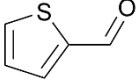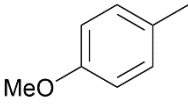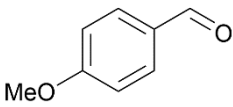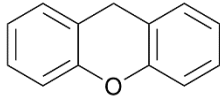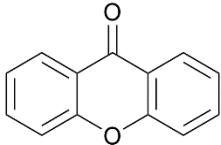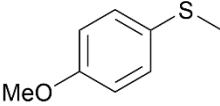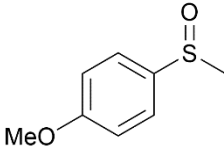
Reaction conditions: 250 mM substrate, 1.5 mg FEAx-COF, 463 nm LEDs, water/MeCN (1 mL, 1:1), 45 °C, O$_2$. Yield after 24 h determined *via* NMR with internal standard [a] *vs*. SCE. [b] Yield after 24 h determined *via* HPLC. [c] 1.52 V *vs*. Ag/AgCl. [d] 0.76 V *vs*. Ag/AgCl. [e] Side product MBAcid formed.
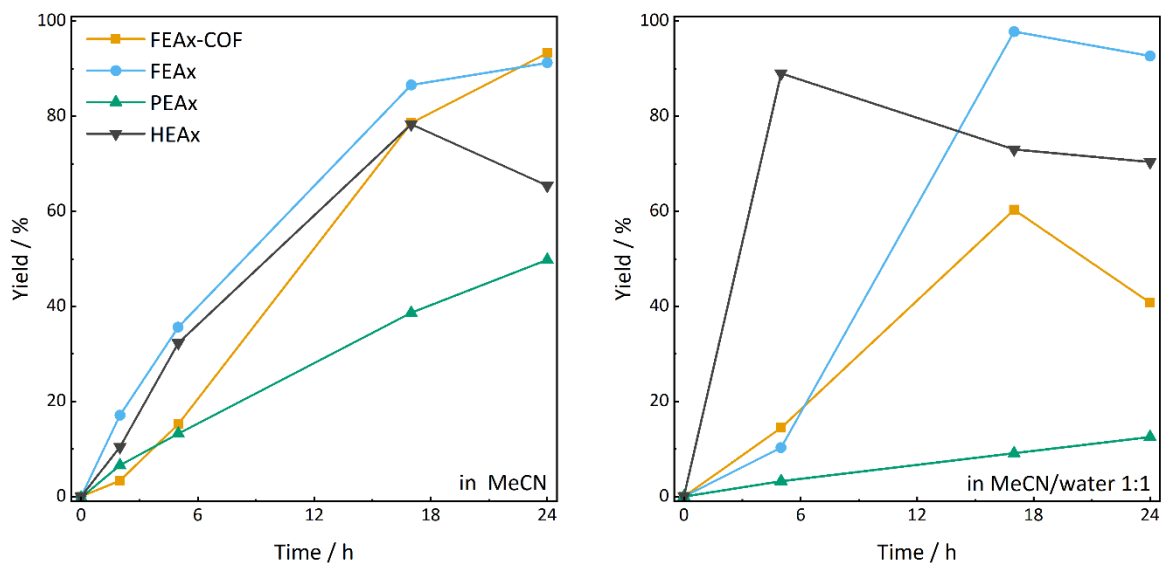
Figure S3-31: Comparison of photocatalytic yields of FEAx COF and the model compounds FEAx, PEAx, and HEAx in acetonitrile (left) and acetonitrile /water 1:1 (right). Reaction conditions: 20 mM MBA in 1 mL solvent, 2 mM molecular alloxazine or 1.5 mg FEAx-COF, O_2, 404 nm LEDs, rt. Decreasing yields with progressing reaction time are due to overoxidation of MBAld to MBAacid.
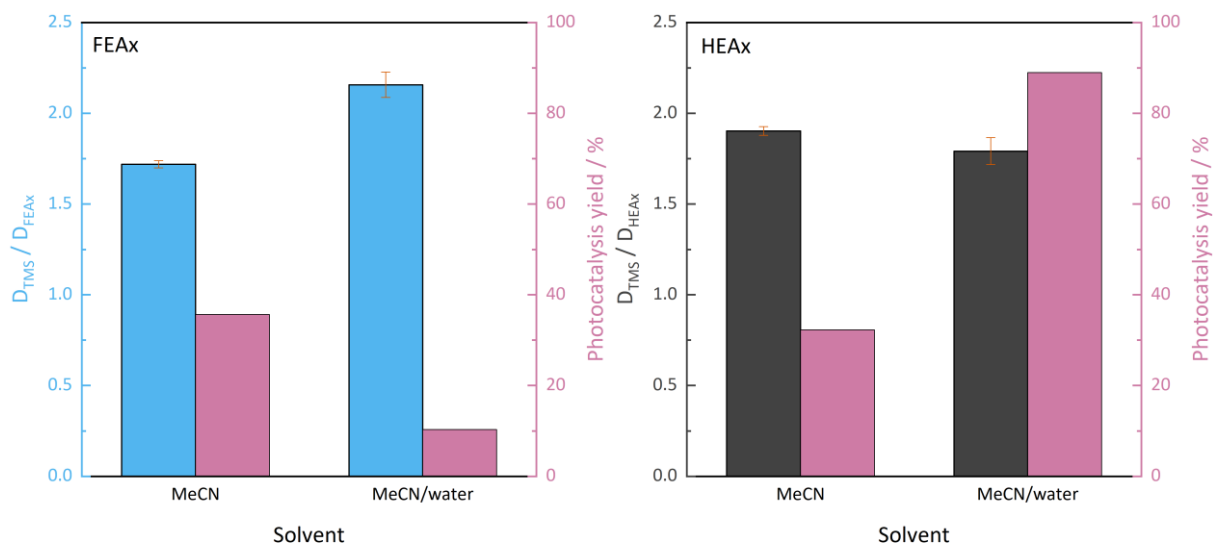
Figure S3-32: Relative diffusion coefficients and photocatalytic activity in different solvents (c = 2 mM) for FEAX (left) and HEAX (right). Photocatalysis reaction conditions: 20 mM MBA (1 mL solvent), 1.5 mg COF, 404 nm LEDs, O_2, rt. Yield determined *via* HPLC after 5 h, since longer irradiation with 404 nm LEDs in MeCN/water leads to overoxidation (see Figure S3-21). Error bars represent the standard deviation of at least three measurements.

The relative diffusion coefficient is proportional to the hydrodynamic radius of the diffusing species. An increase in D_{TMS}/D_M between the different solvents is thus caused by an increase in aggregate size. While HEAX deaggregates in MeCN/water 1:1, following the reported trends for similar flavins,[31] FEAX shows an opposite trend with more pronounced aggregation in the aqueous solvent mixture. It can be seen that the photocatalytic activity is higher for the respective less aggregated species.
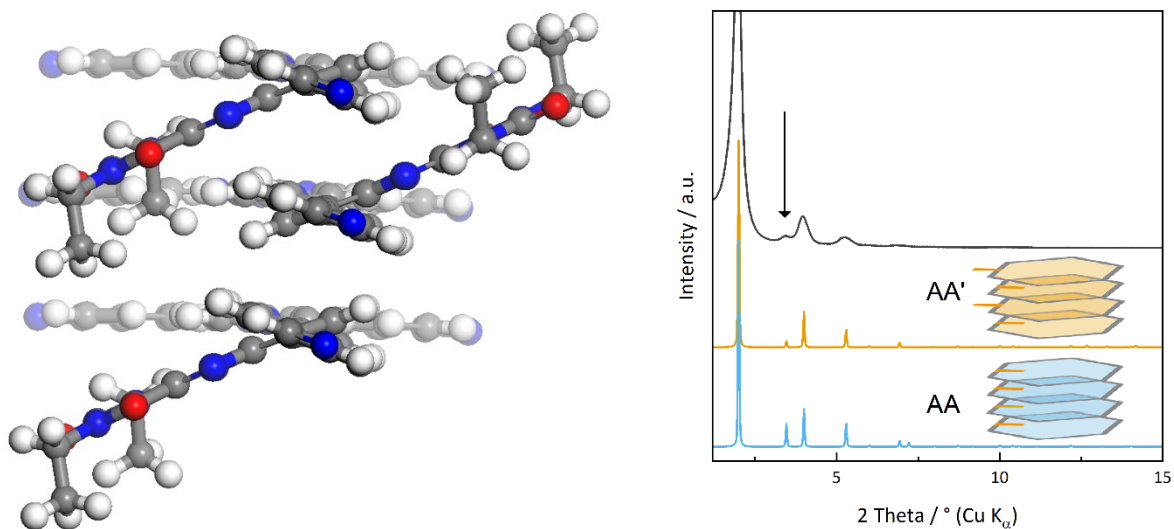
Figure S3-33: Schematic representation of alloxazine orientation in FEAx-COF (left) and simulated XRPD patterns for FEAx-COF with different alloxazine stacking modes compared to experimental data (right). Alloxazine orientation visualized as orange lines.

The structural model for FEAx-COF that best fits the experimental XRPD data consists of COF layers with alternating orientation of the alloxazine core (AA', orange model, Figure S3-33). When all alloxazines are stacked on top of each other (AA, blue model), the simulated pattern shows varying intensities especially at 3.93° (200), which is not represented in the experimental data.
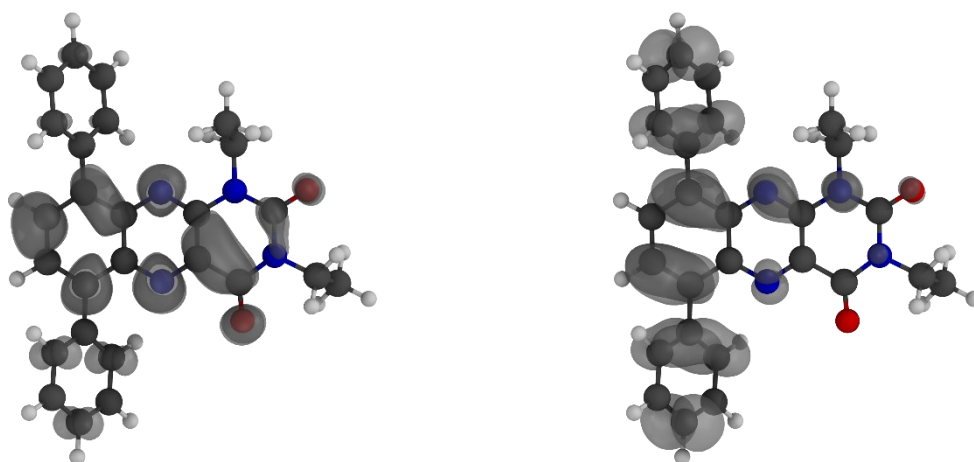
Figure S3-34: Calculated spin densities for the PEAx model compound, radical anion (left) and radical cation (right).

Table S3-4: Calculated vertical radical stabilization energies, obtained as total energy differences between radical anionic (Vertical Radical Anion Stabilization Energy, VRASE), radical cationic (Vertical Radical Cation Stabilization Energy, VRCSE), and neutral states.

Radical Cation				Neutral		Radical Anion		
VRCSE [kcal/mol]	VRCSE [H]	Total Energy [H]		Total Energy [H]		Total Energy [H]	VRASE [H]	VRASE [kcal/mol]
173.58	0.276622	-1372.213663		-1372.490285		-1372.545593	-0.055308	-34.71

Table S3-5: Calculated Total Energies and Reaction Enthalpies as corresponding differences for investigated model systems on PBE0-D3/def2-TZVP level of theory. Solvation effects have been considered using the implicit solvation model COSMO with a value of 36.64 as the dielectric constant to represent acetonitrile.[32]

	Gas Phase	Acetonitrile	Delta Total Energy		
	Total Energy [H]	Total Energy [H]	[H]	[kcal/mol]	[kJ/mol]
PEAx	-1372.490285	-1372.512292	-0.022007	-13.81	-57.78
MBA	-460.947382	-460.961837	-0.014455	-9.07	-37.95
	Reaction Enthalpy (Gas Phase)		0.217118	136.24	570.04
	Reaction Enthalpy (Acetonitrile)		0.199992	125.50	525.08
PEAx-RA	-1372.553223	-1372.629172	-0.075949	-47.66	-199.40
MBA-RK	-460.667326	-460.644965	0.022361	14.03	58.71
	Reaction Enthalpy (Gas Phase)		-0.128895	-80.88	-338.41
	Reaction Enthalpy (Acetonitrile)		-0.114866	-72.08	-301.58
PEAx-H-R	-1373.069373	-1373.097628	-0.028255	-17.73	-74.18
MBA-R	-460.280071	-460.291375	-0.011303	-7.09	-29.68
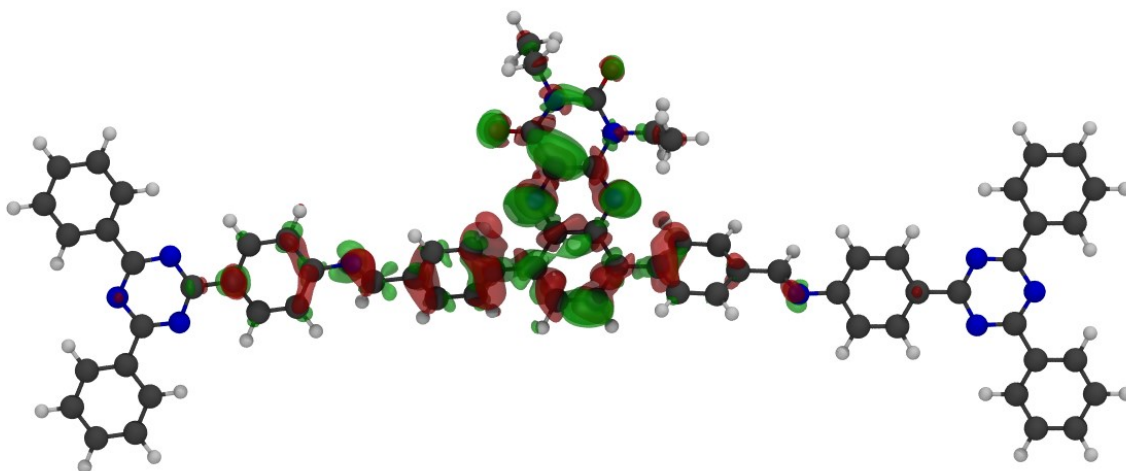
Figure S3-35: Calculated difference density for the lowest vertical excitation for the FEAx-COF pore edge model, obtained on the TD-PBE0-D3/def2-TZVP level of theory. Red isosurfaces depict regions with lower electron density in the excited state whereas green isosurfaces represent higher electron density in the excited state, both in comparison to the electron density of the ground state. The extent of the isosurfaces shows a coverage along the COF pore edge and visualize the conjugation of the alloxazine cores in FEAx-COF.
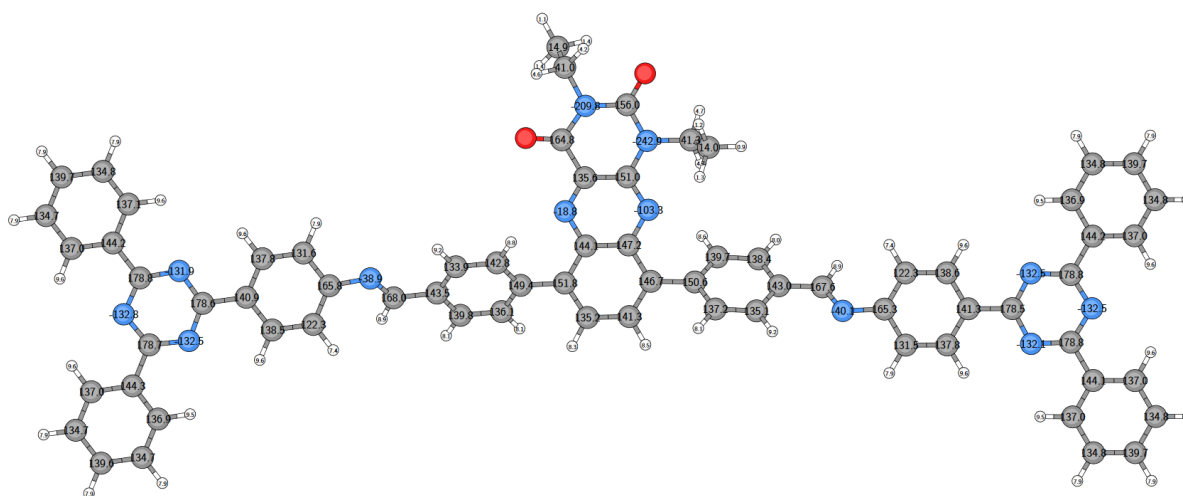
Figure S3-36: Calculated NMR chemical shifts for the FEAx-COF pore edge model, obtained at the B97-2/pcsSeg-2//PBE0-D3/def2-TZVP level of theory.
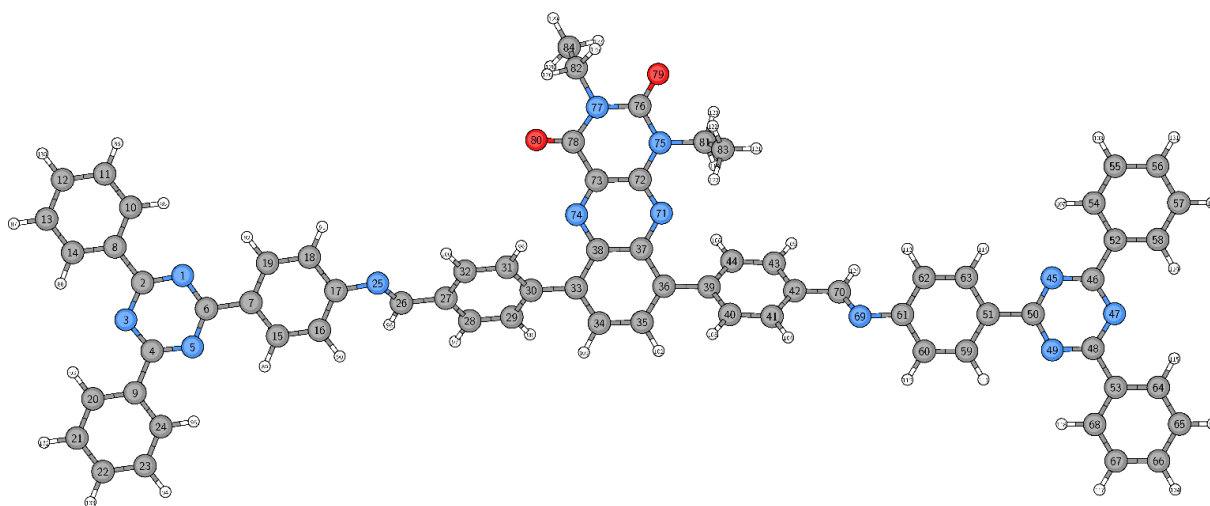
Figure S3-37: Atom labels for the FEAx-COF pore edge model.

Table S3-6: Calculated NMR chemical shifts for the FEAx-COF pore edge model, obtained at the B97-2/pcsSeg-2//PBE0-D3/def2-TZVP level of theory.

Number	Atom	NMR Chemical Shielding [ppm]	NMR Chemical Shift [ppm]
1	N	-11.35	-131.9
2	C	6.51	178.8
3	N	-10.44	-132.8
4	C	6.62	178.7
5	N	-10.75	-132.5
6	C	6.70	178.6
7	C	44.41	140.9
8	C	41.11	144.2
9	C	41.00	144.3
10	C	48.23	137.1
11	C	50.50	134.8
12	C	45.65	139.7
13	C	50.63	134.7
14	C	48.36	137.0
15	C	46.77	138.5
16	C	62.98	122.3
17	C	19.55	165.8
18	C	53.70	131.6
19	C	47.52	137.8
20	C	48.30	137.0
21	C	50.58	134.7
22	C	45.74	139.6
23	C	50.61	134.7
24	C	48.40	136.9

Number	Atom	NMR Chemical Shielding [ppm]	NMR Chemical Shift [ppm]
25	N	-104.32	-38.9
26	C	17.29	168.0
27	C	41.79	143.5
28	C	45.55	139.8
29	C	49.18	136.1
30	C	35.88	149.4
31	C	42.47	142.8
32	C	51.36	133.9
33	C	33.54	151.8
34	C	50.12	135.2
35	C	44.05	141.3
36	C	38.65	146.7
37	C	38.10	147.2
38	C	41.17	144.1
39	C	34.75	150.6
40	C	48.10	137.2
41	C	50.19	135.1
42	C	42.27	143.0
43	C	46.88	138.4
44	C	45.62	139.7
45	N	-10.77	-132.5
46	C	6.54	178.8
47	N	-10.75	-132.5
48	C	6.47	178.8
49	N	-11.20	-132.1
50	C	6.85	178.5
51	C	44.04	141.3
52	C	41.13	144.2
53	C	41.18	144.1
54	C	48.42	136.9
55	C	50.56	134.8
56	C	45.60	139.7
57	C	50.51	134.8
58	C	48.30	137.0
59	C	47.53	137.8
60	C	53.82	131.5
61	C	19.97	165.3
62	C	62.99	122.3
63	C	46.70	138.6

Number	Atom	NMR Chemical Shielding [ppm]	NMR Chemical Shift [ppm]
64	C	48.32	137.0
65	C	50.55	134.8
66	C	45.58	139.7
67	C	50.51	134.8
68	C	48.31	137.0
69	N	-103.11	-40.1
70	C	17.72	167.6
71	N	-39.98	-103.3
72	C	34.33	151.0
73	C	49.72	135.6
74	N	-124.46	-18.8
75	N	99.64	-242.9
76	C	29.35	156.0
77	N	66.57	-209.8
78	C	20.47	164.8
81	C	144.02	41.3
82	C	144.31	41.0
83	C	171.34	14.0
84	C	170.41	14.9
85	H	22.07	9.6
86	H	23.73	7.9
87	H	23.78	7.9
88	H	22.08	9.6
89	H	22.02	9.6
90	H	24.21	7.4
91	H	23.72	7.9
92	H	22.02	9.6
93	H	22.07	9.6
94	H	23.74	7.9
95	H	22.08	9.5
96	H	22.75	8.9
97	H	23.58	8.1
98	H	23.56	8.1
99	H	22.80	8.8
100	H	22.43	9.2
101	H	23.30	8.3
102	H	23.17	8.5
103	H	23.58	8.1
104	H	22.44	9.2

Number	Atom	NMR Chemical Shielding [ppm]	NMR Chemical Shift [ppm]
105	H	23.59	8.0
106	H	23.06	8.6
107	H	22.09	9.5
108	H	23.73	7.9
109	H	23.77	7.9
110	H	22.07	9.6
111	H	22.02	9.6
112	H	23.77	7.9
113	H	24.20	7.4
114	H	22.01	9.6
115	H	22.08	9.6
116	H	23.77	7.9
117	H	23.73	7.9
118	H	22.08	9.5
119	H	26.94	4.7
120	H	26.96	4.7
121	H	30.74	0.9
122	H	30.46	1.2
123	H	30.33	1.3
124	H	22.73	8.9
125	H	27.42	4.2
126	H	27.08	4.6
127	H	30.20	1.4
128	H	30.22	1.4
129	H	30.52	1.1
130	H	23.74	7.9
131	H	23.73	7.9
132	H	23.78	7.9
133	H	23.74	7.9
134	H	23.74	7.9
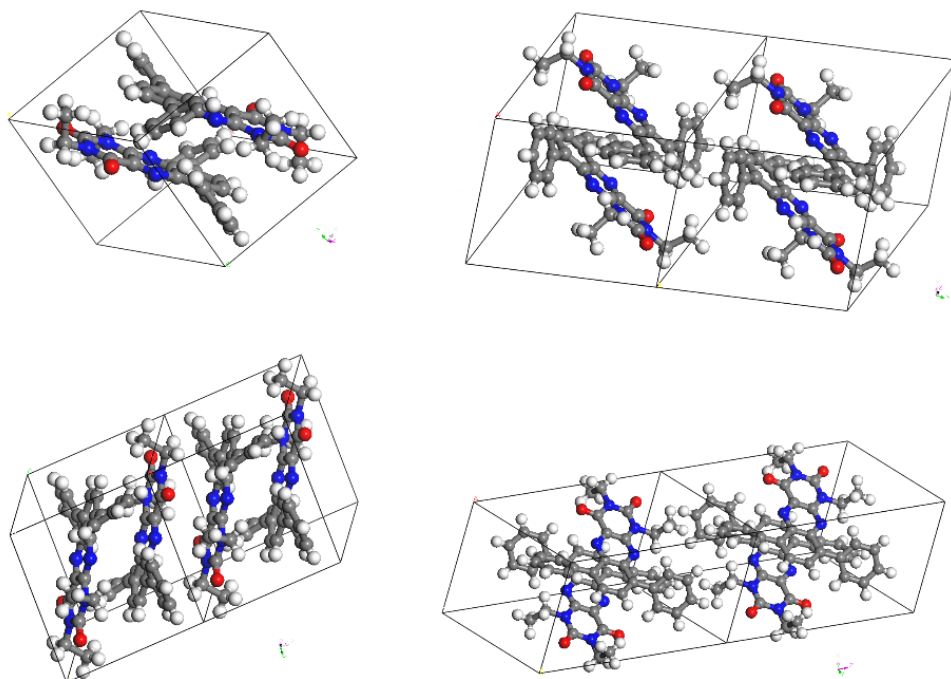
Figure S3-38: Crystal structure of PEAx.
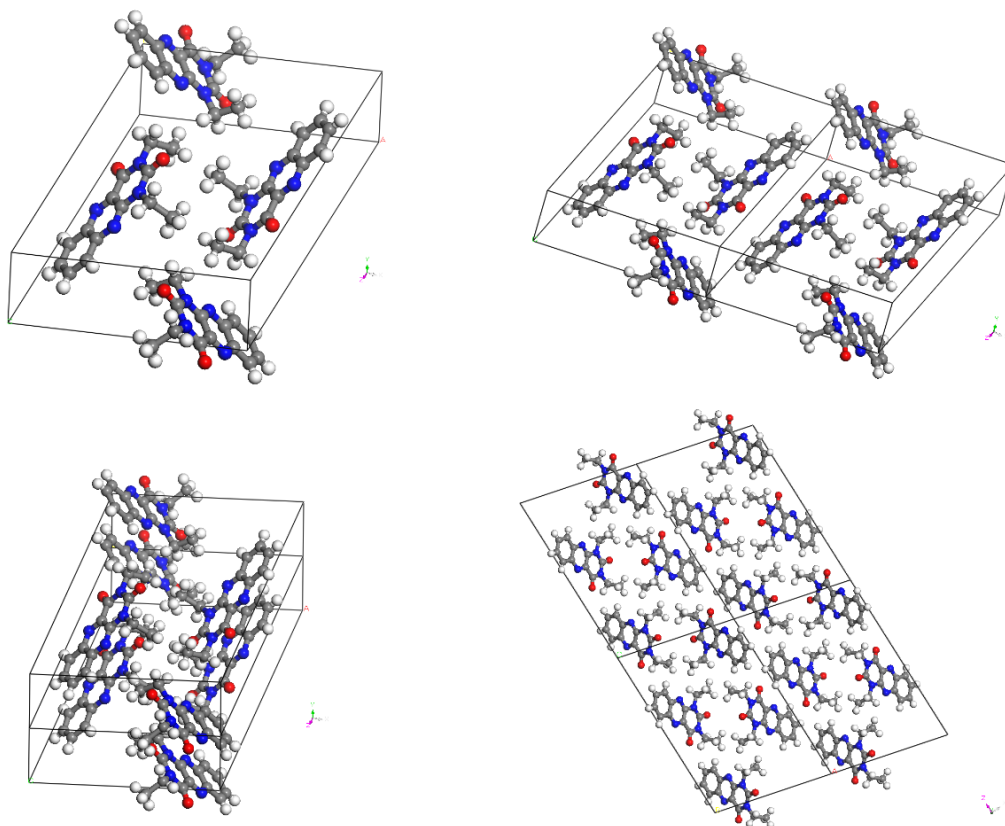
Figure S3-39: Crystal structure of HEAx.
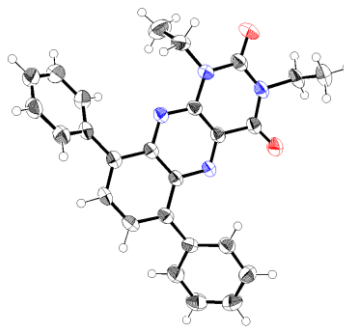
Figure S3-40: Molecular structure of PEAx with thermal ellipsoids (50% probability).

Table S3-7: Crystallographic data and structure refinement for PEAx.

Identification code	STB226_P-1
Empirical formula	$C_{26}H_{22}N_4O_2$
Formula weight	422.47
Crystal Size/mm	0.030 x 0.005 x 0.005
Crystal color	Yellow
Temperature/K	298.7
Crystal system	triclinic
Space group	P-1
a/Å	8.4529(6)
b/Å	10.7933(6)
c/Å	13.3520(8)
α/°	67.316(2)
β/°	71.863(3)
γ/°	87.153(3)
Volume/Å^3	1064.65(12)
Z	2
ρ_{calc}g/cm^3	1.318
μ/mm^{-1}	0.086
F(000)	444.0
Radiation	MoKα (λ = 0.71073)
2Θ range for data collection/°	5.088 to 55
Index ranges	-10 ≤ h ≤ 10, -14 ≤ k ≤ 13, -17 ≤ l ≤ 17
Reflections collected	13350
Independent reflections	4827 [R_{int} = 0.0539, R_{sigma} = 0.0712]
Data/restraints/parameters	4827/0/291
Goodness-of-fit on F^2	1.069
Final R indexes [I>=2σ (I)]	R_1 = 0.0702, wR_2 = 0.1419
Final R indexes [all data]	R_1 = 0.1381, wR_2 = 0.1691
Largest diff. peak/hole / e Å^{-3}	0.21/-0.21

Table S3-8: Fractional Atomic Coordinates (×10^4) and Equivalent Isotropic Displacement Parameters (Å^2×10^3) for PEAx. U$_{eq}$ is defined as 1/3 of the trace of the orthogonalised U$_{IJ}$ tensor.

Atom	x	y	z	U$_{eq}$
O001	9761(3)	2964(2)	4267.4(17)	52.7(6)
N002	6506(3)	5463(2)	6316.8(17)	33.6(5)
N003	7905(2)	5167(2)	4229.2(17)	32.7(5)
N004	9237(3)	2286(2)	6180.6(19)	40.1(6)
O005	8613(3)	1536(2)	8109.2(18)	65.6(7)
N006	7545(3)	3468(2)	7232.0(18)	39.3(6)
C007	6943(3)	6202(2)	4280(2)	31.4(6)
C008	7363(3)	4438(2)	6239(2)	33.3(6)
C009	6284(3)	6366(2)	5339(2)	31.8(6)
C00A	8111(3)	4312(2)	5183(2)	32.9(6)
C00B	5344(3)	7491(3)	5399(2)	34.4(6)
C00C	6622(3)	7120(2)	3266(2)	34.3(6)
C00D	4676(3)	7720(2)	6481(2)	37.1(6)
C00E	7274(3)	7004(3)	2140(2)	36.1(6)
C00F	7366(3)	5772(3)	2028(2)	40.4(7)
C00G	3040(3)	8066(3)	6806(2)	44.6(7)
C00H	5059(3)	8343(3)	4412(2)	39.2(7)
C00I	9117(3)	3158(3)	5132(2)	37.3(6)
C00J	5661(3)	8156(3)	3381(2)	41.5(7)
C00K	8472(4)	2383(3)	7235(3)	43.8(7)
C00L	2397(4)	8301(3)	7790(3)	52.1(8)
C00M	7884(4)	5716(3)	958(2)	48.3(7)
C00N	5632(4)	7616(3)	7181(2)	44.2(7)
C00O	10164(4)	1079(3)	6214(3)	47.2(7)
C00P	6788(4)	3613(3)	8337(2)	48.7(8)
C00Q	3360(4)	8203(3)	8471(3)	55.1(9)
C00R	8324(4)	6878(3)	-16(3)	56.9(9)
C00S	4983(4)	7859(3)	8166(3)	54.5(8)
C00T	7759(4)	8170(3)	1139(2)	51.9(8)
C00U	8996(4)	-102(3)	6484(3)	54.9(8)
C00V	8269(4)	8104(3)	76(3)	62.5(9)
C00W	7965(5)	4373(4)	8575(3)	74.2(11)
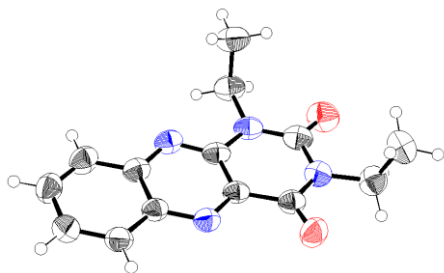
Figure S3-41: Molecular structure of HEAx with thermal ellipsoids (50% probability).

Table S3-9: Crystallographic data and structure refinement for HEAx.

Identification code	STB228-P2 1 c
Empirical formula	$C_{14}H_{14}N_4O_2$
Formula weight	270.29
Crystal Size/mm	0.300 x 0.060 x 0.040
Crystal color	Yellow
Temperature/K	298.6
Crystal system	monoclinic
Space group	$P2_1/c$
a/Å	13.3313(5)
b/Å	5.0391(2)
c/Å	19.8573(7)
α/°	90
β/°	103.665(2)
γ/°	90
Volume/Å^3	1296.21(8)
Z	4
ρ_{calc}g/cm^3	1.385
μ/mm^{-1}	0.097
F(000)	568.0
Radiation	MoKα (λ = 0.71073)
2Θ range for data collection/°	8.29 to 58.816
Index ranges	-18 ≤ h ≤ 18, -6 ≤ k ≤ 6, -27 ≤ l ≤ 27
Reflections collected	23975
Independent reflections	3523 [R_{int} = 0.0505, R_{sigma} = 0.0358]
Data/restraints/parameters	3523/0/183
Goodness-of-fit on F^2	1.070
Final R indexes [I>=2σ (I)]	R_1 = 0.0615, wR_2 = 0.1510
Final R indexes [all data]	R_1 = 0.0976, wR_2 = 0.1683
Largest diff. peak/hole / e Å^{-3}	0.20/-0.14

Table S3-10: Fractional Atomic Coordinates (×10^4) and Equivalent Isotropic Displacement Parameters (Å^2×10^3) for HEAx. U$_{eq}$ is defined as 1/3 of the trace of the orthogonalised U$_{IJ}$ tensor.

Atom	x	y	z	U(eq)
O001	8664.7(11)	4816(3)	5798.0(7)	61.2(4)
O002	6242.7(13)	-925(3)	4641.0(9)	72.4(5)
N003	7473.9(12)	5255(3)	3343.9(8)	48.3(4)
N004	8858.5(11)	7063(3)	4562.8(8)	44.6(4)
N005	7483.7(12)	1886(3)	5219.1(9)	49.8(4)
N006	6831.4(12)	2164(3)	4002.0(9)	49.4(4)
C007	8160.0(14)	3991(4)	5248.0(10)	46.6(4)
C008	8199.6(13)	5134(4)	4570.8(9)	42.2(4)
C009	8171.8(14)	7202(4)	3322.8(9)	46.0(4)
C00A	9566.4(14)	10195(4)	3896.1(10)	50.5(5)
C00B	8869.4(13)	8121(4)	3936.7(9)	43.3(4)
C00C	7503.1(13)	4221(4)	3954.1(9)	43.8(4)
C00D	9571.0(16)	11289(5)	3269.9(11)	55.3(5)
C00E	6813.5(15)	922(4)	4615.3(11)	52.6(5)
C00F	6628(2)	2214(5)	6187.6(13)	71.6(7)
C00G	6051.3(16)	1346(4)	3379.4(11)	57.5(5)
C00H	8884.7(17)	10374(5)	2661.0(11)	59.6(5)
C00I	8204.9(17)	8395(5)	2686.8(10)	57.8(5)
C00J	7392.3(18)	718(4)	5881.1(12)	60.4(5)
C00K	5071.7(17)	2913(5)	3305.5(14)	71.6(7)
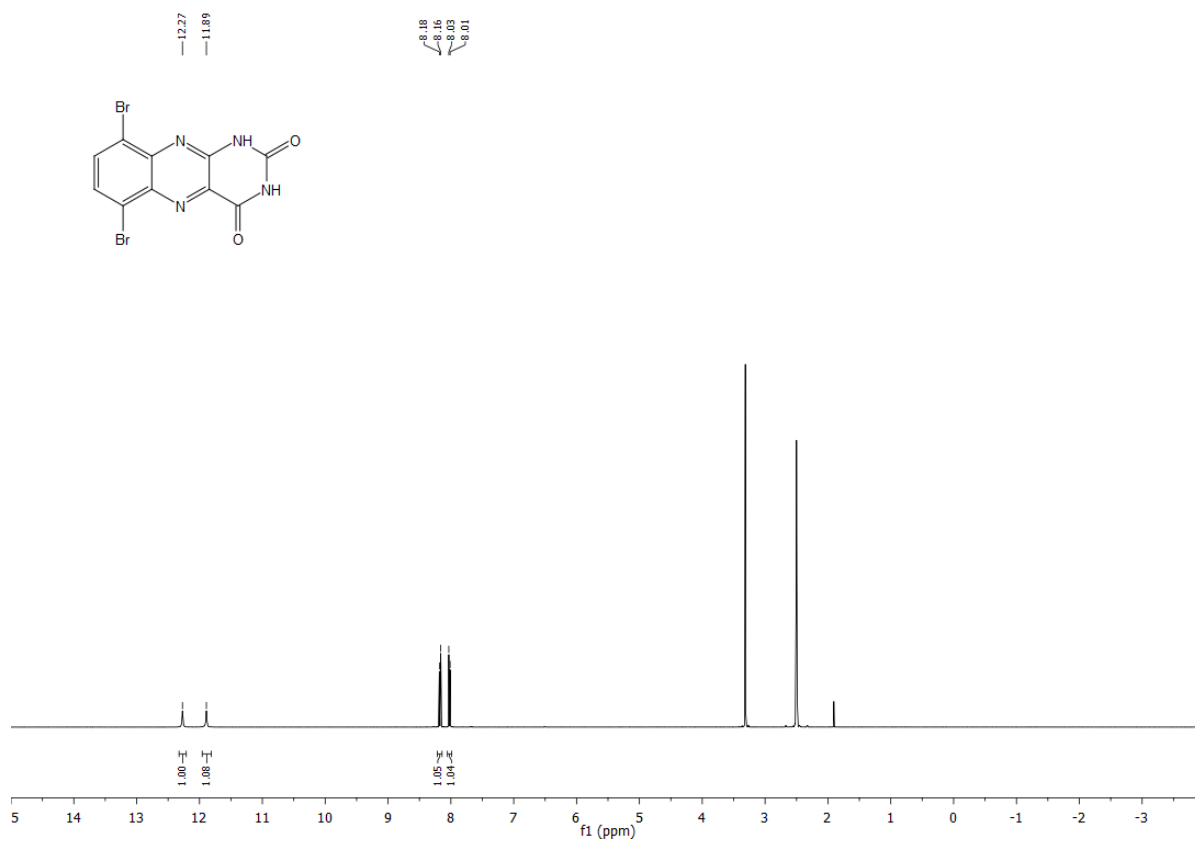
Figure S3-42: ^{1}H-NMR spectrum of 6,9-dibromoalloxazine **S2** (DMSO-d_6, 400 MHz).
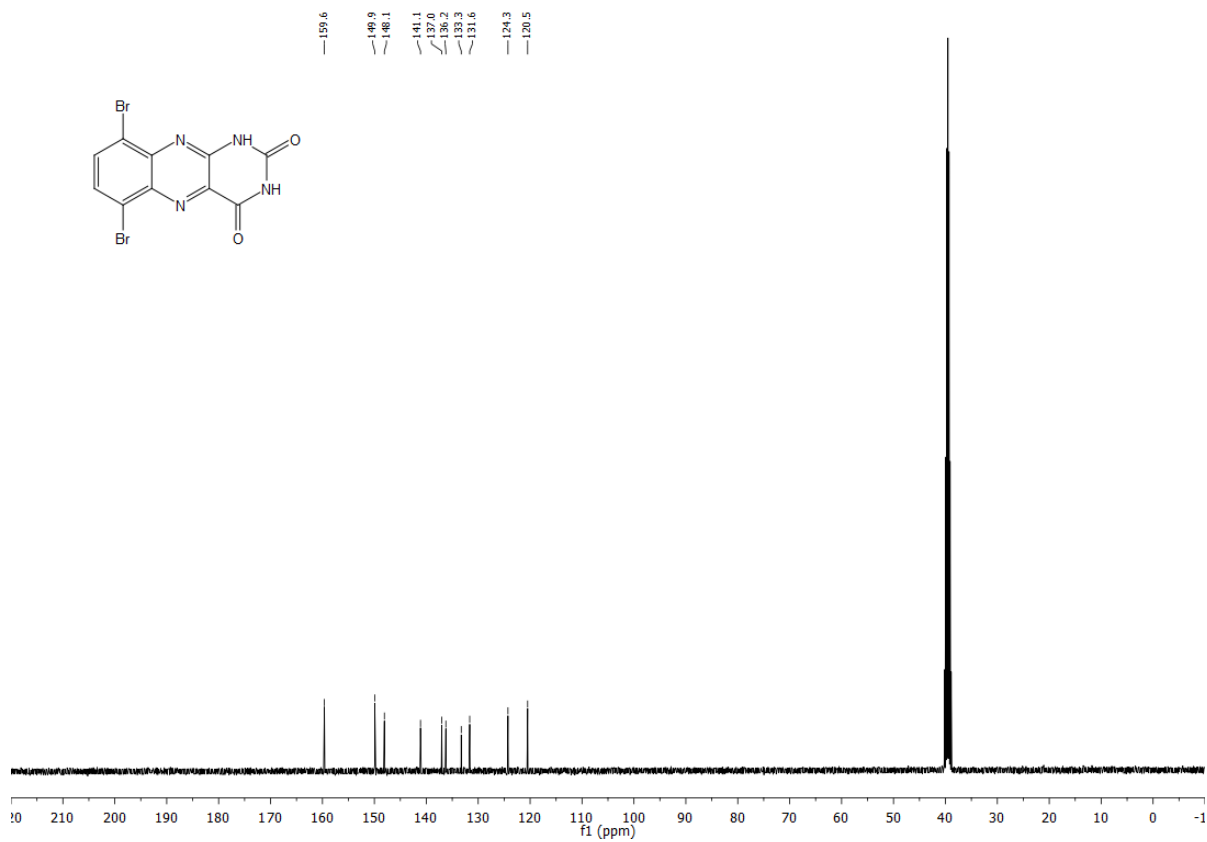
Figure S3-43: ^{13}C-NMR spectrum of 6,9-dibromoalloxazine **S2** (DMSO-d_6, 101 MHz).
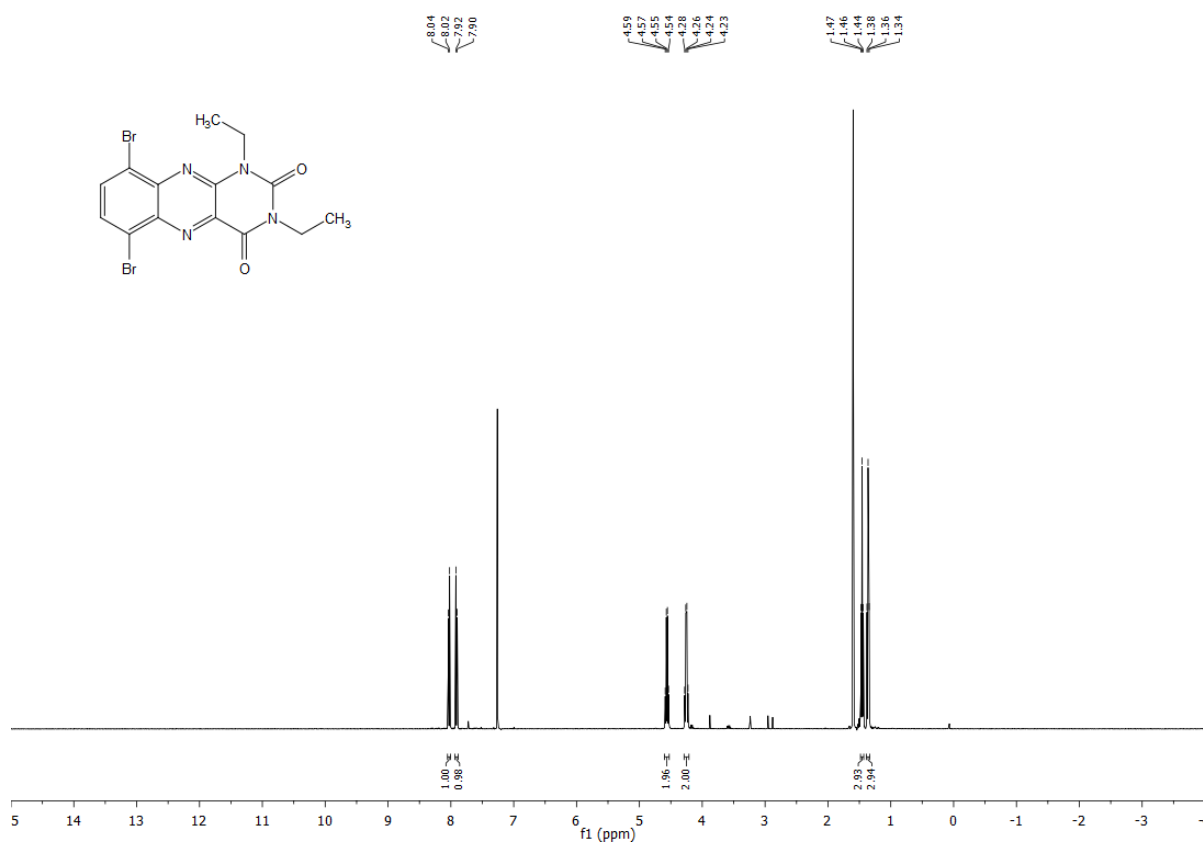
Figure S3-44: ^{1}H-NMR spectrum of 1,3-diethyl-6,9-dibromoalloxazine **S3** (CDCl$_3$, 400 MHz).
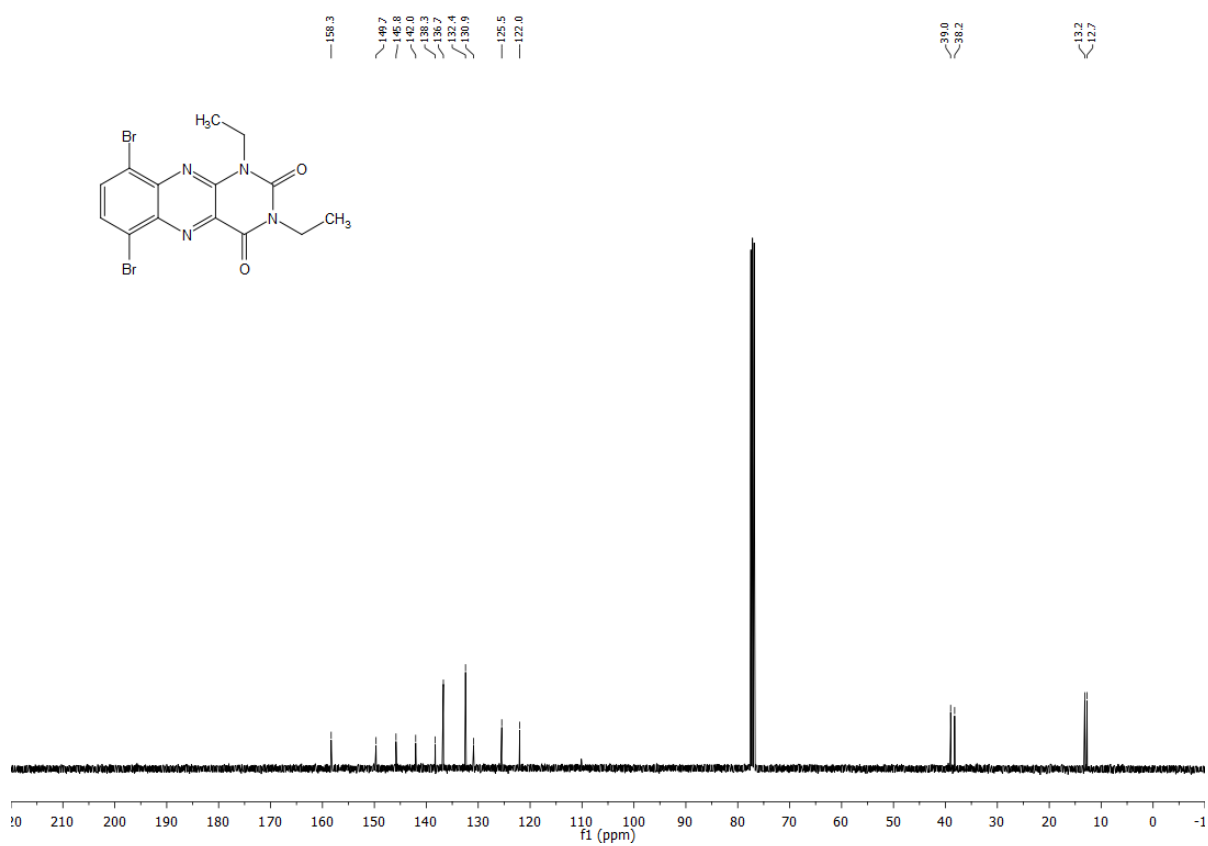
Figure S3-45: ^{13}C-NMR spectrum of 1,3-diethyl-6,9-dibromoalloxazine **S3** (CDCl$_3$, 101 MHz).
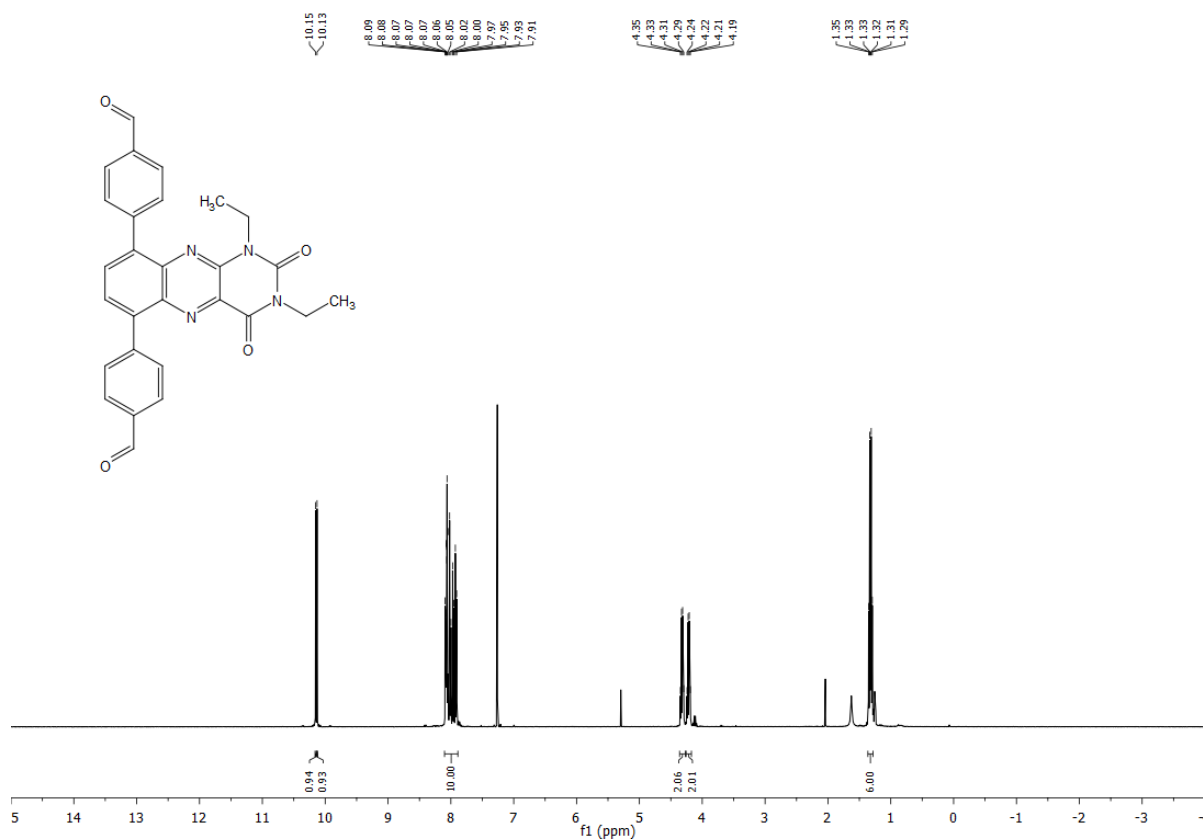
Figure S3-46: ^{1}H-NMR spectrum of 1,3-diethyl-6,9-bis-(4-formylphenyl)-alloxazine FEAx (CDCl$_3$, 400 MHz).
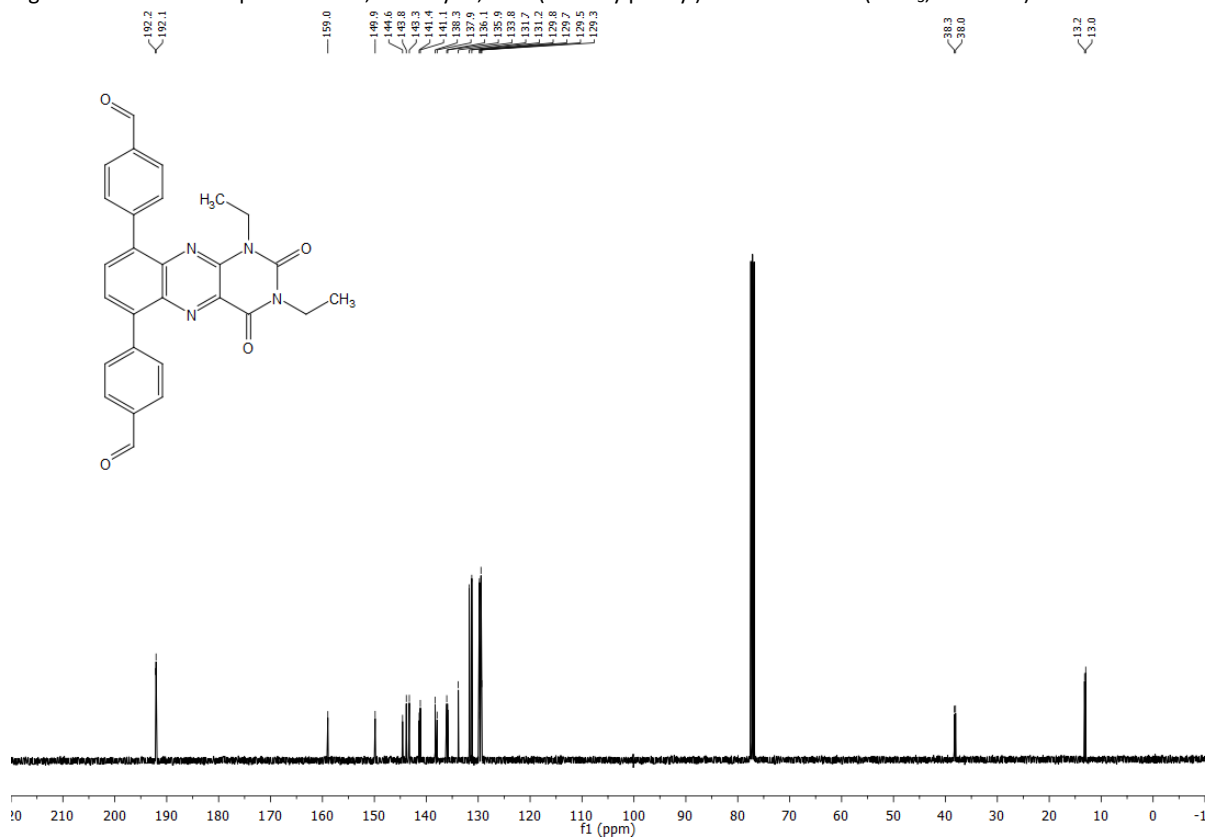
Figure S3-47: ^{13}C-NMR spectrum of 1,3-diethyl-6,9-bis-(4-formylphenyl)-alloxazine FEAx (CDCl$_3$, 101 MHz).
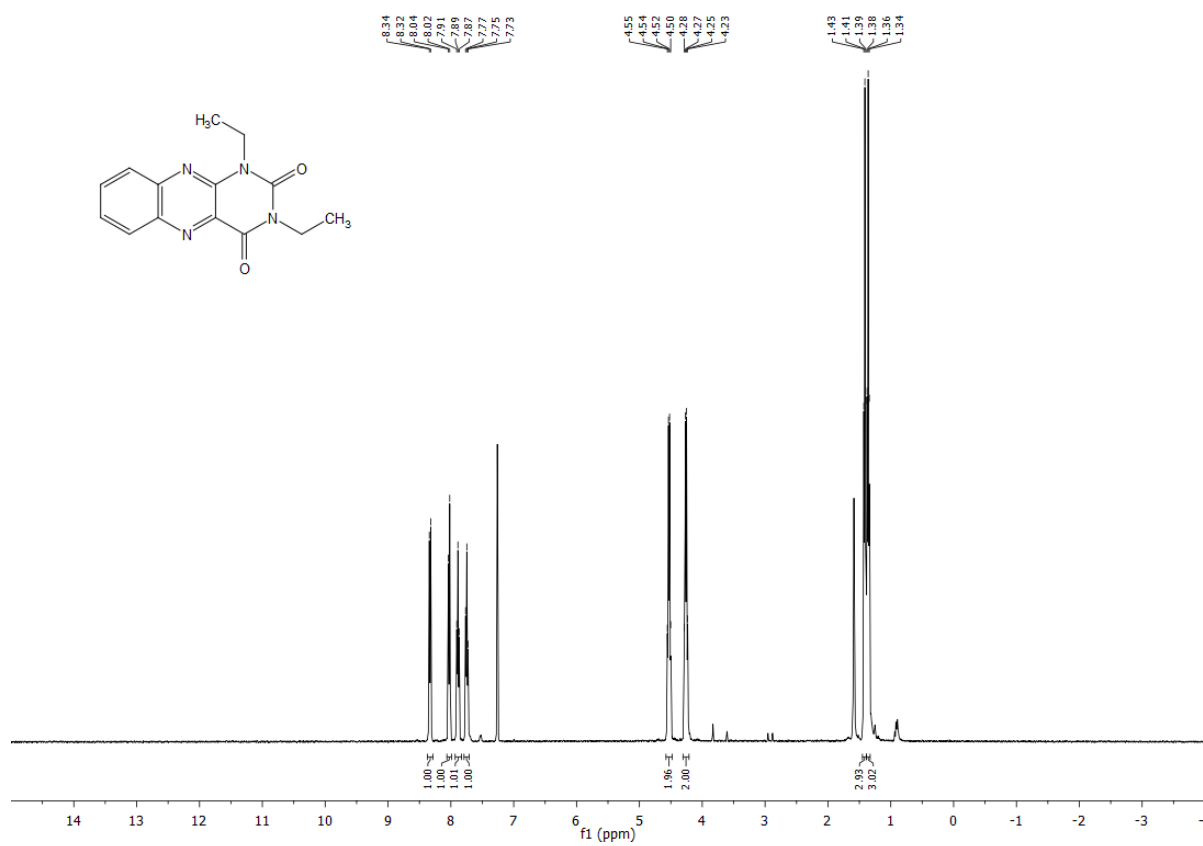
Figure S3-48: ^{1}H-NMR spectrum of 1,3-diethyl-alloxazine HEAx (CDCl$_3$, 400 MHz).
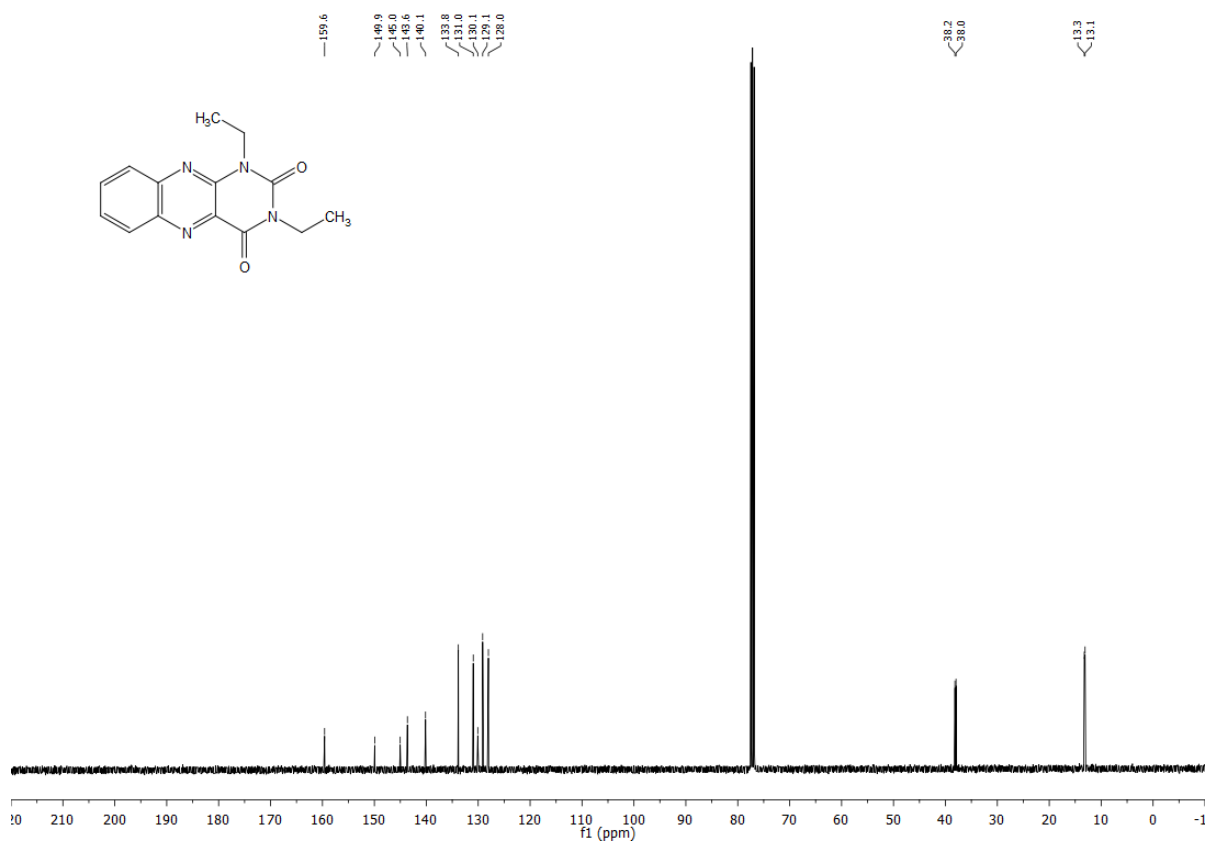
Figure S3-49: ^{13}C-NMR spectrum of 1,3-diethyl-alloxazine HEAx (CDCl$_3$, 101 MHz).
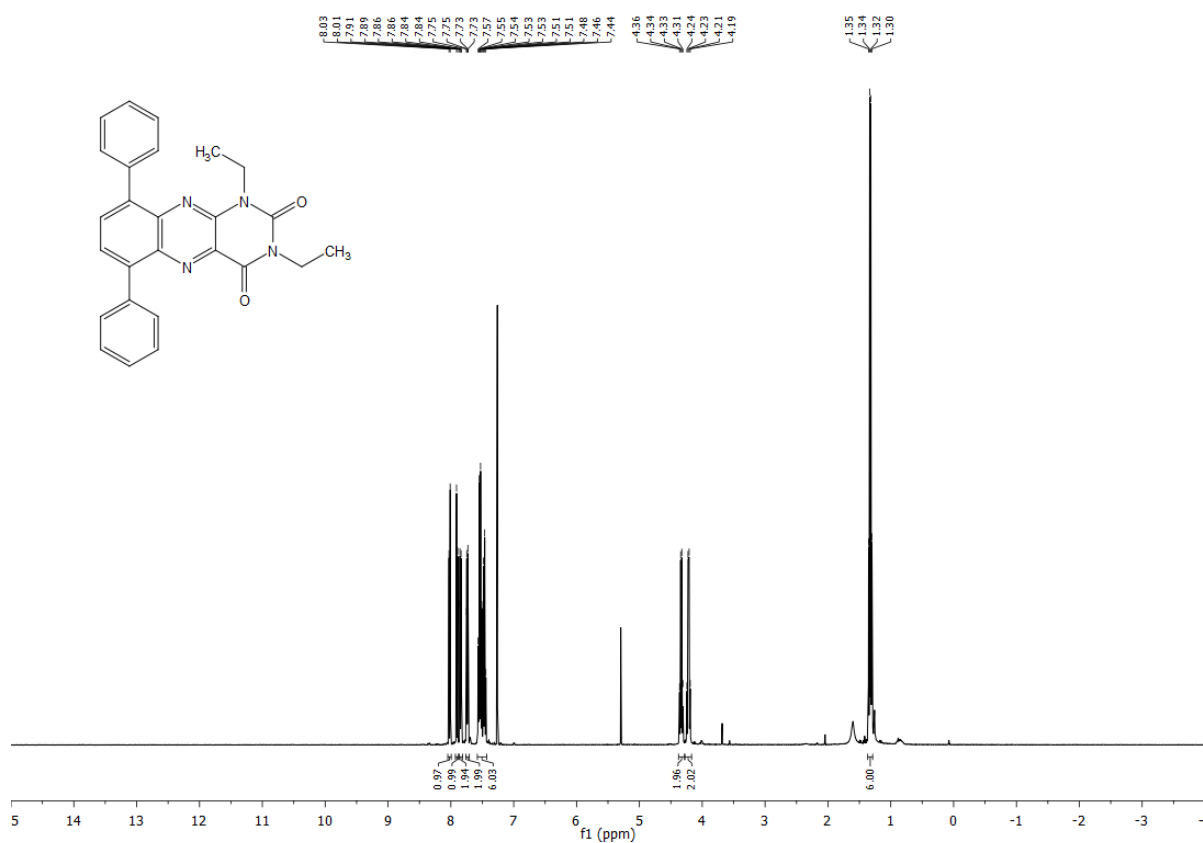
Figure S3-50: ^{1}H-NMR spectrum of 1,3-diethyl-6,9-diphenyl-alloxazine PEAx (CDCl$_3$, 400 MHz).
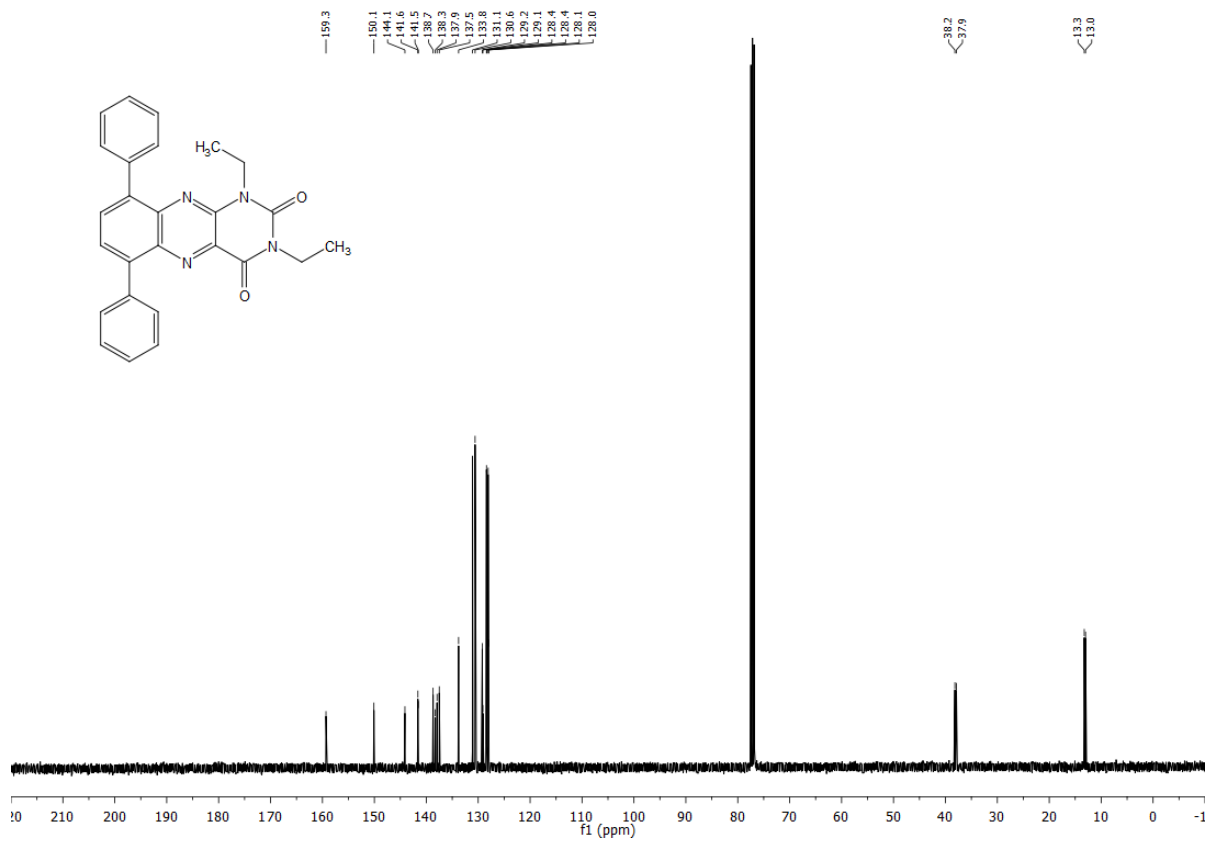
Figure S3-51: ^{13}C-NMR spectrum of 1,3-diethyl-6,9-diphenyl-alloxazine PEAx (CDCl$_3$, 101 MHz).
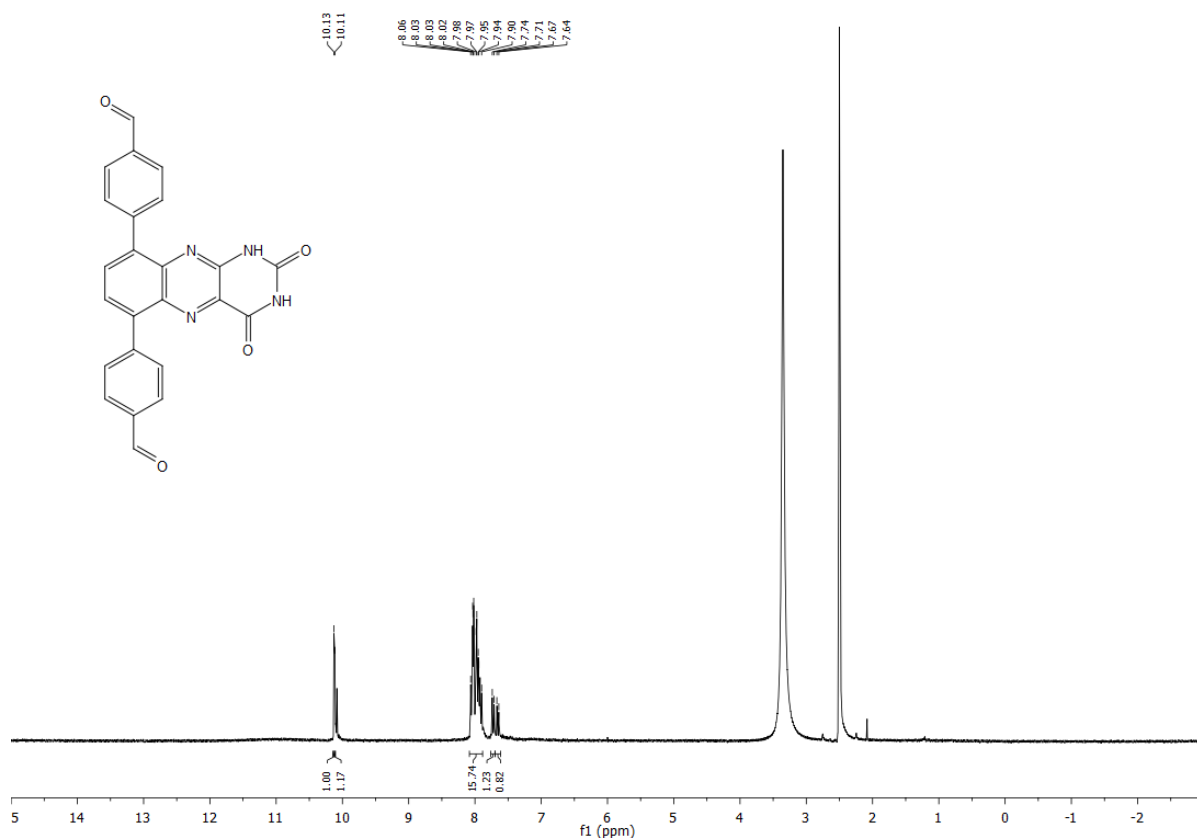
Figure S3-52: ^{1}H-NMR spectrum of 6,9-bis-(4-formylphenyl)-alloxazine (FAx) (DMSO-d_6, 270 MHz).

6.3.4 References

1   G. M. Sheldrick, *Acta Crystallogr., Sect. A* **2015**, *71*, 3–8.

2   G. M. Sheldrick, *Acta Crystallogr., Sect. C* **2015**, *71*, 3–8.

3   O. V. Dolomanov, L. J. Bourhis, J. A. K. Howard, H. Puschmann, *J. Appl. Crystallogr.* **2009**, *42*, 339.

4   A. Macchioni, G. Ciancaleoni, C. Zuccaccia, D. Zuccaccia, *Chem. Soc. Rev.* **2008**, *37*, 479–489.

5   J. E. Tanner, *J. Chem. Phys.* **1970**, *52*, 2523–2526.

6   C. Adamo, V. Barone, *J. Chem. Phys.* **1999**, *110*, 6158–6170.

7   M. Ernzerhof, G. E. Scuseria, *J. Chem. Phys.* **1999**, *110*, 5029–5036.

8   S. Grimme, J. Antony, S. Ehrlich, H. Krieg, *J. Chem. Phys.* **2010**, *132*, 154104.

9   A. Schäfer, C. Huber, R. Ahlrichs, *J. Chem. Phys.* **1994**, *100*, 5829–5835.

10   R. Ahlrichs, M. Baer, M. Haeser, H. Horn, C. Koelmel, *Chem. Phys. Lett*. **1989**, *162*, 165–169.

11   P. J. Wilson, T. J. Bradley, D. J. Tozer, *J. Chem. Phys.* **2001**, *115*, 9233–9242.

12   J. Kussmann and C. Ochsenfeld, *J. Chem. Theory Comput.* **2015**, *11*, 918–922.

13   J. Kussmann and C. Ochsenfeld, *J. Chem. Phys.* **2013**, *138*, 134114.

14   N. G. Connelly and W. E. Geiger, *Chem. Rev.* **1996**, *96*, 877–910.

15   B. P. Biswal, H. A. Vignolo-González, T. Banerjee, L. Grunenberg, G. Savasci, K. Gottschling, J. Nuss, C. Ochsenfeld and B. V. Lotsch, *J. Am. Chem. Soc.* **2019**, *141*, 11082–11092.

16 C. M. Cardona, W. Li, A. E. Kaifer, D. Stockdale and G. C. Bazan, *Adv. Mater.* **2011**, *23*, 2367–2371.

17 R. Gomes, P. Bhanja and A. Bhaumik, *Chem. Commun.* **2015**, *51*, 10050–10053.

18 L. Liu, D.-J. Hong and M. Lee, *Langmuir* **2009**, *25*, 5061–5067.

19 J. Richtar, P. Heinrichova, D. H. Apaydin, V. Schmiedova, C. Yumusak, A. Kovalenko, M. Weiter, N. S. Sariciftci and J. Krajcovic, *Molecules* **2018**, *23*, 2271.

20 R. L. Greenaway, V. Santolini, M. J. Bennison, B. M. Alston, C. J. Pugh, M. A. Little, M. Miklitz, E. G. B. Eden-Rump, R. Clowes, A. Shakil, H. J. Cuthbertson, H. Armstrong, M. E. Briggs, K. E. Jelfs and A. I. Cooper, *Nat. Commun.* **2018**, *9*, 2849.

21 B. Atkinson and Di M., *Trans. Faraday Soc.* **1958**, *54*, 1331–1339.

22 C. Ayed, W. Huang and K. A. I. Zhang, *Front. Chem. Sci. Eng.* **2020**, *11*, 31.

23 P. K. Walia, M. Sharma, M. Kumar and V. Bhalla, *RSC Adv.* **2019**, *9*, 36198–36203.

24 S. Fukuzumi and S. Kuroda, *Res. Chem. Intermed.* **1999**, *25*, 789–811.

25 S. Higashimoto, N. Suetsugu, M. Azuma, H. Ohue and Y. Sakata, *J. Catal.* **2010**, *274*, 76–83.

26 C. Zeng, N. Zhang, C. M. Lam and R. D. Little, *Org. Lett.* **2012**, *14*, 1314–1317.

27 H. G. Roth, N. A. Romero and D. A. Nicewicz, *Synlett* **2016**, *27*, 714–723.

28 J.-H. Hong, Y.-K. Hwang, J.-Y. Hong, H.-J. Kim, S.-J. Kim, Y. S. Won and S. Huh, *Chem. Commun.* **2011**, *47*, 6963–6965.

29 A. Attour, S. Rode, T. Bystron, M. Matlosz and F. Lapicque, *J. Appl. Electrochem.* **2007**, *37*, 861–870.

30 X. Lu, X.-X. Li, Y.-M. Lee, Y. Jang, M. S. Seo, S. Hong, K.-B. Cho, S. Fukuzumi and W. Nam, *J. Am. Chem. Soc.* **2020**, *142*, 3891–3904.

31 J. Dadová, S. Kümmel, C. Feldmeier, J. Cibulková, R. Pažout, J. Maixner, R. M. Gschwind, B. König and R. Cibulka, *Chem. Eur. J.* **2013**, *19*, 1066–1075.

32 A. Klamt and G. Schüürmann, *J. Chem. Soc., Perkin Trans. 2* **1993**, 799–805.

6.4   Supporting Information for Chapter 4

6.4.1   Materials and Methods

X-ray photoelectron spectroscopy (XPS)

XPS measurements were conducted on KRATOS Axis Ultra X-ray photoelectron spectrometer with a monochromatic Al Kα source and charge compensation. Binding energies were calibrated to the adventitious carbon 1s peak at 284.80 eV.[1,2] The CasaXPS software 2.3.16 was used for data analysis. Powder samples were measured on indium foil.

Supercritical Drying

Supercritical drying of COF samples was performed with a LEICA EM CPD300 using EtOH as exchange fluid. The COFs were contained inside a filter paper enveloped and not allowed to dry out between washing steps and supercritical drying.

Water sorption

Water sorption isotherms were performed using a Quantachrome Instruments Autosorb iQ MP with included vapor option. A water-jacketed water bath connected to a Julabo F12-ED thermostat was used to maintain the specified temperature at the position of the sample. ASiQwin Version 3.01 was used for data analysis. Conversion of volumetric (V_{STP} in cm^3 g^{-1}) to gravimetric water uptake (in g g^{-1}) was done using the following formula:[3]

$$\text{Water uptake / g g}^{-1} = \frac{V_{STP} \cdot 18.015 \text{ g mol}^{-1}}{22414 \text{ cm}^3\text{mol}^{-1}}$$

Inert gas sorption

Argon and nitrogen sorption measurements at 87 K and 77 K, respectively, were performed with a Quantachrome Instruments Autosorb iQ MP. Samples of more than 20 mg were preheated *in vacuo* (10^{-7} mbar) at 120 °C for 12 h. ASiQwin Version 3.01 was used for data analysis. Pore size distributions were evaluated using the carbon QSDFT kernel for cylindrical pores for the adsorption branch if not stated otherwise. Expected pore sizes were derived from structural models in Materials Studio v6.0.0.

Hydrogenation reactions

Hydrogenation of aromatic aldehydes were performed in 5 mL Biotage microwave vials. The COF (3.0 mg, if not stated otherwise) was suspended in deionized water (3 mL) together with 4-nitrobenzaldehyde (305.0 mg, 2.0 mmol, 1.0 eq.). Formic acid or sodium formate (7.95 mmol, 4.0 eq.) were added and the reaction mixture was stirred at 80 °C. Samples of 100 μL were used for product quantification *via* NMR (Figure S4-1).
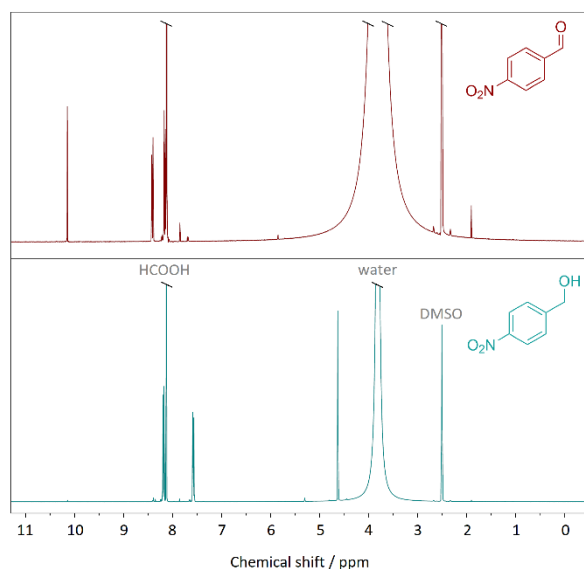
^{1}H NMR (400 MHz, DMSO-d_6) δ = 10.14 (s, 1H), 8.41 (d, J = 8.7 Hz, 2H), 8.16 (d, J = 8.8 Hz, 2H) ppm.

^{1}H NMR (400 MHz, DMSO-d_6) δ = 8.18 (d, J = 8.7 Hz, 2H), 7.57 (d, J = 8.6 Hz, 2H), 4.62 (s, 2H) ppm.

Figure S4-1: NMR spectra and corresponding analysis of an exemplary reaction mixture showing the reduction of 4-nitrobenzaldehyde (top) to 4-nitrobenzyl alcohol (bottom). Signals corresponding to formic acid, water, and DMSO truncated for clarity.

Water-gas shift reactions

6 mg COF or 1.40 mg [Cp*Ir(bpy)Cl]Cl (2.5 µmol) were suspended in 5 mL phosphate buffer (10 mM, pH 7) in a gas-tight photoreactor. The reactor was vacuumed to 30 mbar and replenished with CO (grade 3.7) up to a pressure of 800 mbar five times. In the last cycle, the reactor was filled up to 1.5 bar of CO. Dräger XXS CO LC sensors were used to probe for CO leaking throughout the experiments. A SHIMADZU GCMS-QP2010 gas chromatograph with MS and BID detection was used to analyze the reaction headspace composition ($V_{headspace}$ = 300 mL). The BID detector was calibrated with H_2 calibration gas in various concentrations prior to WGS experiments. A class AAA Newport 94023A solar simulator was used for illumination. The COF suspensions were stirred at 500 rpm and at a water-jacket-controlled temperature of 25 °C during experiments. Hydrogen concentrations in ppm were converted to µmol using the ideal gas law. Data was baseline-corrected by about 20 ppm H_2 to compensate for background signal due to impurities in the supplied CO gas. The exact correction value was based on the first GC data point, which was measured prior to illumination.

In-situ optical microscopy

Color changes of COFs upon exposure to carbon monoxide were monitored in a custom-built steel chamber with three inlet valves.[4] One valve was connected to a vacuum pump for chamber evacuation. A second inlet valve was connected to a set of gas washing bottles to supply humidified Ar of CO gas. A third connection was used as gas outlet. Due to the toxicity of CO, appropriate gas sensors were employed and outlet gas was discharged into the fume hood. COF samples were mortared briefly and transferred to the sample chamber inside a small plastic bowl for containment. After closing the sample chamber, residual air was removed three times *via* vacuum/argon cycling before switching the inlet to CO gas. Microscopic images were obtained with a Leica DM 2500M microscope (Leica Microsystems GmbH, Germany) and an DFC295 digital camera. Spectroscopy was conducted with an USB4000-XR1-ES spectrophotometer (Ocean Optics Inc., USA) connected to the microscope.

6.4.2 Synthetic Procedures
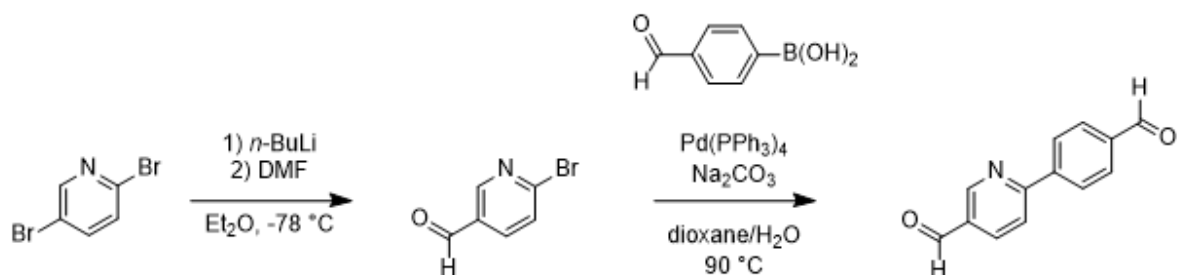
Scheme S4-1: Synthetic route to 2-(4-Formylphenyl)-5-formylpyridine (PPY-CHO).

2-(4-Formylphenyl)-5-formylpyridine (PPY-CHO) was synthesized according to a literature procedure (Scheme S4-1).[5] The analytical data matches the literature values:

^{1}H NMR (101 MHz, CDCl$_3$): δ = 10.18 (s, 1H), 10.11 (s, 1H), 9.18 (dd, J = 2.2, 0.9 Hz, 1H), 8.31 – 8.24 (m, 3H), 8.05 – 8.01 (m, 2H), 7.99 (dt, J = 8.2, 0.7 Hz, 1H) ppm. ^{13}C NMR (101 MHz, CDCl$_3$) δ = 191.9, 190.4, 160. 7, 152.5, 143.4, 137.4, 137.0, 130.6, 130.4, 128.3, 121.4 ppm. R$_f$: 0.28 (n-hexane/EtOAc 2:1).

Synthesis of TAPB-PPY COF

TAPB (16.0 mg, 0.042 mmol, 2 eq.) and PPY-CHO (13.4 mg, 0.63 mmol, 3 eq.) were combined in a 5 mL BIOTAGE microwave vial sealed with a rubber septum. The vial was evacuated using high vacuum, and replenished with argon three times. Mesitylene (1.33 mL) and 1,4-dioxane (0.66 mL) were added and the mixture was sonicated for five minutes before degassing the suspension three times. Acetic acid (6 M, 100 µL) was added, the vials were sealed with a crimp cap and heated to 130 °C for 72 h in a preheated muffle furnace. After cooling to r.t., the solids of five paralleled reactions were combined, filtered off, and washed with DMF (50 mL), THF (50 mL), acetone (100 mL), and MeOH (50 mL). Soxhlet extraction with MeOH overnight and subsequent supercritical drying with CO$_2$ yielded TAPB-PPY COF as an orange powder (98.1 mg, 80%).

TAPB-BPY COF and TT-BPY COF were synthesized accordingly, but using different linkers.

Synthesis of Ir@TAPB-PPY COF

TAPB-PPY COF (44.1 mg, ca. 0.108 mmol ppy units, 1 eq.), [Cp*IrCl$_2$]$_2$ (20.8 mg, ca. 0.052 mmol Ir, 2 eq.), and NaOAc (8.2 mg, 0.1 mmol, 1 eq.) were combined in a 20 mL BIOTAGE microwave vial. DMF (6.5 mL) were added and the suspension was shaken at 150 rpm for 20 h. The solid was filtered off and washed with DMF (30 mL), THF (30 mL), acetone (50 mL), EtOH (30 mL), water (20 mL), and MeOH (50 mL). Supercritical drying with CO$_2$ yielded Ir@TAPB-PPY COF as an orange powder (32.5 mg, 2.05 wt% Ir, 74%).

Synthesis of Ir@TT-BPY COF

TT-BPY COF (69.6 mg, ca. 0.169 mmol ppy units, 1 eq.), [Cp*IrCl$_2$]$_2$ (90.0 mg, ca. 0.226 mmol Ir, 0.75 eq.) were combined in a 20 mL BIOTAGE microwave vial. DMF (6.7 mL) was added and the suspension was slowly stirred for 68 h. The solid was filtered off and washed with copious amounts of

MeOH, DCM, acetone, and MeOH again. Soxhlet extraction with MeOH overnight and subsequent supercritical drying with CO_2 yielded Ir@TT-BPY COF as a red-orange powder (101 mg, 83%). By varying the amount of iridium precursor, the resulting iridium-loading can be tuned (Table S4-1).

Ir@TAPB-BPY COF was synthesized accordingly.

6.4.3 Additional Data
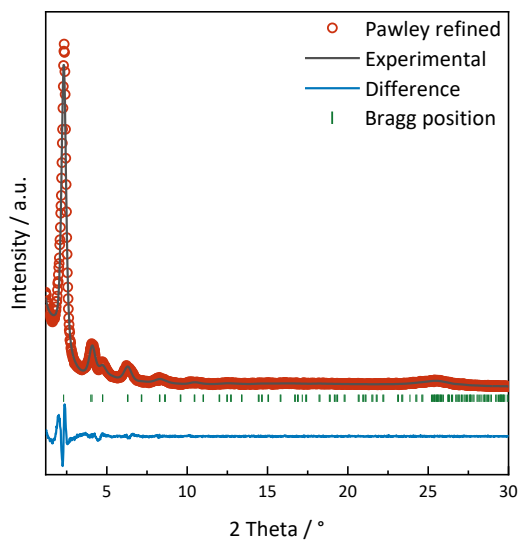
Figure S4-2: Pawley refinement data for TT-BPY COF.
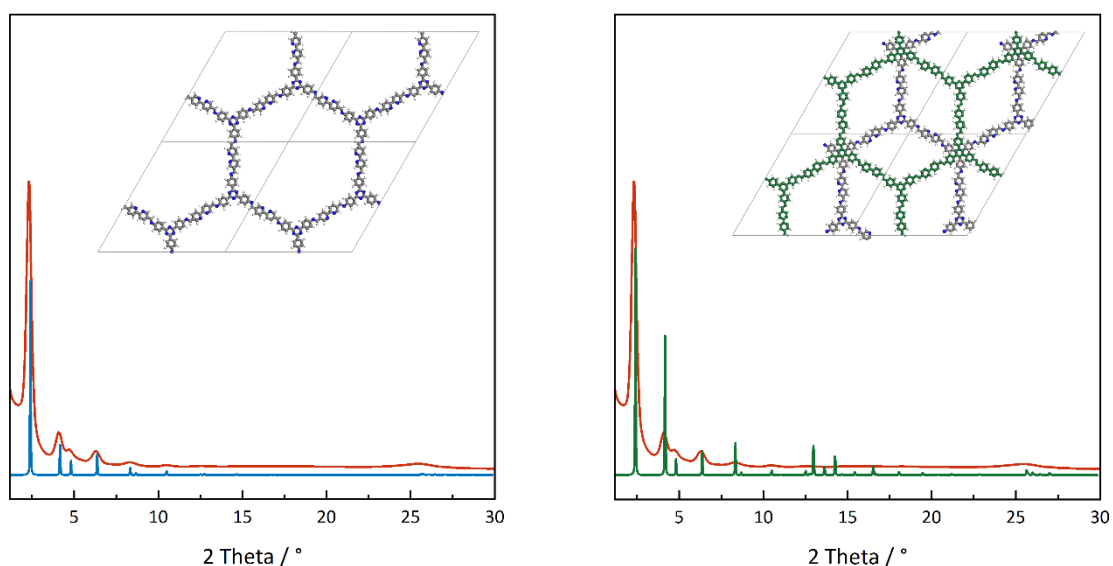
Figure S4-3: Comparison of experimental XRPD data for TT-BPY COF with simulated patterns for an AA-eclipsed (left) and an AB-staggered (right) crystal structure. Respective underlying models shown as insets.
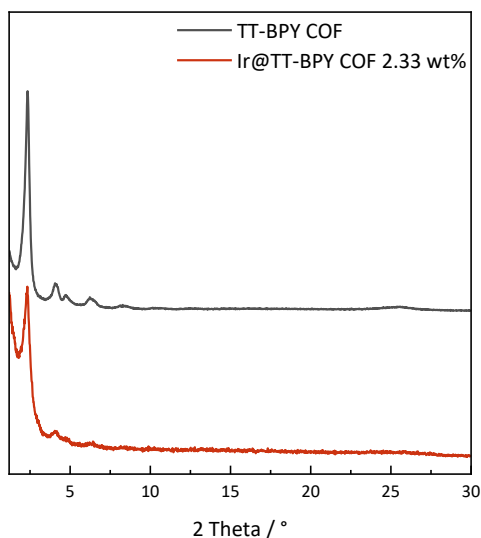
Figure S4-4: XRPD pattern for TT-BPY COF compared to Ir@TT-BPY COF synthesized from partially pre-metallated bipyridine linkers.
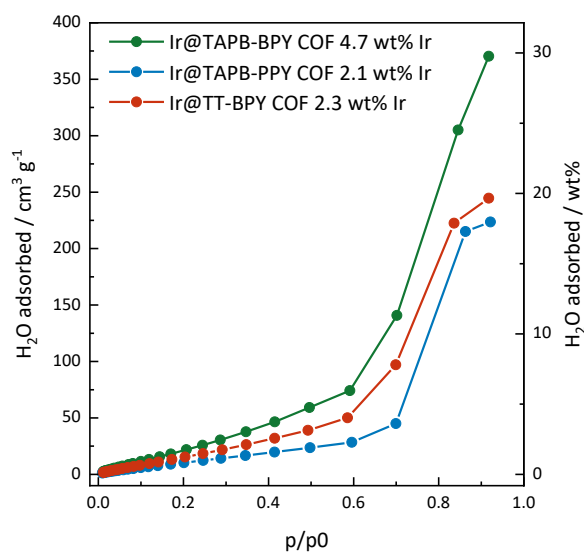
Figure S4-5: Comparison of water sorption isotherms (273 K) for iridium-loaded COFs. Only the adsorption branch is shown for clarity.
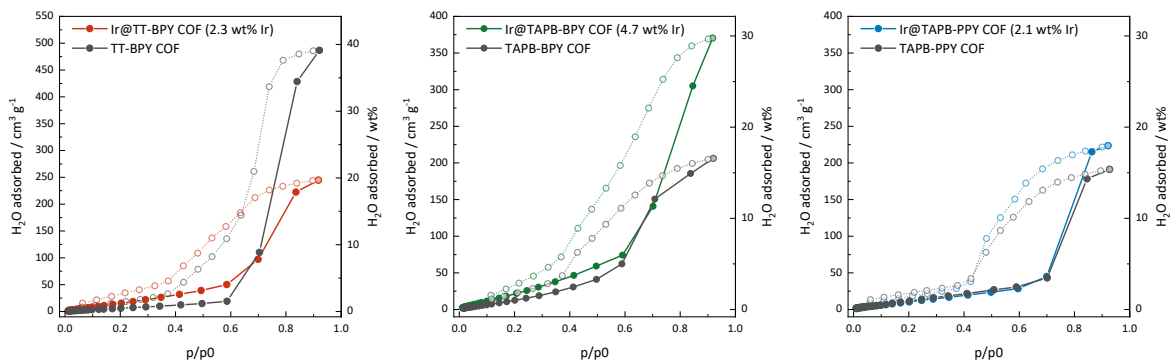
Figure S4-6: Water sorption isotherms at 273 K for Ir@TT-BPY COF, Ir@TAPB-BPY COF, and Ir@TAPB-PPY COF and their respective metal-free counterparts.
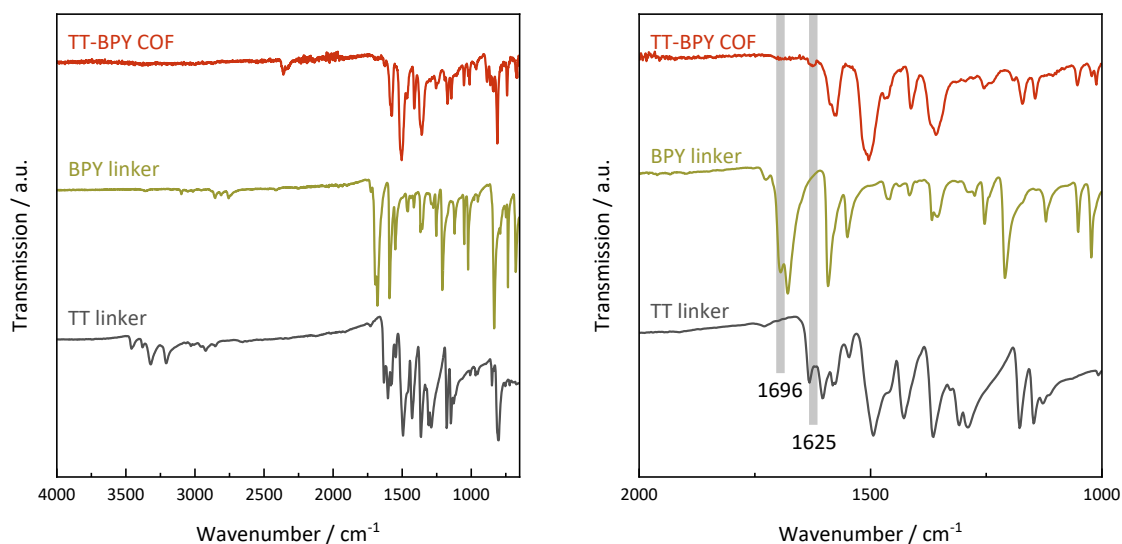
Figure S4-7: FTIR spectra for TT-BPY COF and the underlying building blocks BPY and TT. Annotations mark the aldehyde (1696 cm^{-1}) and imine bond (1625 cm^{-1}).
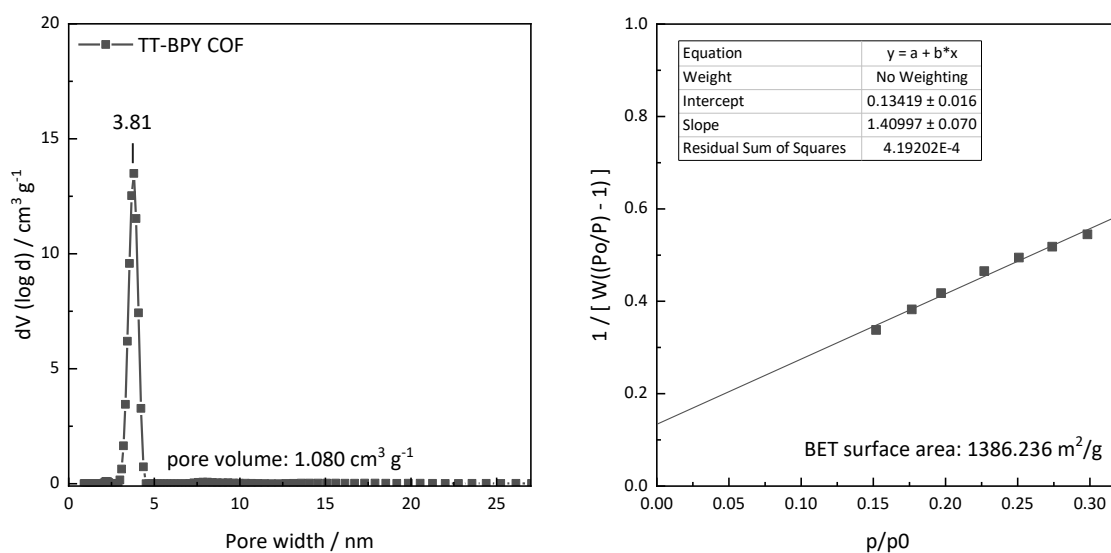
Figure S4-8: Pore size distribution for TT-BPY COF derived from the respective Ar isotherm using a QSDFT equilibrium kernel for cylindrical pores (left). Corresponding BET plot (right).

Table S4-1: Variation of iridium content in the post-synthetic loading of TT-BPY COF with [Cp*IrCl$_2$]$_2$.

Entry	Ratio Ir / bpy	Ir wt% expect.	Ir wt% meas.
1	1 / 24	1.87	1.56
2	1 / 12	3.59	2.42
3	1 / 6	6.67	4.76
4	1 / 3	11.66	7.57
5	1 / 0.75	23.71	15.07
6[a]	1 / 0.75	23.71	1.56

[a]: Loading conducted in MeOH instead of DMF
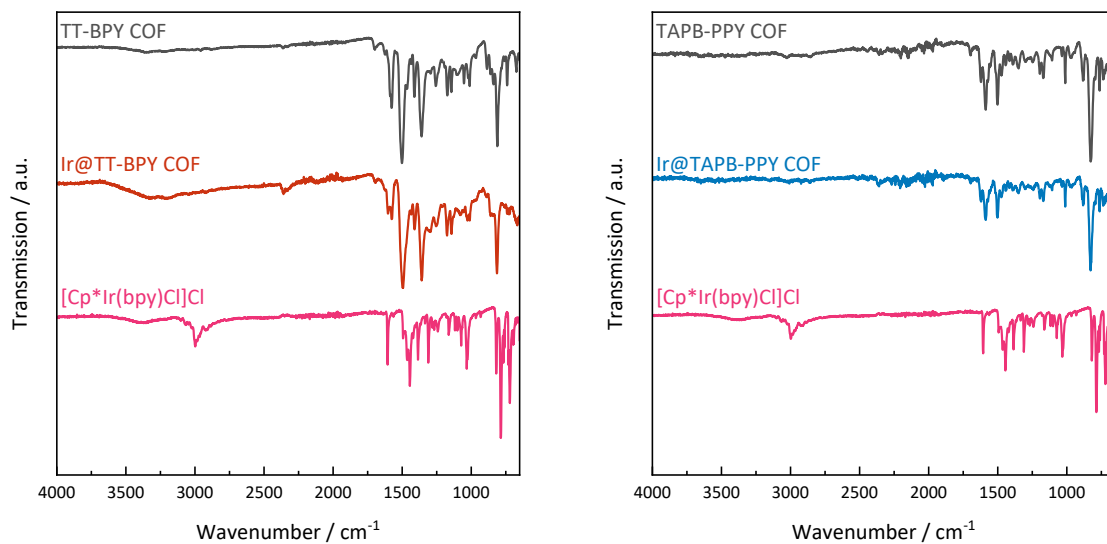
Figure S4-9: FTIR spectra for the loading of TT-BPY COF and TAPB-PPY COF with Cp*Ir.
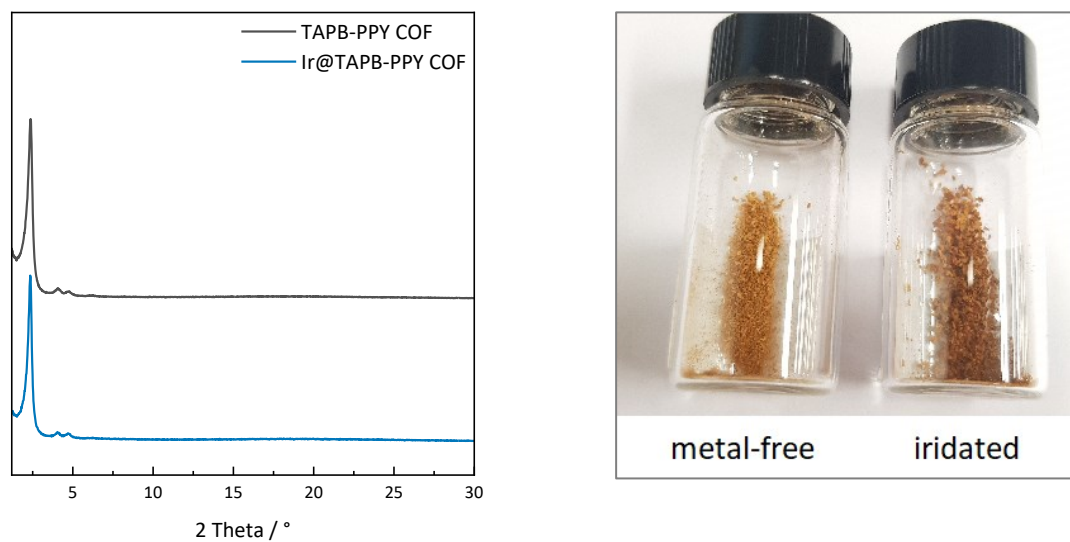
Figure S4-10: XRPD patterns (left) and photographic image (right) of TAPB-PPY COF and Ir@TAPB-PPY COF (ICP: 2 wt% Ir).
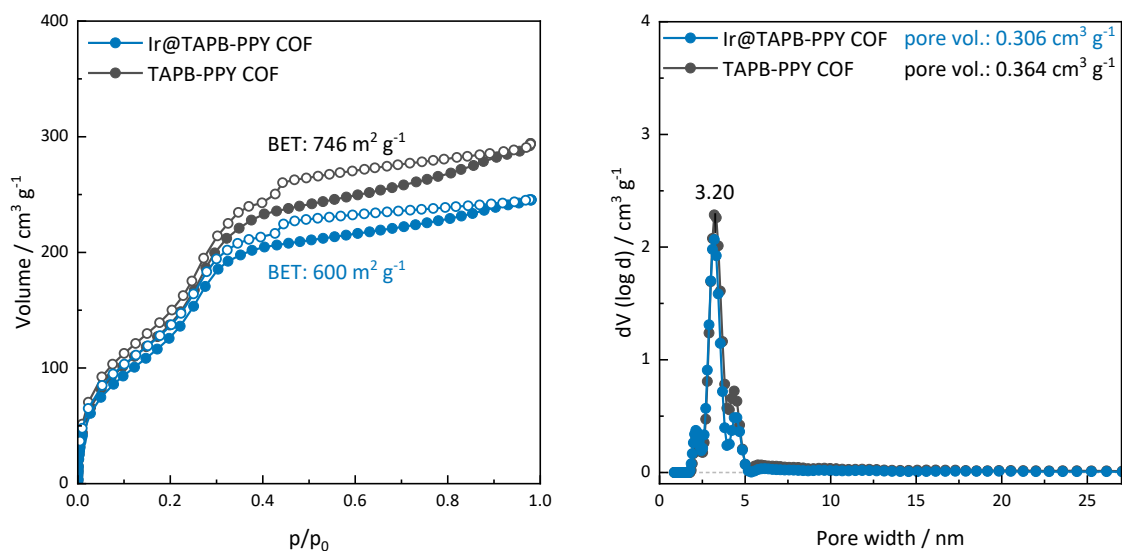
Figure S4-11: Argon sorption isotherm at 87 K for Ir@TAPB-PPY COF (ICP: 2 wt% Ir) and TAPB-PPY COF (left), and derived pore-size distribution (right; QSDFT equilibrium kernel, cylindrical pores).
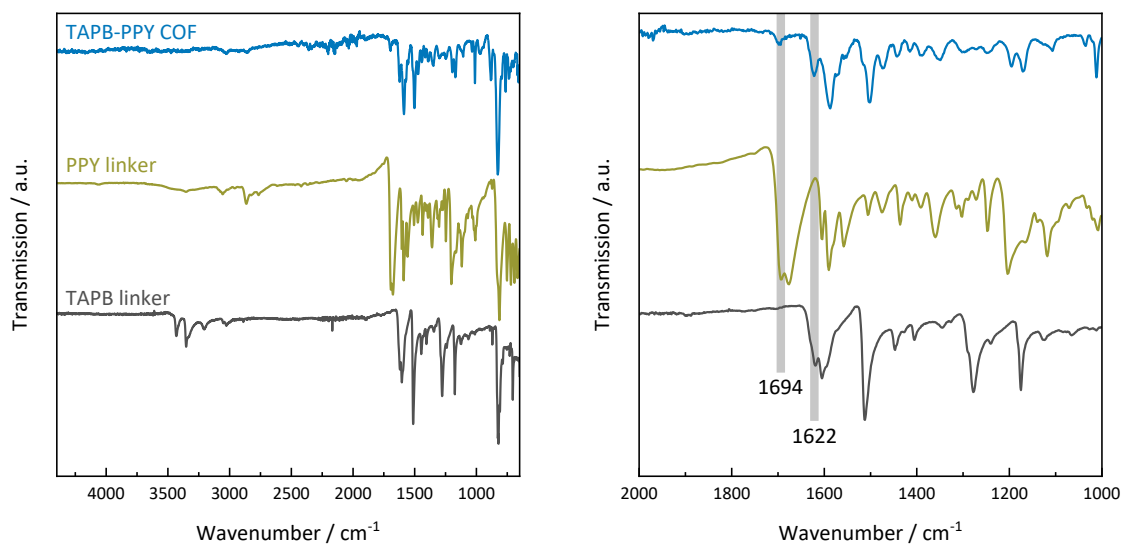
Figure S4-12: FTIR spectra for TAPB-PPY COF and the underlying building blocks PPY and TAPB. Annotations mark the aldehyde (1694 cm^{-1}) and imine bond (1622 cm^{-1}).
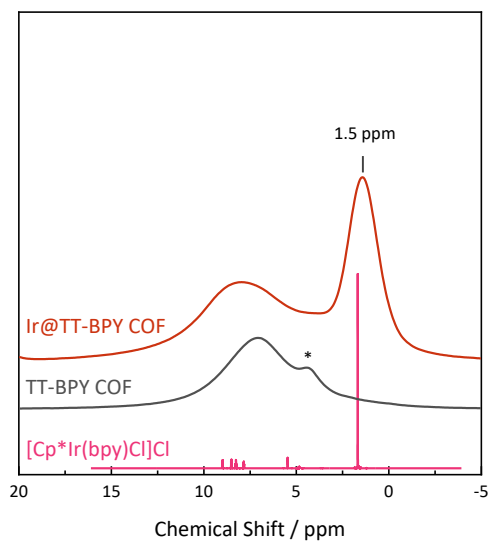
Figure S4-13: ^{1}H ssNMR spectra for TT-BPY COF before and after postsynthetic treatment with [Cp*IrCl$_2$]$_2$ compared to the NMR spectrum of [Cp*Ir(bpy)Cl]Cl dissolved in D$_2$O. Solvent residual signal at 4.79 ppm truncated for clarity. The signal around 5.47 ppm is assigned to residual dichloromethane.
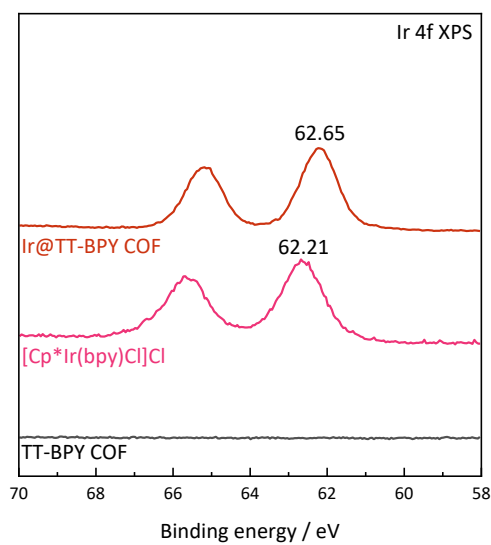
Figure S4-14: Iridium 4f XPS spectra for Ir@TT-BPY COF, [Cp*Ir(bpy)Cl]Cl, and parent TT-BPY COF.
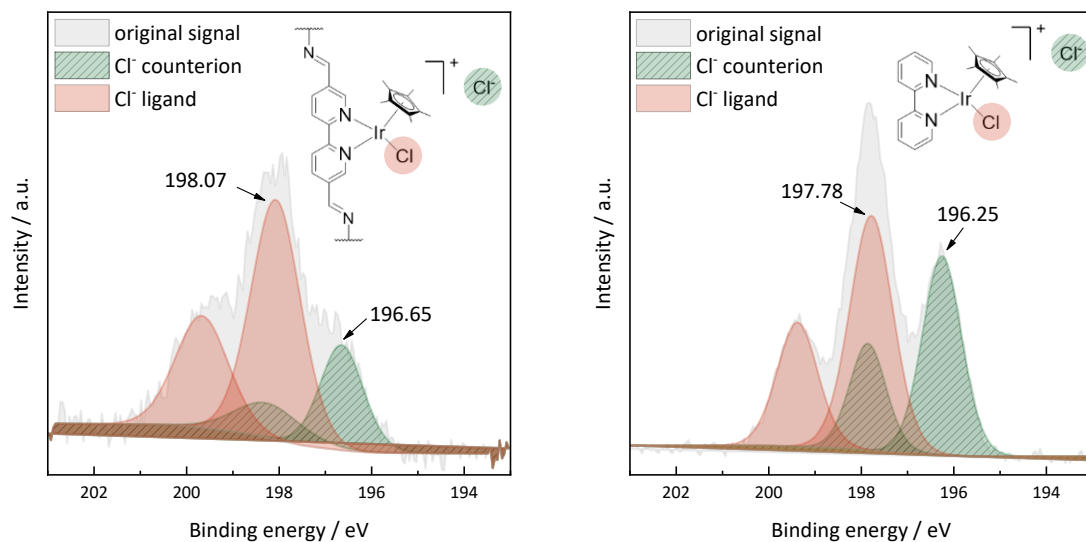
Figure S4-15: Chlorine 2p XPS spectra for Ir@TT-BPY COF (left) and [Cp*Ir(bpy)Cl]Cl (right) including deconvolution. The ratio of coordinated/bound Cl⁻ is 1:2.6 for Ir@TT-BPY COF and 1:1.3 for [Cp*Ir(bpy)Cl]Cl, respectively.
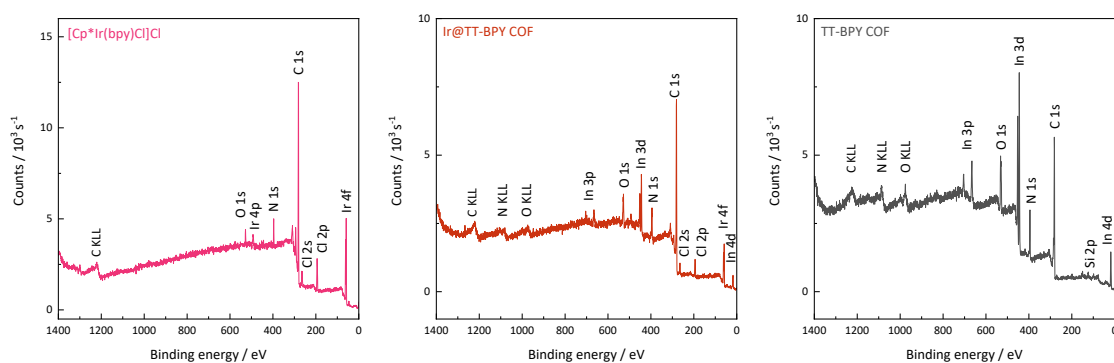
Figure S4-16: XPS spectra for [Cp*Ir(bpy)Cl]Cl (left), Ir@TT-BPY COF (middle), and parent TT-BPY COF (right).
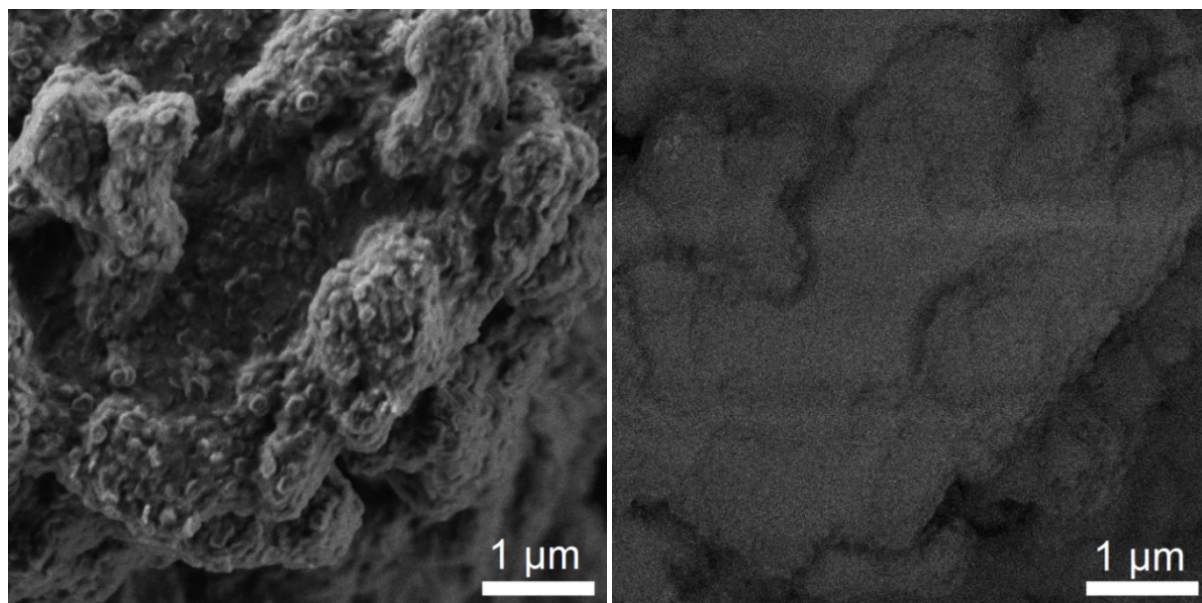
Figure S4-17: SEM images of TT-BPY COF with secondary electron detection (left) and energy selective backscattered electron detection (right).
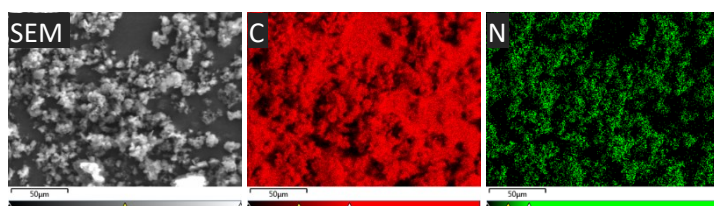
Figure S4-18: Elemental mapping (SEM) of TT-BPY COF.
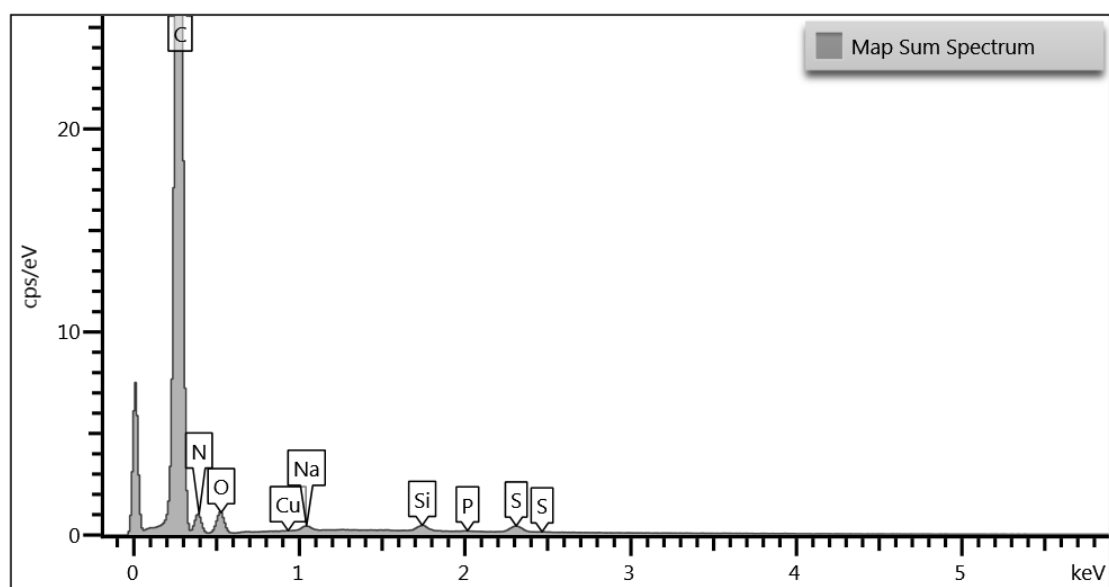
Figure S4-19: EDX sum spectrum for the elemental mapping of TT-BPY COF.
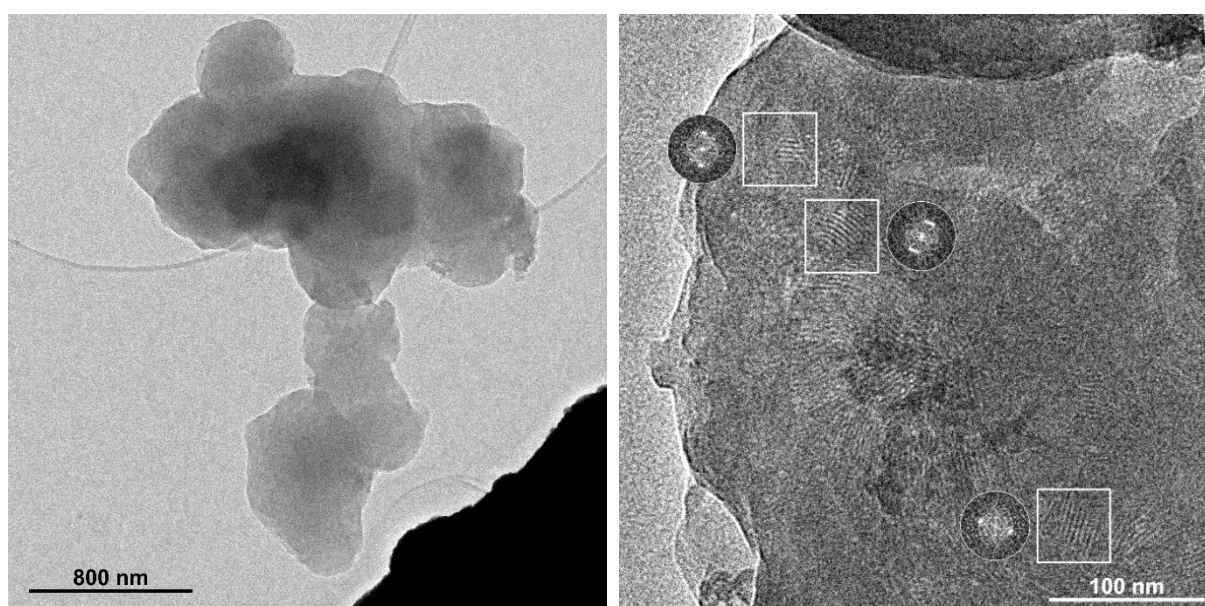
Figure S4-20: TEM images for TT-BPY COF. The FFT (insets, right image) indicate a periodicity of 3.4 nm.
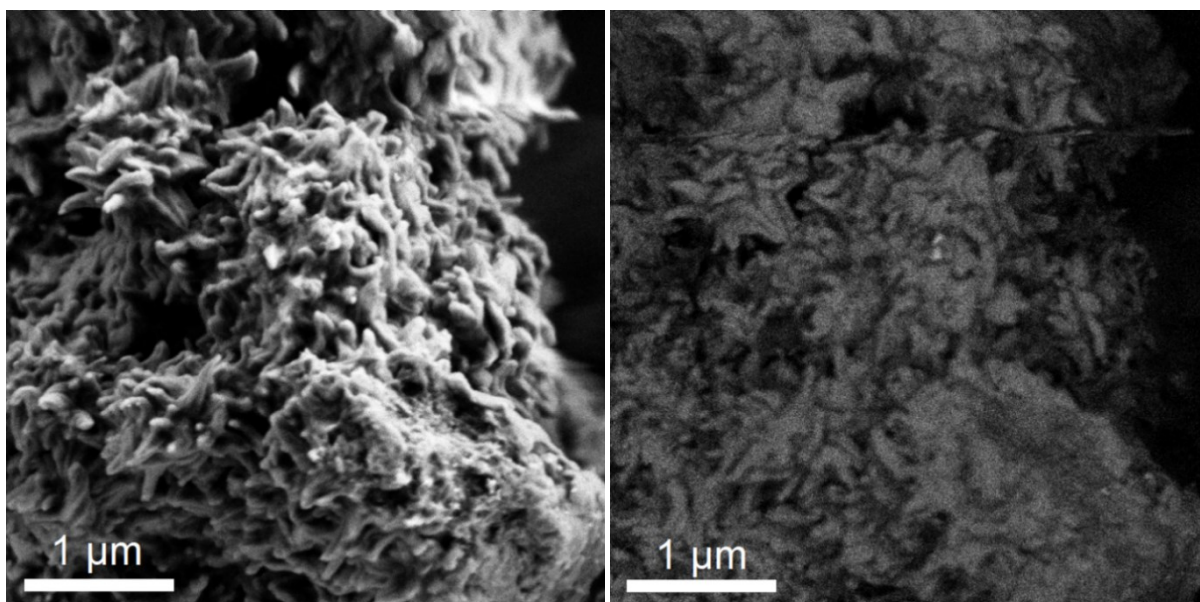
Figure S4-21: SEM images of Ir@TT-BPY COF with secondary electron detection (left) and energy selective backscattered electron detection (right).
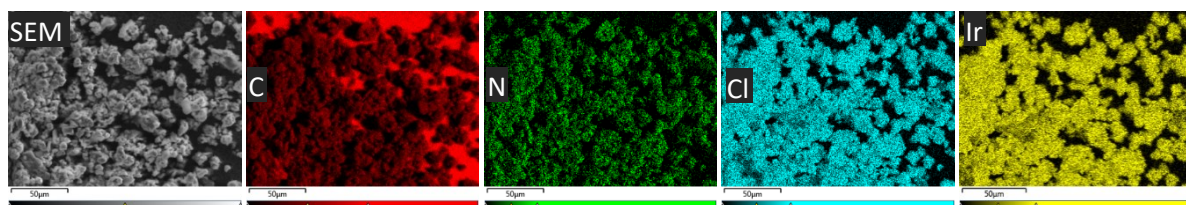
Figure S4-22: Elemental mapping (SEM) of Ir@TT-BPY COF.
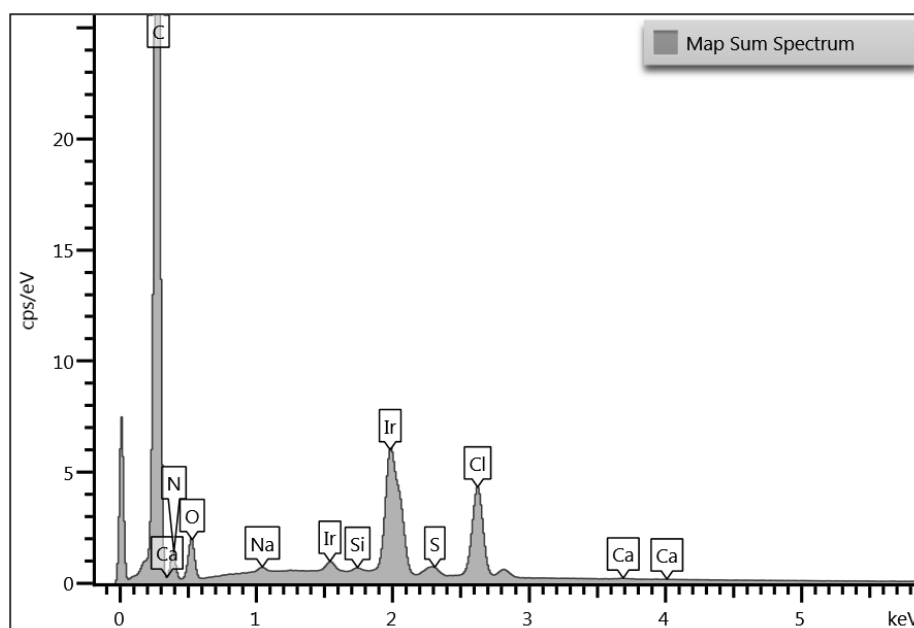
Figure S4-23: EDX sum spectrum for the elemental mapping of Ir@TT-BPY COF.
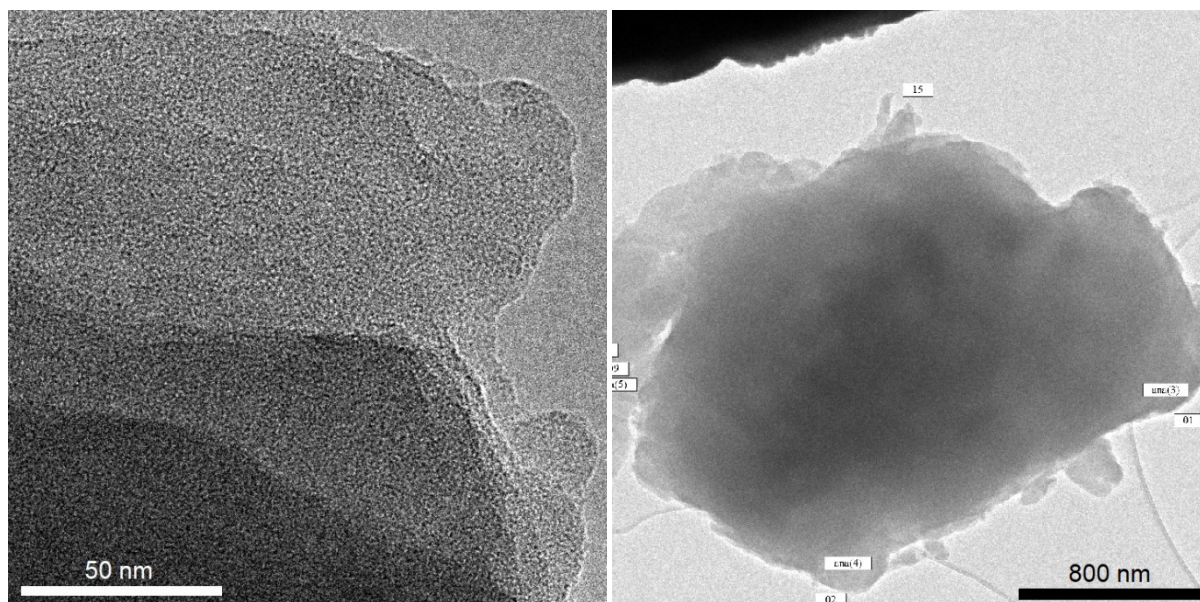
Figure S4-24: TEM images for Ir@TT-BPY COF.
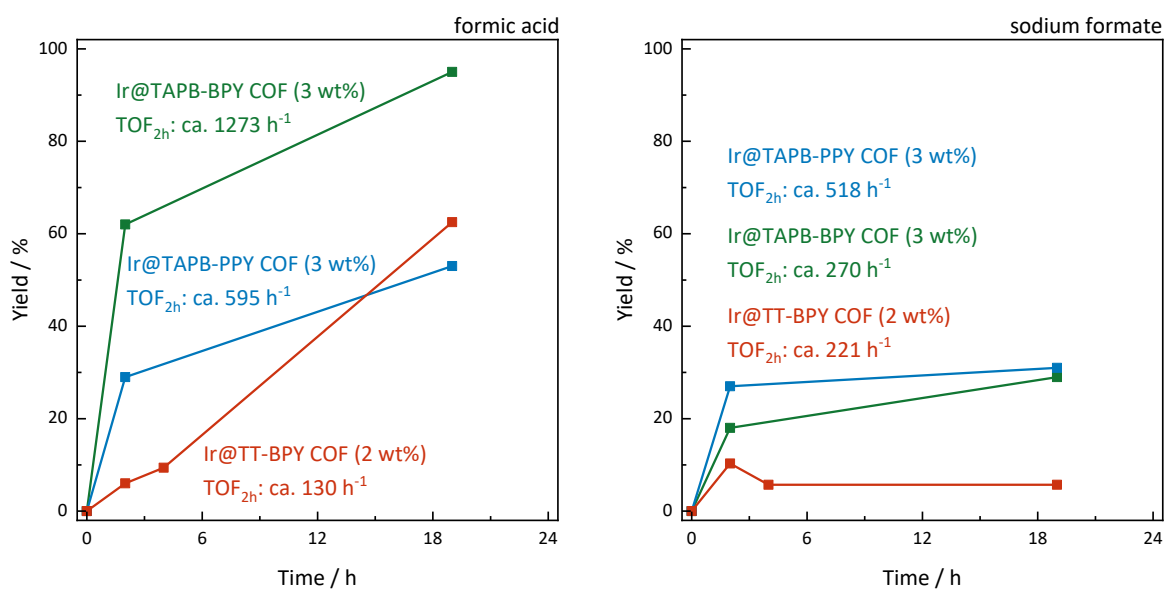
Figure S4-25: Hydrogenation of 4-Nitrobenzaldehyde over iridium-loaded COF catalysts using formic acid (left) or sodium formate (right) as hydrogen source. Varying iridium contents in the COFs were corrected through by the weighted COF amounts, so that the iridium amount is in the range of 4.6-4.9 mmol in either case.
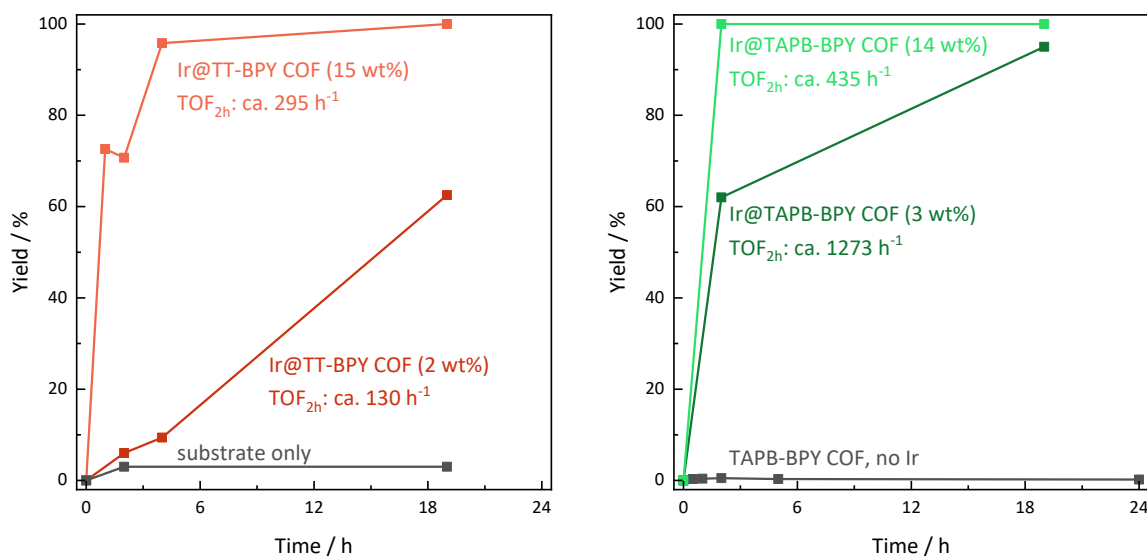
Figure S4-26: Hydrogenation of 4-Nitrobenzaldehyde over Ir@TT-BPY COF (left) and Ir@TAPB-BPY COF (right) with varying iridium content using formic acid as hydrogen source. Control experiments with iridium-free COF or without any additives show no conversion. In either case, the COF amount was 3 mg.
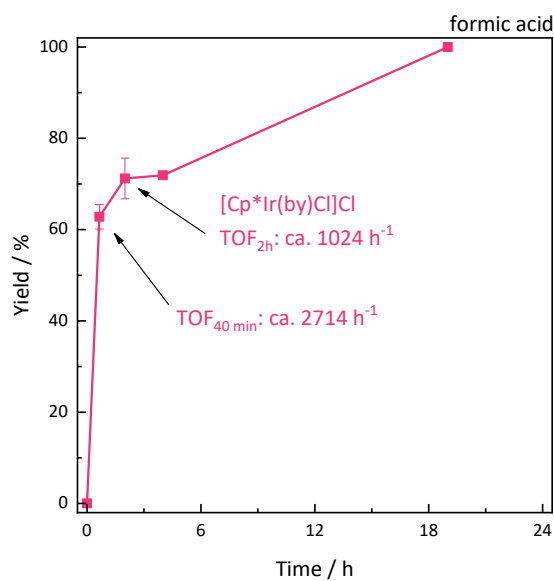
Figure S4-27: Hydrogenation of 4-Nitrobenzaldehyde by molecular [Cp*Ir(bpy)Cl]Cl using formic acid as hydrogen source. Duplicate experiment, error bars show standard deviation. The amount of iridium was 7 µmol in either case, corresponding to a concentration of 2.3 mM.
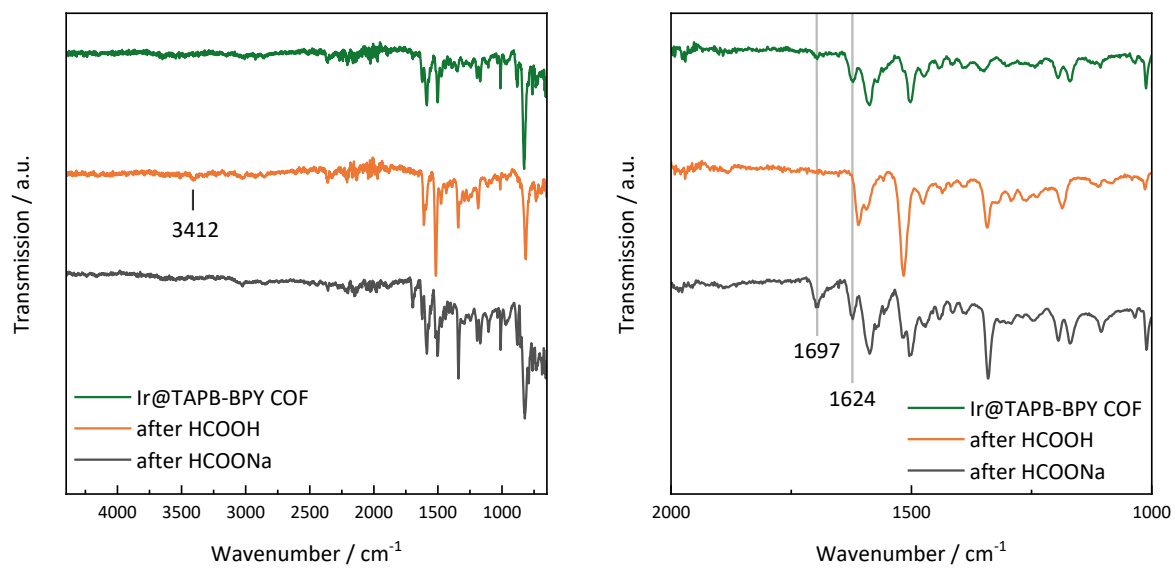
Figure S4-28: FTIR spectra of Ir@TAPB-BPY before and after before and after transfer hydrogenation reactions with formic acid or sodium formate.
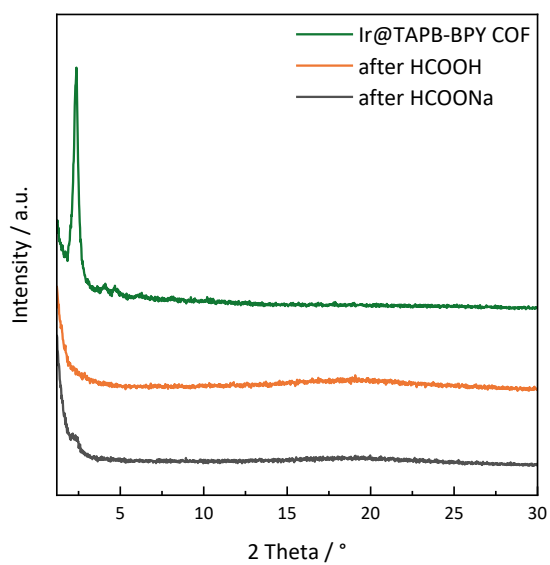
Figure S4-29: XRPD patterns for Ir@TAPB-BPY COF before and after transfer hydrogenation reactions with formic acid or sodium formate.
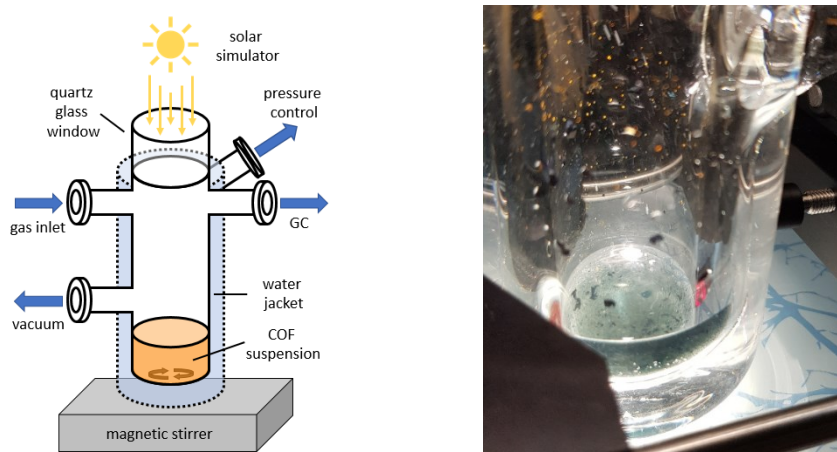
Figure S4-30: Schematic representation of the experimental setup used for WGS photocatalysis (left). After applying 1.5 bar of CO, a suspension of Ir@TT-BPY COF turns blue, whereas unsuspended COF particles show no color change (right, photographic image).

Table S4-12 Color changes during WGS catalysis in relation to catalytic activity.

Entry	Catalyst	Color before	Color under 1.5 bar CO	TOF / h^{-1}
1	Ir@TT-BPY COF	Orange suspension	Blue suspension	0.43
2	Ir@TAPB-BPY COF	Orange suspension	Green suspension	0.37
3	Ir@TB-PPY	Yellow suspension	Yellow suspension	<0.01
4	TT-BPY COF	Orange suspension	Orange suspension	-
5	[Cp*Ir(bpy)Cl]Cl	Dark yellow solution	Dark blue-green solution	3.82

TOF calculated from hydrogen evolution during the first three hours of reaction.
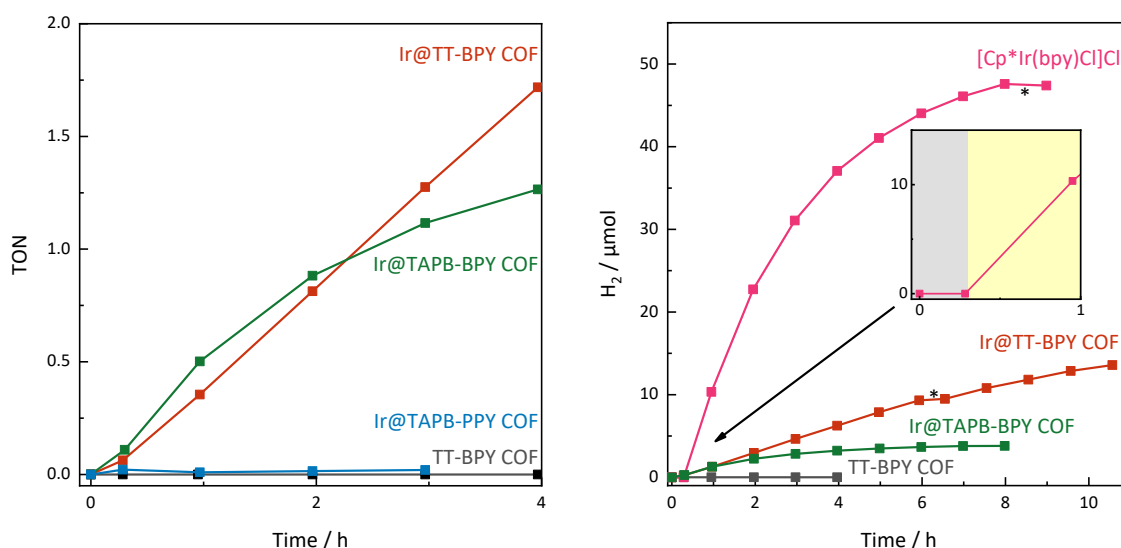

Figure S4-31: TON comparison of the isoreticular series of COFs used for photo-assisted WGS catalysis (left). TON plot for selected COFs in comparison to molecular [Cp*Ir(bpy)Cl]Cl (right). The inset shows the magnified trace for the molecular reference with indication of illumination times, showing that there is no hydrogen evolution in the dark.
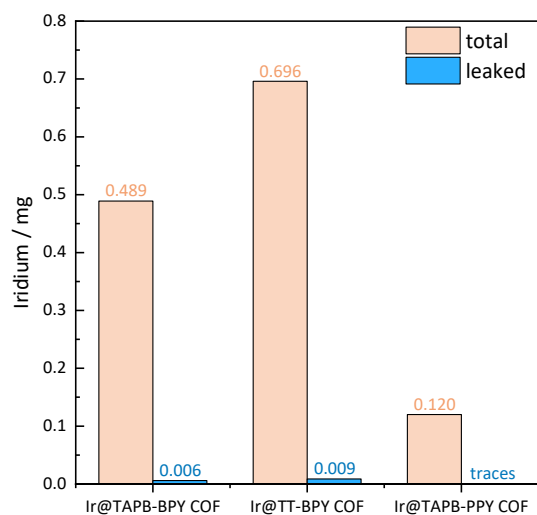
Figure S4-32: Leakage of iridium from Ir-loaded COFs into the reaction medium during WGS experiments.
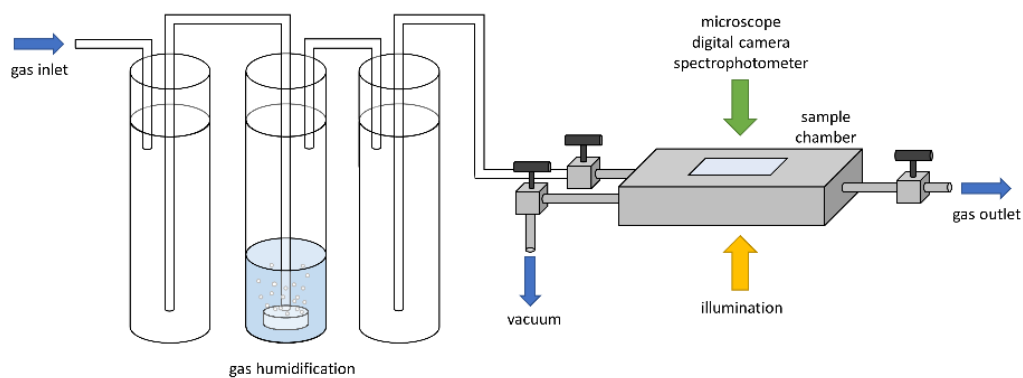

Figure S4-33: Experimental setup for in-situ imaging during CO exposure.
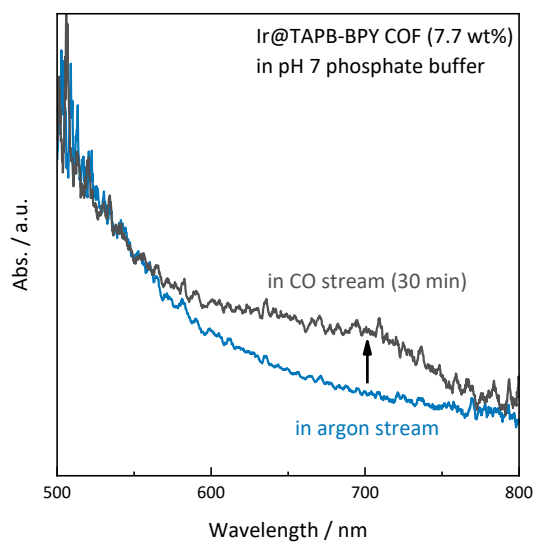

Figure S4-34: UV-Vis spectra of Ir@TAPB-BPY COF suspended in phosphate buffer (pH 7) before and after exposure to a CO stream.
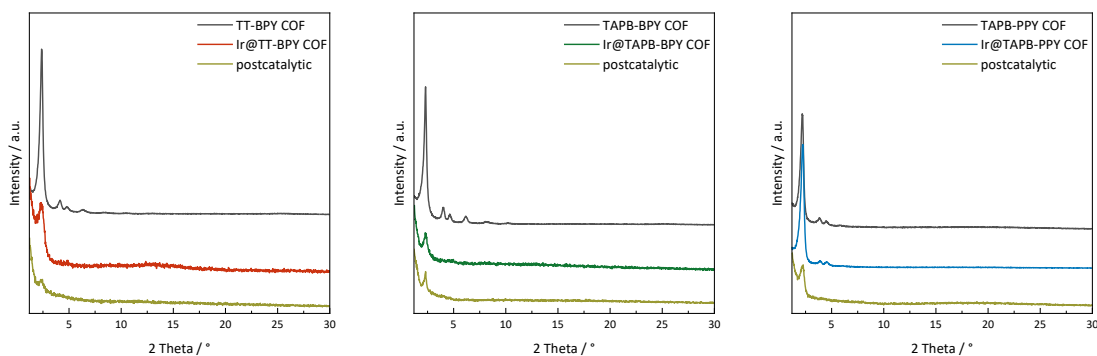
Figure S4-35: XRPD patterns for TT-BPY COF, TAPB-BPY COF, and TAPB-PPY COF before metalation, after iridium loading, and after subsequent WGS experiments.
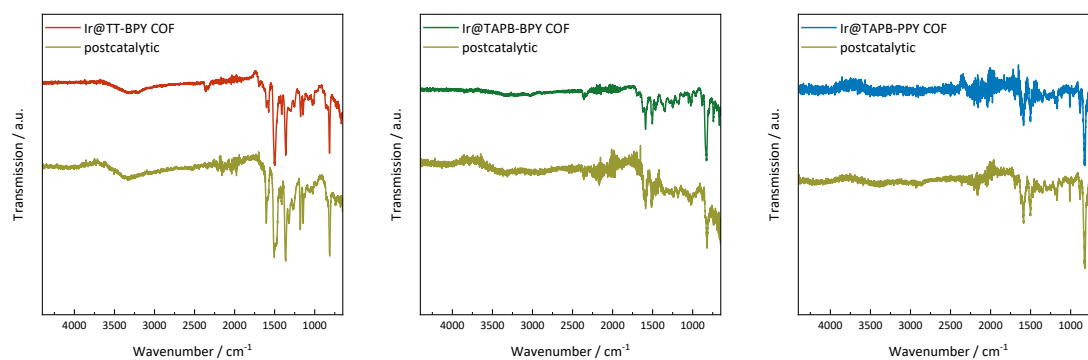

Figure S4-36: FTIR spectra for Ir@TT-BPY COF, Ir@TAPB-BPY COF, and Ir@TAPB-PPY COF before and after WGS experiments.
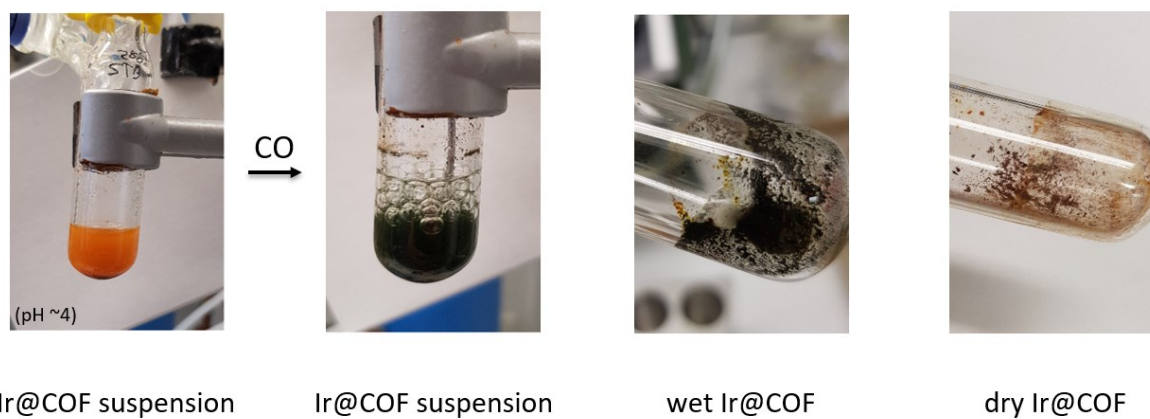
Figure S4-37: Photographic images of various stages during the attempted isolation of Ir-H species through reduction of Ir@TAPB-BPY COF with CO and subsequent removal of the solvent.
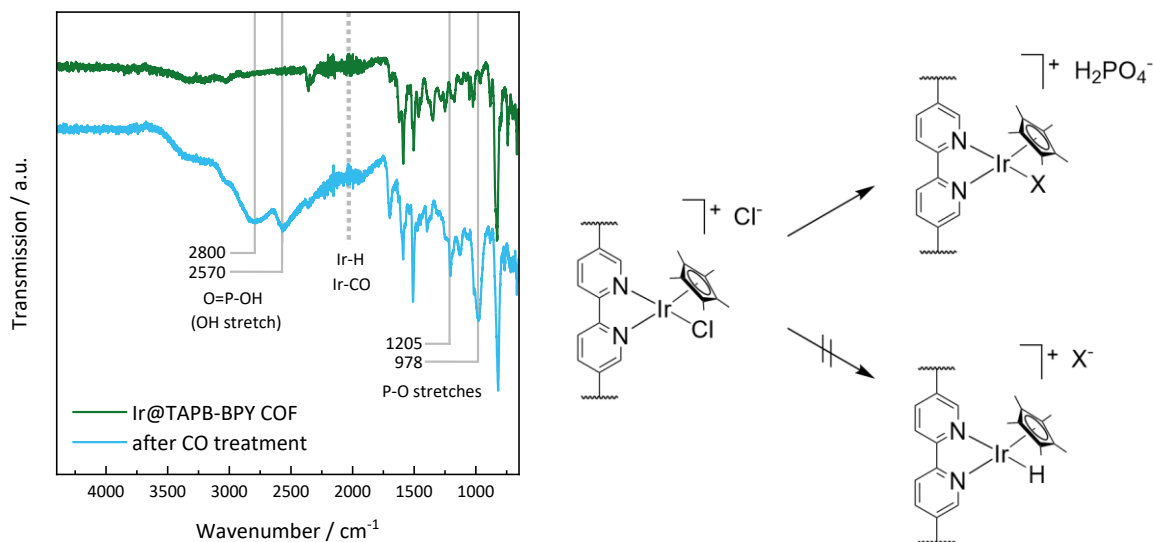
Figure S4-38: FTIR spectra of Ir@TAPB-BPY COF before and after attempted isolation of Ir-H species through reduction with CO (left). Proposed reaction scheme (right). FTIR References: [6,7]

6.4.4   References

1   T. L. Barr, S. Seal, *J. Vac. Sci. Technol. A* **1995**, *13*, 1239–1246.

2   P. Swift, *Surf. Interface Anal.* **1982**, *4*, 47–51.

3   L. Grunenberg, G. Savasci, S. T. Emmerling, F. Heck, S. Bette, A. C. Bergesch, C. Ochsenfeld, B. V. Lotsch, *J. Am. Chem. Soc.* **2023**, *145*, 13241–13248.

4   O. A. D. von Mankowski, Dissertation, **2018**, Ludwig-Maximilians-Universität München, München.

5   M. Y. Wong, G. Xie, C. Tourbillon, M. Sandroni, D. B. Cordes, A. M. Z. Slawin, I. D. W. Samuel, E. Zysman-Colman, *Dalton Trans.* **2015**, *44*, 8419-8432.

6   M.-T. Youinou, R. Ziessel, *J. Organomet. Chem.* **1989**, *363*, 197–208.

7   J. Xu, I. S. Butler, D. F.R. Gilson, *Spectrochim. Acta A* **1999**, *55*, 2801–2809.